SIZE-SELECTED MOLYBDENUM DISULFIDE CLUSTERS FOR HYDROGEN EVOLUTION

by

MARTIN CUDDY

A thesis submitted to
The University of Birmingham
for the degree of
DOCTOR OF PHILOSOPHY

School of Chemical Engineering
College of Engineering and Physical Sciences
The University of Birmingham
September 2013

Abstract

In this work, size-selected molybdenum disulfide (MoS_2) nanoclusters were produced using a magnetron sputter source and time-of-flight mass filter. Magnetron sputtering is a common industrial method for preparation of MoS_2 thin films. The combination of this technology with accurate size control allows us to produce, in high vacuum, lab-scale quantities of size-selected clusters. The strong spatial confinement effects in MoS_2 suggests that such control will modify the catalytic properties. This method also has potential to enhance MoS_2 performance in areas such as hydrodesulfurisation, intercalation batteries and tribology; as well as elucidating the dynamics of compound formation in the gas-phase.

Structural properties of these MoS_2 clusters are studied using aberration-corrected STEM. The optimum catalytic size range of 1-5 nm has not previously been studied in detail for gas phase synthesis. This work bridges the gap in the cluster beam literature between small, few atom clusters and the production of large MoS_2 fullerenes and monolayers.

It has been found that MoS_2 clusters display a characteristic layered structure down to the smallest studied cluster, 50 units of MoS_2. Growth of clusters proceeds by anisotropic growth from the reactive edge sites, subsequent addition of van der Waals bound layers, and finally coalescence of smaller units in the case of large clusters. The electrocatalytic properties of these clusters are explored by cyclic voltammetry and show good activity for the Hydrogen Evolution Reaction despite the presence of surface oxides. The reaction current normalised to loading matches some of the best catalysts produced to date.

Acknowledgments

My supervisors Richard & Neil, for their excellent guidance. Honourable mentions for the efforts of Bruno and Gianluca ;)

Everyone at NPRL, especially Kenton Arkill & Zhiwei Wang, and the Hydrogen Fuel Cell CDT that made this work possible

Anders Laursen at Danish Technical University, Jesse Benck at Stanford University, Alex Walton at Leeds EPSRC Nanoscience & Nanotechnology Facility, Paul Stanley at the UoB Centre for Electron Microscopy and Josh Tibbetts for fruitful collaborations

Steve Brookes & everyone at the Physics Workshop

Mark Cooke & his team for helping me with my IT duties

Mohamed Mughal & Ian Barnett at the Physics Stores

Special thanks to family, super friends, & Sarah

CONTENTS

LIST OF FIGURES

LIST OF ABBREVIATIONS

AFM	- Atomic Force Microscopy
CT	- Charge Transfer
EDS	- Energy Dispersive X-Ray Spectroscopy
EELS	- Electron Energy Loss Spectrometry
EIS	- Electrochemical Impedance Spectrometry
EPSRC	- The Engineering & Physical Sciences Research Council
GC	- Glassy Carbon
HAADF	- High Angle Annular Dark Field
HDS	- Hydrodesulfurisation
HER	- Hydrogen Evolution Reaction
HOPG	- Highly Oriented Pyrolytic Graphite
HV	- High-Vacuum
IF	- Inorganic Fullerene
LEED	- Low Energy Electron Diffraction
NPRL	- Nanoscale Physics Research Laboratory

RDE - Rotating Disk Electrode

RHE - Reversible Hydrogen Electrode

SCCM - Standard Cubic Centimetre per Minute

SCE - Standard Calomel Electrode

SHE - Standard Hydrogen Electrode

SPM - Scanning Probe Microscopy

STEM - Scanning Tranmission Electron Microscopy

STM - Scanning Tunnelling Microscopy

TEM - Transmission Electron Microscope

ToF - Time-of-Flight

TSP - Titanium Sublimation Pump

UHV - Ultra-High Vacuum

WDS - Wavelength Dispersive X-Ray Spectroscopy

XRD - X-Ray Diffraction

CHAPTER 1

INTRODUCTION

1.1 Motivation

1.1.1 Hydrogen Economy

The energy landscape is soon to see a shift as fossil fuel depletion continues. Cleaner energy systems than gasoline have started to gain attention as the rising fossil fuel price makes them more competitive [1] and climate change becomes a greater concern [2]. The focus of research has been on sustainable power, especially utilising renewable resources such as solar and wind. A major barrier for renewables is that the intermittent generation prohibits matching supply-demand cycles of consumer use. One possible solution is to control the power of renewable energy by transforming it into a storable energy vector. Unfortunately storing electricity on a large scale is not cost effective with battery technology, so an alternative is needed. The logical step is a transformation to chemical energy, with the inherent energy loss balanced by the more predictable nature and increased usability. Electrochemical generation of hydrogen as an energy vector is one of the simplest solutions, as the reaction requires water and energy, produces only hydrogen and oxygen and the recombination step is just as clean. This leads to the idea of a Hydrogen Economy [3, 4, 5, 6, 7, 8, 9], in which hydrogen is generated from renewable or waste energy [10], stored until needed and used to generate power in a zero-emission system [11] (Fig 1.1).

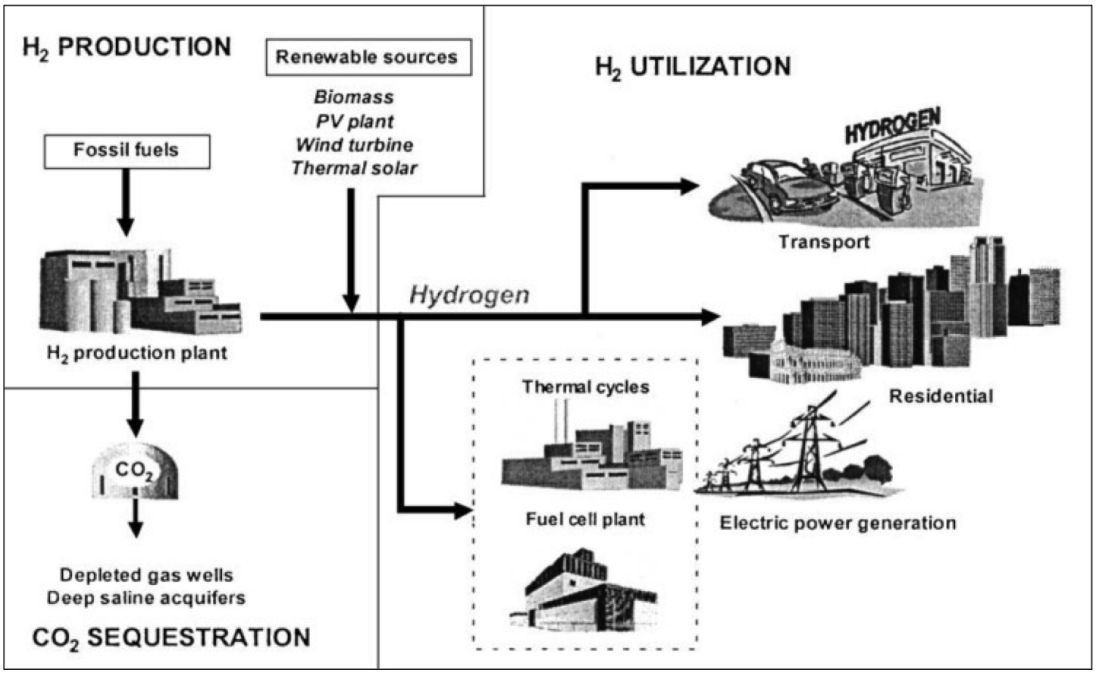

Figure 1.1: The Hydrogen Economy envisions a cycle of hydrogen production, sourced from renewable energy, which can then be used for diverse applications with no local pollution, from [12].

The distributed usage of fossil fuels, in transport for example, generates the most difficult pollution to clean in the fossil fuel cycle, so by moving to Hydrogen this could be reduced significantly. Even used in a hybrid system, in which the hydrogen was generated from fossil fuels, there would still be environmental benefits as it is easier to capture emissions from single large sites as opposed to mobile exhausts.

1.1.2 Replacement of Critical Metals

Next generation and emerging technologies in the energy sector are fast growing and putting pressure on resources, particularly critical metals used for catalysis. Platinum is used as a fuel cell and hydrogen generation catalyst, but the price is a significant barrier to expansion of the technology and scarcity hinders large-scale use [13] (Fig 1.2). Analogues and methods of reducing use of critical metals are an important part of current catalyst research. Molybdenum disulfide (MoS_2) has been identified as a cheap, abundant alternative to platinum [14, 15], with the further benefit over noble metals that the

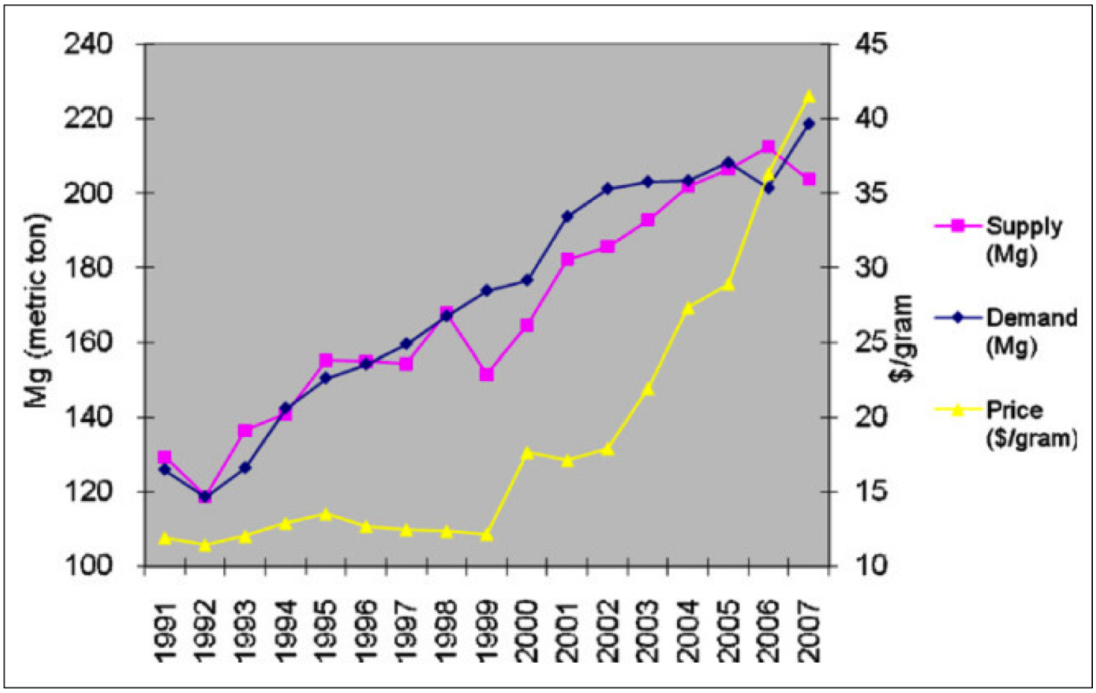

Figure 1.2: The price of platinum continues to rise with supply only just matching demand, from [13].

semiconductor nature allows photocatalysis and tuning of electronic states by quantum confinement [16].

1.2 Novelty

1.2.1 Controlled Fabrication

The majority of nanoscale MoS_2 production methods use high temperature sulfidation to achieve stoichiometric nanostructures [17, 18, 19, 20]. The use of hazardous sulfiding chemicals such as H_2S and high temperature that is incompatible with sensitive devices [21] prevents these methods for some applications. Furthermore, such sulfidation processes and chemical syntheses do not allow accurate size control of these nanoparticles, which is necessary for characterisation of size effects and optimisation of structure.

This work highlights the benefits of gas-phase catalyst production. The magnetron fabrication could directly use the abundant raw material molybdenite, the ore of molybde-

num, thus reducing cost and complexity in refining steps. The deposition of MoS_2 thin films as a lubricant commonly uses gas-phase fabrication [22, 23]. Often such films are discovered to be sulfur-deficient in composition and the lamellar structure is disordered. The detailed analysis of small clusters produced by direct magnetron sputtering of an MoS_2 target may provide insights into the thin film constituents and how they coalesce to form a continuous layer. This could then lead to improved lubrication in space and vacuum applications.

Furthermore, the ability to mass-select clusters in a catalytically relevant size regime opens the possibility of determining the most active size and structure of the catalyst without ligands and liquid contamination. High resolution microscopy can correlate clear structural features with electrochemical testing to identify the active sites at the atomic scale. The final industrial output can also benefit in material efficiency by picking out the most active species with continuous in-flight mass-selection and recycling of discarded sizes.

1.2.2 Binary Materials

Finally, selective reactivity and efficient nanoscale processes are reaching the limit of what can be achieved with conventional materials. The fabrication of binary clusters is important to gain the benefits of multiple materials and even achieve synergistic effects not possible with each individual element [24, 25, 26]. Size-selected magnetron sputtering can be used to produce alloys and compounds with core-shell or mixed structures in a range of sizes [27, 28, 29]. There is increasing interest in nanostructures of MoS_2 for electronic applications in transistors [30, 31], catalysts [32, 33] and intercalation electrodes [34, 35]. Gas phase fabrication provides potential for precise control of binary materials and the ratio of their constituents, in order to tailor the material to the application.

CHAPTER 2

BACKGROUND

2.1 Bulk MoS_2

Molybdenum disulfide (MoS_2) in the bulk is a semiconductor that occurs naturally as the molybdenum ore, molybdenite. Bulk MoS_2 has a lamellar structure with covalently bonded trilayers of molybdenum sandwiched between two sulfur layers. These trilayers are loosely bound with Van der Waals interactions, analogously to graphite layers. There are three main polytypes of bulk MoS_2 crystal structure: 1T [36], 2H and 3R [37], with 2H being the most stable form [38]. This structure consists of the stacked trilayer structure with every 2 stacks offset such that two MoS_2 trilayers are included in the unit cell. The van der Waals gap, the (002) plane, has a spacing of around 0.6 nm (Fig 2.1A). Each individual Mo atom is coordinated in a trigonal prismatic manner with six adjacent S atoms [39], this gives rise to a hexagonal structure when viewed along the c axis (normal to layers) (Fig 2.1B). The characteristic spacing of the (100) plane in the hexagonal lattice is 0.26 nm and 0.16 nm for the (110) plane. The covalent bonding results in an oxidation state of +4 for the Mo unit and -2 for the two sulfur atoms.

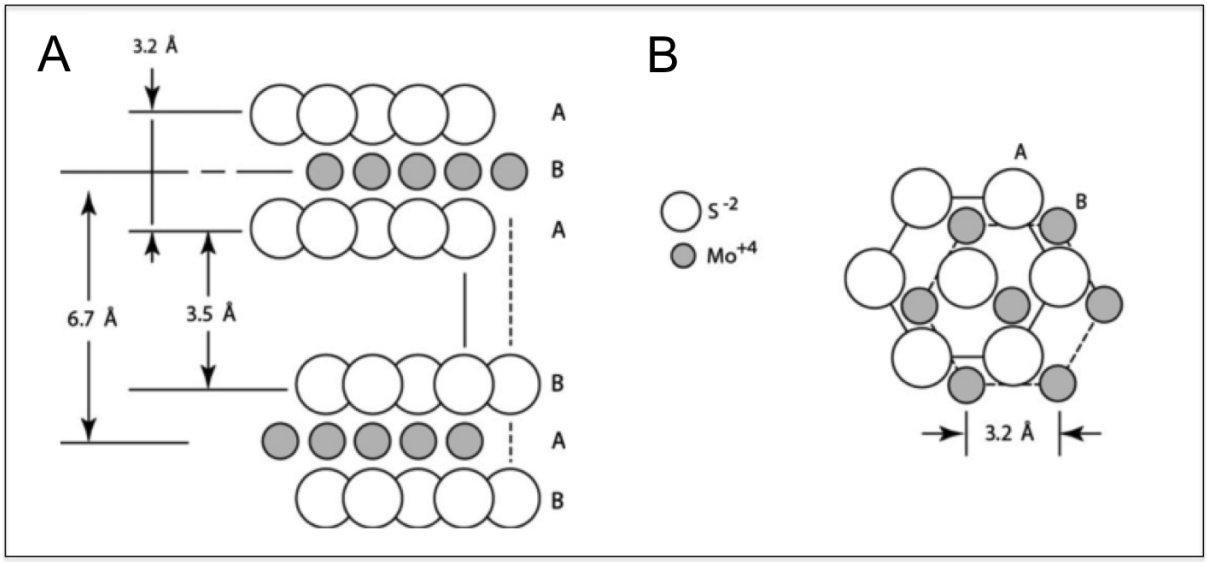

Figure 2.1: (A) Bulk MoS_2 viewed parallel to basal plane shows stacked trilayer structure. (B) Perpendicular to the basal plane the trigonal crystal structure can be seen. Adapted from [40]

2.2 Nanoscale Fabrication Methods

There are many ways to fabricate nanoscale structures of MoS_2 (and other materials), which include layered platelets similar to the bulk, closed shells analogous to fullerenes and macroscopic monolayers. Common methods for making nanostructures of MoS_2 start with either bulk MoS_2, molybdenum or elemental precursors. The method discussed in this work uses the bulk material, in the form of a hot-pressed powder, that is sputtered and condensed to produce clusters. This method opens the option of eventually using the raw ore for mass-production at low cost. Other nanofabrication methods for MoS_2 nanostructures in the literature will now be briefly discussed for comparison.

2.2.1 Mo Sulfidation

Elemental Mo or MoO_3 is heated to temperatures around 673°K while in the presence of a sulfur source, such as thiourea, H_2S gas or sulfur itself (Fig 2.2). This temperature is sufficient to create single crystal nanoparticles, however for large sheets it produces micro-crystalline defect-rich MoS_2 unless a temperature of 1073°K is used [41]. The

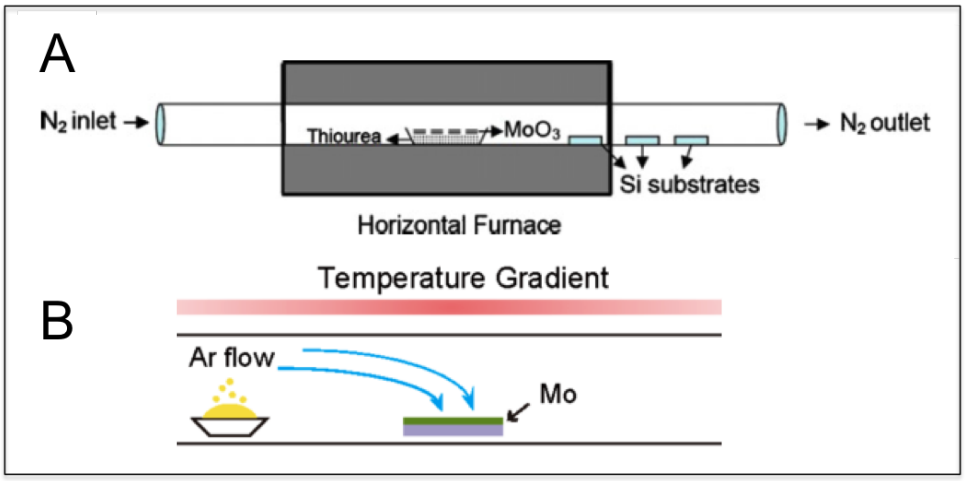

Figure 2.2: (A) Sulfidation process in which both Mo and S components are in the gas-phase [42]. (B) Sulfidation of supported molybdenum by elemental sulfur [43].

molybdenum precursor nanoparticle is usually pinned to a support to prevent sintering during the high temperature process. Nanoparticles produced by this method are usually well crystallised but size control is difficult.

2.2.2 Reactive Furnace

A furnace with multiple temperature regions is used to heat a crucible of elemental Mo or MoO_3 in a H_2S gas flow [44], this can be achieved in a simple tube furnace as above but bespoke systems have been produced to enhance yield (Fig 2.3). The nanostructures grow in the gas-phase and move through the furnace via gas-flow to be deposited in the form of a powder. This powder can then be filtered to remove ash components from the nanoparticles. This process is very similar to the Mo sulfidation described above, however such furnaces are primarily used to produce inorganic fullerene-type MoS_2 (IF-MoS_2). In an unoptimised system, platelets are formed as with the supported sulfidation, however with correct gas-flow, condensation lengths and diffusion parameters a yield of 100% fullerene MoS_2 can be obtained [45].

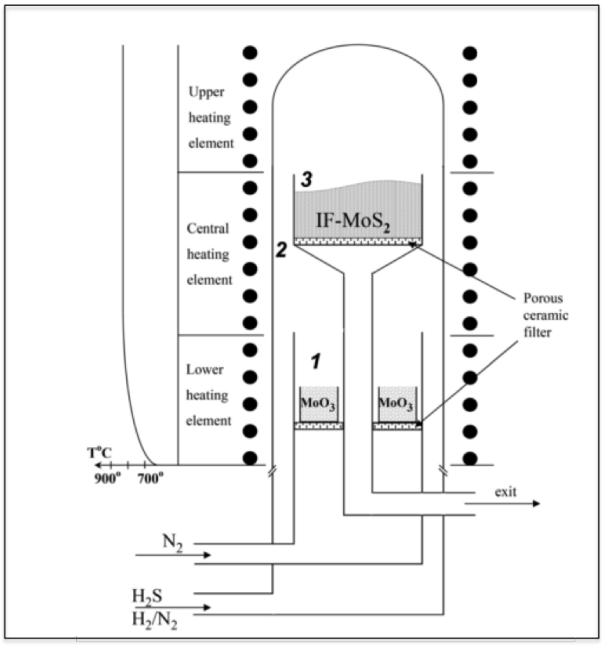

Figure 2.3: An advanced furnace used for continued production of IF-MoS_2 from sulfidised MoO_3 powder, from [46]

2.2.3 Pulsed Cluster Sources

Laser ablation and pulsed arcing sputter atomic seeds from a target material [47] (Fig 2.4). This can be MoS_2, but more frequently an Mo rod is used with a sulfur source, such as H_2S. Helium gas, with a small percentage of sulfiding gas, is admitted into a nucleation chamber which induces the seeds to condense into nanoparticles (This method is discussed in more detail in Section 3.2). The charged nanoparticles can be size-selected by their mass-charge ratio with a quadrupole mass filter. A similar concept also uses pulsed arcs on a target rod immersed in water, the nanoparticles produced at the arc site immediately enter suspension and can be centrifuged out subsequently. Similarly to the non-cluster based methods above, these sources can produce both platelets and IF-MoS_2 depending on conditions.

2.2.4 Electron Irradiation

Prolonged irradiation of powdered MoS_2 with a 0.5 MeV electron beam causes restructuring of the material due to the high energy density [48]. The availability of Mo and S is fixed

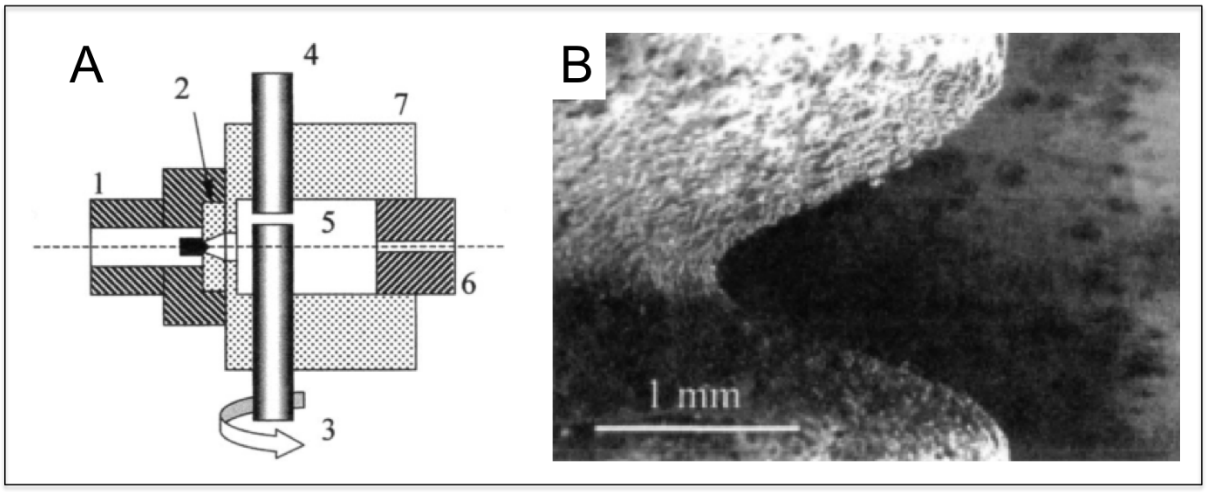

Figure 2.4: (A) The Pulsed Microplasma Cluster Source (PMCS) injects a pulse of helium around a target cathode, which is then ionised by a pulsed discharge between the cathode rod (3) and an anode (4). (B) The localisation of the He plasma creates a uniform sputter trench in the cathode rod, from [47].

from the start, unlike the fabrication processes that use an abundant flow of sulfiding gas. Restructuring can also be seen in this study by rastering a 0.2 MeV electron beam, from a scanning transmission electron microscope, over a nanoparticle while imaging (Section 5.6.6). The extent of this reconstruction is dissociation and modification of the crystal structure in the platelet. The 0.5 MeV electron beam provides enough energy to create IF-MoS_2 nanoparticles, either due to layer bending or dissociation and condensation. The lack of control over reactants means platelets are still abundant, however the high energy beam causes rotation between layers resulting in Moiré patterns (Fig 2.5).

2.2.5 Exfoliation

The method of mechanical exfoliation made famous by graphene [49], has also been applied to MoS_2 [50, 51]. A bulk crystal is cleaved with adhesive tape repeatedly over a substrate, with single and few layer fragments settling on the surface (Fig 2.6). The fragments produced will be of different layer heights and lateral dimensions, so this technique is not suited for producing uniform nanostructures on a large scale. This method usually involves locating a single nanostructure of interest on the substrate and microfabricating

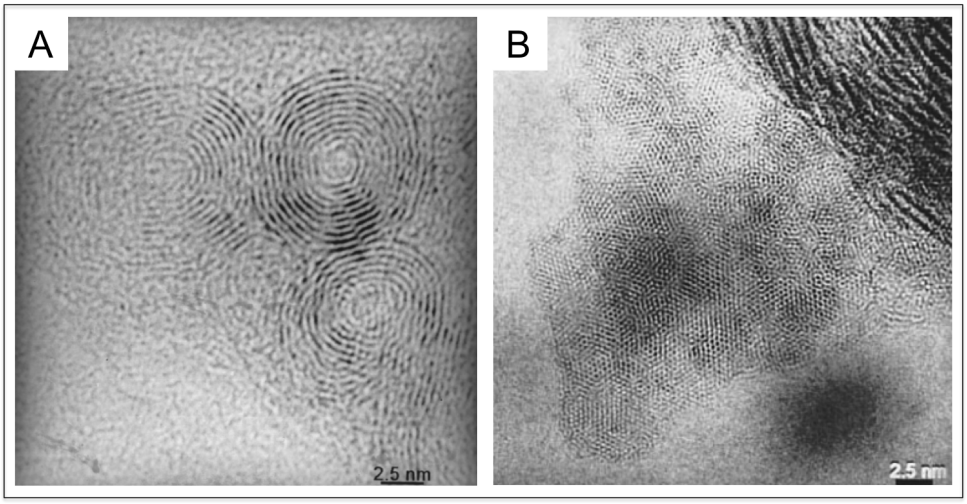

Figure 2.5: (A) Multi-walled nanoshells created after electron beam irradiation. (B) Another irradiated region shows two MoS_2 layers rotated by 10 degrees to produce a Moire pattern, from [48].

measurement electronics around it.

Exfoliation of a whole crystal or collection of nanoparticles can be achieved by intercalation of lithium [38]. The MoS_2 is soaked in a lithium solution for several hours to saturate the interlayer gaps, then exposed to water. The subsequent hydrolysis reaction produces hydrogen gas which causes the exfoliation. The suspension of few layer nanosheets can be produced in the presence of a support such as alumina to generate industrial catalyst material.

2.2.6 Etching

Standard lithography techniques can be applied to bulk MoS_2 to etch arrays of nanopillars or remove layers (Fig 2.7). Several methods have been performed at NPRL by Ahmed Abdela to obtain different etched structures. Firstly, a mask of size-selected metal clusters is deposited on a crystal of MoS_2, this surface is etched to produce a disordered, but monodispersed, array of well size-controlled nanopillars (Section A.2). Secondly, a more complex procedure based on previous work at NPRL [53], requires evaporation of metal into the interstices of a polymer nanosphere film, the nanospheres are then removed to allow etching with an ordered metal mask. This produces an array of uniformly spaced

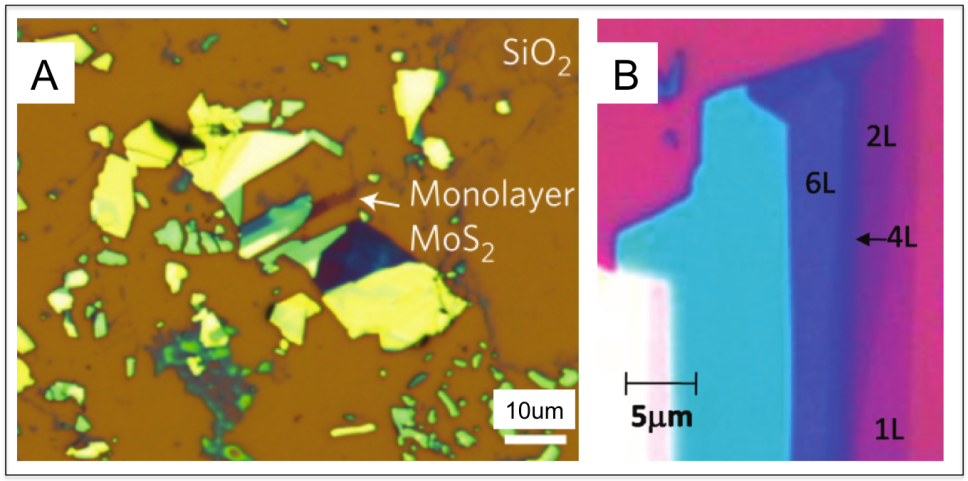

Figure 2.6: (A) Few and Single layer sheets of MoS_2 can be deposited by mechanical exfoliation of a bulk crystal, from [52]. (B) Monolayers of MoS_2 can be simply identified by contrast change, from [51].

nanopillars but with reduced diameter control. The final method simplifies the second by using the nanosphere film itself as an etch mask, this produces an array of nanopillars similar to the second method. Elsewhere in the literature etching of MoS_2 is uncommon, but there are instances of its use to thin MoS_2 flakes to produce monolayers [54, 55].

2.2.7 Precursor Reduction

The compound ammonium tetrathiomolybdate (ATM) contains an MoS_4^{2-} anion that is reduced to produce MoS_2 (Discussed in Section 3.6.1). ATM is the most common precursor used in literature, but there are other variants [56, 57]. The precursor can be used to synthesise nanoparticles by hydrothermal reduction in the presence of a stabilising polymer [58]. This simple method is used as the basis for chemically produced nanoparticles in Section 3.6. The reduction can also be achieved in an electrochemical cell in order to produce coatings on flat substrates [59, 60], graphene [24] and carbon nanotubes [61].

2.2.8 Inverse Micelles

Surfactant molecules in a nonpolar medium will form small closed cages to prevent contact of the hydrophilic end groups with the medium. This process can be used to encapsulate

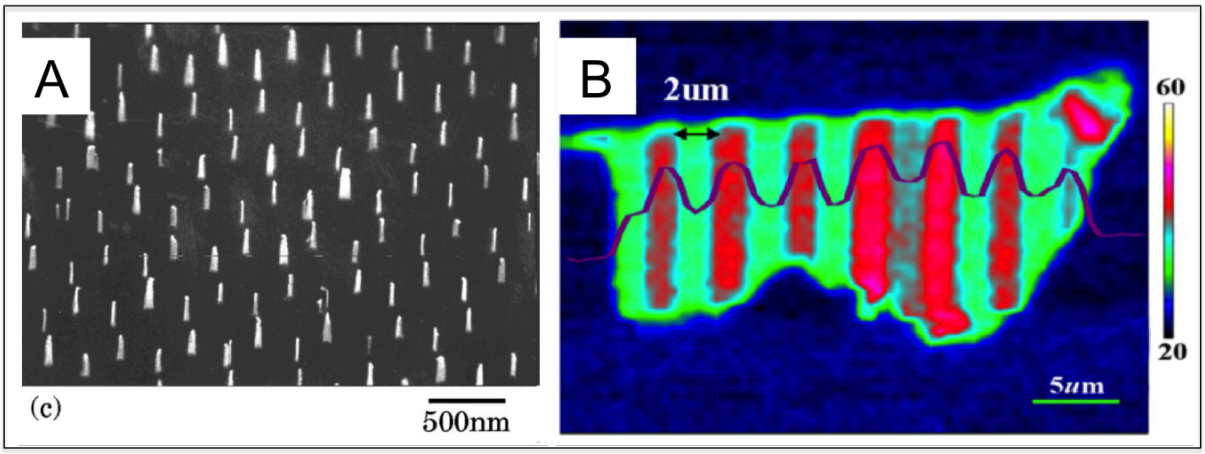

Figure 2.7: (A) Silicon nanopillars etched by depositing a metal etch mask in the interstices of a nanosphere array, from [53]. (B) A PMMA polymer mask is used to create MoS_2 structures of different layer height after Ar sputtering. The intensity of a characteristic Raman peak in bulk MoS_2 is used to identify thinned sections, from [55].

precursor salts of molybdenum and sulfur in individual cages. The two are then brought together in an appropriate ratio and reduced to form small nanoparticles of MoS_2 [62, 16]. Such advanced chemical methods have some of the benefits of gas-phase production, such as size-selection by liquid chromatography, however the ligands and surfactants in synthesis remain as contaminants. This method was patented by Wilcoxon [63] and involves unstable Mo halides, so has not seen as widespread use as ATM in the literature.

2.3 MoS_2 Nanostructures

The fabrication methods above can be used to produce a variety of MoS_2 allotropes. Often the reactants or gas-flow conditions can be varied such that the same technique produces different proportions of these structures. The long-term stability of these nanostructures is dependant on the free-energy minima that they occupy and their storage conditions. The latter can strongly affect MoS_2 structures as the surface layer begins to oxidise in the presence of water to produce MoO_3 and H_2SO_4 [64, 65], this then becomes a worse problem at the nanoscale when the majority of the nanoparticle consists of surface sites. Such nanoparticles are usually analysed immediately, in-situ or with minimal atmospheric

exposure to mitigate this effect.

The challenges of nanoscale fabrication are generally outweighed by the advantages. The benefits of decreasing size are scalable, with increased utilisation of material as there is less unused bulk. This corresponds to greater efficiency and reduced costs. At the level of clusters, there is a non-scalable regime of benefits due to the significant changes in structure caused by adding or removing single atoms. This presents itself in different stable surface configurations to the bulk, which may be more chemically active for example. The most favourable surface facets for nanostructures are strongly dependent on size. The electronic structure, as well as the physical, undergoes changes in this non-scalable regime. Quantum confinement effects, when the size approaches the Bohr radius (2 nm for MoS_2 [66, 67]), shift the energy of the conduction and valance bands. This can be used to tune a system for better electron transport or optical absorption. The following nanostructures represent systems that are using some of these benefits for diverse applications (Section 2.4).

2.3.1 Few-Atom Clusters

Cluster beam sources, using magnetron sputtering [19], laser ablation [28] or arc discharge [47], produce a plasma of Mo and S, which is then caused to condense into clusters by collisions with a carrier gas such as Helium. Starting from single atoms allows the production of stable and metastable structures of just a few atoms size. Since these structures often do not contain sufficient atoms to recreate the bulk crystal, the atoms form unique stable configurations that appear as peaks in the mass spectra (Fig 2.8).

2.3.2 Platelets

At the nanoscale the structure can remain similar to the bulk, as is the case with MoS_2 platelets that are a single or multilayer segment of the bulk. When it is reduced to a single trilayer the structural designation is simplified to 1H-MoS_2 due to the lack of trilayer offset. The first clear demonstration of MoS_2 nanoplatelets used sulfidation of evaporated Mo

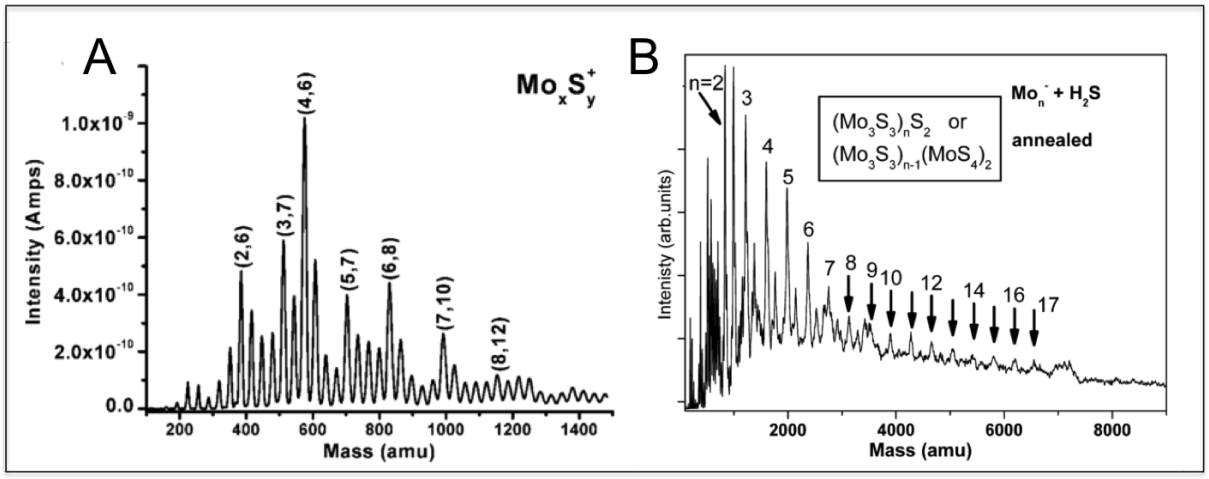

Figure 2.8: (A) Mass spectrum of MoS_x clusters produced by reactive Magnetron Sputtering of Mo with H_2S gas, from [19]. (B) Mass Spectrum of Mo-S clusters produced by a Pulsed Arc cluster source with an Mo target and H_2S gas, from [68]

nanoparticles [69]. The small platelets self-assembled, as monolayer triangles, on the low coordination sites of the herringbone reconstruction of the Au(111) substrate (Fig 2.10A), chosen for its chemical inertness [70, 71]. The triangular structure indicates one of the edge terminations, Mo or S, is more stable than the other. Atomic resolution imaging showed this to be the Mo-edge ($10\bar{1}0$), with what appeared to be a 50% sulfur saturation due to being out of registry with the interior crystal structure (Fig 2.9). The saturation of sulfur was later found to be 100%, with S dimers on the Mo-edge, a configuration that has almost the same stability as 50% as each Mo atom is coordinated with 6 S atoms. The appearance of being out of registry, that led to the 50% assumption, has more recently been attributed to overlapping states from the S dimers being maximal at the interstitial sites [72]. The terminations also have a strong size dependence, with triangles larger than 21 Mo atoms having fully sulfided Mo-edges, but smaller triangles favouring the fully sulfided S-edge [73].

The formation of flat structures when deposited on a surface with potentially strong Au-S bonds is not surprising [74], however similar structures were shown to occur on a graphite substrate [75]. Mo sulfidised on Highly Oriented Pyrolitic Graphite (HOPG) interacts more weakly with the substrate [76], as expected for two van der Waals layered materials, requiring the use of sputter defects as pinning sites. Weak binding to carbon substrates

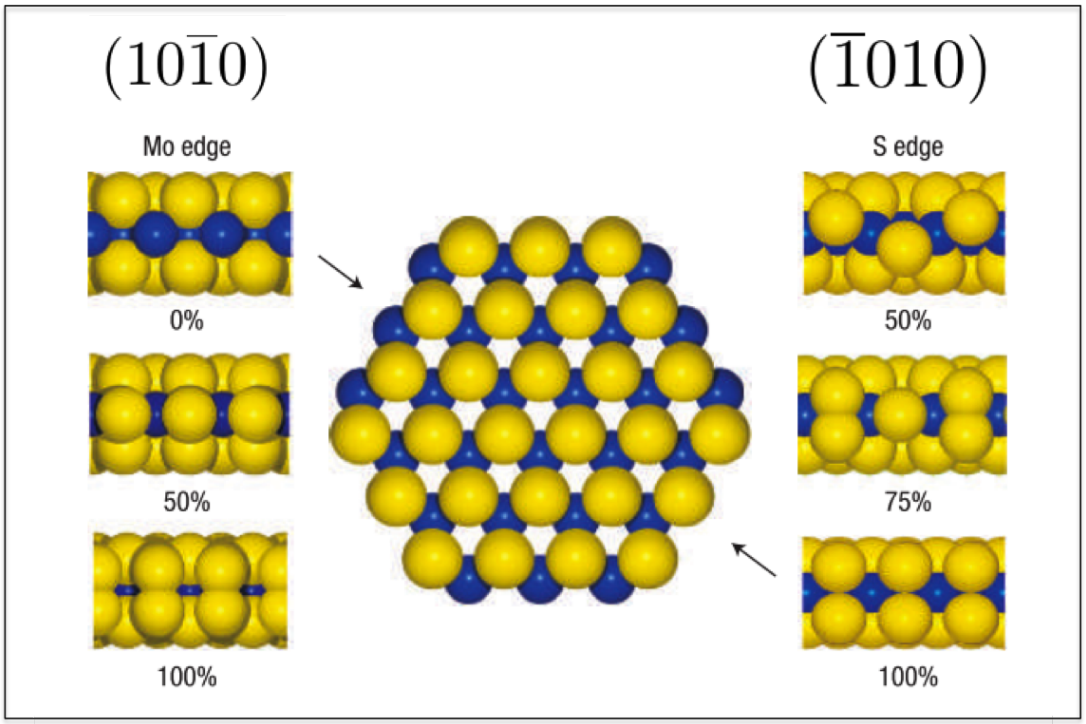

Figure 2.9: The platelets have two edge types, an Mo-edge (10$\bar{1}$0) and an S-edge ($\bar{1}$010), which can each have additional sulfur atoms attached to stabilise the structure. Modified from [73]

allows the MoS_2 to approach a more equilibrium structure. The edge terminations are changed on a graphite substrate, from entirely Mo-edge triangles, to truncated triangles and hexagons. This is attributed to the 2H-MoS_2 displaying alternate edge sites with increasing layers, thus cancelling out the free-energy benefit of restructuring to one edge type. This reasoning only works for multilayer platelets, and not the single layer platelets that also display truncated morphology. The stabilisation of the S-edge ($\bar{1}$010) in that case is explained by the increased temperature in these experiments, compared to previous [69, 17], causing a lowering of sulfur chemical potential [77] combined with the stabilising effect of hydrogen adsorption from the H_2S supply. The most significant change between these experiments is from an Au(111) substrate to the weaker binding HOPG, thus it is likely that the support interaction plays a more significant role than is discussed. The sulfidation of Mo on HOPG at 1200°K, but not 1000°K, produces multilayer stacks of MoS_2 platelets, again with hexagonal morphology (Fig 2.10B). The reason for the onset of multilayer stacking at elevated temperatures is that adhesion to HOPG defects is reduced,

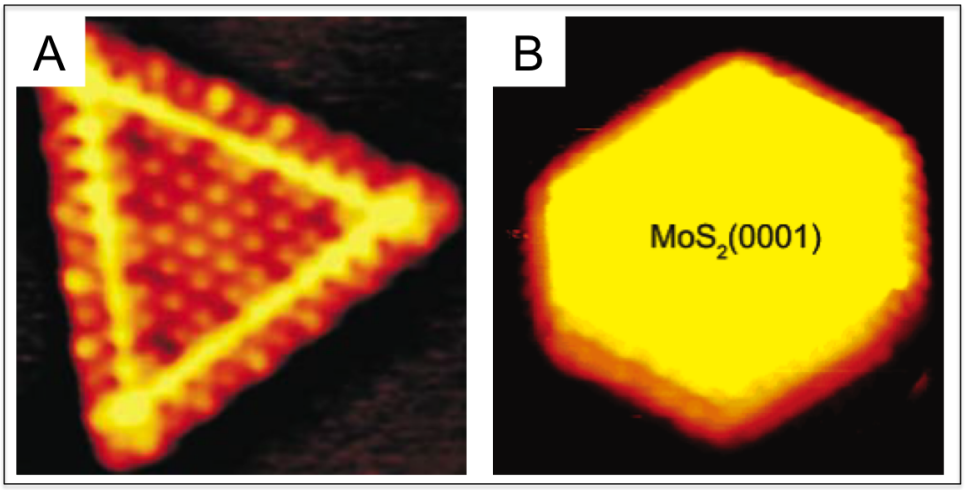

Figure 2.10: (A) Mo islands sulfidised on an Au(111) support produce MoS_2 monolayer platelets (5 nm × 5 nm). The metallic edge states, that promote various catalytic reactions, can be seen as bright lines by STM, from [81]. (B) The same procedure employed on a defect-rich HOPG surface produces multilayer platelets with hexagonal morphology, from [75].

to allow diffusion, followed by stacking to 3D structures. It is suggested that the stronger binding causing the stacking is due, not to van der Waals, but an edge based interaction of the metallic states between layers. Multilayer stacking has also been inferred in gas phase analysis [78] of clusters produced by pulsed arcing. This is especially interesting as gas-phase clusters have no support interaction, allowing the true minimum energy structures to be created.

Chemically prepared MoS_2 nanoparticles are generally in thermodynamic equilibrium, and aside from the influence of passivating adatoms, should display the lowest energy structure. XRD analysis, reaction kinetics and high resolution microscopy also confirm stacked layer models for certain chemical syntheses [79]. Chemical synthesis directly onto supports followed by sulfidation produces multilayer platelets [80], although the platelet structure may only appear after the sulfidation rather than in the as-prepared samples, which tend to be amorphous [58].

2.3.3 Monolayers

Production of many types of monolayers has become increasingly studied in recent years. A simple mechanical exfoliation technique has been used to prepare monolayers of MoS_2 [51]. The strong enhancement of photoluminescence from few-layer MoS_2 to monolayer MoS_2 allows monolayer regions to be identified by optical microscopy. This enhancement is caused by a transition from an indirect bandgap of 1.3 eV to a direct bandgap of about 1.8 eV [82, 83, 84, 85]. The simplicity of fabrication and analysis, as well as the high impact from such a novel material has made their study attractive [86, 87]. Prior to the graphene revolution single and few-layers of MoS_2 were also produced by lithium intercalation [37].

2.3.4 Thin Films

The production of MoS_2 thin films from bulk sputtering has been studied extensively. The aim being to produce thin lubricating coatings to reduce mechanical wear (Fig 2.11A). This technique generally produces films that are not perfect layers, with microscopy showing the platelets do not align parallel to the surface and spectrometry showing sulfur deficiency [88, 89]. It has been shown that low energy Ar^+ ion sputtering causes preferential removal of lighter sulfur from the target [90, 91]. Thus the volatility may reduce the sulfur available to produce compound clusters if it is depleted from the source faster than molybdenum. The loss of sulfur in thin films has been corrected by introduction of H_2S in the sputtering gas, allowing the use of a simple Mo target [89, 92]. The versatile chemical reduction method has also been used to create thin films of MoS_2 [93]. An electrode placed in ATM precursor reduces the MoS_4^{2-} anion to amorphous MoS_2 on the surface. This can be used as-prepared to produce an amorphous film on the electrode (Fig 2.11B) or annealed in Ar to crystallise layers of MoS_2. Preparation by such precursors is also compatible with doping, to produce thin films with enhanced catalytic activity [60].

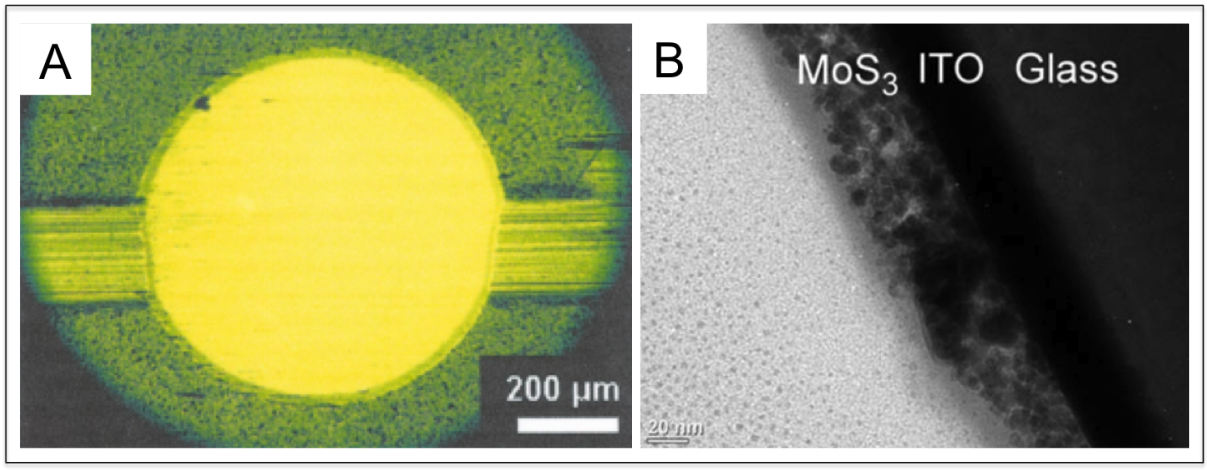

Figure 2.11: (A) Ball crater over a wear track in tribological tests of an MoS_2 film produced by Teer Coatings Ltd, from [94]. (B) A thin film of MoS_3 deposited on a conducting substrate by electrochemical reduction, from [59].

2.3.5 IF-MoS_2

Controlled gas-phase growth conditions, especially at large sizes [95], can produce more varieties of MoS_2 such as single and multi-walled nanotubes, as well as other closed shell allotropes. As with bulk MoS_2 and graphite, nanoscale MoS_2 shows itself to be an inorganic analogue of graphene and carbon fullerenes, in some cases with superior properties [30]. The exact parameters that lead to closed shells rather than platelets are unclear, however it is generally based on high temperatures, either locally by directed energy [96, 97] or in a furnace [45, 46], with a round MoO_3 nanoparticle as a template. The closed shell structures represent an energetic minimum due to the lack of reactive edges and reduced anisotropy, but in order to form them the layers must be curved at a high energy cost. This cost is reduced by using large gas-phase Mo clusters of several nanometres in order to create a curved surface to be sulfidised, the interior is subsequently converted during H_2S exposure [45]. The importance of stoichiometry is also highlighted by the free energy of the fullerene structures. The minimum is at the stoichiometric value of MoS_2 as the large closed shells are complete layers that are merely deformed [98] (Fig 2.12A). The simulations of the smallest fullerenes however, show that some sulfur defects are required to accommodate the necessary curvature [99] (Fig 2.12B). The varieties

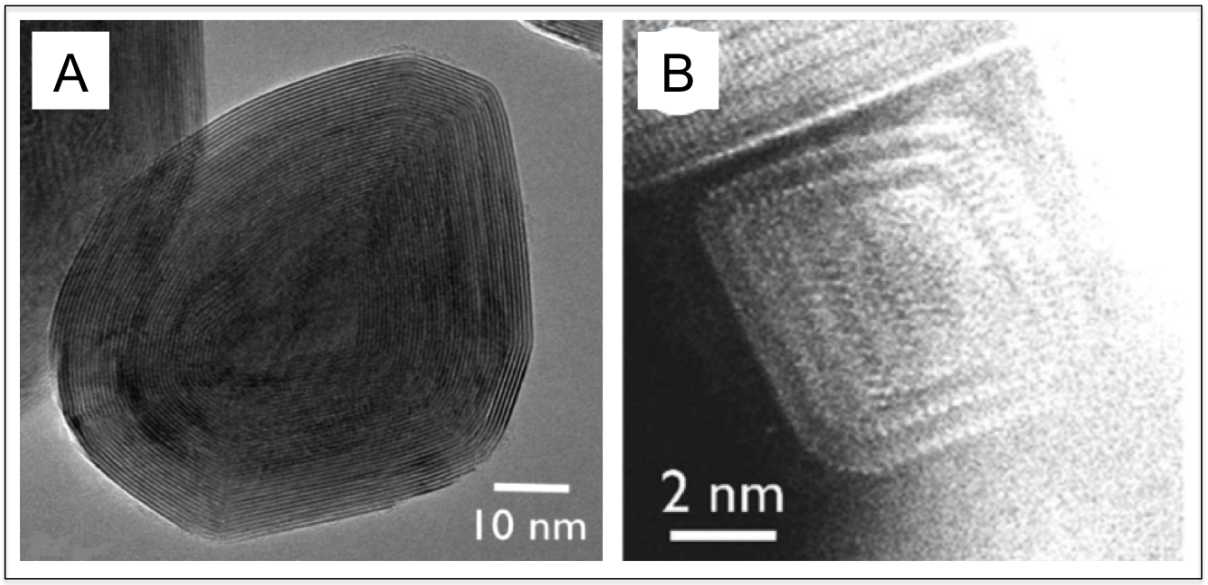

Figure 2.12: (A) Large layered onion-type MoS_2 fullerene, from [101]. (B) Nanooctahedra produced by laser ablation with a Nd:YAG laser, from [102].

of IF-MoS_2 include small nano-octahedra of a few nm diameter, to nanotubes [100] and at larger sizes multilayer shells.

2.3.6 Nanoarrays

A little studied field is that of etching to produce MoS_2 nanostructures. This can be achieved by utilising either a bulk substrate or a thin film, as described in Section 2.3.4, as the starting point. Ahmed Abdela at NPRL, has produced irregular arrays of nanopillars with fine size control by using size-selected metal clusters as etch masks. Regular arrays have also been produced by standard microfabrication techniques. These arrays were produced on both single crystal MoS_2 and chemically prepared thin films. A similar surface engineering approach has been taken to preferentially expose edge sites of MoS_2 (Fig 2.13). This is a wet chemical method using a high curvature silica template, the MoS_2 is grown within the structure in order to expose edges at the curved sites, the silica is subsequently etched away. Both of these structures are designed for optimising the proportion of edge sites for catalytic purposes, however both are hindered by the poor conductivity through the rest of the material. Thus the best designs of MoS_2 catalysts are monolayer or few-layer

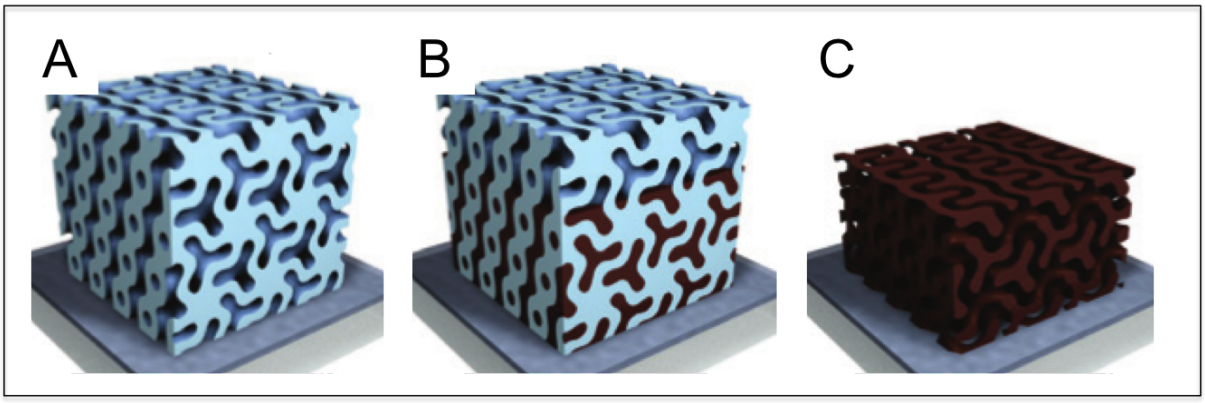

Figure 2.13: (A) Double-Gyroid silica template is made (B) The template is filled with MoO_3 and sulfidised in H_2S (C) The silica template is then etched away by HF gas to leave a high curvature MoS_2 electrode, adapted from [103].

nanoparticles with good connectivity to a conductive substrate [24].

2.4 Electrocatalyst Applications

2.4.1 Model Catalysts

The main catalytic applications in literature are for the Hydrogen Evolution Reaction (HER) and Hydrodesulfurisation (HDS). The hydrogen evolution reaction, in which protons are combined to molecular hydrogen, is crucial for applications in energy storage. HER forms the cathodic reaction of water-splitting, a topic that has received increased attention with the potential use of hydrogen as a fuel and the need to produce it sustainably [10, 104, 105, 106, 107, 108]. The most efficient catalyst for this reaction in acidic electrolytes is platinum, which is geologically scarce and financially prohibitive. This has meant that only alkaline electrolysis with cheaper nickel catalysts has gained popularity, despite low current density and efficiency [109, 110]. Research has focused on replacing platinum with cheaper analogues. The catalytic properties of MoS_2 in both the bulk [111, 112, 113] and nanoscale [18, 114, 115] are dominated by the low-coordination rim and edge sites, with the basal plane being relatively inert.

A detailed STM investigation of model HDS catalysts revealed this metallic state at

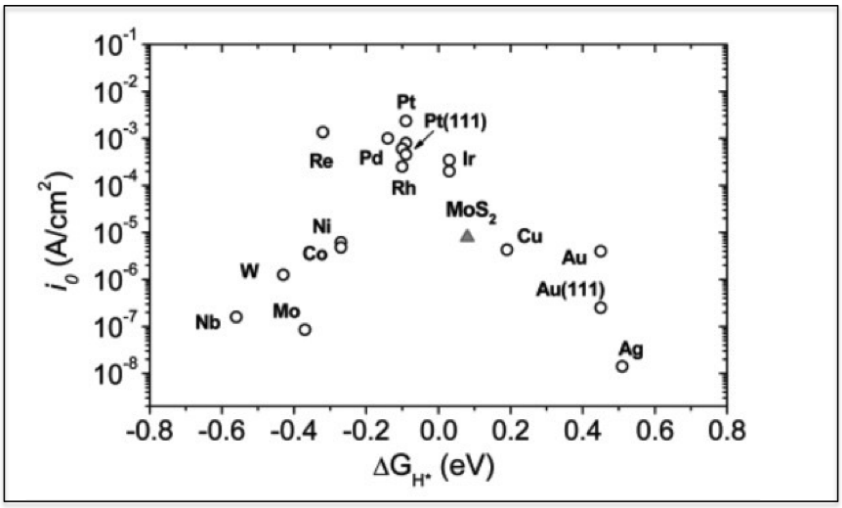

Figure 2.14: Volcano plot of Hydrogen Evolution activity (Exchange Current Density) against hydrogen binding energy, from [18].

the edge of MoS_2 platelets, confirming sites that could weakly bind reactants and release products [69]. This metallic edge state was similar to the binding energy of platinum and hydrogenase, a hydrogen producing enzyme [15]. The suitability of MoS_2 as a hydrogen evolution catalyst was confirmed by DFT calculations showing the hydrogen binding energy of the MoS_2 $(10\bar{1}0)$ partially-sulfided Mo-edge sites near the peak of a 'volcano plot' (Fig. 2.14). In fact the specific edge morphology was found to be complicated further for the HDS reaction by having additional sulfur vacancies in the partially-sulfided Mo edge caused by hydrogen atoms [69].

The typical MoS_2 HER catalyst morphology is a supported platelet, with chemical reactions proceeding on the platelet periphery [18, 24], similar to model HDS catalysts [116]. The initial support for model studies was the Au(111) surface [69], using the herringbone reconstruction to provide nucleation sites for evaporated Mo. Subsequent sulfidation created triangular monolayer platelets immobilised on the surface. In general the platelets produced by Mo sulfidation have a broad size distribution, so experiments cannot identify size effects related to electronic structure. Recent research has moved towards variants of carbon as a support for cheap lab-scale chemistry, which alters the morphology due to the weakened surface interaction. Both types of MoS_2 edge site are exposed when supported on carbon and multilayer structures are formed [75]. These

experiments show the importance of synergistic substrate effects for controlling structure and thus reactivity of clusters. Multilayer stacks have high edge to volume ratio, thus exposing more active sites, but this is countered by reduced conductivity through the layers.

The HER experiments in literature are usually carried out with a three electrode cell setup (See Section 3.5.5), with a carbon or platinum counter electrode, and a standard hydrogen reference electrode. The electrolyte is strong perchloric or sulfuric acid for a plentiful supply of protons. The easiest method for interpreting electrochemical results is to use a flat, strongly binding support to promote well-dispersed monolayer clusters, such as MoS_2 platelets grown on graphene [24]. This produces a catalyst with easily accessible edge sites and good conductivity to the bulk electrode. The system is also simple to model, as the strong binding permits the assumption of monolayer platelets and the dispersion allows plentiful reactants to reach the surface of each cluster.

2.4.2 Enhancing Edge Activity

Beyond these model systems, the general research goals for MoS_2 are to enhance the already effective edge sites and increase the percentage of edge sites on the material. The edge sites, shown by DFT calculations to have similar binding to effective catalysts such as platinum and hydrogenase, can be improved by doping. A hexagonal MoS_2 platelet presents both molybdenum and sulfur terminated edges, but the binding energy of the sulfur edge is too large for catalysis. The addition of Co to these edge sites (Fig 2.15) lowers binding energy thereby activating all the catalyst edge for hydrogen evolution [117]. The addition of Co to MoS_2 catalysts is common for industrial HDS applications. Such doping forms the majority of research into edge enhancement [118, 119, 60].

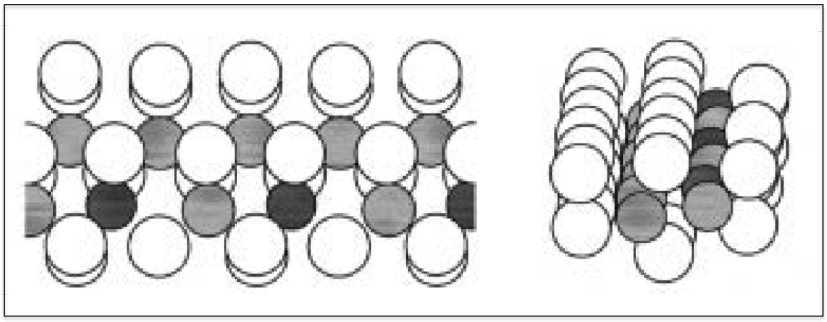

Figure 2.15: Top and side view of the 75% sulfided S-edge, with Mo atoms substituted for Co (White: sulfur, Grey: molybdenum, Black: cobalt). The missing sulfur atoms are caused by reaction with hydrogen to activate the catalyst for HDS. Adapted from [120]

2.4.3 Enhancing Edge Abundance

The main focus of research, rather than improving edge activity, is towards the issue of engineering the nanostructure to expose more of these active sites. The problem with most MoS_2 catalysts is that there is wasted inactive material forming the interior. However, obtaining an abundance of edge sites is difficult given that the edge surface energy is 100× greater than that of the basal plane [121]. Novel strategies, such as isolating the active component of the hydrogenase enzyme [122] (Fig 2.16A) and growing MoS_2 in a way that exposes edges [103, 123] (Fig 2.16B), have also been investigated.

The results for increasing the availability of edge sites have been varied depending on fabrication method and support, but ultimately the results follow a trend approaching the properties of platinum. The best results for the MoS_2 onset potential are around -0.15 V vs RHE [18, 24] compared to an almost negligible overpotential on platinum [124]. Electrochemical analyses for the best MoS_2 catalysts have a Tafel slope limited to 40 mV/decade, slightly worse than the 30 mV/decade of platinum. This suggests the HER proceeds on MoS_2 by the Volmer-Heyrovksy mechanism (Section 3.5.8), with an already adsorbed proton bonding to a proton in solution to produce a H_2 molecule. The reaction steps on platinum are Volmer-Tafel (Section 3.5.8), whereby two adsorbed protons diffuse together and desorb as H_2[24, 20]. The absolute performance of platinum is hard to compete with, but with the price and abundance, MoS_2 becomes an attractive alternative.

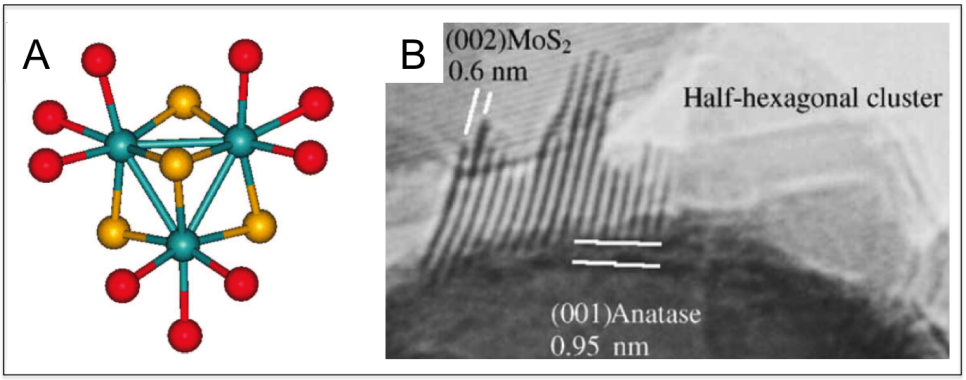

Figure 2.16: (A) Molecular Structure of an $[Mo_3S_4]^{4+}$ cubane (Blue = molybdenum, Yellow = sulfur, Red = ligands), from [122]. (B) MoS_2 grown on γ-Al_2O_3 (111) and (110) surfaces bond basally, but edgewise on the (100) face. The same is observed for the (001) face of anatase TiO_2 (pictured) and in both cases attributed to minimising lattice mismatch, from [125].

2.4.4 Novel Developments

Recently a new class of catalyst has appeared, deviating from the supported nanoparticle design. A partially reduced thin film with composition between MoS_2 and MoS_3 [93] has been fabricated from an ATM precursor. Imaging of this film finds the surface to be amorphous, with no crystal peaks by XRD. The electrochemical activity for hydrogen evolution was large, against the expectations that MoS_2 edge sites are required for catalysis on this material. This leads to the hypothesis that defect-rich MoS_x surfaces are equally active due to the low coordination.

In a similar way, thin films of crystalline MoS_2 were used for top down fabrication of nanopillar arrays by Ahmed Abdela. These high-aspect ratio features present an abundance of active edge sites, thus a corresponding activity increase was expected. Unfortunately the poor conductivity through the basal planes limited the transport of electrons to the upper layers. Converse to expectations, the most active samples found were those that were briefly etched to produce a roughened surface. The activity of these sputter defects is in agreement with the high activity found by chemically prepared amorphous MoS_3 films [59].

The active edge sites of MoS_2 are also used in multi-component systems, in which the MoS_2 conduction band edge receives electrons from another component. This is common in

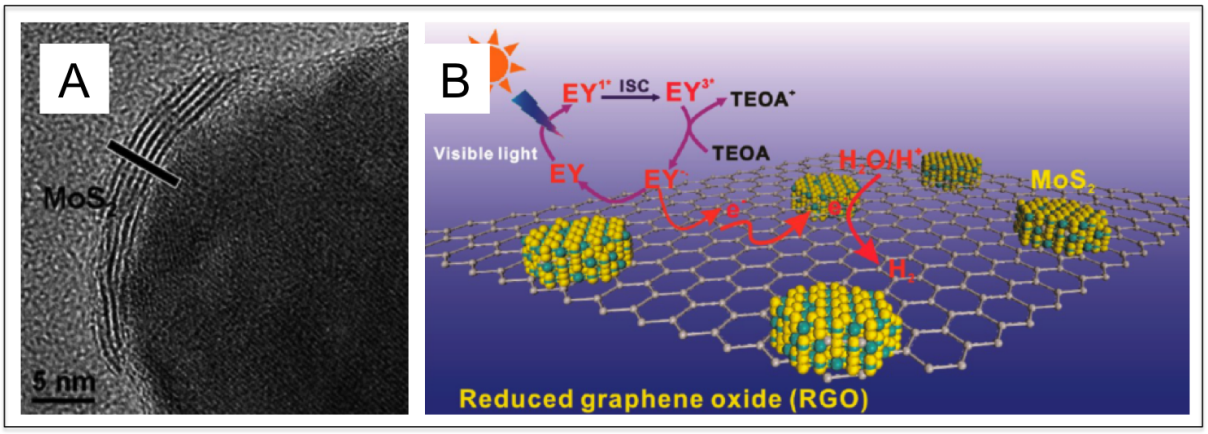

Figure 2.17: (A) MoS_2 as a HER catalyst on a CdS nanoparticle, from [126]. (B) MoS_2 on Graphene acts as the HER catalyst for electrons produced by photo-active dyes, from [129].

photocatalytic systems, with excitons generated in CdS [126] (Fig 2.17A), TiO_2 [127, 128], Si [25] and dyes [129] (Fig 2.17B), which use the ideal band edges of MoS_2 for charge separation and catalysis.

2.5 Other MoS_2 Applications

2.5.1 Photocatalyst

There has been a smaller amount of research into using the semiconductor properties of MoS_2 for photon absorption and subsequent catalysis using the excitons. The bandgap of bulk MoS_2 is 1.29 eV, in the infrared. The minimum required energy for this reaction can be estimated by taking 1.23 eV, the thermodynamic limit, and adding the overpotentials associated with the two redox reactions. The oxygen evolution reaction (OER), not discussed in this thesis but a subject of great interest in the fuel cell community, requires a high overpotential around 0.4 V [20]. The HER reaction, seen above, can be catalysed with as low as 0.1 V, giving a total band-gap requirement around 1.7 eV (Fig 2.18A). At a nanoparticle radius less than 2 nm [67], quantum confinement effects shift the MoS_2 bandgap from IR to visible at around 2.25 eV [16] (Fig 2.18B). This 3D confinement effect

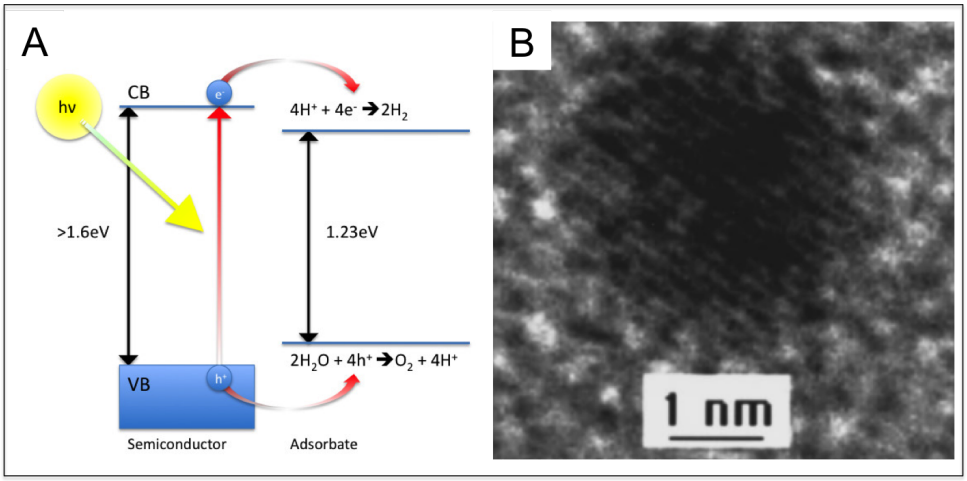

Figure 2.18: (A) Electronic band structure requirements for a water-splitting photocatalyst. (B) A 3D quantum confined (radius $<$ 2nm) MoS_2 nanoparticle produced by the inverse micelle method, from [67].

is greater than the shift achieved by 1D confinement in monolayer MoS_2 to 1.8 eV, which is to be expected as the layers are weakly interacting.

The most commonly used photocatalyst for many applications is the ubiquitous titanium dioxide (TiO_2), this is an ultra-violet absorber, so it finds use in sun-screen and paint pigments. The high energy excitons generated by the UV light, either artificial or solar, can catalyse correspondingly high energy reactions, however in many applications a lower energy will suffice. In that case efficiency savings can be made, especially with solar light which has an irradiance peak in the visible spectrum. The use of MoS_2 as a photocatalyst has been shown in pollutant degradation [130, 131] (Fig 2.19) and for hydrogen evolution [58] using visible light. The visible absorption of nanoscale MoS_2 has led to increased interest in a climate where clean energy and efficiency savings are becoming more crucial.

In general, the complexity of a system that involves absorption of photons and catalysis means that there are few uses of a single material to perform all these functions, which has deterred the use of MoS_2 for this purpose. Instead other systems based on multiple specialised components dominate the research. Z-scheme photocatalysis uses two distinct materials with band edges more closely matched to reactions and a redox couple in solution to transfer electrons between the two nanoparticles. These systems require a photon for each nanoparticle, so efficiency is automatically halved even before taking into account the

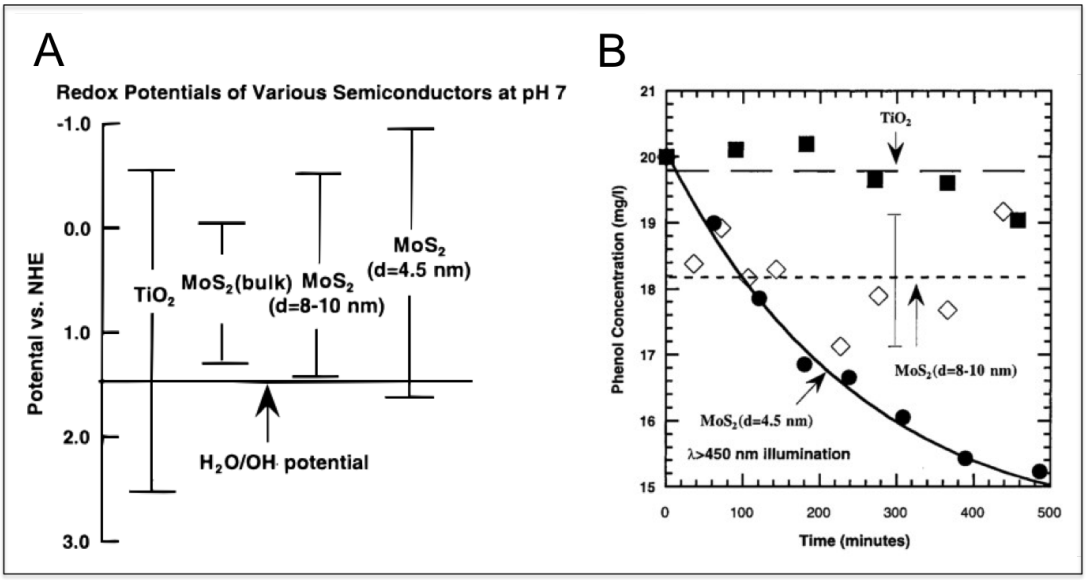

Figure 2.19: (A) Bandgap measurements from UV-Vis spectroscopy indicate quantum confinement effects in 3D confined MoS_2. (B) Phenol Degradation using visible light, TiO_2 shows no activity as the photon energy is too small to excite electrons. MoS_2 activity increases with decreasing size suggesting the band edges are shifted to more favourable energies for redox processes, from [16].

extra reaction steps [132]. Alternatively, one material can be used for exciton generation, and have adsorbed co-catalysts with active sites tailored to oxidation or reduction reactions [133, 105, 134, 135]. Similarly to electrocatalytic HER, platinum is frequently used as a co-catalyst with photons generated by Silicon or TiO_2 [136, 137]. This system is effective and has been heavily investigated in the TiO_2 literature, however it retains the problems of a system involving platinum. MoS_2 has been shown to be an effective replacement in such systems as an electrocatalyst [138, 139, 129, 25, 140].

2.5.2 Dry Lubrication

The main industrial use of MoS_2 outside of catalysis is as a dry lubricant where graphite is impractical. The lubrication is achieved by the easy shearing plane of the van der Waals interlayer gap [23]. Graphite functions best when the graphene layers are lubricated by water vapour, whereas the opposite is the case for MoS_2. So MoS_2 finds use in space, vacuum and high temperature applications. This is often in the form of suspended micron

scale MoS_2 particles in a grease for low-end applications. High quality lubricating surfaces can be produced by coating components with a thin film of MoS_2, usually by magnetron sputtering. Significant research in tribology is geared towards the optimum coating parameters, the quality of the thin film is dependent on elemental composition, alignment of the layers and presence of defects. Much of the considerations for lubrication are the same as for catalysis, however for the former, the MoS_2 surface should ideally present the basal plane for shearing as opposed to the edges, which are best for catalysis. The IF-MoS_2 structures have potential use in tribology [141] or self-lubrication of composites though the mechanisms are not well understood. They do not have the same shearing properties as the lamellar structure, but their composites have shown enhanced strength and flexibility [142]. The large scale industrial usage of this material also demonstrates the possibility of global scale up, should MoS_2 prove to be successful as a platinum replacement.

2.5.3 Hydrodesulfurisation (HDS)

The predominate industrial catalytic use of MoS_2 is as a hydrodesulfurisation (HDS) catalyst to remove pollutants from fossil fuels. The sulfur contained in petroleum is formed into sulfur dioxide after combustion and there are tight regulations governing exhaust emissions that limit these. The ubiquity of the fossil fuel industry has caused this application to grow rapidly, showing again that this material is capable of rapid scale up to cope with worldwide demand. The MoS_2 catalyst is produced by sulfiding chemically deposited MoO_3 supported on γ-Al_2O_3 or by reduction of ATM precursors on γ-Al_2O_3. It is common to add a transition metal dopant such as Ni or Co to enhance performance [17]. The active site for this reaction is the basal plane edge, specifically sulfur vacancies generated by hydrogen atoms [143, 144]. The first detailed characterisation of MoS_2 platelets was intended as a model system for HDS [69], and more recent work by members of the same group [116] has since shown the triangular shape becomes truncated at larger sizes, and further truncated with the addition of dopants [80] (Fig 2.20). The morphology of real HDS catalysts is therefore also expected to be of the platelet type,

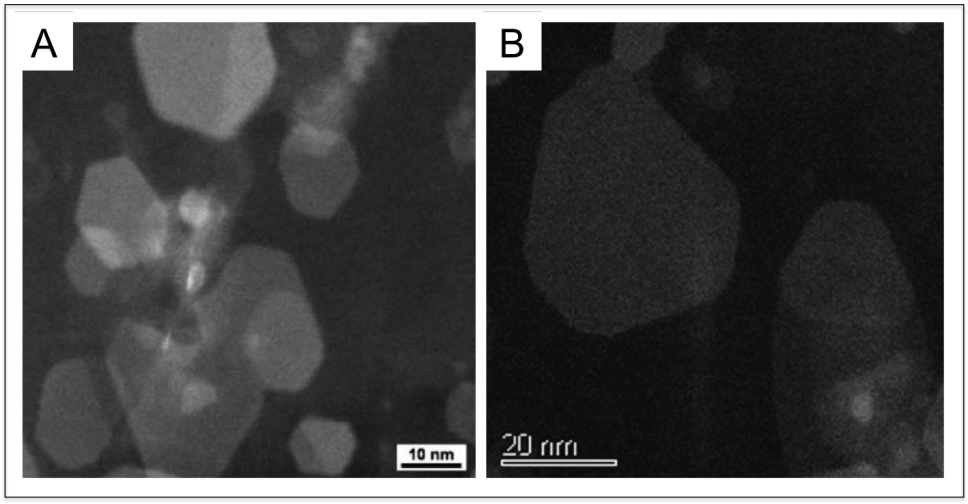

Figure 2.20: (A) Ni-Mo-S platelets, from [80]. (B) Co-Mo-S platelets from [145]. Both platelets show truncated triangle shapes consistent with the S-edge approaching the free energy of the Mo-energy. The truncations are also more rounded with the addition of more high index sites $(11\bar{2}0)$ compared to undoped MoS_2.

using the favourable binding energy at the low coordination edge sites.

2.5.4 Cluster Physics

Cluster physics usually probes the size regime in the region of few atom clusters to clusters equivalent to $(MoS_2)_{100}$. This regime produces unique structures, especially with binary systems in which there are not enough atoms to reproduce the bulk compound motifs. Fabrication of these clusters uses low flux nucleation sources, such as laser ablation, pulsed arc and magnetron sputtering. In the case of compound clusters, such as MoS_2, the sulfur is added separately with a reactive gas. This allows the ratio of the constituent atoms in the plasma to be controlled. These cluster beams are generally size-selected with a quadrupole mass filter and analysed in flight by spectroscopic techniques. At the lowest cluster masses a stable structure, Mo_4S_6, was identified, but after reaching 8 Mo atoms platelets begin to emerge [78]. These platelets grow anisotropically by addition of elemental Mo and S to the edge sites. Bilayers also emerge in the mass spectra despite the weak van der Waals binding, though the exact mechanisms of nucleation are yet to be fully understood for growth of layers in gas-phase. The plentiful sulfur source is important for

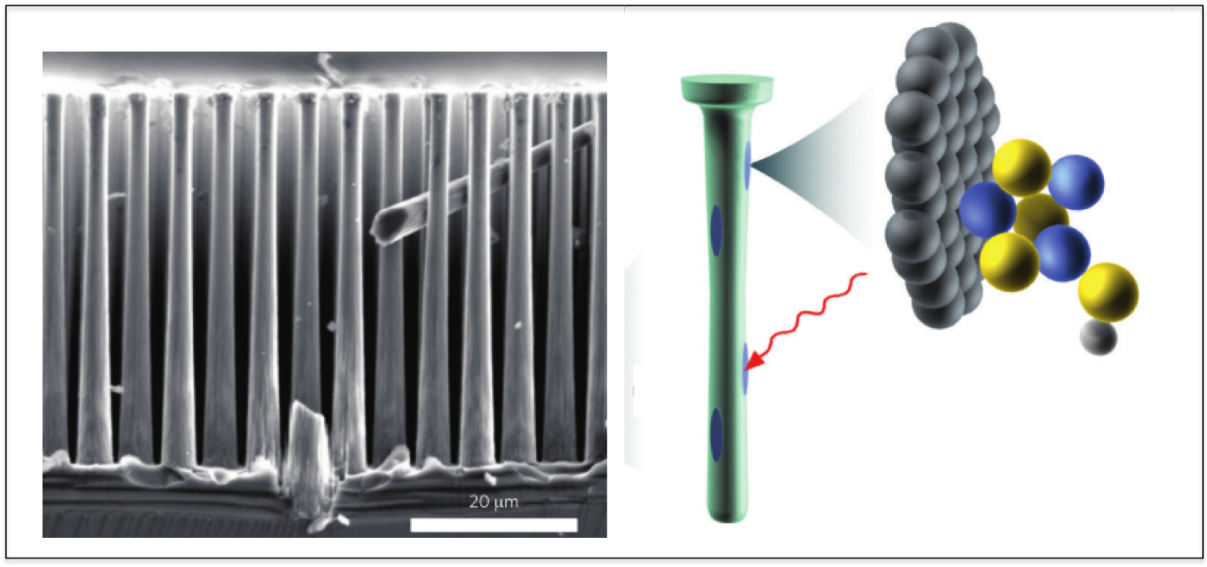

Figure 2.21: Mo_3S_4 cubanes are adsorbed to a Si nanopillar to catalyse HER, using electrons generated by the Si, modified from [139]

small platelet clusters because the $(\bar{1}010)$ sulfur-edge was calculated to be the most stable and at small sizes the edge has a bigger proportional contribution to the total volume. Thus smaller platelets have a sulfur-rich composition compared to stoichiometric MoS_2. The smallest calculated structure that displayed the platelet structure was Mo_3S_{12}.

Although clusters of this size are not usually used for industrial catalysis, they can provide a means of studying active components of biological catalysts, such as enzymes. The active component of hydrogenase, was the inspiration for the platelet work [15], and ultimately led to the isolation of this active component and use in a hydrogen evolving system (Fig 2.21). Despite the small size of just 7 atoms, it performed well as a supported catalyst, suggesting such small clusters could pave the way for catalysts with no inactive material.

2.5.5 Intercalation Electrodes

The field of lithium-ion batteries has had great amounts of research into cathode materials that change the cell properties depending on application. The anode, which binds the lithium ions by intercalation in the charged state, has remained graphite for generations.

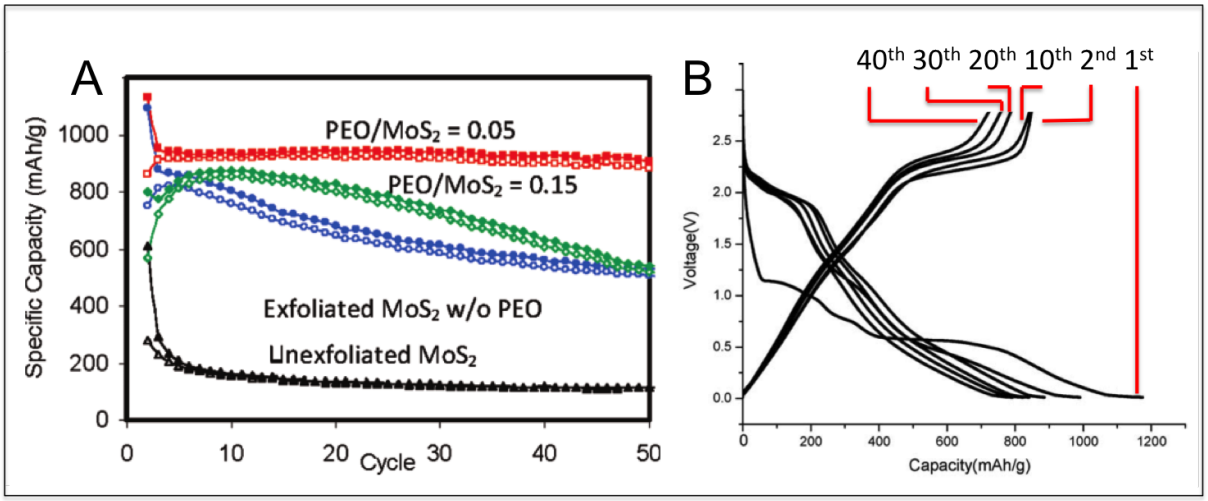

Figure 2.22: (A) Capacity of an MoS_2/PEO (Poly Ethylene Oxide) nanocomposite Li-cell anode under repeated cycling. The polymer stablises the MoS_2 structure during intercalation, from [147]. (B) MoS_2 nanotubes are used as Li intercalation anodes with increased capacity due to storage in the inter-tube sites as well as the usual inter-layer sites, from [139]. The standard graphite anodes used in commercial cells have a capacity around 350 mAh/g.

The similarities to graphite has led to MoS_2 being researched as a replacement as it can bind more Lithium ions [146, 147]. The formation of the lithiation product Li_2S is an inherent problem for MoS_2, but carbon additives prevent its interaction with the cell electrolyte [35]. Novel structures taking advantage of the fullerene morphologies also promise to hold more Lithium by using the intertubular spaces [148].

2.5.6 Electronics and Photonics

The graphene revolution has led to growth in fundamental research of similar layered materials [149]. The uses of graphene in catalysis have been largely limited to its use as a high area support [24], so these new materials have potential to improve upon use in real world applications. Despite the hype surrounding the electronic properties of graphene, MoS_2 monolayers have more potential in many areas. There is a strong electronic structure shift, from an indirect gap to direct, when reducing from few layer MoS_2 to monolayer. The semiconducting properties make it useful for new types of transistors [150] and the strong layer dependence of luminescence allows simple characterisation by optical microscopy

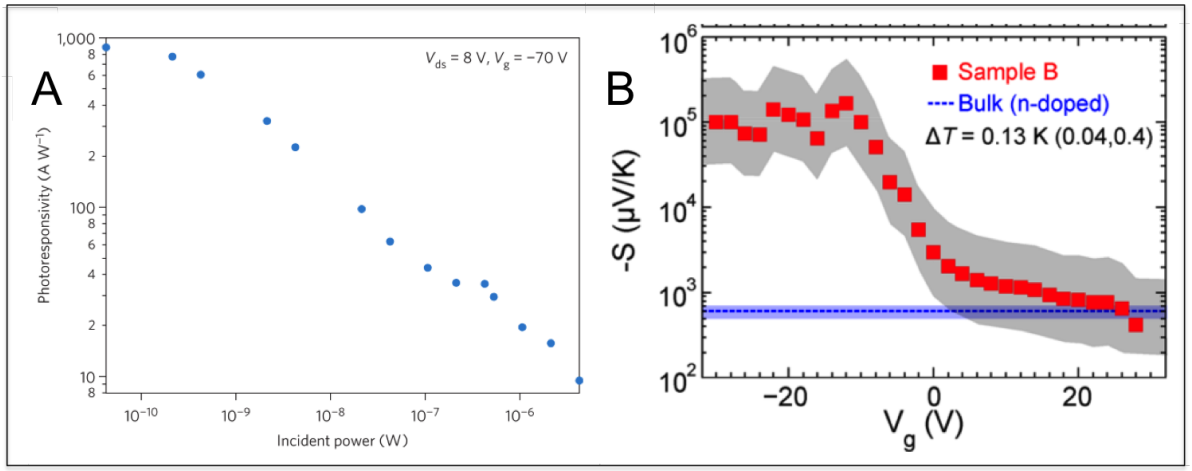

Figure 2.23: (A) A phototransistor that reaches a photoresponsivity of 880 A/W, around 10^6 times better than graphene, due to the direct bandgap in monolayer MoS_2, from [52]. (B) MoS_2 demonstrates a large and tunable Seebeck coefficient, the value which quantifies thermoelectric power, which paves the way for enhanced thermal power generation. The value of -3E+5 μV/K is 70-250000 times greater than reported graphene values, from [31].

[55]. The simple fabrication by exfoliation has provided easy access to fundamental research of the modified electronic properties. The direct band-gap is a distinct advantage over graphene in field-effect transistors and other electronic applications (Fig 2.23). The industrial applications become even more appealing with new methods to reliably produce macroscopic quantities of monolayers [151, 152, 153].

2.6 Research Outlook

The research into MoS_2 electrocatalysis has successfully isolated the form of the active sites at the atomic scale, and has generated several methods of fabrication to optimise the utilisation of these sites. While the Mo sulfidation, pulsed techniques and chemical synthesis have been shown to produce platelets, the situation has not been confirmed with magnetron sputtering nucleation sources. In the literature there have been some cluster beam experiments using magnetron nucleation sources, but confined to very small sizes before the onset of platelets [28]. The nucleation process of magnetron sources, in helium gas followed by supersonic expansion, is similar to pulsed cluster sources, so similar

structures should be expected.

The enhancement of intrinsic activity has received less attention and mainly focuses on dopants. The size-dependent activity shown by Wilcoxon for chemically prepared MoS_2 below 4.5 nm has not been extended to HER catalysis. This work intends to address this knowledge gap and isolate non-linear size effects in electrochemical activity associated with an optimum band structure for HER redox reactions. The use of magnetron sputtering of bulk MoS_2 also provides a simple route towards cheap manufacture of catalyst nanoparticles from abundant material.

CHAPTER 3

EXPERIMENTAL METHODS

3.1 UHV and HV Procedures

The cluster source system consists of a differentially pumped high vacuum (HV) section, feeding through to an ultra-high vacuum (UHV) analysis section (Fig 3.1). The construction and operational techniques for both of these systems are similar, with some additions for UHV. Stainless steel chambers are bolted together with soft copper gaskets to create semi-permanent seals, frequently opened sections at lower vacuum can use temporary Viton gaskets for easier removal. A backing vacuum of 10^{-2} mbar is achieved by oil-based rotary pumps, and in sensitive deposition sections by dry scroll pumps. The majority of the pumping is performed by turbo-molecular pumps, which work by high-speed fans imparting momentum to incident gas molecules to attain a final pressure around 10^{-7} mbar. This pressure is sufficent for high vacuum and is all the pumping that is performed in the cluster source section. The caveat for this section is that in operation the magnetron at full gas flow produces pressures of 2 mbar, which must be reduced for the high voltage lenses and sensitive instruments to function. The cluster source is split into three separate chambers, each with independent backing and turbomolecular pumps, that reduce the pressure in steps down to 10^{-6} mbar at the deposition chamber while in operation. A gate valve is used to seal the operational cluster source from the UHV system to maintain the low pressure in the latter system.

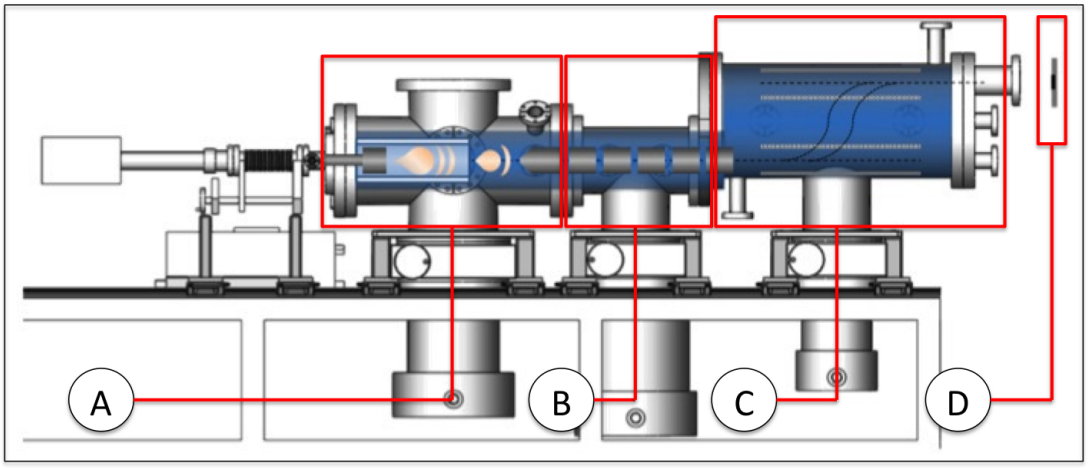

Figure 3.1: The cluster source system consists of three differentially pumped systems, capable of depositing to a UHV sample preparation chamber. (A) Nucleation Chamber, (B) Ion Optics Chamber, (C) Time-of-Flight Chamber, (D) Substrate.

UHV is achieved following additional procedures after the HV stage. After exposure to atmosphere all vacuum chambers are coated with adsorbates such as water vapour, these will slowly desorb in vacuum and prevent the very low pressures required for UHV. The adsorption is an inevitable effect of atmospheric exposure but it can be mitigated by heating the chamber during pumping, a process called baking. This accelerates the desorption of adsorbates and causes their removal via the backing pumps. Typically this baking process involves holding the chamber around 200°C for 48 hours while keeping a high vacuum with turbomolecular pumps. Once adsorbates are removed ion pumps are activated, which use electrons to ionise gas molecules subsequently attracted to a reactive cathode. These attain a pressure of around 10^{-10} mbar and are assisted by addition of reactive titanium metal deposited by a titanium sublimation pump (TSP) to strongly adsorb gas molecules. UHV is maintained only as long as these pumps are running because the trapped gas molecules will desorb over time. The low pressure in this chamber increases the mean free path of electrons such that e-beam techniques like HREELS and LEED are possible.

3.2 Cluster Beam Fabrication

3.2.1 Cluster Beam System

A bulk target (50.8 mm diameter × 4 mm thickness) of hot-pressed MoS_2 powder (Pi-Kem, purity 99.9%) is fixed inside the nucleation chamber on a water-cooled copper plate. The system is regularly used for other materials so heavily contaminated components such as the target mount and the dark-shield are cleaned down to the original stainless steel to reduce the probability of foreign elements in the clusters. The MoS_2 target is also filed down to reach unsputtered material due to the preferential sputtering of sulfur from the target [90, 91]. The nucleation chamber is sealed with a greased viton seal and the cluster system is pumped as described in Section 3.1.

A DC magnetron is used to sputter the target of cluster material to create positively charged cluster seeds. Argon gas flows into the chamber from an inlet behind the target, with a high potential applied between the target (cathode, -500 V) and the shield (anode, ground) causing the Argon to become ionised to a plasma state (Glow Discharge). The Ar^+ ions impact the negatively charged target, sputtering target atoms and ejecting secondary electrons. The secondary electrons ionise further Ar atoms to enhance the plasma. Magnets behind the target confine the secondary electrons to helical orbits to increase the probability of ionisation, thus more Ar^+ ions and free electrons are produced. The magnetic field lines also confine the plasma to the region above the target to prevent plasma damage to other parts of the system. The advantage of using magnetron sputtering is that at least 30% of the sputtered material is ionised by the plasma [154] and can be directly focused into a cluster beam without a further ionisation stage. The charged cluster seeds nucleate and grow by three-body collisions following the addition of helium gas with cryo-cooling. The magnetron can be moved along the axis of the cluster beam in order to decrease the time that clusters have to nucleate. The nucleation chamber (Fig 3.2) is a relatively high pressure region, around 1 mbar during operation, connected by an adjustable nozzle to the rest of the differentially pumped system. The fully formed

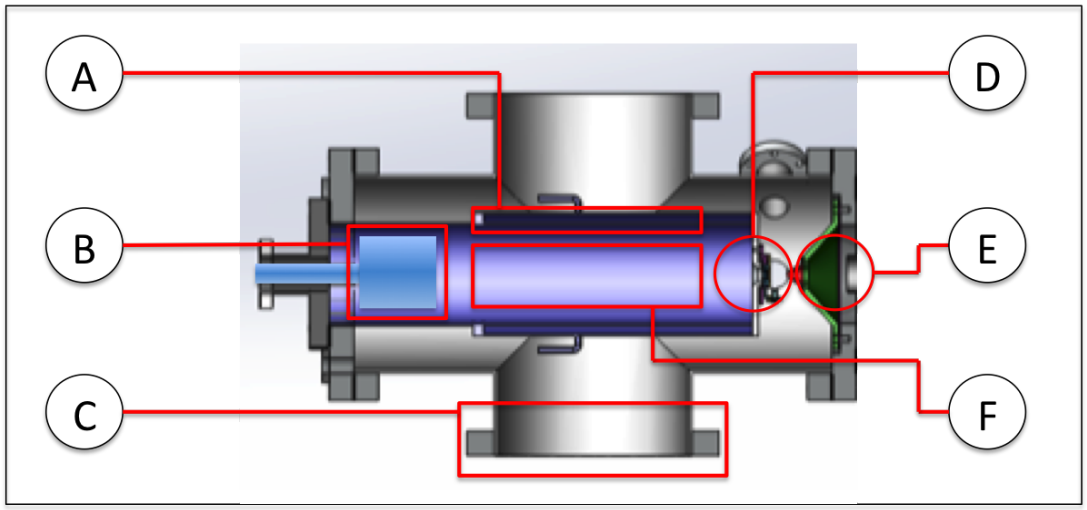

Figure 3.2: Nucleation Chamber Schematic. (A) Liquid Nitrogen Jacket, (B) Movable Magnetron, (C) To Turbo-molecular Pump with Rotary Pump backing, (D) Variable Iris (Nozzle), (E) Skimmer to Ion Optics, (F) Nucleation Region

clusters exit the nucleation chamber in a supersonic gas expansion. The collimated central portion of this flow is selected by a conical skimmer, while the outer turbulent portions are removed and pumped away in the first chamber.

This beam is processed by the ion optics (Fig 3.3) to provide the well collimated and monochromatic cluster beam required by the mass filter (Fig 3.4). The cluster beam is accelerated to a known beam potential, usually 500 eV, through the ion optics and focused to a spot size of approximately 10 mm. In ideal conditions the cluster beam should follow a defined central line through the various lens elements, however due to material build-up and misalignment the beam may be shifted in the axial direction. Any momentum in this plane can reduce flux and also cause clusters to appear anomalously heavy or light in mass spectra. Thus split deflector lenses are used in the ion optics section to correct the beam position before the mass filter.

The linear Time of Flight mass filter (Fig 3.5) consists mainly of 4 isolated plates, 2 central mesh plates enclose a field-free drift zone and 2 more plates, at the top and bottom, provide electrostatic pulses [155]. The cluster beam enters at the bottom via a variable entrance aperture, between 1-8 mm in height, which selects a vertical portion of the cluster beam to enhance resolution at the expense of flux. A second exit aperture after the mass

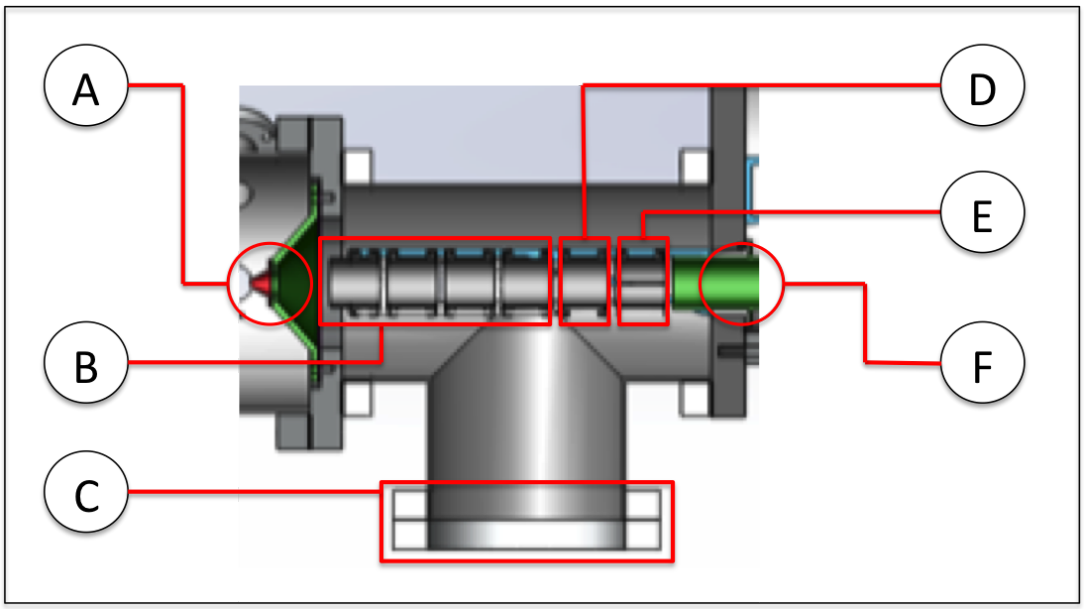

Figure 3.3: Ion Optics Schematic. (A) Skimmer from Nucleation Chamber, (B) Focusing Einzel Lenses, (C) To Turbo-molecular Pump with Rotary Pump backing, (D) X (horizontal axis) deflector, (E) Y (vertical axis) deflector (F) Exit to Time of Flight Chamber

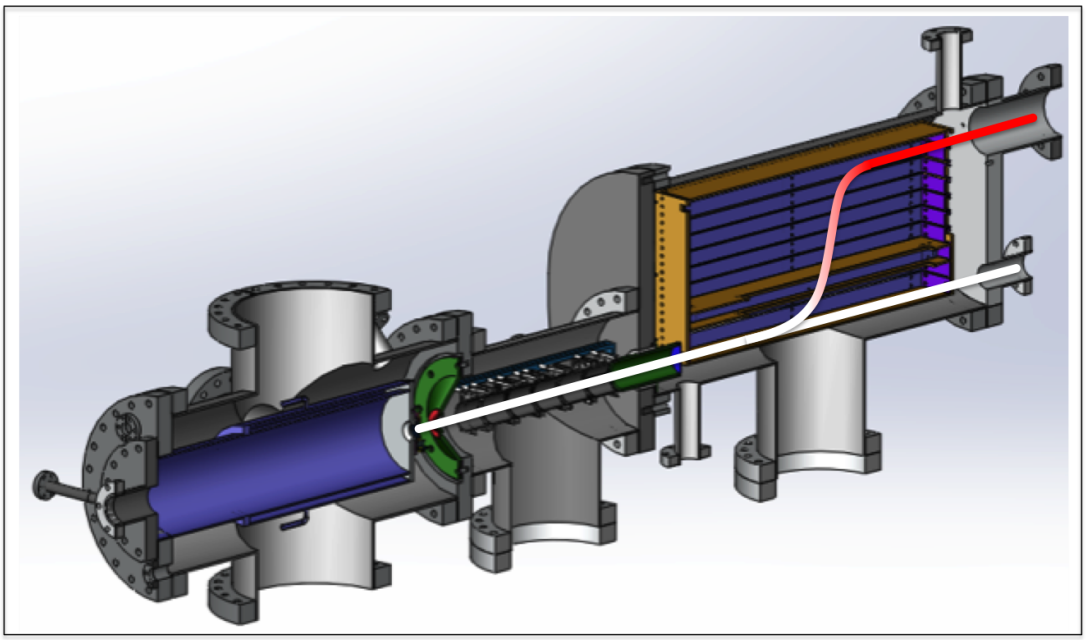

Figure 3.4: Isometric representation of the cluster beam source interior (Birmingham Instruments Nanobeam) with marked cluster beam trajectory, (white) unfiltered beam or white beam, (red) time-of-flight filtered beam. Adapted from Jinlong Yin, Birmingham Instruments

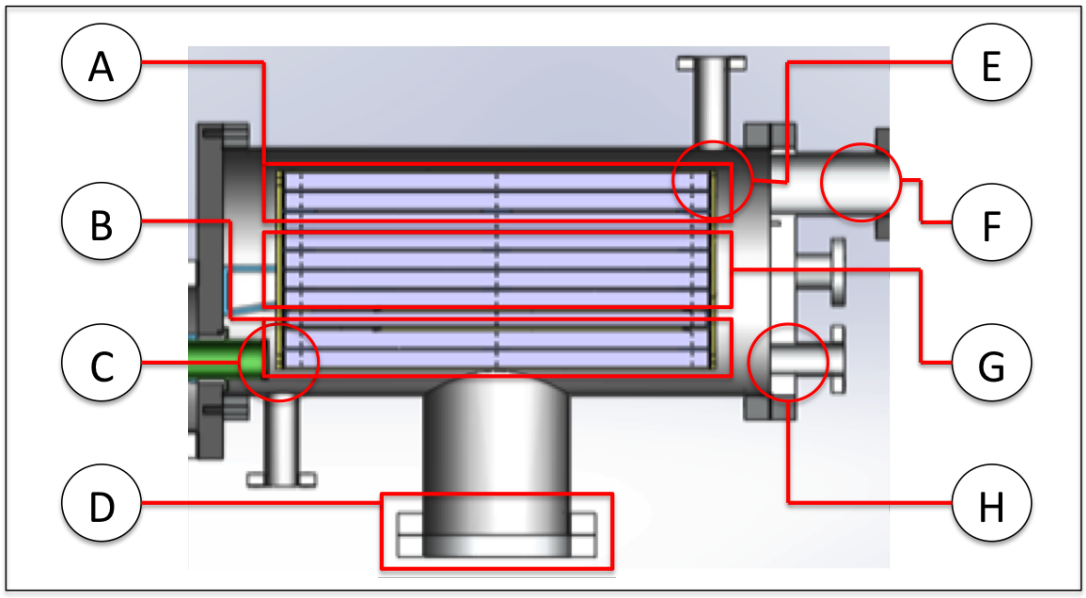

Figure 3.5: Time of Flight Chamber Schematic. (A) Exit Pulse Region, (B) Entrance Pulse Region, (C) Variable Height Entrance Slit, (D) To Turbo-molecular Pump with Scroll Pump backing, (E) Variable Height Exit Slit, (F) Exit to Deposition Chamber, (G) Field-free Drift Region, (H) Faraday Cup Array

filter functions in the same way. The permitted beam fills the field-free entrance section, while the bottom plate is held at the beam potential, until the signal generator initiates a positive 0 V pulse to push the clusters upwards through the first mesh plate. The clusters disperse in the drift region, with heavier clusters moving slower than the lighter ones, and pass through the top mesh plate into a field-free exit section, with the top pulse plate held at beam potential. After a specified interval, calculated to be the flight time of the desired cluster size, the signal generator pulses a second, opposing positive 0 V pulse on the top plate to return the selected cluster size to their original trajectory. This second pulse is also applied to plates in the drift region to simultaneously clear this volume of the remaining heavy clusters, if these were left they might be overtaken by the light faster particles in the next cluster packet and be selected by the mass filter.

The size-selected beam is finally focused to a beam of approximately 1 mm diameter by focusing optics positioned before a deposition chamber. A sample stage suspended vertically holds two omicron style sample plates, each with two substrates (Fig 3.6). The sample stage consists of a slotted stainless steel block isolated from the support shaft by a

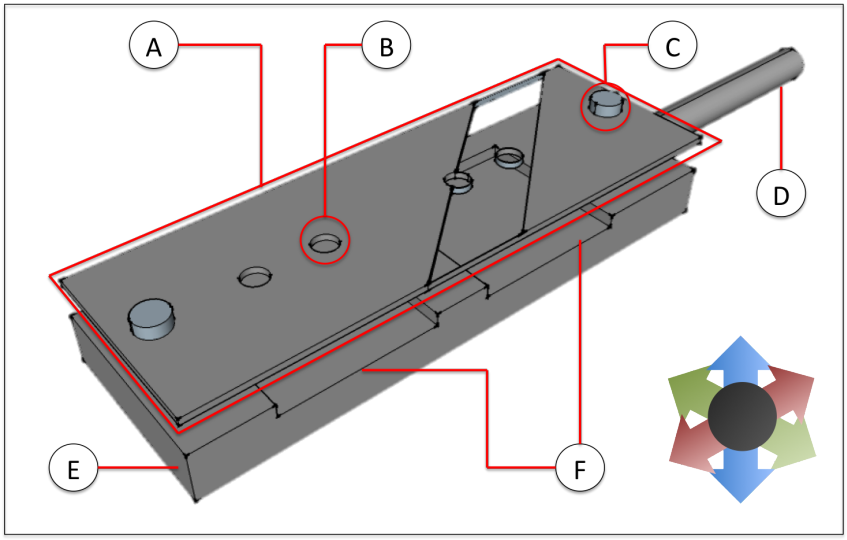

Figure 3.6: Sample Holder Schematic. (Axes: Red = Y (Vertical), Green = X (Horizontal), Blue = Z (In-Beam Plane)) (A) Isolated Aperture Plate (with section removed for clarity), (B) Aperture, (C) Insulated Aperture Support, (D) Insulated Sample Holder Support with Linear (X,Y,Z) and Rotary (About Y) motion, (E) Sample Holder, (F) Slots for Omicron-style Sample Plates

Teflon spacer. The substrate potential at which the block is held determines the impact energy of the clusters on the substrates, this value ranges from 0-1500 V (and up to 4000 V with a secondary power supply). The sample bias can be low to soft-land the cluster with minimal impact damage or increased to several kV to pin or even implant clusters into the surface [156, 157, 155, 158]. Current from the block is measured by a picoammeter to determine the flux of charged clusters incident on the surface. An aperture plate, isolated but held at substrate potential, means current is only measured when the cluster beam is above a substrate. The substrate apertures are 4 mm diameter circles, which is larger than the optimum beam spot size, so to attain a uniform coverage the beam is rastered over the aperture during deposition. The system is compatible with Transmission Electron Microscope (TEM) sample grids, 5 × 10 mm graphite wafers and 3 mm length × 5 mm diameter Rotating Disk Electrodes (RDE). Samples are then transferred through a loadlock chamber to atmosphere for analysis or stored in an Argon-filled desiccator.

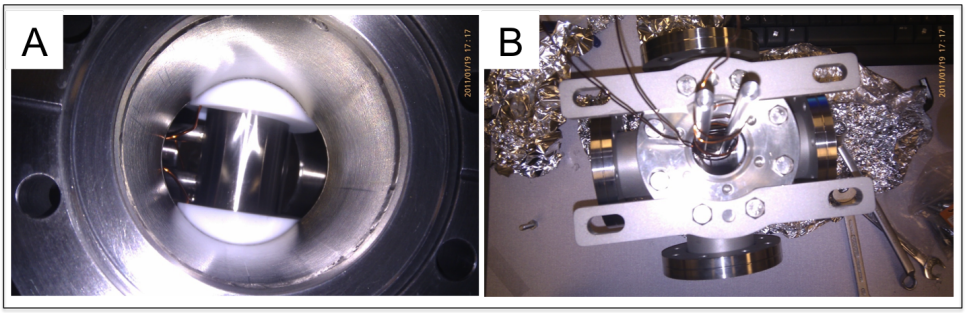

Figure 3.7: (A) Movable lens section in Teflon spacers, this space is usually occupied by the sample stage. (B) the movable lens supports from below.

3.2.2 In-Situ HREELS Deposition

A gate valve separating the HV cluster beam system from the UHV HREELS Preparation chamber can be opened to allow HREELS analysis of samples without exposure to atmosphere. The main sample stage is lifted out of the path of the cluster beam and a movable lens section (Fig 3.7) is raised from beneath to slot into Teflon spacers. This creates an ion optics section that bridges the two systems to allow deposition on the HREELS sample stage.

3.2.3 Cluster Nucleation

The nucleation parameters controlling cluster formation are the input gas flows (Argon and Helium), the magnetron power, the diameter of the nucleation zone exit aperture (hereafter referred to as the nozzle) and the distance of the magnetron target from the exit aperture (hereafter referred to as condensation length (CL)).

The helium gas flow is introduced to increase the proportion of three body collisions in the nucleation chamber as any two sputtered target atoms have a kinetic energy exceeding their binding energy. An increase in collisions slows the target atoms to the point where few-atom cluster seeds can be formed (Fig 3.8).

The argon gas flow is supplied to fuel the sputtering plasma, however excess argon gas can also function in the same way as helium gas to reduce kinetic energy of cluster seeds. The gas flow rates are one parameter responsible for total pressure in the nucleation

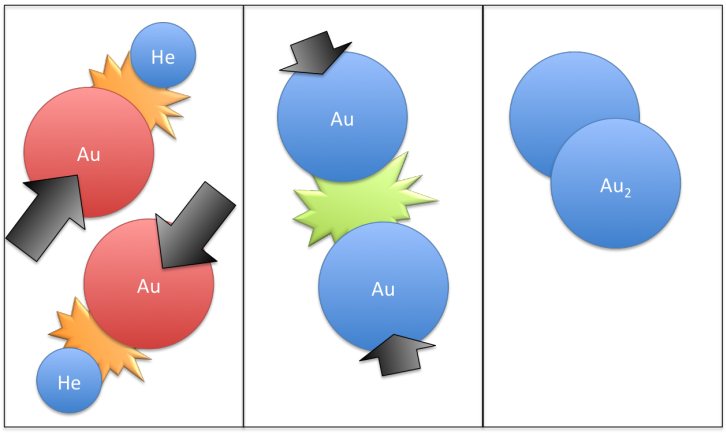

Figure 3.8: Cold Helium atoms are used to reduce the kinetic energy of sputtered target material. Their energy is reduced sufficiently to permit binding. A cluster is then formed and grows by continuation of this process.

zone. The nozzle controls the total pressure by limiting the rate of gas flow out of the nucleation chamber. The pumping rate of the magnetron chamber can be reduced by throttling the gate valve above the turbo pump in order to reduce the outflow from the nucleation chamber, effectively increasing the nucleation pressure without varying the nozzle. This may be necessary if higher pressures are required than can be provided by full gas flow and the fully closed nozzle (around 2 mbar). At higher pressures than this it may be difficult to keep the plasma ignited, furthermore the pressure differential between nucleation chamber and the outer magnetron chamber causes the supersonic expansion to create the initial cluster beam. The variation of this parameter might increase the turbulent flow region of the expansion causing an uncollimated beam to pass through the skimmer. The condensation length is controlled by a linear drive that translates the magnetron head along the cluster beam axis through a vacuum bellows. This determines the time that clusters have to nucleate before being ejected through the nozzle, however the expansion and contraction of the bellows also has the effect of changing the nucleation chamber pressure. The magnetron power determines the energy and flux of argon ions impacting the target, causing some change in nucleation pressure.

The main tuning procedure of the nucleation parameters is simply to achieve the highest cluster flux at the desired cluster size. Unlike most cluster research groups, small few-atom

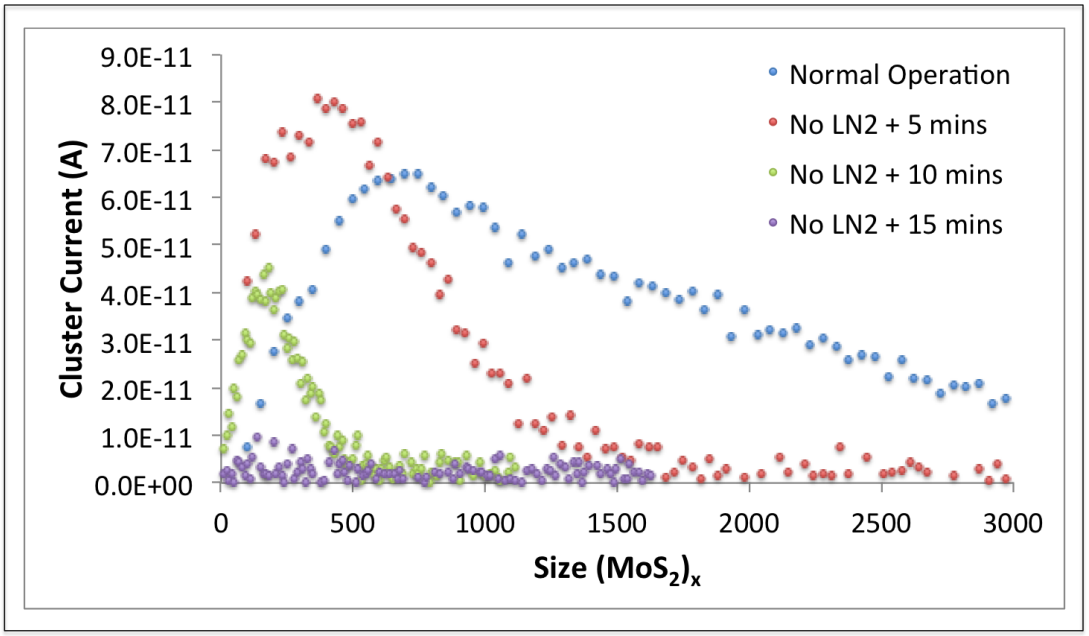

Figure 3.9: Mass Spectra of a typical MoS_2 continuum as the nucleation chamber warms due to absence of liquid nitrogen cooling [Ar flow 55 sccm, He flow 130 sccm, DC Power 55 W, Condensation Length 200 mm, Nozzle Diameter 3.7 mm, Nuc Pressure 0.7 mbar]

clusters are not frequently produced, due to the group focus on 'real-world' applications and the limitations of exposing samples directly to atmosphere without in-situ analysis. Thus the common tuning procedures are tailored to large sizes, straddling the boundary between clusters and nanoparticles. The most dramatic shifts in produced cluster size are seen by changing the basic thermodynamic parameters, temperature and pressure. The nucleation chamber temperature is held constant by a continuous liquid nitrogen flow, however when the dewar is exhausted the cluster distribution shifts rapidly (Fig 3.9), signifying the importance of keeping the cooling constant throughout experiments. The size of the dewar is an issue on long production runs greater than 5 hours, but as the system is generally used to make low coverage samples this has not been a significant problem. The nucleation pressure is used to tune the magnetron output size to the desired cluster size, as mentioned earlier the pressure is dependent on many controlled parameters.

3.2.4 Typical Operation

The plasma is first ignited with a low argon flow of 20 sccm, at a magnetron power of 10 W. In order to look at single ions the nucleation pressure should be as low as possible, thus the nozzle is fully opened and the argon flow is reduced to 10 sccm after the plasma ignition. This argon ion beam can be used to provide an estimate of the instrument resolution by reading the Full Width Half Maximum (FWHM) of the 40 amu mass peak measured at the sample stage, or used to sputter substrates to create defect sites. If the pressure and magnetron power are increased further there is an onset of sputtered atoms and few-atom clusters. As discussed, these few-atom clusters are well-studied in fundamental cluster physics, but the focus in this study is the fabrication of much larger structures in the continuum. The tuning conditions for few-atom clusters are useful to identify contamination, oxygen in the gas flow for example, however for MoS_2 this is difficult due to molybdenum and sulfur atomic masses being multiples of oxygen.

A standard safety procedure is to frequently check for an atomic copper signal at 63.5amu. If this is present in a non-copper sample it indicates that the target has been sputtered through to the copper cooling plate below. As well as introducing Cu contaminants, the most serious problem is the possibility of sputtering through the copper plate to release cooling water into the vacuum chamber. The Cu signal is a final indicator that a target needs to be changed, however with targets being changed several times a month the depth of the sputter pits can usually be measured to prevent complete breakage. Such an indicator is shown in Fig 3.10, a strong peak is noted around the copper mass of 63.5 amu, however when operated with certain materials interpretation is still required. The peak could be attributed to S_2^+ dimers or SO_2^+ compounds, the weak peak at 48 amu could be attributed to the uncommon SO^+ compound or doubly charged Mo^{2+}. The presence of oxides is most likely to be detected after a target change, before the oxidised outer layers are sputtered off. Otherwise a leak in the vacuum system or gas feed could be the cause. Systems opened regularly are prone to leaks when gaskets do not bind properly or feedthroughs become damaged. Leak testing was performed with a commercial leak

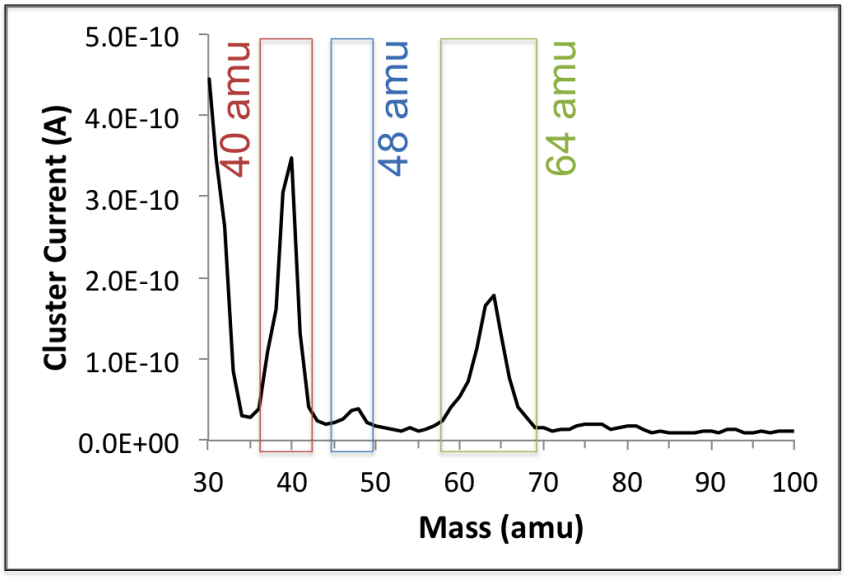

Figure 3.10: Mass Spectra taken during the Argon tuning phase. A peak is noted at 64 amu, which could be attributed to copper at 63.54 amu, and at 48 amu, which is likely to be sulfur oxides. The 40 amu peak is certainly Ar^+. [Ar flow 10 sccm, He flow 0 sccm, DC Power 35 W, Condensation Length 220 mm, Nozzle Diameter 3.8 mm, Nuc Pressure 0.07 mbar]

tester for the HV system or manually tested with a mass spectrometer for UHV. Both involve use of directed helium gas to penetrate the small leaks. In the case of the HV cluster beam system, which does not need baking after venting, any leaks or copper signals are fixed with only a few days downtime.

On completion of these preliminary procedures the cluster tuning process can begin. The initial setup of the cluster source was performed by a Birmingham Instruments engineer, Dr Jinlong Yin. The initial settings of the ion optics were set by a combination of SimIon calculations and iterative optimisation. This produced a set of typical lens voltages for Cu clusters of varying sizes that were used as a starting point for clusters of other elements. The coarse voltages on ion optics are similar for all elements, providing some measurable transmission to the sample stage. The first use of a new target material brings up many unknown parameters that must be defined to make reproducible clusters. To some extent the first tuning requires some trial and error, based on previous materials, to tune both the nucleation and the ion optics to attain a signal at the sample plate. Once a signal has been acquired tuning becomes more procedural. If there is difficulty

in acquiring an initial signal there are some techniques to help, such as measuring the cluster beam before the mass filter (the white-beam), which causes a large loss of flux. The cluster current can also be measured at positions along the beam path by connecting the picoammeter to a lens element and setting an earlier lens to deflect the beam.

The nucleation and optics parameters are stable and reproducible between sessions, so a cluster signal is usually attainable by simply copying parameters of the previous session. This, usually smaller, signal is then used as a starting point to tune for new clusters. Firstly the nucleation parameters are optimised to produce the highest measurable cluster flux, then the ion optics are tuned starting with the elements closest to the nucleation chamber. The ion optics are tuned semi-automatically, an interface allows a voltage range to be scanned over while monitoring the current at the sample plate. The voltage ranges are defined by the limitations of the associated electronics. The current should be increased after one pass, but usually two to three more passes are performed to maximise cluster current. Usually the size of clusters initially tuned is the size from the previous session or the size that was initially found to be produced by the nucleation chamber parameters. The nucleation parameters must be changed to shift this size peak, usually high pressures, long condensation length and high power sputtering give larger clusters, with the reverse for small clusters. After shifting the cluster peak to the desired size, the ion optics must be optimised again to account for the new mass to charge ratio.

3.2.5 System Resolution

The system resolution is defined by measuring the FWHM of a well-defined mass peak. This is usually performed by measuring the single argon atom peak at 40 amu. Argon ions are unaffected by isotopic broadening with 99.6% of argon atoms weighing 40 amu. It would be most representative to measure resolution at the size that is being selected, far larger than single Ar atoms, but at large sizes the clusters are in a continuum leaving no defined peaks to measure. Molybdenum disulfide has the added problem that molybdenum has significant isotopic broadening from 92-100 amu (96 is chosen as a median value)

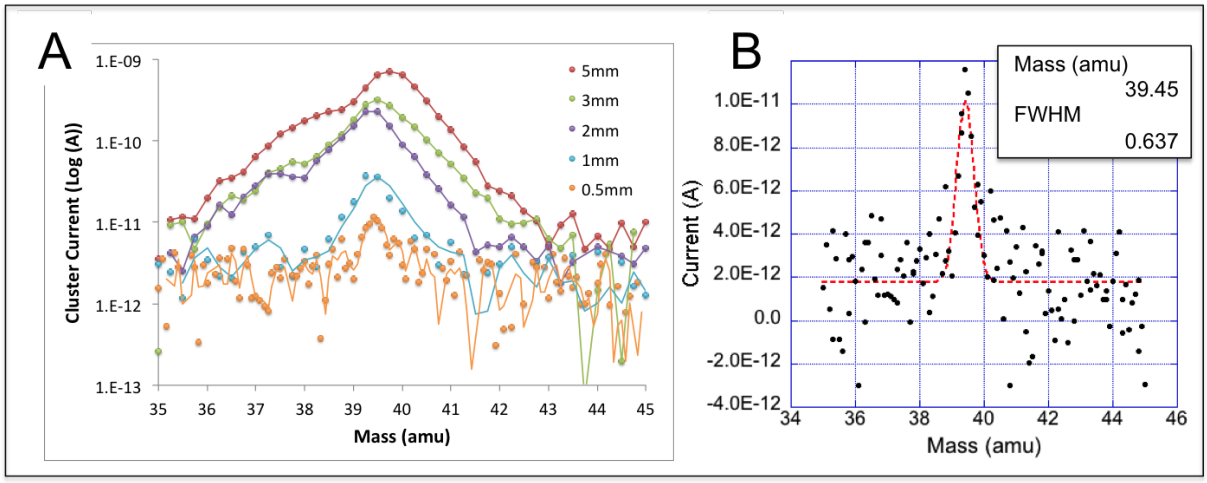

Figure 3.11: (A) Argon flux at deposition stage for decreasing entrance and exit aperture size. System resolution can be increased at the expense of flux by reducing the entrance and exit apertures to the time of flight filter. (B) Argon peak taken at minimum slit sizes of 0.5 mm with resolution of m/δm=61.74 or 1.6%, the absolute position is lower than 40 amu due to a vertical velocity component of the beam entering the ToF [Ar flow 12 sccm, He flow 114 sccm, DC Power 75 W, Condensation Length 220 mm, Nozzle Diameter 3.8 mm, Nuc Pressure 0.7 mbar]

and its median mass is a multiple of the sulfur mass (95.02% at 32 amu). Thus Mo-S compound peaks will have multiple equivalent configurations with the same mass and those with higher molybdenum content will be artificially broadened.

The argon peak has been used to determine nominal system resolutions for different Time of Flight aperture settings (Fig 3.11). The mass resolution at the highest flux is typically 6% and can be improved to less than 2% at the lowest slit size. The highest mass resolution of the system, achieved by Dr Feng Yin, is 0.8%. These resolutions can be assumed when producing clusters with the same aperture settings. The real size distribution measured by statistical analysis of electron micrographs is always broader than implied by the theoretical system resolution. This is due to a combination of effects, such as the difference in focusing between large clusters and single Ar ions, impact effects upon landing and electron beam damage during imaging.

Material	Au_{309}	Pd_{923}
Recipient	Kenton Arkill	Dongsheng He
Ar Flow (sccm)	190	90
He Flow (sccm)	70	100
DC Magnetron Power (W)	20	10
Condensation Length (mm)	250	250
Nozzle Diameter (mm)	7.03	2.09
Nucleation Pressure (mbar)	0.14	0.40

Figure 3.12: Formation parameters for Au and Pd clusters produced on the cluster beam system for group members

3.2.6 Operation as a Facility

The cluster source is operated as a facility style instrument for use by group members and collaborators. Clusters of a variety of materials and other required specifications, such as impact energy for pinning, are produced on a range of substrates (Fig 3.12). The cluster source is a versatile instrument capable of operating with a downtime of 1 day between magnetron target changes and pump/vent cycles. Procedures are largely identical for working with different cluster materials, just requiring modification of previously determined optimum parameters.

The most frequent use of size-selected clusters is as a mass standard against other less well-defined nanoparticles. The HAADF-STEM technique (Section 3.4.1) can use the total integrated intensity of a mass standard to define the mass of another nanoparticle, and even compensate for the mass of known ligands. The accurate size control also finds use as fiducial markers for TEM tomography and as model catalysts.

3.3 X-Ray Photoelectron Spectrometry

3.3.1 System

XPS was performed at Leeds EPSRC Nanoscience and Nanotechnology Facility (LENNF) by Dr. Alexander Walton and uses a VG Escalab 250 (Fig 3.13). The spot size was 200 μm

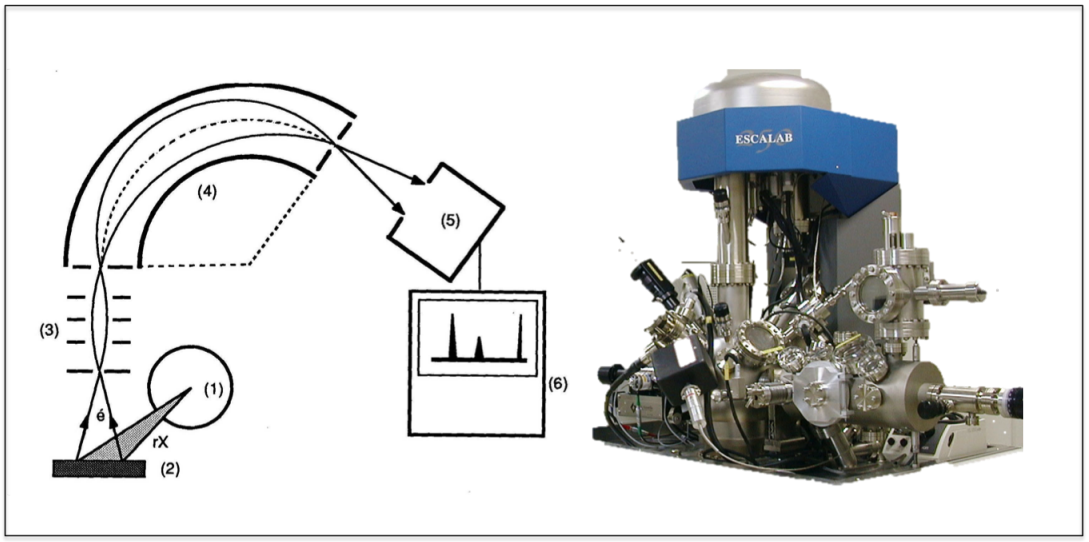

Figure 3.13: (1) X-ray tube, (2) Sample, (3) Electronic focusing system, (4) Spectrometer, (5) Electron detector (channeltron), (6) Data acquisition. Adapted from iramis.cea.fr

in diameter on the sample with an energy resolution of 0.6 eV FWHM. MoS_2 clusters for XPS measurements were deposited on a 4 mm spot at the centre of a freshly cleaved 5 × 10 mm Highly Oriented Pyrolytic Graphite (HOPG) wafer (NT-MDT, Grade ZYB). Automated sample stage manipulation centred the X-ray beam on each sample and took a survey scan as well as detailed scans for molybdenum, sulfur, oxygen and carbon peaks.

3.3.2 Data Processing

The Mo 3d, S 2p and O 1s peaks were chosen for detailed analysis, using the eXPFIT 1.5 application (Dr Roger Nix, Queen Mary University of London). The raw data was processed by an iterative convolution fitting routine using Lorentzian (the initial X-Ray line shape) and Gaussian (Instrument Broadening) peak shapes, with the most defined peak in a region (Mo 3d, S 2p, O 1s) determining peak shape for all fits in the region. The fitted line shape in most cases was closest to Gaussian, on average 90% Gaussian to Lorentzian. Known relationships, such as the peak area-ratio for doublets and the doublet energy separation [159] were used to constrain the relative peak positions. The FWHM of doublets was constrained to be the same and the energies of the peaks before fitting were chosen based on values in the literature [41]. Shirley background subtraction was

performed on the raw data before fitting.

The oxygen photoelectrons, from the S subshell, have no spin-orbit splitting so fitting was accomplished with single peaks. These were chosen from literature to correspond with appropriate chemical species, such as oxidised Mo and adsorbed water [159, 160]. The Mo 3d peaks are doublets due to spin orbit splitting of the D subshell. Three doublets were chosen for fitting to represent Mo in oxidation states of 4, 5 and 6. These doublets are fitted assuming 3.15 eV spin-orbit intervals and a doublet area ratio of 2/3 for D electrons [161]. A 7th peak is required in this region for the S 1s singlet. The S 2p peaks are again represented by doublets due to spin orbit splitting in the P subshell. Two doublets are fitted to represent the differing electronic environments of terminal sulfides and bridging sulfides. These doublets are fitted assuming 1.2 eV spin-orbit intervals and a doublet area ratio of 1/2 for p electrons [161].

The elemental ratios for the sample can be calculated by measuring the areas associated with each peak. This must first be normalised by the photoemission cross section for each element. Atomic (or Relative) Sensitivity Factors used to normalise peaks were 2.75 for Mo 3d, 0.54 for S 2p and 0.66 for O 1s [160].

3.4 Scanning Transmission Electron Microscopy

STEM imaging was performed by Zhi-Wei Wang and Kenton Arkill on a Jeol JEM-2100F with CS corrector, followed by detailed analysis and image processing by myself. Aberration correction improves spatial resolution and also gives a much higher intensity than an uncorrected beam. High Angle Annular Dark Field (HAADF) STEM detects highly scattered electrons to produce micrographs with intensity proportional to atomic number, Z^{α}.

3.4.1 Dark Field Imaging

The technique of Scanning Transmission Electron Microscopy (STEM) with aberration correction allows atomic precision imaging of nanostructures. The contrast in the bright-field mode is provided by phase differences induced by the material the electrons travel through, this contrast is most clear with well ordered lattices. At small sizes many nanoparticles do not have such well-defined order to allow them to be easily picked out from the carbon background. The speed at which the small nanoparticles can be imaged is crucial for ensuring they are not significantly damaged by the beam during focusing and acquisition. The use of High Angle Annular Dark Field (HAADF), as a simultaneous technique that detects strongly scattered electrons, provides much better contrast due to its dependence on atomic number. The low atomic number of carbon generally means it has a very weak signal in comparison to nanoparticles that are usually composed of some metal. Contrast is further enhanced by stacked columns of atoms in the nanoparticles, allowing some height information to be extracted from the intensity data.

The atomic number dependence of this technique is generally used in a qualitative way to provide good image contrast, but calibration turns it into an invaluable quantitative tool. Differences in detector sensitivities and inner and outer acceptance angles of the annular detector mean this calibration should be done for each specific microscope configuration. The calibration relies on using two sets of size-selected nanoparticles with different atomic number based on a basic mass-intensity relationship (Eqn 3.1) [162].

$$N_{Standard}\left(\frac{I_{Cluster}}{I_{Standard}}\right) = N_{Cluster}\left(\frac{Z_{Cluster}}{Z_{Standard}}\right)^{\alpha} \tag{3.1}$$

Statistically determining the intensity of both nanoparticle types, combined with their known atomic numbers, leaves the only variable being the exponent of Z dependence. This was calibrated using Au_{923} and Pd_{923} mass standards [163, 164], to give an exponent of $\alpha = 1.46 \pm 0.18$. The following mass balance formula (Eqn 3.2) can be used to convert intensity of MoS_2 clusters (with $N_S = 2N_{Mo}$) to absolute mass compared to Au_{309} magic

number clusters.

$$309 \times \frac{I_{MoS_2}}{I_{Au}} = N_{Mo}\left(\frac{Z_{Mo}}{Z_{Au}}\right)^{1.46} + N_S\left(\frac{Z_S}{Z_{Au}}\right)^{1.46} \tag{3.2}$$

The mass standard is chosen to be a similar size to the cluster being measured, so as to have a similar degree of plural scattering, which adds to the detected intensity. The mass balance technique can even be used with single atoms as mass standards, common due to dissociation from beam energy. The difficulty of distinguishing and accurately imaging single atoms gives this a larger error, so large stable mass standards are used when possible.

3.4.2 STEM Electron Energy Loss Spectrometry

The bright field detector can be replaced by a cylindrical deflector to detect the energy distribution of the transmitted electrons. The majority will retain the originally monochromatic beam energy, usually 200 keV, due to direct transmission or elastic scattering. Some electrons interacting with the sample will lose energy due to inelastic scattering and cause some quantum of excitation in sample atoms. The quantised nature of the energy losses causes peaks in the detected electron intensity at the energy of the excited atomic state. Such detectable features are excitations of bound electrons from inner core levels to the vacuum level or collective oscillations of the electrons about atoms (plasmons). The energy between vacuum and bound core orbitals is characteristic of certain elements so it can be used to determine the composition of nanoparticles. This becomes useful when working with nanoparticles of multiple elements as the use of Z-contrast alone can be misinterpreted. The high energy (200 keV) of the incident beam results in a low energy resolution of around 1 eV.

The ability for the STEM to image in the dark field while acquiring spectroscopic information in the bright field at atomic resolution, is an ideal tool for nanoparticle characterisation. Binary systems may produce nanostructures of varying composition,

these nuances are difficult to confirm in ensemble methods such as XPS. In particular core-shell structures are often produced in cluster beam sources when one element condenses into a core before the other, this would not be desirable when producing compound clusters.

The small size of the clusters compared to the large volume of amorphous carbon on the TEM grid produces a low signal to background. Thus the clusters that could be measured were limited to those on thin areas of carbon or preferably suspended on the edge of a hole in the carbon. The core-loss signals were quantified by measuring total counts in a 25 eV window from the edge energy after subtraction of a smooth background preceding the edge. The integrated counts were normalised by the electron scattering cross-section for each element, defined by the beam energy of 200 keV, inner collection angle of 19 mrad, and outer collection angle of 32 mrad.

3.5 Electrochemistry

3.5.1 Three-Electrode Measurements

Electrochemical measurements are commonly performed with three electrodes in an electrolyte (Fig 3.14). The first electrode, known as the working electrode, supports the nanoparticles to be tested. The electrode itself is usually composed of an inert material to provide a low background reactivity. The second electrode is a reference with a stable redox potential to calculate the potential applied at the working electrode. In aqueous electrolytes there are several possible reference electrodes which can be used depending on compatibility with chemical species in the cell. The electrode used in this work is a form of Standard Hydrogen Electrode (SHE) consisting of platinum mesh in contact with pure hydrogen and perchloric acid ($HClO_4$) electrolyte. Finally, the counter electrode (CE) is another platinum mesh behind a glass frit, to prevent contamination of the working electrode with platinum atoms, which balances the redox reactions at the working electrode. The reduction of protons at the working electrode (WE) is balanced by oxidation of hydrogen

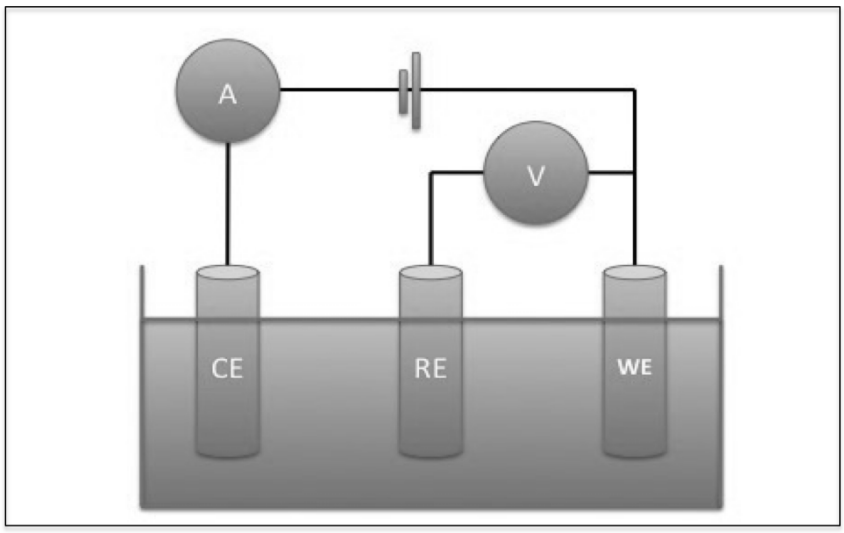

Figure 3.14: A standard three electrode setup schematic. A working electrode (WE) to be analysed is immersed in electrolyte, with its potential measured relative to a reference electrode (RE) and the reaction current measured through the counter electrode (CE).

at the counter electrode.

3.5.2 Working Electrode

Working electrodes made of carbon were used for electrochemical studies. The preliminary work was performed on freshly-cleaved Highly Oriented Pyrolitic Graphite (HOPG), an atomically flat substrate commonly used for surface science. The HOPG was sputtered with Ar^+ ions before depositing clusters in order to create defect sites for pinning. The second type of carbon substrate is a hard, inert, conducting ceramic-like material known as glassy carbon (GC) (HTW, Germany; SIGRADUR G). The preparation of this material involves polishing with graded alumina down to 0.05 μm until it attains a mirror finish. At the nanoscale the material looks like close-packed fullerene fragments, not atomically flat like cleaved HOPG [165]. The mobility of clusters on the glassy carbon surface was assumed to be insignificant, unlike on HOPG, which exhibited aggregation and ripening under reaction conditions (Section 6.3). The discs are polished then transported to the cluster source deposition chamber where they are inserted into a steel sample holder. A steel lip holds an annulus of 0.5 mm width around the face of the discs, leaving an

exposed 4 mm diameter area in the centre for deposition. The prepared substrates are then removed and pressed into a Teflon holder by pressing the outer 1 mm width annulus until the disc is flush with the Teflon surface. Experiments use the same shared Teflon holder with 10 discs that are repolished after experiments and reused.

3.5.3 Reference Electrode

The measurement of potential is based on the proton reduction half cell (Eqn 3.3), the same as being measured at the working electrode. A true standard hydrogen electrode requires a platinised platinum electrode with hydrogen continuously bubbled over it, immersed in a strong acid. A simpler system is employed for our work by removing the continuous hydrogen flow. A platinum mesh is first platinised using chloroplatinic acid to create a layer of 'platinum black' nanoparticles to increase surface area and enhance reaction kinetics. The mesh is then sealed in a glass pipette and filled with perchloric acid. Electrolysis is performed with another platinum electrode in perchloric acid to evolve hydrogen inside the pipette. The hydrogen volume is increased such that there is a three-phase boundary between perchloric acid, platinum mesh and hydrogen gas.

$$2H^+ + 2e^- \rightarrow H_2 \tag{3.3}$$

This pseudo-SHE is compared to a commercial AgCl reference (in saturated KCl) between measurements to ensure it is stable. The SHE reference should measure -0.197 V against the AgCl reference. The homemade SHE reference is used, instead of the AgCl directly, to prevent contamination of the electrolyte by the KCl solution in the AgCl electrode. The potentials in these experiments are converted to the RHE scale by correcting for electrolyte acidity and ohmic losses (Eqn 3.4). Resistance values are taken from the real part of electrochemical impedance spectrograms at 0 V.

$$E_{RHE} = E_{Measured} + (0.059 \times pH) - iR \tag{3.4}$$

3.5.4 Electrolyte

The experiments were conducted in acidic aqueous electrolyte, either 0.1M or 1mM perchloric acid ($HClO_4$). The experiments with 0.1M acid replicate the standard procedures for testing HER activity in the literature. The 1mM acid has a lower proton concentration, in order to reach a mass transport limited state, to explore the kinetics of the reaction. The 0.1M $HClO_4$ electrolyte is prepared by mixing 4.31 mL 70% $HClO_4$ (100.46 g/mol) in 500 mL UHQ water. The 1mM $HClO_4$ electrolyte is prepared by mixing 43.1 μL 70% $HClO_4$ in 500 mL UHQ water, with the addition of 6.12 g of $NaClO_4$ (122.44 g/mol) powder to produce a 0.1M supporting electrolyte.

3.5.5 Cell Design

The electrochemical cell uses a small volume of electrolyte with closely spaced electrodes to reduce solution resistance. The first design of cell used a compression design to be more compatible with the HOPG substrates used for surface science studies (Fig 3.15). A 5 $\times$ 10 mm wafer of HOPG was compressed between two 4 mm diameter O-rings with a reservoir of electrolyte above. The counter and reference electrodes were placed in the reservoir while the HOPG working electrode was connected electrically from beneath. There were problems with this initial cell design that resulted in some failed experiments. The compression force had to be large to avoid electrolyte leakage, but this compression caused deformation of the HOPG. The electrical connection was also difficult, connecting the edge planes usually resulted in breakage of the thin substrate, while connecting from the underside caused a large cell resistance due to low inter-plane conductivity. These problems could be reduced by use of a larger HOPG substrate and a more advanced method of electrical contact to the top layer. The results of scanning probe and preliminary electrochemistry on HOPG (Sections 4.3 and 6.3) indicated that the surface was too flat to strongly pin the clusters.

A new substrate system was used as an alternative to designing a new cell compatible

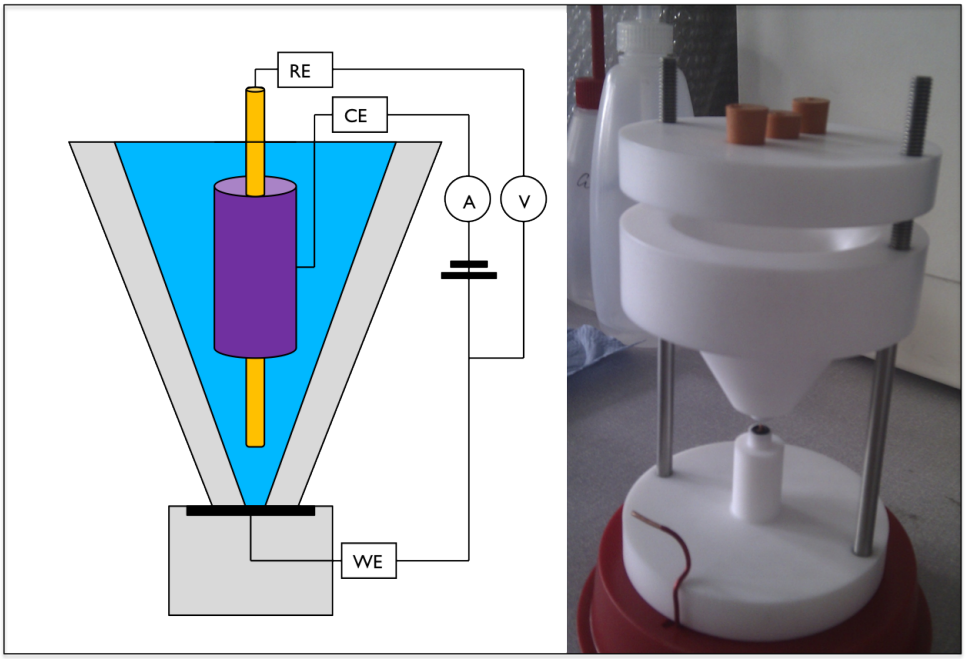

Figure 3.15: (Left) Teflon compression cell schematic in three electrode configuration, (Right) Teflon compression cell designed by myself and machined by the Physics workshop

with surface science type substrates. Glassy carbon discs mounted in a Teflon sleeve are a common electrode design compatible with standard Pyrex glassware cells. The electrodes are mounted on a rotor shaft, allowing rotation of 3000 RPM, to test mass transport limitations. The full electrode assembly is 10 mm diameter × 50 mm height, too large to be directly inserted into the cluster source deposition chamber. Instead, smaller glassy carbon discs of 5 mm diameter × 3 mm height are coated in the deposition chamber and subsequently removed to be inserted into a Teflon sleeve. A spring-loaded gold contact then makes electrical connection from the uncoated side. The electrode assembly is then attached to the rotor and vertically suspended in electrolyte. The rotor is held stationary during experiments but activated between scans at 2000 RPM to remove evolved hydrogen bubbles blocking the electrode surface.

3.5.6 Cell Setup

The cells can be sealed to create an airtight chamber, preventing reactive atmospheric gases from contaminating the electrolyte. A continuous flow of nitrogen gas is used

to create positive pressure in order to prevent ingress of atmosphere through any gaps. Nitrogen flows through a split tube, one into the electrolyte, the other above to provide an inert gas layer. A second tube carries hydrogen gas into the electrolyte to replace lost protons. The cell is sparged vigorously for 30 minutes with nitrogen before use to remove dissolved oxygen in the electrolyte then switched to the upper tube to keep the electrolyte undisturbed by bubbles during experiments. The hydrogen flow is kept at a low rate throughout to produce one small bubble each second. The internal pressure is prevented from building up with an electrolyte-filled U-bend tube, which releases bubbles of gas from the cell without admitting atmosphere. After each use, the cell and accessories are subsequently cleaned in a 1:1 mixture of H_2SO_4 and HNO_3. The entire cell is situated in a closed cabinet lined with foil, this acts as a Faraday cage to reduce electrical noise and additionally reduces light levels in the cell to prevent possible photocatalytic current.

3.5.7 Cyclic Voltammetry

The three electrode system can measure current generated by the working electrode in response to its potential. This reaction current is caused by reaction products forming once a certain potential threshold is reached to achieve the reaction. The threshold has a defined minimum energy associated with the Gibbs free energy of the system, plus additional components such as resistive losses and activation barriers to form transition states. The use of catalysts to form these transition states at lower energies means the total energy required for the reaction approaches the minimum value.

A common method for testing the efficacy of a catalyst is to cycle through a potential range, effectively supplying a varying amount of energy for the reaction to proceed, and measuring the reaction current simultaneously. An efficient catalyst will produce high reaction current with only a small potential increase above the thermodynamic minimum. The catalytic activation barrier can be measured by finding the onset of exponential current increase. This is usually achieved by slope analysis of an overpotential versus log I plot (Tafel plot). The experiment is performed by setting a potential range and a scan

rate to determine the speed of potential change. The positioning of the potential range about the thermodynamic potential determines whether reductive or oxidative processes occur. The scan rate can also be used to investigate mobility of reaction constituents.

3.5.8 Hydrogen Evolution Reaction (HER)

The reaction being studied in all cases is the Hydrogen Evolution Reaction (HER), in which protons are reduced to molecular hydrogen on a suitable catalyst. The reaction starts by adsorption of protons, from protonated H_2O, to the catalyst surface, known as the Volmer reaction (Eqn 3.5).

$$Volmer : H_3O^+ + e^- \rightarrow H_{ads} + H_2O \tag{3.5}$$

On MoS_2 this begins with strongly bound hydrogen atoms, at any overpotential, on the active edge sites. These initial adsorbed hydrogen atoms are too strongly bound to desorb as molecular hydrogen, but at a coverage of 25% the adsorption free energy of hydrogen increases to 0.1 eV, such that an overpotential of around 100 mV is required to add further hydrogen atoms [15, 21]. This hydrogenated edge obeys the Sabatier principle by having an ideal binding energy that allows adsorption to the catalyst surface but also permits desorption. The principle can be proven for HER catalysts by plotting the hydrogen binding energy against the exchange current density, with a resulting volcano plot [20, 18].

The initial Volmer step of protons adsorbing to the surface is fast, however the desorption step is not and is thus rate limiting [32]. There are two main pathways for desorption on HER catalysts, Tafel (Eqn 3.6) and Heyrovsky (Eqn 3.7). The Tafel chemical desorption mechanism involves the diffusion of two adsorbed protons on the catalyst surface and subsequent reaction to form molecular hydrogen that then desorbs. The Heyrovsky electrochemical desorption mechanism requires only one adsorbed proton, which then reacts with another proton in solution, then desorbing as molecular hydrogen.

$$Tafel : H_{ads} + H_{ads} \rightarrow H_2 \tag{3.6}$$

$$Heyrovsky : H_{ads} + H_3O^+ + e^- \rightarrow H_2 + H_2O \tag{3.7}$$

The rates of these reactions can be calculated by reference to the Tafel slope (Eqn 3.8), where b is the Tafel slope, R is the universal gas constant, T is the absolute temperature and F is Faraday's constant. The parameter α (Eqn 3.9) is a scaling relationship based on electron transfer and the ease of those transfer processes, where n_1 is the number of electrons transferred before the rate determining step (RDS), n_{RDS} is the number of electrons transferred during one elementary act of the RDS, either one if the reaction is electrochemical or zero if it is chemical. The term β is dependant on whether a reaction is energetically favourable, varying from 0 to 1, however at low overpotentials this can be approximated to 0.5 meaning that both the initial and final reactant state have a similar free energy [166]. An experimental Tafel slope can be extracted from voltammograms by plotting the log of the reaction current against the overpotential. Matching the slopes of the experimental data to the theoretical rates can give an indication of which reaction mechanism is occurring [24].

$$b = \frac{2.3RT}{\alpha F} \tag{3.8}$$

$$\alpha = n_1 + n_{RDS}\beta \tag{3.9}$$

The Volmer-Tafel reaction mechanism has a theoretical Tafel slope of exactly 30 mV/decade, with $\alpha = 2$, based on 2 electrons transferred before the rate determining step, followed by a chemical reaction to produce H_2. The Volmer-Heyrovsky reaction mechanism has a theoretical Tafel slope around 40 mV/decade, with $\alpha = 1.5$, based on one electron transferred before the rate determining step followed by one more electron transfer in the

rate determining step.

The Volmer-Tafel mechanism is assumed for platinum catalysts, as the most active facet of platinum, (100), has a Tafel slope of 28 mV/decade[167]. The adsorption of hydrogen on the platinum surface is close to 100% [168], thus the mean free path of diffusing hydrogen atoms would be small, providing further qualitative justification of this process.

The lowest observed Tafel slopes for MoS_2 catalysts are around 40mV/decade [24] suggesting HER proceeds by the Volmer-Heyrovsky mechanism. Again, using a qualitative argument, given the active sites for MoS_2 are on the layer edges, the diffusion is likely reduced, thereby preventing the Volmer-Tafel mechanism.

3.6 Chemical Synthesis

The most common MoS_2 nanoparticle catalyst preparations are based on solution syntheses, such as inverse micelles [67]. In order to better understand the advantages and disadvantages compared to methods such as gas-phase fabrication I collaborated with a catalysis group at the Danish Technical University, Copenhagen. The project involved hydrothermal synthesis of MoS_2 nanoparticles from precursors combined with doping, under the supervision of Ib Chorkendorff and Soren Dahl, in collaboration with Anders Laursen. The following sections describe the procedures for synthesis of the nanoparticles and methods of enhancement. The testing equipment and methodology was the same as described above aside from small differences in the type of electrodes. The working electrode in this case was carbon paper with the nanoparticle solution drop cast and dried before testing. The reference electrode was a Standard Calomel Electrode (SCE), connected to the main cell compartment with a salt bridge.

3.6.1 Synthesis from Ammonium Tetrathiomolybdate

A simple solvothermal synthesis following the procedure of Zong [58] was performed using an Ammonium Tetrathiomolybdate precursor (ATM, $(NH_4)_2MoS_4$, 260.27 g/mol) in methanol

solution, with hydrazine hydrate ($(N_2H_4)H_2O$) reducing agent and Polyvinylpyrrolidone (PVP, $(C_6H_9NO)_n$, 111.15 g/mol) polymer to reduce aggregation of the growing nanoparticles. This solution was heated in a Teflon-lined autoclave at 373°K for 3 hours, followed by centrifugation and resuspension of the nanoparticle precipitate in methanol.

Typically 2 mg of Ammonium Tetrathiomolybdate was dissolved and sonicated in 75 mL methanol for a 0.1 mM stock solution, suitable for preparing three 25 mL solutions of 2.5 μmol MoS_2. This was followed by the addition of PVP at a Molar ratio (PVP/MoS_2) of 5, after determination of the optimum ratio by electrochemical and TEM analysis (Section 6.2.1).

The PVP k-value was 12-18, with a typical polymer weight of 10000 amu or 10000 g/mol, the average chain length was therefore 90 PVP monomers. This was less than the 270 monomers, PVP k-value 27-33, used in the synthesis by Zong [58]. The 25 mL solution was added to a Teflon lined autoclave with 100 μL hydrazine hydrate to begin the reduction process. The autoclave was sealed and baked for 3 hours at 373°K.

The autoclave was quench cooled in water after baking and the contents centrifuged at 7000 rpm for 10 minutes followed by resuspension in fresh methanol. In the case of washed nanoparticles, this step is preceded by centrifugation and suspension in ethanol overnight. Removal of the stabilising polymer from the MoS_2 was achieved by manipulation of the charge of the molecules in the solvent. The isoelectric point (IEP) of a molecule is the pH at which it has no net electrical charge, this value varies between materials. At a pH below its IEP a molecule will carry positive charge, and at a pH above its IEP a molecule will carry negative charge. The IEP of MoS_2 is around 2-3 [169] and PVP around 7.3 [170], so with both in ethanol at a pH of 7.95 they will have the same charge and repel. After synthesis, either as-prepared or washed, the MoS_2 solution was expected to be amorphous, thus the solution was bubbled with Argon in a sealed vessel for storage to prevent oxidation.

The working electrodes were prepared by pipetting 100 μL (10 nmol) of sonicated nanoparticle solution onto a carbon paper electrode with a Teflon barrier to prevent the

solution reaching the electrical contact point. These substrates were then connected to a three-electrode system similar to the setup described in Section 3.5 and measured for catalysis of proton reduction by cyclic voltammetry. The reaction current produced was normalised to a geometric area of the carbon paper of 2.8 cm^2.

3.6.2 H_2S Sulfidation

A further processing step was added to selected samples to transform the nanoparticles from amorphous to crystalline MoS_2. The nanoparticles, supported on carbon paper electrodes, were placed in a Pyrex tube and heated to 723°K for 4 hours. During this process a mixture of 95% Argon 5% H_2S was flowed over the samples to provide a sulfur source and energy for restructuring. This is a high energy process, so as well as the desired nanoparticle reconfiguration, there could also be increased diffusion of nanoparticles on the surface and consequent aggregation. The sulfidised samples were then measured for catalytic activity in the same way as the as-prepared/washed samples.

3.6.3 Dopants (Co, Ni, Cu)

MoS_2 catalysts in the HDS reaction are often promoted using Co and Ni dopants. Similar cheap metals were added to the synthesis procedure of these MoS_2 nanoparticles to provide promotion for HER. Stock solutions of Co, Ni and Cu dopants were prepared by adding metal nitrate hexahydrate to 25 mL (5mM) (Fig 3.16) of methanol. The nanoparticle methanol suspension was pH-adjusted by addition of hydrochloric acid (HCl) to a pH of 4-5, to bring the pH below the isoelectric point of the metal nitrate and cause them to gain positive charge. The metal nitrate was added to the adjusted solution and sonicated for 30 minutes. An average doping level of 8% and 50% of Metal ions to MoS_2 precursor was achieved by adding 100 μL (0.032 mg dopant) and 667 μL (0.21 mg dopant) of 5mM dopant solution respectively to 25 mL (0.4 mg MoS_2) of the washed nanoparticles. The isoelectric point of MoS_2 is around 1-2 [169], so the nanoparticles carry a negative charge,

Dopant	Cu	Ni	Co
Precursor	$Cu(NO_3)_2.6H_2O$	$Ni(NO_3)_2.6H_2O$	$Co(NO_3)_2.6H_2O$
Molar mass (g/mol)	295.65	290.79	291.03
Precursor mass for 25 mL at 5 mM (g)	0.037	0.036	0.036

Figure 3.16: Mass of metal nitrate salt added to methanol to prepare 5 mM dopant solutions

causing the positive dopants to adsorb. The doped nanoparticles were then centrifuged to remove excess dopants and resuspended in fresh methanol to be drop cast onto carbon paper electrodes.

The carbon paper supported clusters are measured as-prepared and after sulfidation. The sulfidation is performed at low temperature, 373°K, and high temperature, 723°K, in order to explore the strength of binding of the dopants with the clusters. The high temperature processing is expected to transfer the dopant atoms from a physisorbed state to chemisorbed atoms, similarly to Mo substitution in doped HDS catalysts (Fig 2.15).

3.6.4 Lithium Intercalation

The poor through-plane conductivity of MoS_2 nanoparticles limits the efficacy of reactions, but there are various methods to split multilayer particles to their constituent monolayers. A recent method uses an ionic liquid to disrupt the van der Waals bonds [14] to cause gentle cleaving to a monolayer suspension. A more vigorous method involves saturating nanoparticles with butyl-lithium to intercalate the layers with lithium ions, then subsequent exposure to water causes rapid hydrogen production to break the interlayer bonds (Fig 3.17). This method was performed on washed MoS_2 nanoparticles immobilised on carbon paper.

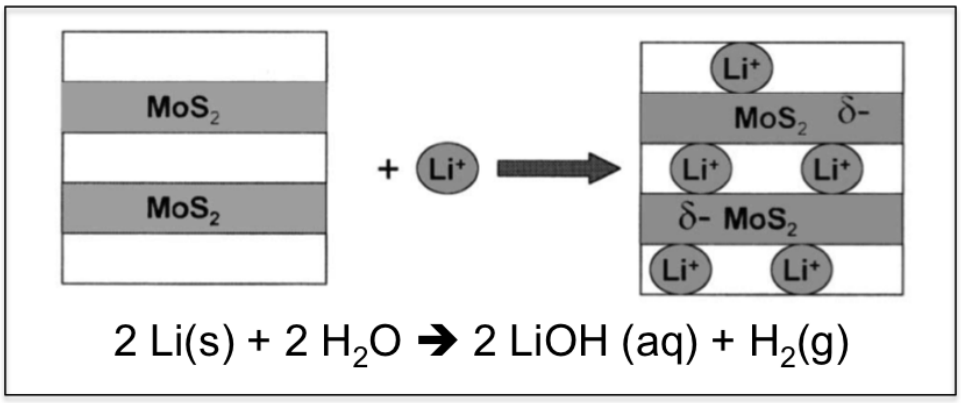

Figure 3.17: Schematic of the Lithium intercalation process. Hydrolysis of intercalated Lithium produces hydrogen gas that cleaves the layered material. Adapted from [171]

CHAPTER 4

SURFACE SCIENCE STUDIES OF SIZE-SELECTED MOLYBDENUM DISULFIDE CLUSTERS

4.1 Introduction

This work marks the first attempt at sputtering a compound target to produce compound clusters. Previous work in this group [27] has shown it is possible to produce binary materials by this method, however the resulting structures were core-shell due to preferential nucleation of one of the materials followed by coating with the other. This behaviour should be avoided for compound materials as they must form with a stoichiometric mixture of the constituent atoms.

This chapter details the initial steps of working with the unusual MoS_2 target material and preliminary analysis of the clusters being produced. The nucleation parameter space was explored to test the stability of the initial structures using in-situ mass spectrometry, ex-situ scanning probe measurements and microscopy presented in the following chapter. Post-processing was also investigated as a means of controlling the cluster structure. The compound nature of the clusters necessitated spectroscopic techniques, to compliment microscopy, in elucidating the composition. Spectrometry on the nanoscale is challenging as the signal to background is very low for such small structures. Despite these challenges the composition was established for cluster ensembles of different size and impacted energy.

4.2 Mass Spectrometry of MoS_2 Clusters

4.2.1 Initial MoS_2 Tuning

A stoichiometric pressed-powder target of MoS_2 is exposed to magnetron sputtering to produce MoS_2 clusters. The initial tuning process for the MoS_2 clusters proceeded as shown in Section 3.2.4. DC sputtering was chosen based on the greater stability over RF. Subsequent tests with RF sputtering did not produce clusters under the same conditions as DC, however due to the satisfactory performance of DC sputtering this was not investigated further. The target was sputtered using conditions optimised for Cu targets, which produced individual atoms of Mo and S (Fig 4.1). It should be noted that the molybdenum peak may be broadened due to the large range of stable isotopes of molybdenum, this would have the effect of further broadening the dimer peak and associated compounds such as Mo_2S. At low instrument resolution this effect is not observed, as the FWHM of all peaks are approximately the same, but it could be evident at higher resolution. There is also additional peak shifting in this spectrum due to vertical displacement of the beam entering the ToF filter, causing the Argon peak at 40 amu to appear at 42 amu, and the molybdenum peak at 96 amu to appear at 100 amu. This can be corrected by shifting the cluster beam with the Y deflection lens prior to mass selection.

Small compounds form with greater nucleation pressure, consisting of strong Mo peaks with weaker peaks representing the associated sulfides (Fig 4.2A). The lack of an independent, plentiful sulfur source prevents the formation of sulfur-rich magic clusters, as observed in other cluster beam methods [172]. The study of MoS_x clusters by mass spectrometry is complicated by the constituent masses being multiples, Mo being exactly 3 times the mass of S. This means distinguishing signal from Mo_2 from MoS_3, for example, cannot be achieved by mass spectrometry alone and must rely on simulation or additional spectroscopic techniques. Contamination by oxygen, which can occur through damaged gas lines, is also difficult to observe as it has a mass exactly 6 and 2 times less than Mo and S respectively.

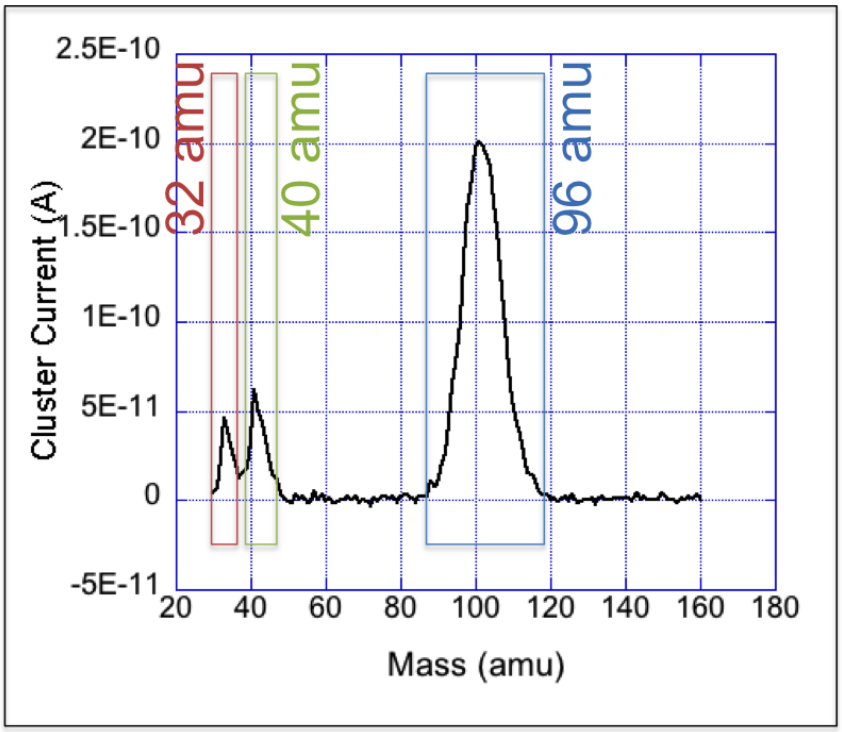

Figure 4.1: Mass Spectra of sputtered material at low nucleation pressure from 30 to 160 amu. The error, based on FWHM, on the sulfur peak, Argon peak and Mo peak is 12%. [Ar flow 12 sccm, He flow 114 sccm, DC Power 75 W, Condensation Length 220 mm, Nozzle Diameter 3.8 mm, Nuc Pressure 0.7 mbar]

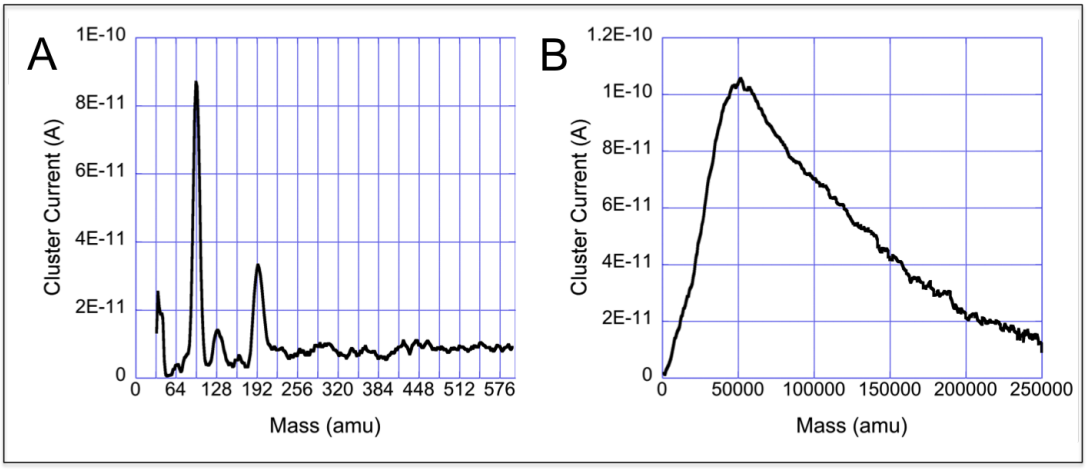

Figure 4.2: (A)Strong Mo monomer and dimer peaks with associated sulfide compounds. [Ar flow 144 sccm, He flow 180 sccm, DC Power 45 W, Condensation Length 150 mm, Nozzle Diameter 2.7 mm, Nuc Pressure 0.6 mbar] (B) At higher pressures a continuum of MoS_x clusters is produced. [Ar flow 195 sccm, He flow 200 sccm, DC Power 45 W, Condensation Length 250 mm, Nozzle Diameter 3.2 mm, Nuc Pressure 0.5 mbar]

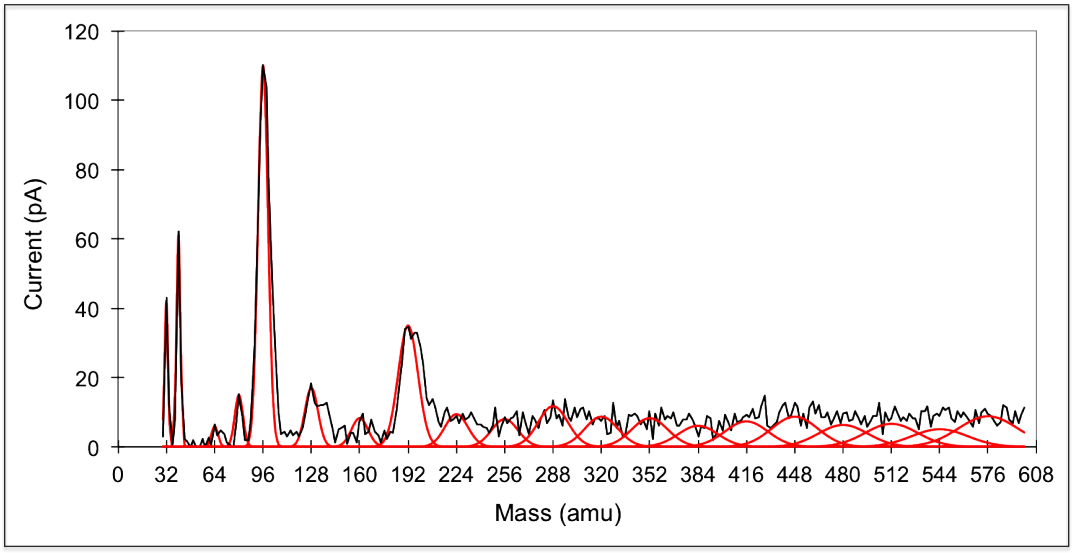

Figure 4.3: Mo-S compound peaks fitted to the continuum transition. Peaks broaden with increasing size. The [Ar flow 144 sccm, He flow 180 sccm, DC Power 45 W, Condensation Length 150 mm, Nozzle Diameter 2.7 mm, Nuc Pressure 0.6 mbar]

Mass spectra of MoS_x clusters by a molybdenum rich seed mixture is an interesting parallel study, with potential applications in explaining tribological effects in MoS_2 thin films. A typical mass spectra of small MoS_x clusters was deconvoluted (Fig 4.3) to determine if there are any preferential structures formed in this regime. The results (Fig 4.4) show that in this Mo-rich regime the main features are the Mo and multiple Mo peaks. These are followed by weaker peaks associated with the Mo sulfides, and enter a continuum regime beyond Mo_3 in which all Mo sulfides are equally stable. This is in contrast to processes that supply plentiful sulfur during nucleation, which result in strong peaks at very stable cluster structures such as Mo_4S_6 (Section 2.3.1).

The system resolution can be increased, to create more defined peak shapes, by decreasing the ToF entrance and exit apertures (Section 3.2.5). Unfortunately this lowers the final cluster flux, which can be problematic. The intensity of the MoS_2 continuum is already low due to the wide size distribution and volatility of sulfur, causing a reduction in available sulfur for cluster formation. So to produce a useful cluster current, especially for deposition, requires operation at a lower mass resolution, around $m/\delta m$=6%.

Mass spectra were used as a simple in-situ tool to analyse the types of particles being

Mass	Designated	Height (pA)	Area	Mass	Designated	Height (pA)	Area
32	S	42	114	288	Mo_3 (Mo_2S_3)	12	288
40	Ar	61	208	320	Mo_3S	9	237
64	S_2	6	33	352	Mo_3S_2	8	247
80	Ar_2	15	102	384	Mo_4 (Mo_3S_3)	6	199
96	Mo (S_3)	110	899	416	Mo_4S	7	260
128	MoS (S_4)	17	185	448	Mo_4S_2	9	332
160	MoS_2	8	113	480	Mo_5 (Mo_4S_3)	6	258
192	Mo_2 (MoS_3)	35	572	512	Mo_5S	7	289
224	Mo_2S	9	180	544	Mo_5S_2	5	235
256	Mo_2S_2	8	174	576	Mo_6 (Mo_5S_3)	9	432

Figure 4.4: Mo-S compound deconvoluted peak height and area identified from Fig 4.3, with alternate designations in parentheses. FWHM of all fits determined from Ar peak of $m/\delta m = 6.25$ (16%)

produced, however at the larger sizes desirable for catalysis there are no peaks in the spectra. Thus other ex-situ tools were used to optimise the nucleation parameters for the preferred crystalline platelet clusters. The nucleation parameters were varied and the beam periodically deposited on TEM grids for STEM analysis, resulting in a set of parameters that reproducibly created platelet type clusters (Section 5.4). Ex-situ STEM analysis was also used to test equilibration by annealing, which was unsuccessful for the temperature and grid-type used, and to confirm Mo and S content in individual clusters.

4.3 Scanning Probe Microscopy of MoS_2 Clusters

The first measurements of MoS_2 platelets were made by STM on atomically flat substrates [69]. The gas phase platelets produced in this work were first intended to be studied by scanning probe to measure the layer height and observe the metallic edge state. The MoS_2 platelets were prepared as described in Section 5.4.3 and deposited on Highly Oriented Pyrolytic Graphite (HOPG). A beam of argon ions impacting at 500 eV was first rastered over a freshly cleaved HOPG wafer to create surface defects. A typical sputtering dose is double the intended cluster coverage to ensure there are sufficient sites to pin all deposited clusters. After sputtering, the cluster beam was retuned for MoS_2 clusters of the desired

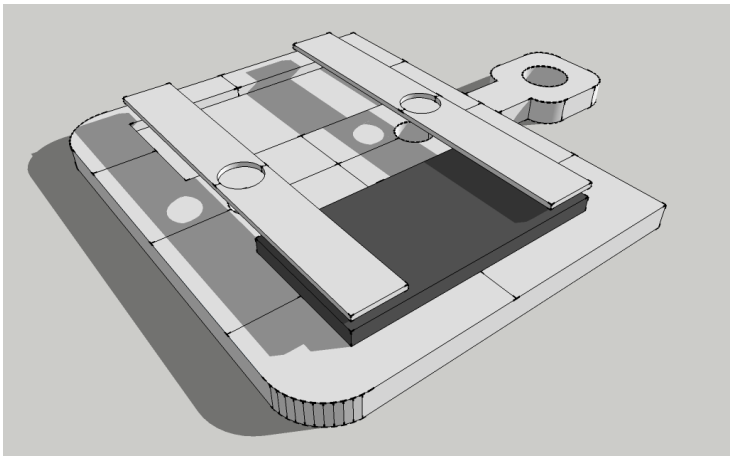

Figure 4.5: Omicron style HOPG Sample plate holds two 5x10 mm HOPG wafer. Designed by Martin Cuddy and machined by School of Physics and Astronomy workshop

size and rastered over the same area. The samples are then removed from the deposition chamber and transferred via atmosphere for scanning probe analysis.

4.3.1 Scanning Tunnelling Microscopy of MoS_2/HOPG

A Digital Instruments Nanoscope Scanning Tunnelling Microscope (STM) was used to image the graphite supported clusters using a freshly cut Pt/Ir tip. The default scanning parameters of the system (Current setpoint: 200 pA, Bias: 400 mV) were used, assuming that the HOPG defects would provide sufficient pinning, however this was not the case. The STM images with these parameters showed monodisperse peaks on the HOPG surface, that represent Argon defects (Fig 4.6). Lower interaction energy was used by decreasing the current setpoint and increasing the bias voltage (Current setpoint: 50 pA, Bias: 3000 mV). At this distance the tip could image portions of the clusters before dragging (Fig 4.7). The height of the clusters is between 2-6 layers (Fig 4.8), assuming deposition parallel to the substrate, in good agreement with similar STM of MoS_2 [75].

Attempts were made to achieve atomic resolution with these clusters by moving the tip closer to well pinned clusters, despite the stronger interaction. The feedback was switched from constant current to constant height (Current setpoint: 2000 pA, Bias: 50 mV) and scan rate increased. At this distance the carbon atoms in the HOPG are clearly defined

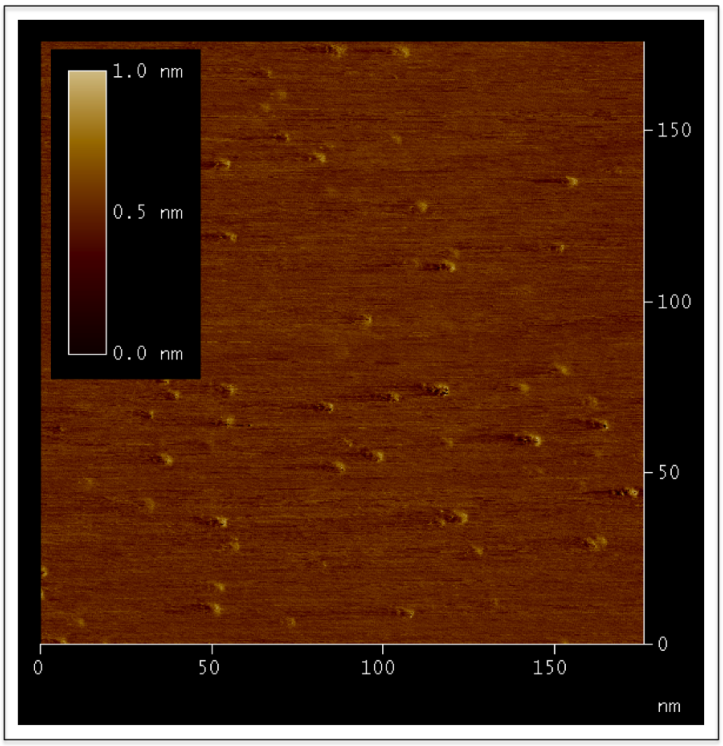

Figure 4.6: STM (constant current) image of (MoS_2) clusters shows Argon defects on the HOPG surface [Current 200 pA, Bias 400 mV, Scan Rate 1 Hz].

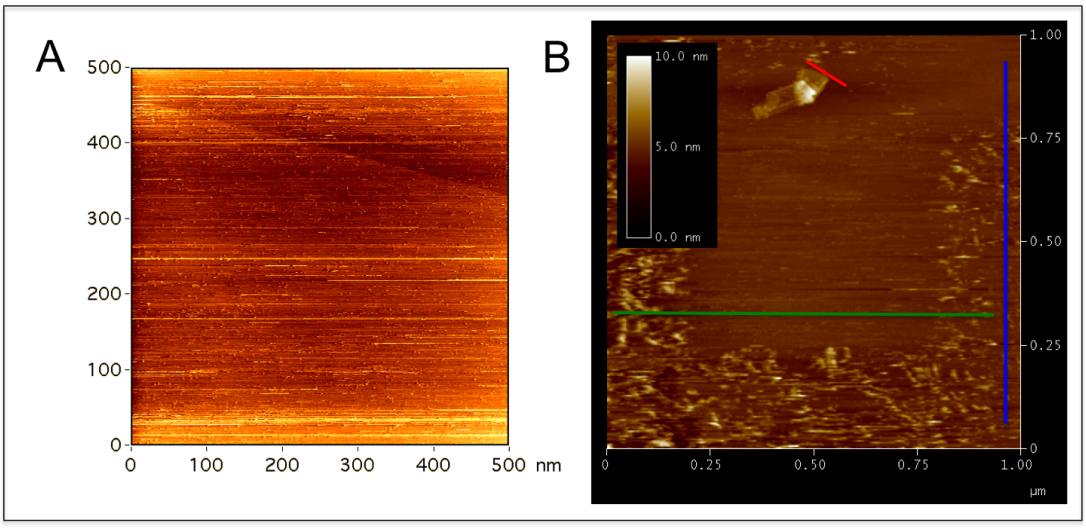

Figure 4.7: (A) STM (constant current) image of (MoS_2) clusters shows a square area with argon defects [Current 200 pA, Bias 400 mV, Scan Rate 1 Hz]. (B) The area imaged earlier is surrounded by indistinct features representing weakly pinned MoS_2. Image taken by Dr. Feng Yin [Current 50 pA, Bias 3000 mV, Scan Rate 1 Hz].

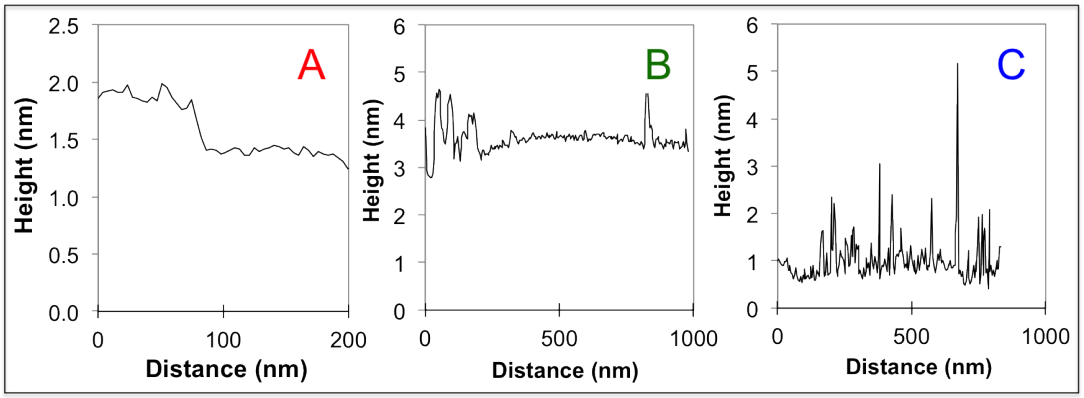

Figure 4.8: Line profiles from Fig 4.7B. (A) A step edge in the HOPG of 0.4 nm height, in good agreement with literature [173]. (B) Line profile across the swept region shows an absence of large MoS_2 features in the central swept region, which are present on the edges. (C) Line profile away from the boundary of the swept region shows MoS_2 cluster height between 1-4 nm, corresponding to between 2-6 layers.

(Fig 4.9), however the MoS_2 structure is amorphous. This is in agreement with microscopy in Chapter 5 for the disordered top layer, however in this case it may just be due to tip interaction damaging the cluster. The graphite structure loses sharpness on the regions adjacent to the MoS_2 cluster as the tip has been broadened by atoms from the cluster. The bright points on the cluster may represent regions of metallic conductivity as found on MoS_2 edge sites [69, 81].

4.3.2 Atomic Force Microscopy of MoS_2/HOPG

A Park Systems XE-100 Atomic Force Microscope (AFM) was used to image the same cluster samples as STM in non-contact mode. It was hoped that this low energy interaction would allow the clusters to be imaged without disturbing them. Large scale distributions of the clusters were obtained by AFM at low resolution (Fig 4.10), showing good monodispersity. The MoS_2 clusters have a higher density on graphite step edges, indicating that they are diffuse on the surface, to reach these regions of stronger pinning after landing (Fig 4.10A-Inset). A raised, flat region surrounds the clusters. The clusters are being imaged in air, so either atmospheric decomposition of MoS_2 in humid atmospheres to MoO_3 and H_2SO_4, or catalytic generation of carbon is a possibility for this feature. At

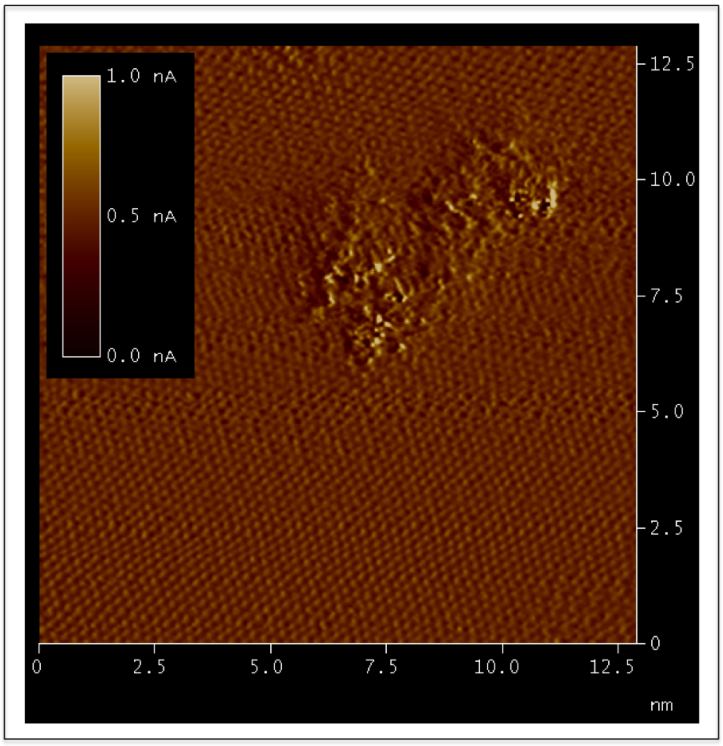

Figure 4.9: STM (constant height) image shows carbon atoms in the HOPG surface, as well as a strongly bound cluster [Set Current 2nA, Bias 50mV, Scan Rate 10 Hz].

higher resolution the tip interaction causes dragging of the clusters, which can then be imaged at low resolution (Fig 4.11A). The interaction is still sufficiently weak even on step edges that the clusters are swept from these regions as well as the terraces (Fig 4.11B). The lateral cluster dimensions measured by AFM are much greater than expected, around 60 nm diameter, however this can be explained by tip convolution effects and the reduced sensitivity of scanning probes in this plane (Fig4.12). The typical cluster height, shown by line profiles (Fig4.12C), is a more reasonable 3-4 nm in agreement with the STM measurements. The height of a single MoS_2 layer, assuming a similar van der Waals gap between the graphite and MoS_2, is 0.62 nm, meaning these clusters consist of 4-6 layers. This is similar to the value of 2-3 layers determined by statistical analysis of STEM micrographs (Section 5.6.4).

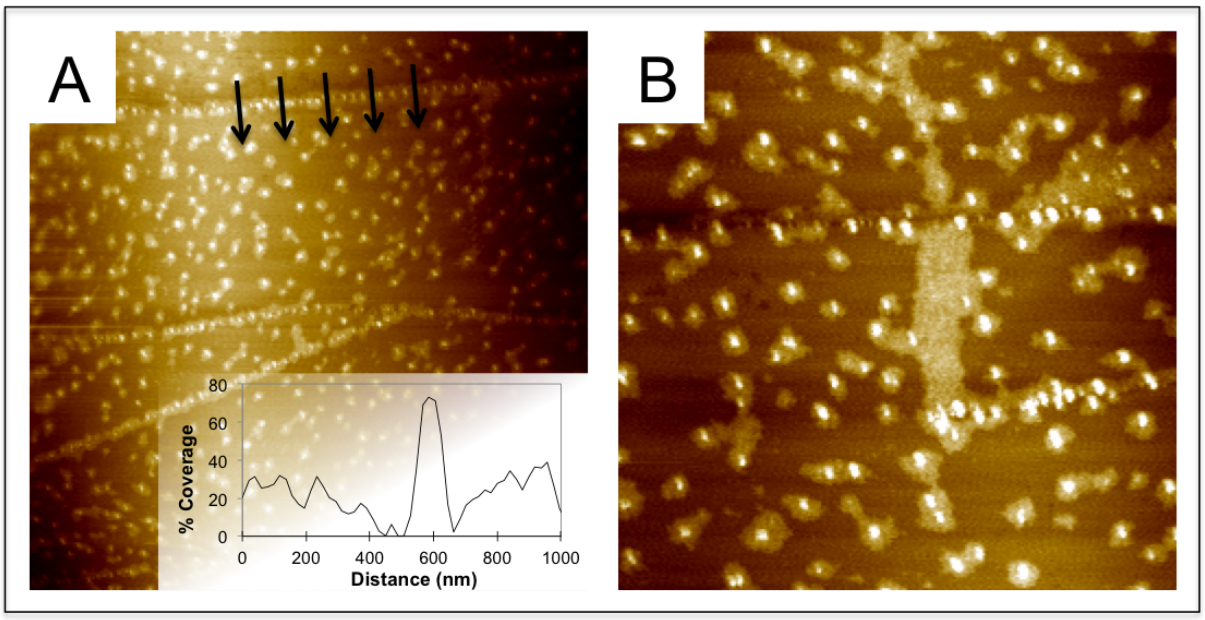

Figure 4.10: AFM images of $(MoS_2)_{500}$/HOPG in non-contact mode (A) 5 μm $\times$ 5 μm image show monodisperse clusters and a higher density of clusters on graphite edges. (A-Inset) Line profile averaged over the step region indicated by black arrows shows a peak in cluster coverage at the steps and denuded zones adjacent in which diffusing clusters migrated to the preferential step sites. (B) 2 μm $\times$ 2 μm image shows these clusters are surrounded by a halo of material.

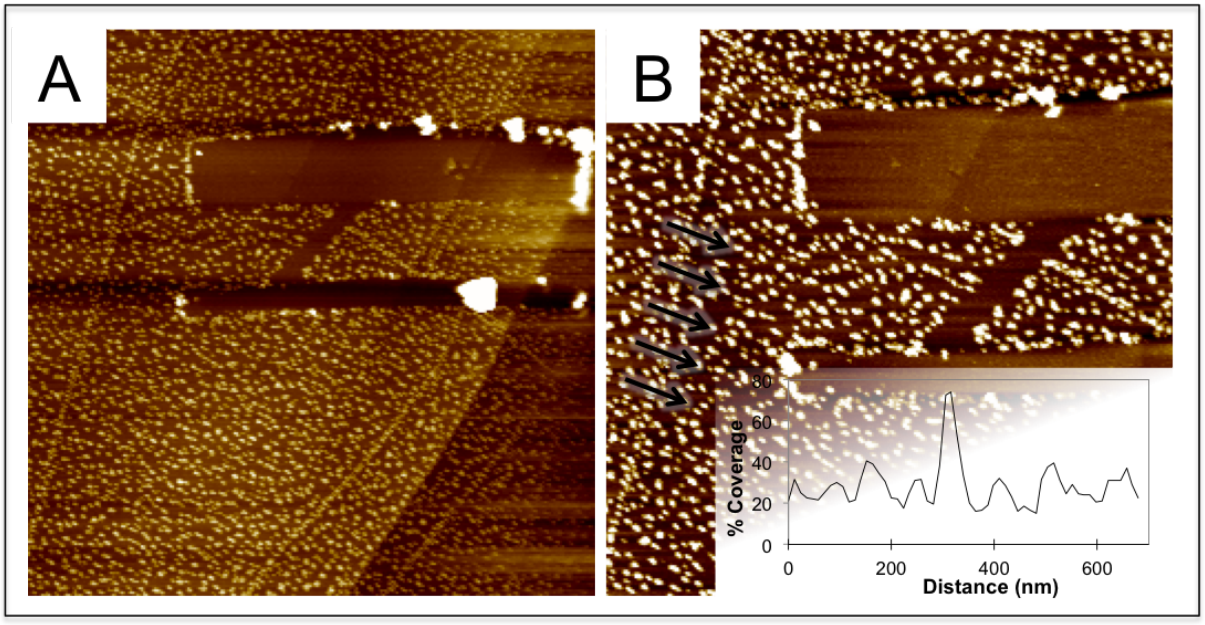

Figure 4.11: AFM images of $(MoS_2)_{350}$/HOPG in non-contact mode (A) 5 μm $\times$ 5 μm image shows clusters swept by the tip when scanning at higher magnification. (B) 3 μm $\times$ 3 μm image of the same region shows a step edge of HOPG has also been cleared of clusters. (B-Inset) Line profile averaged over the step region indicated by black arrows shows a peak in cluster coverage at the steps, but with no obvious denuded zones.

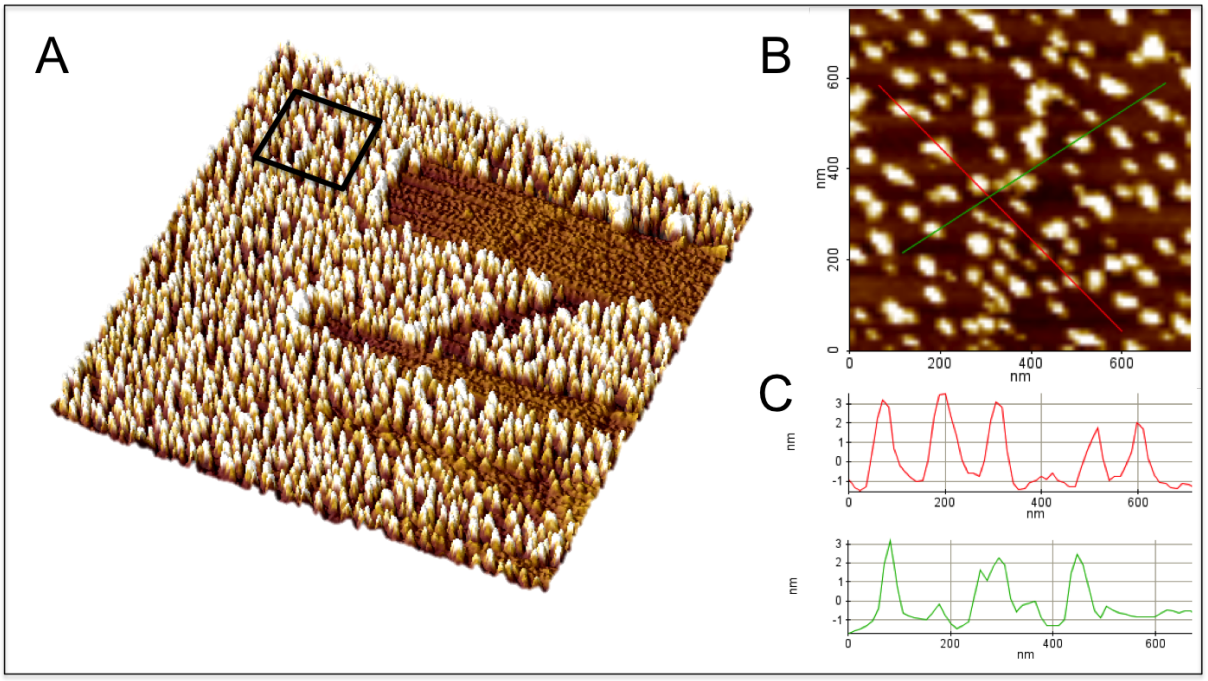

Figure 4.12: (A) 3D profile of Fig 4.11B. (B) Enlarged section from black square in (A). (C) Line profiles corresponding to Red and Green lines in (B).

4.4 X-Ray Photoelectron Spectrometry of MoS_2 Clusters

The composition of the MoS_2 clusters is important for presenting the correct active facets for catalysis and stability during reaction. The clusters, deposited on HOPG by the same method as used for scanning probe studies, were analysed at the Centre for Electron Microscopy, with Dr Paul Stanley, using Wavelength Dispersive X-Ray Spectroscopy (WDS). This technique is similar to the more common Energy Dispersive X-Ray Spectroscopy (EDS) that uses a high energy electron beam to excite core-electrons, which then relax by emitting characteristic X-Rays. In WDS, rather than detect the whole X-Ray spectrum, each wavelength is measured individually by Bragg diffraction through a crystal. This provides greater energy resolution at the expense of scan time. The fine energy resolution is necessary for analysis of MoS_2, as the S K_α (2.29 eV) and Mo L_α (2.31 eV) peaks are so closely spaced (Fig 4.13). Comparing the height of these two peaks for the MoS_2 cluster samples gave an elemental ratio of $MoS_{1.46}$. This suggests that either sulfur is not fully integrated into the clusters in the nucleation process or it is in an unstable state that is

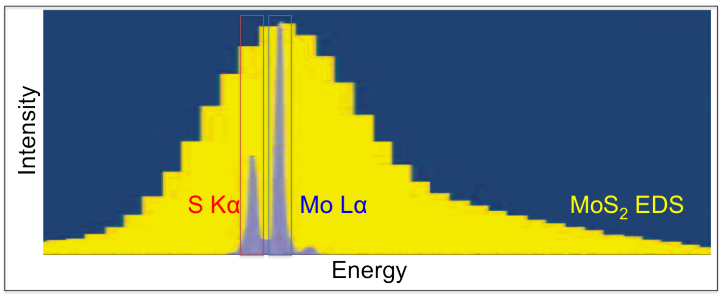

Figure 4.13: Comparison of EDS and WDS spectra for analysis of MoS_2. Adapted from Oxford Instruments IncaWave brochure

oxidised and desorbs on exposure to atmosphere.

The WDS technique is only sensitive to individual elements and not their binding state, so although Mo and S are detected on the same sample, it cannot be confirmed whether they exist as elements or a compound. Furthermore the serial acquisition of WDS scans could be a problem if the sulfur is volatile, as it could be being desorbed while the Mo peak is being measured. Thus other spectroscopic techniques, X-Ray Photoelectron Spectrometry (XPS) and Electron Energy Loss Spectrometry (EELS), were explored that provide more detailed information. The binding state of the clusters is provided by XPS in order to confirm which compounds exist, while EELS, in the Scanning Transmission Electron Microscope (STEM), shows spatially resolved spectroscopic information on the scale of a single cluster (Section 5.4.4).

The experimental setup of the XPS system and the methodology of data analysis is discussed in Section 3.3. A monolayer coverage (200,000 pAs) of $(MoS_2)_{350}$ and $(MoS_2)_{650}$ in a 4 mm diameter spot was deposited on freshly cleaved HOPG. A high coverage was chosen to provide good signal to background for peak deconvolution. The following day the samples were taken to Leeds EPSRC Nanoscience and Nanotechnology Facility (LENNF) for XPS measurements performed by Dr Alex Walton. Exposure to atmosphere is estimated to be around 5 hours during transit. The Mo 3d, S 2p and O 1s peaks were chosen for high resolution analysis to decompose the chemical composition involving these elements (Fig 4.14). The other peaks in the XPS survey were also identified to rule out contamination. All data were calibrated for the graphitic carbon 1s peak at 284.5 eV [160]

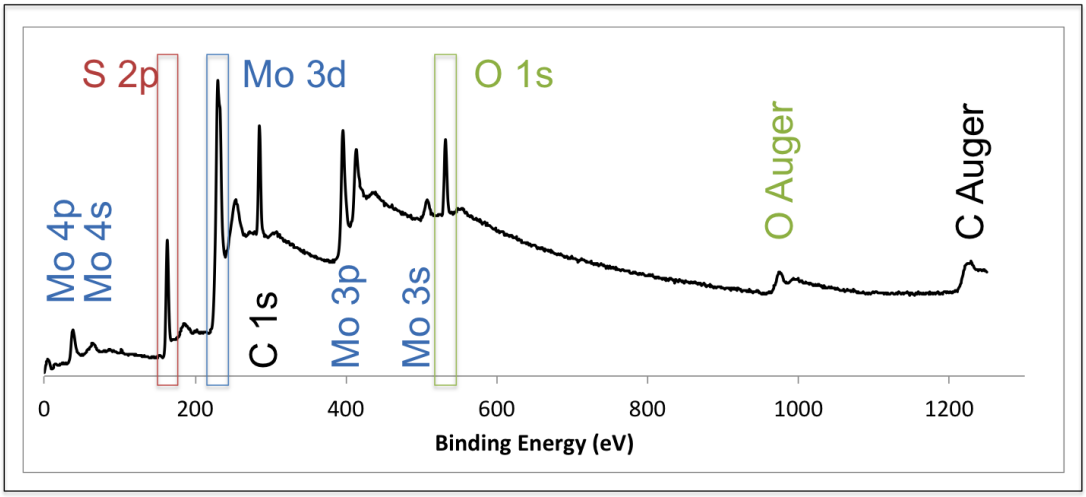

Figure 4.14: Typical XPS survey scan of MoS_2 multilayer ($(MoS_2)_{650}$ at 1500 eV), with main peaks highlighted. The remaining peaks include the carbon background, contributions from other Mo orbitals and Auger peaks at high energy.

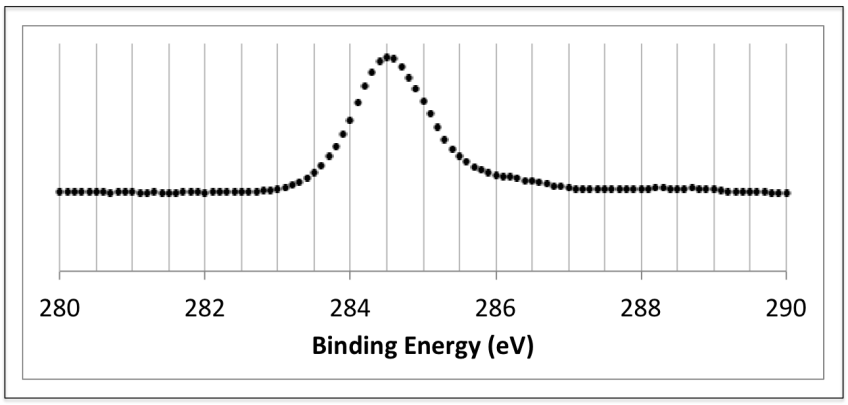

Figure 4.15: XPS Spectra of graphitic carbon 1s peak at 284.5 eV is used to calibrate the XPS spectrum

(Fig 4.15).

All XPS peak intensities were corrected with a Shirley background before deconvolution (Fig 4.16). Shirley background subtraction works on the principle that a proportion of photoelectrons will be generated deep in the material and lose energy as they escape. These photoelectrons will appear at a higher binding energy, resulting in a different background level from one side of the peak to the next. This effect can be seen most clearly in the survey scans as each photoelectron peak creates a step-like background increase due to these inelastically scattered electrons. The Shirley background shape comes from the summation of photoelectron intensity preceding each energy interval [174], in order to

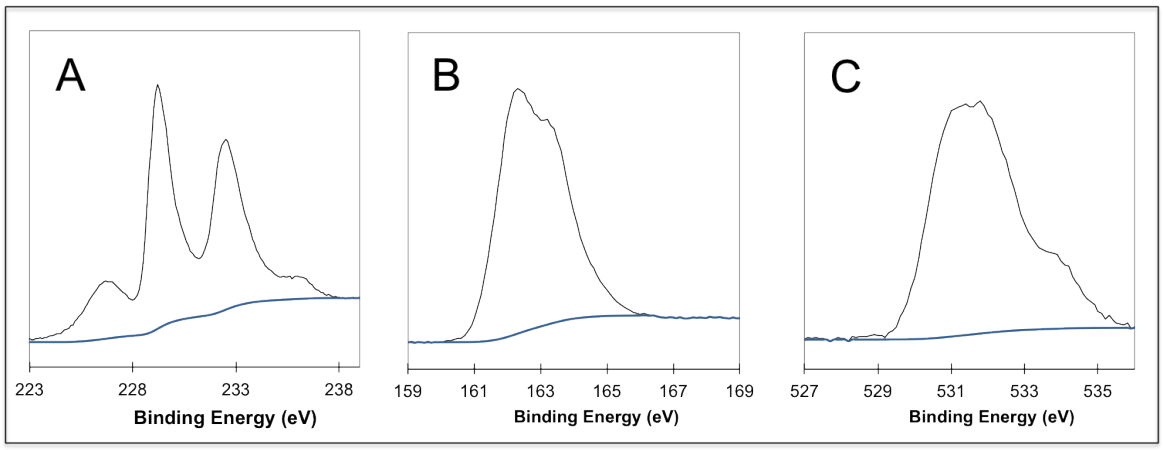

Figure 4.16: Shirley Background subtraction (Blue) from (A) Mo 3d, (B) S 2p and (C) O 1s XPS data (black) of $(MoS_2)_{650}$ clusters Deposited at 400 eV.

simulate the increasing background they generate.

4.4.1 Composition of $(MoS_2)_{650}$ Monolayer

Four monolayer samples of MoS_2 on HOPG were prepared to explore the effect of size and impact energy on binding state. Three samples of $(MoS_2)_{650}$ were deposited at impact energies of 400, 1000 and 1500 eV in order to determine the effect of impact damage on binding state. The fourth sample of $(MoS_2)_{350}$ deposited at 400 eV provides a comparison of chemical binding by size.

The $(MoS_2)_{650}$ cluster multilayer deposited at the lowest energy, 400 eV, has a normalised atomic ratio of $MoS_{1.58}O_{1.36}$ (Fig 4.17D). Some of this oxygen will be due to surface adsorbates such as water, but the high concentration indicates there is oxidation of parts of the clusters, likely the more reactive defects and edge sites.

The O 1s oxygen peak deconvolution shows water adsorbates and oxides gained during atmospheric oxidation (Fig 4.17C), identified as MoO_3 (530.8 eV), hydroxyls (531.9 eV) and water (533.9 eV) [159, 160]. There is also the possibility of other adsorbed oxygen species, such as SO_x from MoS_2 decomposition [175, 176, 177], but with few constraints for these adsorbates the deconvolution was limited to the three peaks discussed.

The S 2p sulfur peak deconvolution shows 45% is composed of a doublet at 161.8 eV

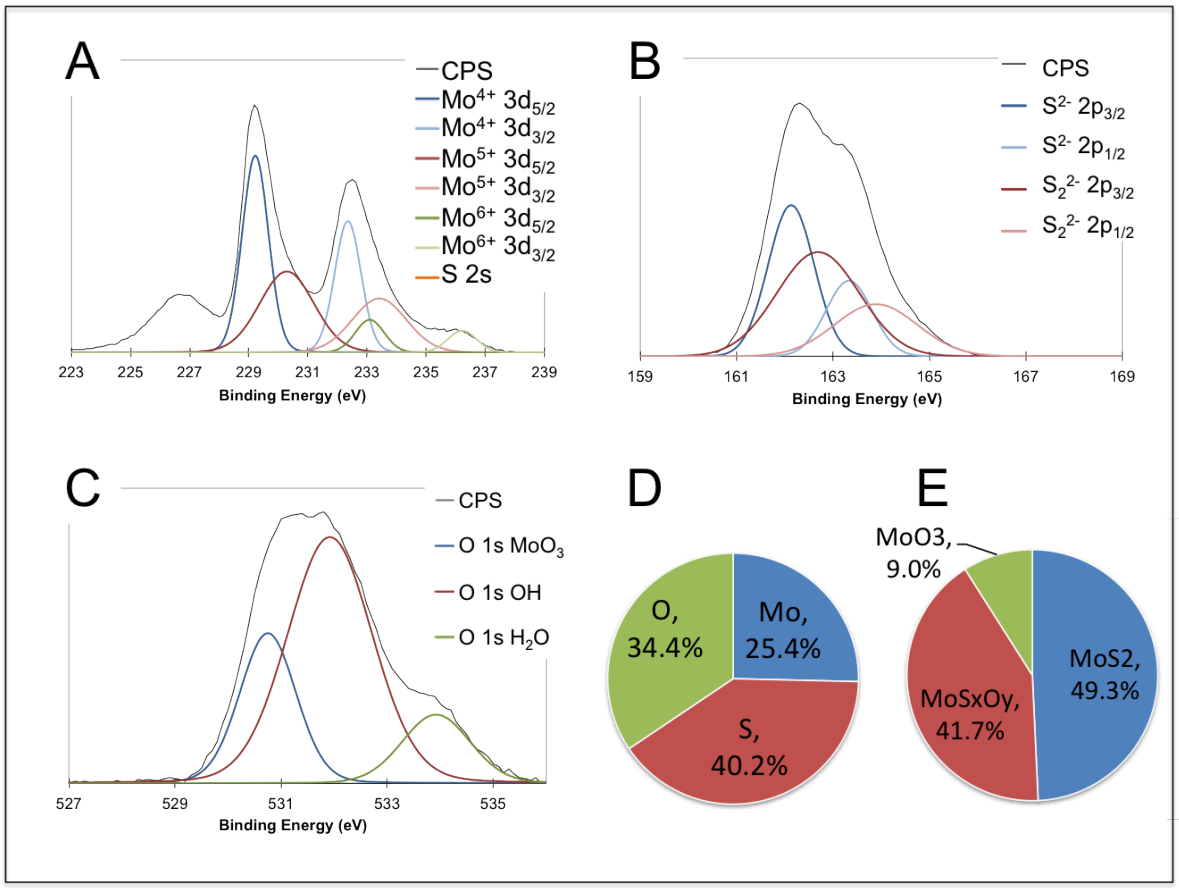

Figure 4.17: XPS Spectra of $(MoS_2)_{650}$ multilayer deposited at 400 eV on HOPG. (A) The Mo 3d peak can be deconvolved into 3 doublets associated with MoS_2, Mo oxysulfides and MoO_3 (B) S 2p peak with sulfide and disulfide contributions. (C) O 1s peak with oxide species and contaminants. (D) Normalised Elemental % of Mo, S and O. (E) Area ratio of deconvoluted Mo 3d peaks. Average oxysulfide composition calculated to be $MoS_{0.47}O_{0.16}$.

and the remaining 55% is a higher energy doublet at 163.0 eV (Fig 4.17B). The low energy peak is associated with the S^{2-} sulfide species in MoS_2, however terminal disulfide (S_2^{2-}) ligands would also contibute to this peak [41]. The extra peak indicates sulfur in a different oxidation state, formally identified as belonging to bridging disulfides (S_2^{2-}). The presence of the bridging disulfides suggests some of the low energy peak is indeed due to terminal disulfides, and that the sulfide species themselves may not all represent MoS_2. These peaks could represent partially sulfided Mo, oxysulfides associated with the more reactive edge sites.

The Mo 3d molybdenum peak in pure MoS_2 is represented by a doublet at 229 eV, very close to the peak observed from this cluster multilayer (229.2 eV)(Fig 4.17A). The asymmetry towards higher energy suggests the existence of weak Mo 3d peaks, shifted due to molybdenum in higher oxidation states. Peak deconvolution shows contributions from doublets of Mo^{4+}, Mo^{5+} and Mo^{6+}. Peak areas show 49% arises from Mo^{4+} at 229.2 eV, 42% from Mo^{5+} at 230.3 eV and 9% from Mo^{6+} at 233.1 eV. The dominant 4+ oxidation state is associated with MoS_2, with a small component of MoO_3 in the 6+ state. The remainder in the 5+ state and to some extent, portions of the 4+ and 6+, must be represented by intermediate oxysulfides such as MoO_2, MoO_2S, $MoOS_2$, MoO_2S_2, MoOS, MoS, MoS_3, MoO_3S [178, 179]. The average composition of the ensemble is given by $MoS_{1.58}O_{1.36}$. The average oxysulfide composition (Figs 4.17E, 4.18E and 4.19E) was calculated by assigning a stoichiometric proportion of the sulfur signal to the Mo^{4+} signal, and similarly a stoichiometric proportion of the oxide signal to the Mo^{6+} signal. The remaining oxygen and sulfur signal is then assigned to the Mo^{5+} signal.

This mixed composition of molybdenum sulfides and oxides has been shown in the literature for incomplete sulfidation of MoO_3 annealed in H_2S at 523°K [41] and matches well to the deconvoluted ratios of molybdenum and sulfur species found in these clusters. The sulfidation process of MoO_3 [41, 180], and the oxidation of these clusters approach from opposite starting points but indicate that the energy threshold for these clusters to form fully stable MoS_2 clusters has not been reached in the sputtering and condensation

process. Subsequent exposure to atmosphere then reverts the partially-sulfidised regions of the clusters to a more stable amorphous oxide or oxy-sulfide form. It can be expected that low coordination sites, such as the reactive edges, should be preferentially oxidised due to their increased activity.

The total oxy-sulfide and oxide content of the cluster is 50.7% (Fig 4.17E), which should be proportional to the percentage of reactive edge atoms measured from STEM for $(MoS_2)_{650}$ in Chapter 5 (Section 5.6.4). The percentage of edge atoms is only 33.2%, so there must also be oxidised material on the top layer. In order to provide this amount of oxidation sites, 29% of the top layer must also be in an oxidised state, suggesting 29% of the top layer consists of defects or edge sites. This is consistent with incomplete top layers observed by STEM (Section 5.6.1).

The reduced sulfur content seen by XPS of the sputtered clusters is consistent with MoS_x thin film production using Mo sputtered in H_2S [181, 182, 183, 184]. The effect could be related to the composition of the cluster seeds that condense into the final cluster. Patterson et al shows that the dominant structure for small MoS_x clusters is a sulfur deficient Mo_4S_6 [19].

4.4.2 Composition due to Impact Transformation

As impact energy is increased the clusters may undergo structural changes that affect the proportion of low coordination sites. Greater amounts of defects sites will increase the proportion of oxidised material, which would be evident from XPS. This would reveal information about the stability of the clusters to physical deformation. The ability to form more active sites by this method has the potential increase utilisation of catalyst material.

The effect of increasing impact energy from 400 eV to 1000 eV (Fig 4.18) and 1500 eV (Fig 4.19) does not greatly change the raw atomic ratio of elements deposited, with maximum deviation from the low energy deposition of 4%, 10% and 12% for Mo, S and O respectively. The magnitude of the variance matches with the volatility of the constituents. Molybdenum and sulfur have the same coverage when deposited, but sulfur can be oxidised

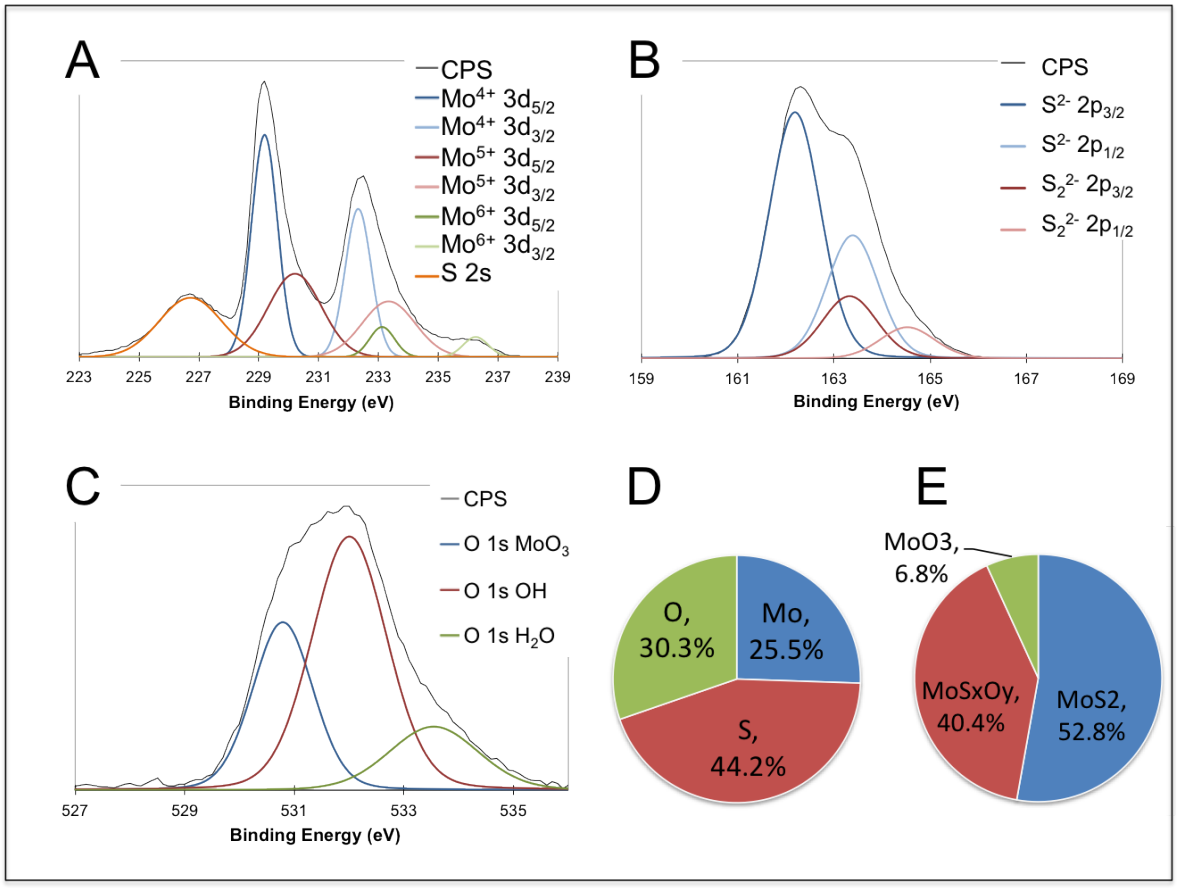

Figure 4.18: $(MoS_2)_{650}$ multilayer deposited at 1000 eV on HOPG. (A) The Mo 3d peak can be deconvolved into 3 doublets associated with MoS_2, Mo oxysulfides and MoO_3 (B) S 2p peak with sulfide and disulfide contributions. (C) O 1s peak with oxide species and contaminants. (D) Normalised Elemental % of Mo, S and O. (E) Area ratio of deconvoluted Mo 3d peaks. Average oxysulfide composition calculated to be $MoS_{1.25}O_{0.35}$.

to form compounds that will desorb. The percentage of oxygen is based on atmospheric adsorption and as this is not a controlled parameter the variation is correspondingly larger. The Mo 3d peak features also remain roughly constant in proportion, with 52.5±0.4% in the 4+ MoS_2 state and the remainder as oxysulfides (40.8±0.5%) or oxides (6.7±0.2%). The percentage of oxidised Mo in the high impact energy clusters is less than for the lowest energy deposition. This is in contradiction to the expected result that higher impact energy will create more active defects, and can instead be explained by higher impact energy causing implantation of the clusters. In conclusion, the effects of impact energy are minor, as the impact range of 0.6 to 2.3 eV per MoS_2 unit induces no structural changes that affect the composition or reactivity.

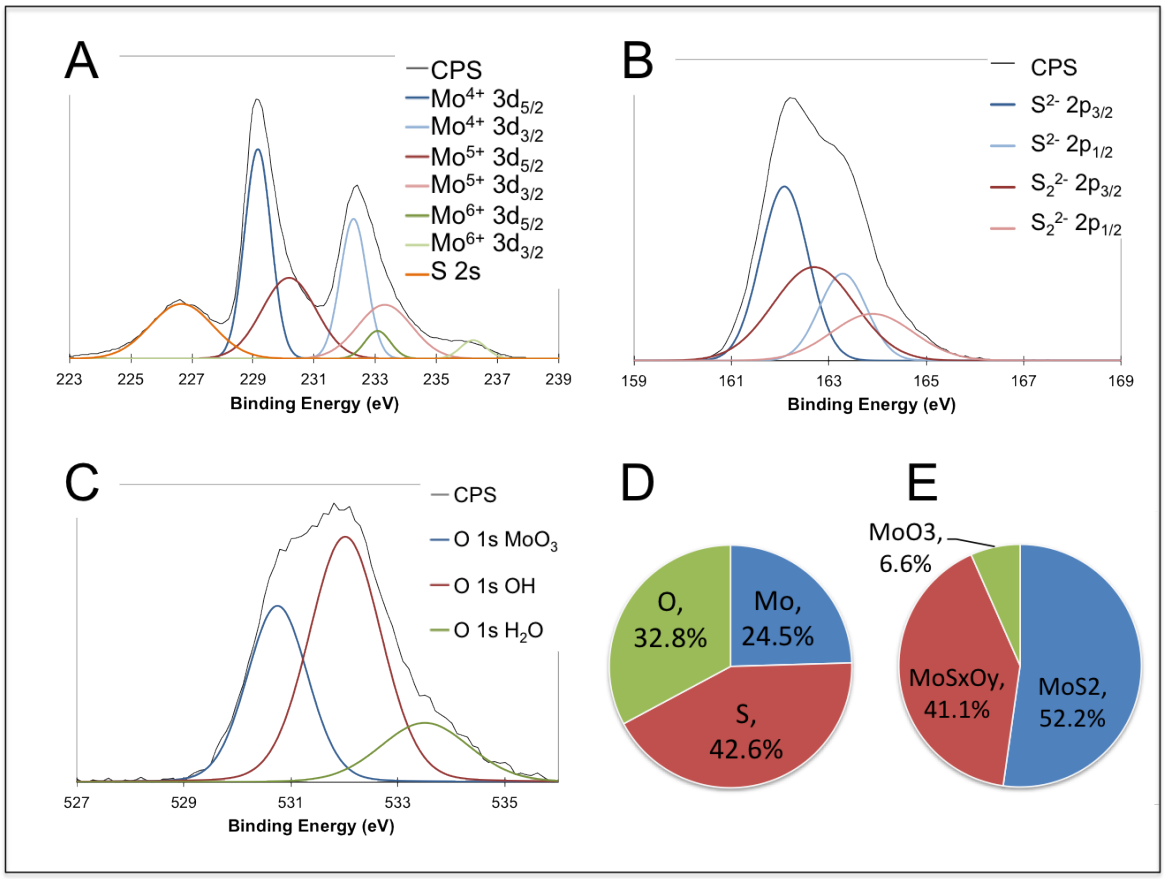

Figure 4.19: $(MoS_2)_{650}$ multilayer deposited at 1500 eV on HOPG. (A) The Mo 3d peak can be deconvolved into 3 doublets associated with MoS_2, Mo oxysulfides and MoO_3 (B) S 2p peak with sulfide and disulfide contributions. (C) O 1s peak with oxide species and contaminants. (D) Normalised Elemental % of Mo, S and O. (E) Area ratio of deconvoluted Mo 3d peaks. Average oxysulfide composition calculated to be $MoS_{0.75}O_{0.55}$.

4.4.3 Composition of $(MoS_2)_{350}$ Monolayer

A cluster multilayer of $(MoS_2)_{350}$ was tested to check for differences in composition due to size (Fig 4.20). The intrinsic composition of as-prepared clusters was not expected to change greatly as the target material and nucleation processes should be the same. The effect of the oxidation on smaller clusters however should be increased due to the higher ratio of edge to interior atoms. This is indeed suggested by the higher percentage of oxygen on this sample, with an ensemble average composition of $MoS_{1.59}O_{1.95}$. The percentage of Mo in an oxidised or partially oxidised state in $(MoS_2)_{350}$ is indeed greater than $(MoS_2)_{650}$, 52.9% and 50.7% respectively. The total elemental content of oxygen is also increased for the smaller clusters, 43.0% compared with 34.4% in $(MoS_2)_{650}$. Comparing to the measured edge ratios from microscopy (Section 5.6.4), the Mo oxidation again exceeds the expected availability of reactive sites, and requires 21% of the top layer in the form of defects or otherwise active sites to explain the measured oxidation. This is smaller than the 29% active top layer calculated for $(MoS_2)_{650}$, explained by the decreasing cluster uniformity with size (Section 5.6.4). These results suggest the defect-rich cluster morphology produced by this method has the potential for greater catalytic activity than perfect nanocrystals, similarly to other studies of defective MoS_2 [121, 59, 115]

4.4.4 Background and Alternate Fits for XPS

The assumption of Mo in three oxidation states, as well as the fits to oxygen and sulfur peaks, were tested to ensure they were reasonable. The fitting procedure was constrained according to relationships described in Section 3.3, and tested for other likely combinations of peaks to compare the best fit. The Root Mean Square (RMS) deviation for each set of peaks was used to confirm the best models (Fig 4.21).

Different fits for the Mo 3d peak were compared, with the clear S 2s peak at 226.7 eV held constant (orange peak in fits). This is the most complex, but also the most constrained peak due to the spin splitting of the 3d peaks. The first fit tested is for pure MoS_2 (Fig 4.22),

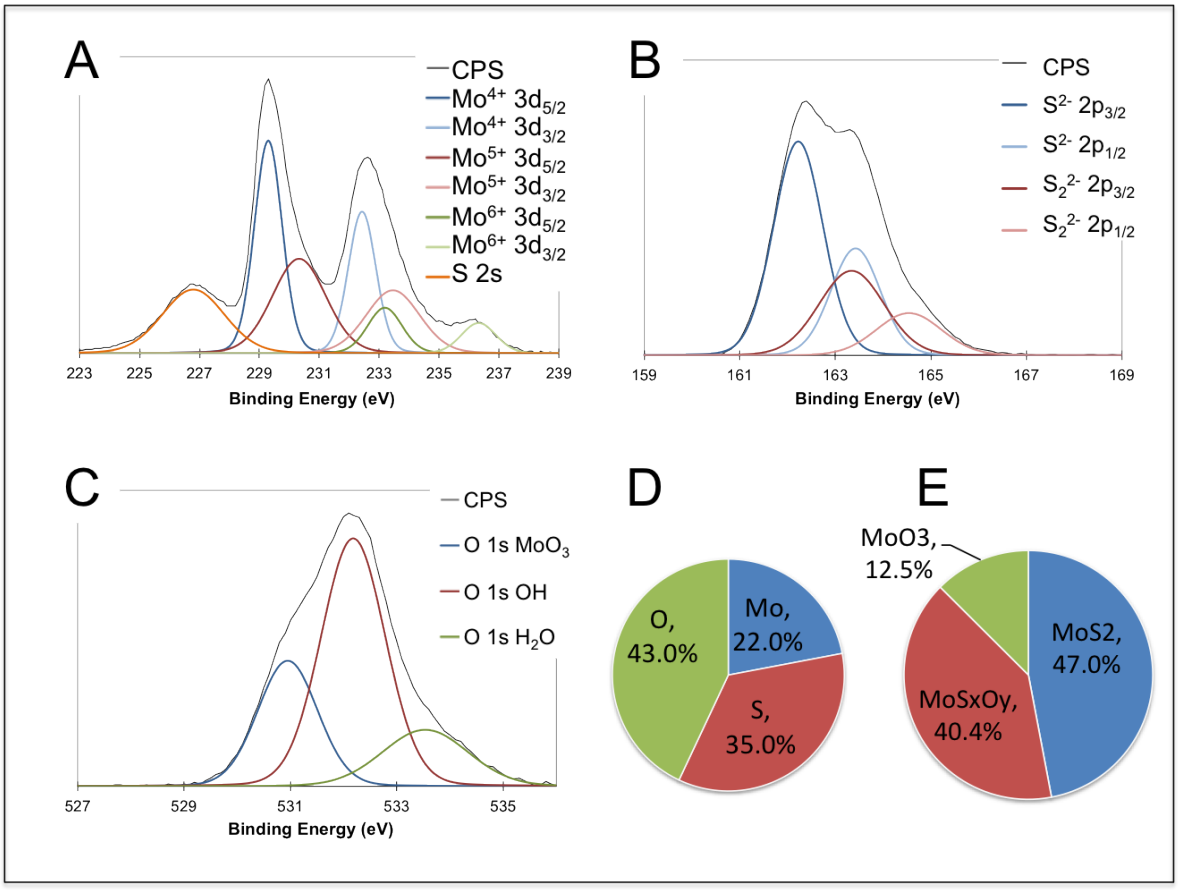

Figure 4.20: $(MoS_2)_{350}$ multilayer deposited at 400eV on HOPG. (A) The Mo 3d peak can be deconvolved into 3 doublets associated with MoS_2, Mo oxysulfides and MoO_3 (B) S 2p peak with sulfide and disulfide contributions. (C) O 1s peak with oxide species and contaminants. (D) Normalised Elemental % of Mo, S and O. (E) Area ratio of deconvoluted Mo 3d peaks. Average oxysulfide composition calculated to be $MoS_{0.99}O_{0.35}$.

Orbital	Species	RMS
Mo 3d	**S, MoS_2, MoS_xO_y, MoO_3**	**357.59**
S 2p	**S^{2-}, S_2^{2-}**	**35.30**
O 1s	**MoO_3, OH, H_2O**	**47.57**
Mo 3d	S, MoS_2	1172.95
Mo 3d	S, MoS_2, MoO_3	762.96
Mo 3d	S, MoS_2, MoO_3, SO_4	399.16
Mo 3d	S, MoS_2, MoS_xO_y, MoO_3, SO_4	244.40
S 2p	S^{2-}	228.06
S 2p	S^{2-}, S_2^{2-}, SO_4	34.24
O 1s	MoO_3, H_2O	205.80

Figure 4.21: Fits used shown in bold, as well as alternative fits below, with RMS deviation from the data.

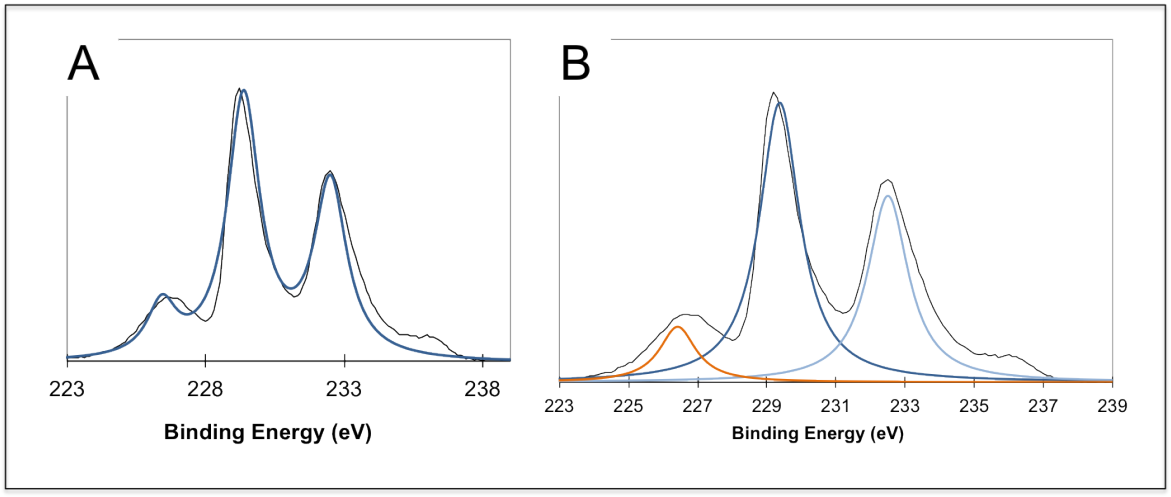

Figure 4.22: (A) Mo 3d data (black) and fit (blue) of $(MoS_2)_{650}$ clusters deposited at 400 eV, (B) fitted to one MoS_2 (blues) doublet [RMS 1172.95]

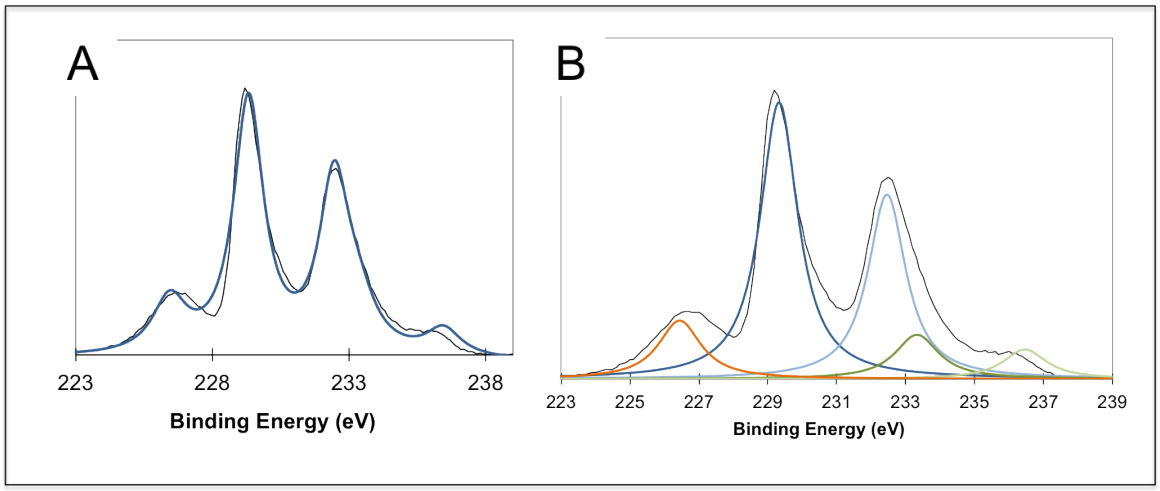

Figure 4.23: (A) Mo 3d data (black) and fit (blue) of $(MoS_2)_{650}$ clusters deposited at 400 eV, (B) fitted to one MoS_2 (blues) and one MoO_3 (greens) doublet [RMS 762.96]

however it is obviously incorrect. The high binding energy side of the peaks are larger, suggesting a slightly higher oxidation state species and there is a clear shoulder at 236 eV that is not accounted for at all.

The second fit was for MoS_2 and MoO_3 (Fig 4.23), which matches the general shape well, indicating that the Mo 3d peak consists of Mo in a sulfided and oxidised state. The exact shape, such as the peak heights and their asymmetry, is not perfectly fitted.

The third fit was for MoS_2, MoO_3 and an SO_4 singlet from the S 2s orbital (Fig 4.24). SO_4 is a decomposition product of MoS_2, as exposure to water creates MoO_3 and H_2SO_4.

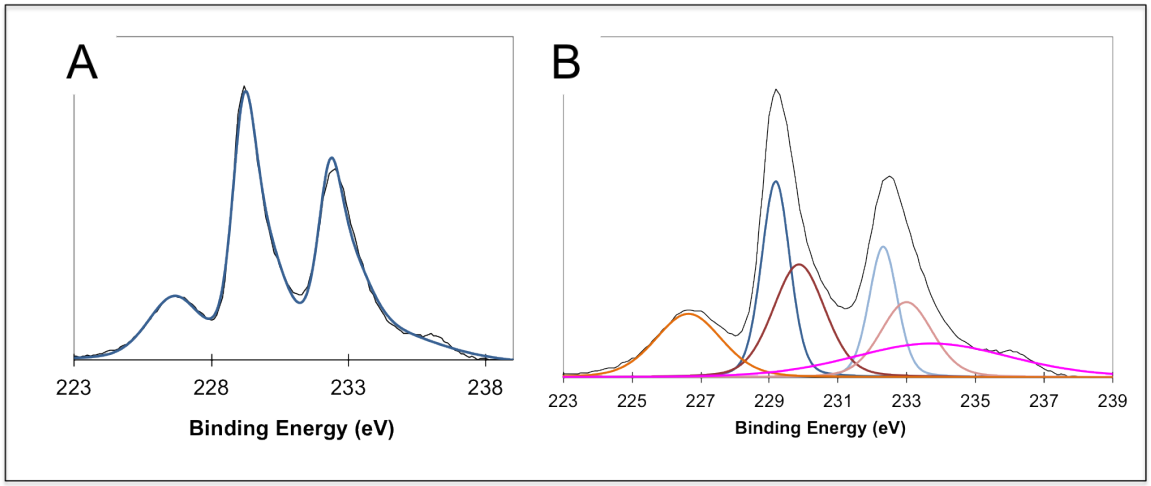

Figure 4.24: (A) Mo 3d data (black) and fit (blue) of $(MoS_2)_{650}$ clusters deposited at 400 eV, (B) fitted to one MoS_2 (blues) and one MoO_3 (reds) doublet, with an additional singlet from the S 2s orbital (pink) [RMS 399.16]

The fit has again improved upon the previous, but the data are still not matched fully, as well as the SO_4 peak being much broader than S peak from the same orbital. The peak FWHM could be decreased by adding a continuum of other SO_x species from the S 2s orbital, but their singlet nature and the obscuring Mo 3d peaks would make interpretation difficult. The existence of significant quantities of SO_x should be mirrored in the S 2p peaks, however these peaks are all associated with MoS_2, so this justifies their omission from the S 2s region.

The fitting used for presentation, of an Mo 3d peak consisting of 3 doublets of Mo^{4+}, Mo^{5+} and Mo^{6+}, and an S 2s singlet, has a better RMS deviation than the previous alternative fits and agrees with the expected species [41]. Although there is a region at 235 eV that still cannot be fitted. Again this would suggest an SO_4 decomposition product, and including this does indeed produce a better fit (Fig 4.25A). The S 2p region does also have a small peak at energies consistent with SO_4 [122] (Fig 4.25D), however this is 35× smaller than it should be for the amount of SO_4 implied by the SO_4 peak in the S 2s orbital. This suggests that the height of the SO_4 in the S 2s region is exaggerated by errors in background subtraction caused by the overlaying complex Mo 3d region.

The S 2p peaks were simpler to fit as these still have the doublet constraints but are

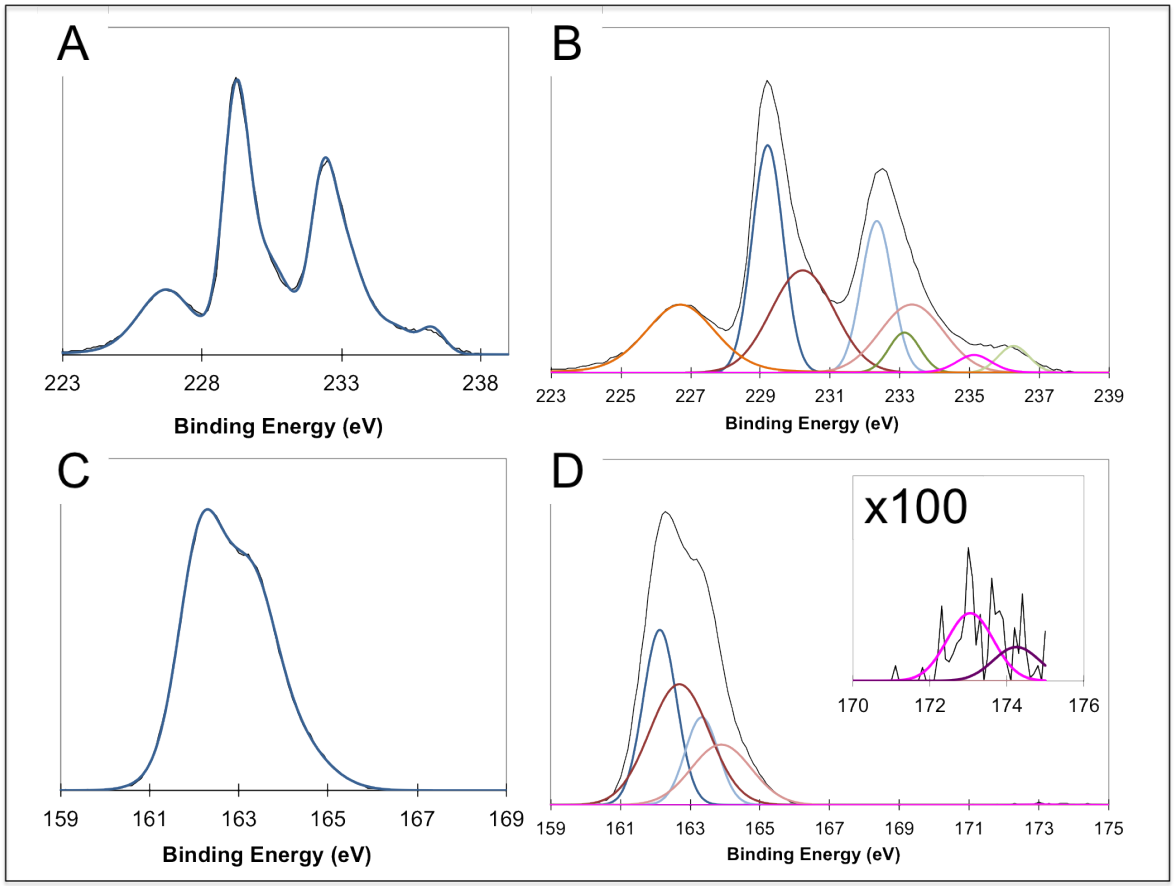

Figure 4.25: (A) Mo 3d data (black) and fit (blue) of $(MoS_2)_{650}$ clusters deposited at 400 eV, (B) fitted to MoS_2 (blues), MoS_xO_y (reds) and MoO_3 (greens) doublets, with an additional SO_4 singlet from the S 2s orbital (pink) [RMS 244.40]. A) S 2p data (black) and fit (blue) of $(MoS_2)_{650}$ clusters Deposited at 400 eV, (B) fitted to S^{2-} (blues), S_2^{2-} (reds) and SO_4 doublets (pink) [RMS 34.24]

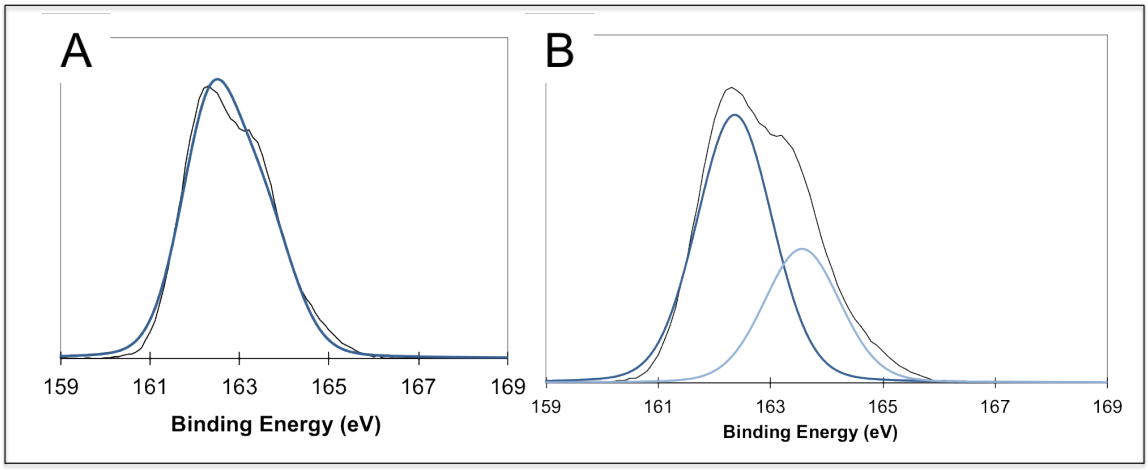

Figure 4.26: (A) S 2p data (black) and fit (blue) of $(MoS_2)_{650}$ clusters deposited at 400 eV, (B) fitted to one S^{2-} doublet (blues) [RMS 228.06]

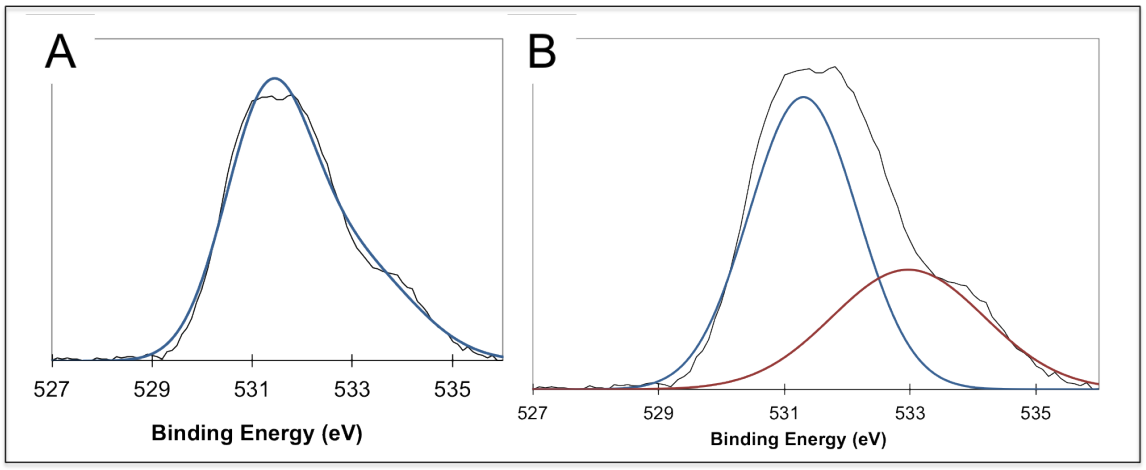

Figure 4.27: (A) O 1s data (black) and fit (blue) of $(MoS_2)_{650}$ clusters deposited at 400 eV, (B) fitted to MoO_3 (blue) and H_2O (red) singlets [RMS 205.80]

convoluted with less neighbours. The fitting used for presentation was of two doublets, consistent with sulfur atoms in the bulk environment and at the edges. The RMS deviation is superior to that of one doublet (Fig 4.26).

The O 1s peaks are singlets, and so have few constraints except having a similar FWHM and choosing appropriate energies for assumed oxygen species. The fitting used for presentation was of three singlets, one for MoO_3 and two for adventitious species such as hydroxyls and water. This fits the data well and has a superior RMS deviation to fitting with one or two peaks (Fig 4.27).

In conclusion, the fits of XPS data in this chapter represent an accurate model of

the chemical species that exist, both in terms of goodness of fit and with agreement to established literature. The existence of some SO_x is likely as the presence of MoO_3 confirms there is atmospheric decomposition, however due to the limited constraints for these singlets their addition would interfere with interpretation of the surrounding peaks. The omission or inclusion of SO_4 changes the total elemental ratio and Mo species ratio by less than 2%, so the conclusions derived from XPS are not affected.

4.4.5 XPS of MoS_2 in long-term Ar storage

The effect of atmospheric degradation and long-term stability of nanoparticles is an important issue for catalysts, especially for these clusters, shown to be rich in defect sites due to non-equilibrium growth. Sub-monolayer MoS_2/HOPG samples were analysed by XPS 61 days after deposition, with an initial exposure to atmosphere after preparation and subsequent storage in Argon. Two samples each of $(MoS_2)_{300}$ and $(MoS_2)_{500}$ were deposited at a sub-monolayer coverage on Argon sputtered HOPG (Fig 4.28). One of each size was annealed in vacuum between 523-573°K for 2 hours prior to XPS. The initial assumption was that the clusters would be stable following the minimal atmospheric exposure and Argon storage. The annealed samples were intended to display increased crystallinity, which would be evident in XPS binding. The sub-monolayer coverage on a sputtered surface was necessary to prevent coalescence of the clusters during annealing, however the signal to background is correspondingly lower in these measurements compared to the multilayer samples.

A coverage of 8,100 pAs, a tenth of the Argon sputter dose, was deposited on freshly cleaved and sputtered HOPG. The coverage over the 4 mm HOPG area was equivalent to 5% of a monolayer. The samples were taken to LENNF for XPS measurements performed by Dr Alex Walton. The Mo 3d and S 2p peaks were chosen for high resolution analysis to decompose the chemical composition involving these elements (Fig 4.29), as oxidation was not expected to be a prominent feature the O 1s peak was not measured in detail. The other peaks in the XPS survey were identified to rule out contamination as far as possible,

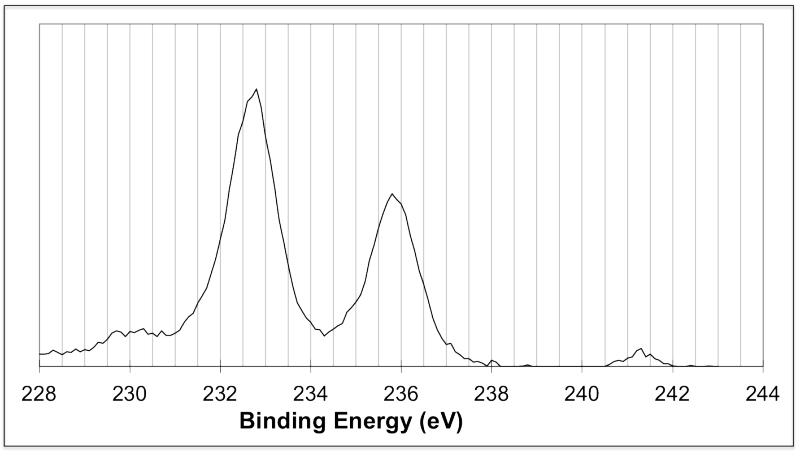

Figure 4.28: The Mo 3d region of all samples contains a small peak at 241.4 eV representing Ar implanted into the graphite surface. The coverage of 81,000 pAs (26,000 Ar^+ per μm^2) and an Ar atomic radius of 0.88Å indicates a sensitivity of at least 0.06% of a monolayer.

however there is an unidentified peak around 107 eV, possibly Si contamination from other samples in storage. All data were calibrated for a carbon 1s peak at 284.5 eV (Fig 4.30).

The unannealed samples of $(MoS_2)_{500}$ and $(MoS_2)_{300}$ both show small percentages of sulfided Mo, with the majority being in the oxidised state (Figs 4.31 and 4.32). The peak fitting has been performed with the same parameters as the fresh multilayer samples, however the two doublets in the S 2p fit now represent S_2^{2-} and SO_x (Labelled in figures as SO_3^{2-}). The molybdenum peaks have shifted to a higher oxidation state, showing a higher percentage in the Mo^{6+} state, consistent with MoO_3. The lower peak consists of Mo^{5+} oxysulfides, with a very small amount of remaining Mo^{4+}. The larger cluster has a significantly higher proportion of remaining sulfide (Fig 4.31D). This is the opposite of the case with the fresh multilayer samples in which the larger clusters were more oxidised due to increased surface defects. In this case, when the clusters are being oxidised beyond the surface layer into the interior, the largest structures will survive the longest. The percentage of Mo compared to sulfur is far above the stoichiometric ratio, with an average of 73.4±3.3% Mo and 24.3±4.3% S across all samples. This is not a flaw in the nucleation process as the fresh samples had a closer to stoichiometric composition of 37.6±1.2% Mo and 62.4±1.2% S. The change must therefore be attributed to substitution of sulfur with oxygen in the Mo structure and generation of volatile sulfur oxide species that desorb.

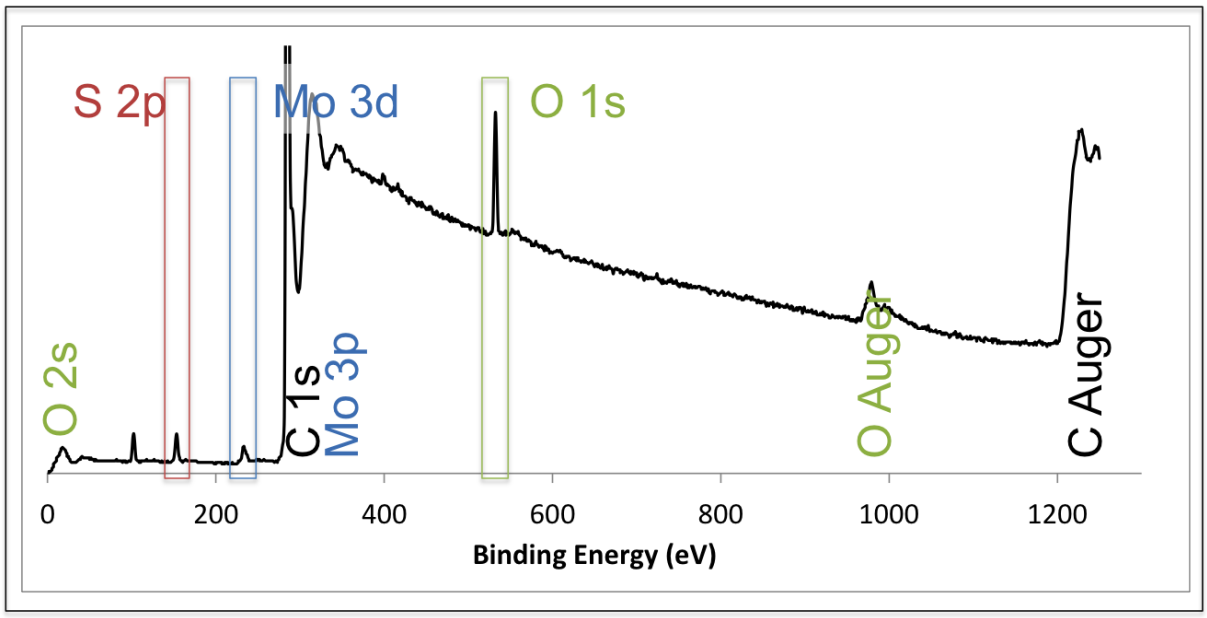

Figure 4.29: Typical survey scan of MoS_2 multilayer ($(MoS_2)_{500}$ at 500eV) after 2 months stored in Argon, with main peaks highlighted. The remaining peaks have been identified to rule out contamination, however there remains an unidentified peak at 107 eV, potentially due to Si contamination from sample storage.

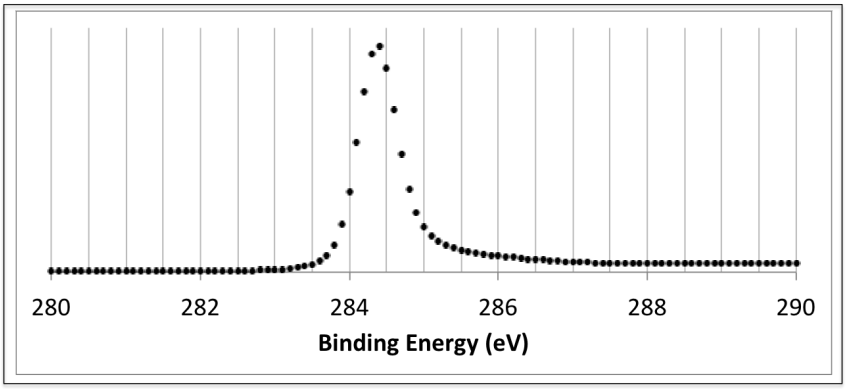

Figure 4.30: Carbon 1s peak at 284.5 eV is used to calibrate the XPS spectrum

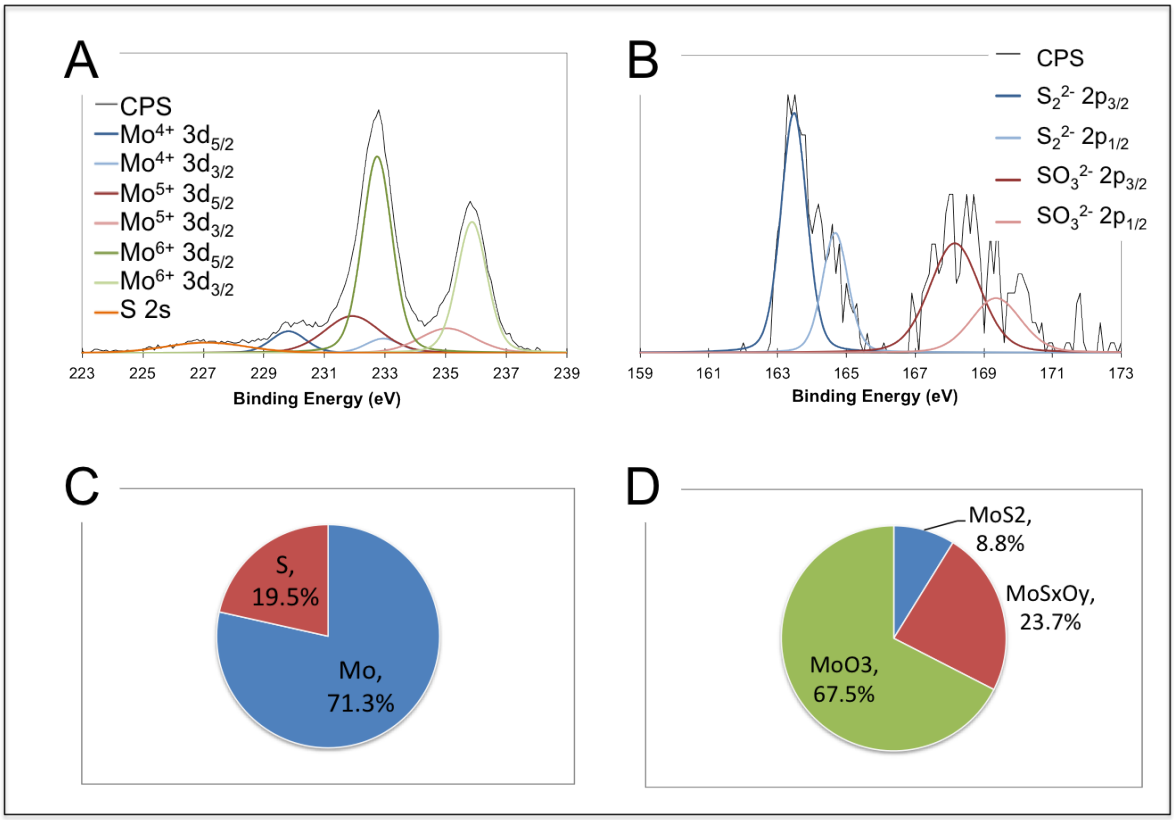

Figure 4.31: $(MoS_2)_{500}$ multilayer deposited at 500 eV on HOPG exposed to atmosphere and stored in Argon for 2 months. (A) The Mo 3d peak can be deconvolved into 3 doublets associated with MoS_2, Mo oxysulfides and MoO_3. (B) S 2p peak with sulfide and sulfate contributions. (C) Normalised Elemental % of Mo and S. (D) Area ratio of deconvoluted Mo 3d peaks.

This is in agreement with data from the S 2p peak deconvolution (Figs 4.31B and 4.32B), which is very different to the fresh samples. There is no peak at 162 eV, associated with the bridging sulfides in MoS_2, instead the majority of the signal has shifted to 168 eV, associated with SO_3 or SO_4.

The Mo^{4+} component of the Mo 3d signal from the annealed samples of $(MoS_2)_{500}$ and $(MoS_2)_{300}$ (Figs 4.33 and 4.34) decreases by over 30% compared to unannealed samples. So the annealing process, rather than improving the crystallinity, speeds up the decomposition of remaining sulfide material to MoO_3 and SO_x. However, the average composition of Mo to S after annealing (Figs 4.33C and 4.34C) is 75.1±4.4% Mo and 24.9±4.4% S, which, to within error, is the same as the pre-annealing ratio of 71.6±0.5% Mo and 23.8±6.0% S. Thus the mechanism for reduced sulfur content for both age and annealing may not be due

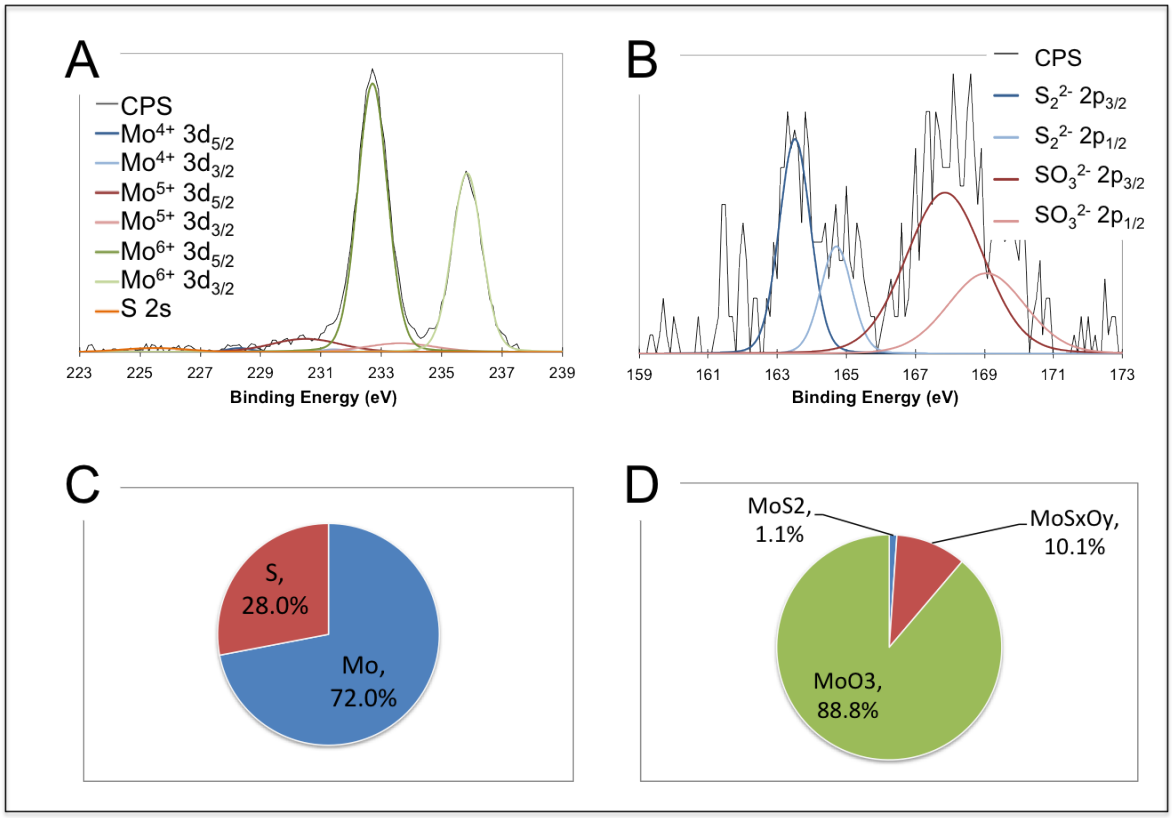

Figure 4.32: $(MoS_2)_{300}$ multilayer deposited at 500 eV on HOPG exposed to atmosphere and stored in Argon for 2 months. (A) The Mo 3d peak can be deconvolved into 3 doublets associated with MoS_2, Mo oxysulfides and MoO_3. (B) S 2p peak with sulfide and sulfate contributions. (C) Normalised Elemental % of Mo and S. (D) Area ratio of deconvoluted Mo 3d peaks.

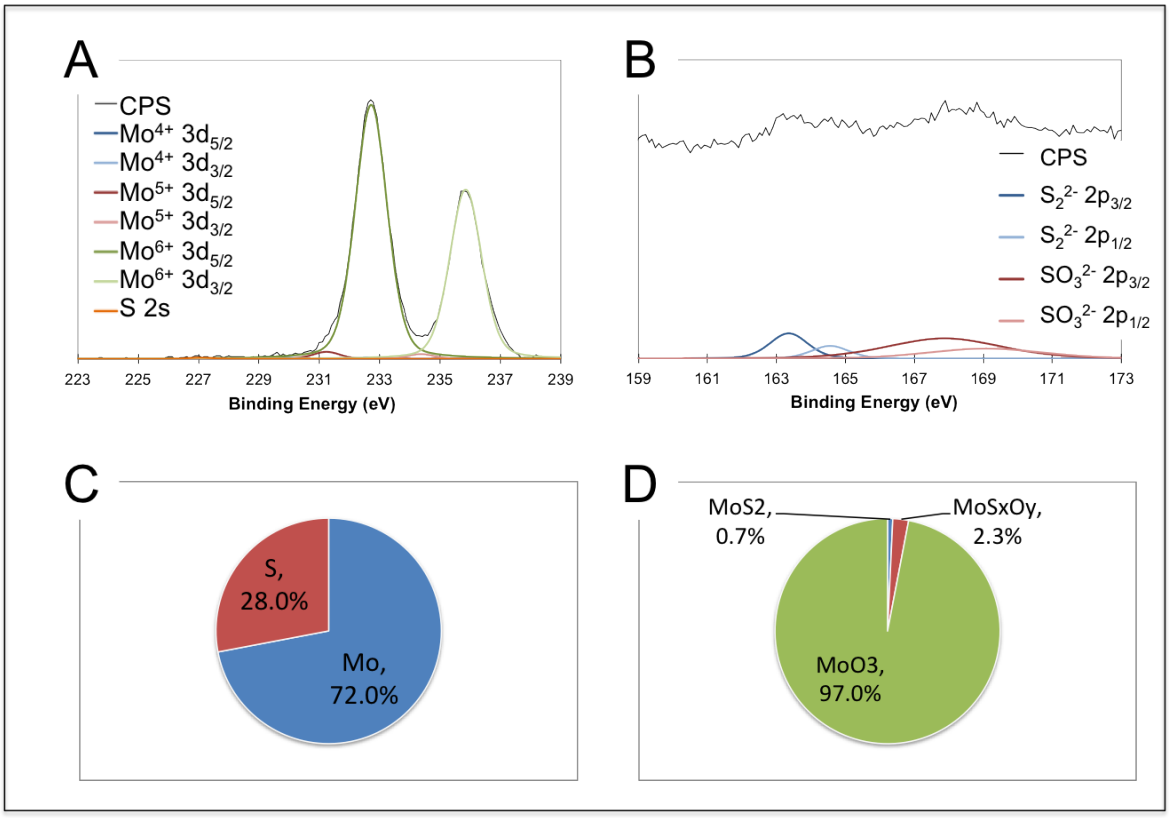

Figure 4.33: $(MoS_2)_{500}$ multilayer deposited at 500 eV on HOPG exposed to atmosphere, stored in Argon for 2 months, then annealed for 2 h at 573°K (A) The Mo 3d peak can be deconvolved into 3 doublets associated with MoS_2, Mo oxysulfides and MoO_3. (B) S 2p peak with sulfide and sulfate contributions. The data was too noisy to apply Shirley background subtraction so a linear background is used instead. (C) Normalised Elemental % of Mo and S. (D) Area ratio of deconvoluted Mo 3d peaks.

to desorption of sulfur oxides but instead diffusion across the substrate. The conclusion of the ageing experiments is that these clusters are unstable in atmosphere. Storage in an Argon desiccator will reduce the rate of decomposition, but does not completely prevent exposure to water vapour for long-term storage. Thus clusters should be immediately stored in Argon after deposition (or remain in the HV deposition chamber) and analysed by microscopy and electrochemistry within a week.

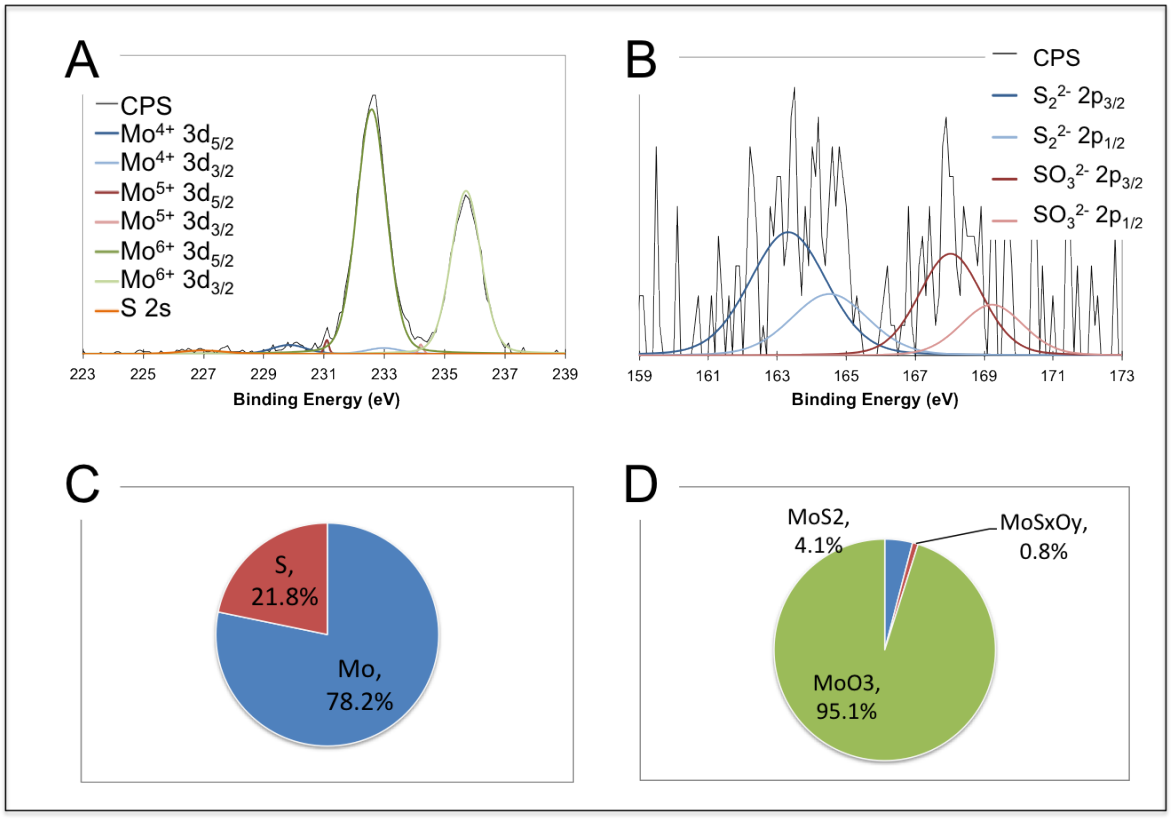

Figure 4.34: $(MoS_2)_{300}$ multilayer deposited at 500 eV on HOPG exposed to atmosphere, stored in Argon for 2 months, then annealed for 2 h at 523°K (A) The Mo 3d peak can be deconvolved into 3 doublets associated with MoS_2, Mo oxysulfides and MoO_3. (B) S 2p peak with sulfide and sulfate contributions. The data was too noisy to apply Shirley background subtraction so a linear background is used instead. (C) Normalised Elemental % of Mo and S. (D) Area ratio of deconvoluted Mo 3d peaks.

4.5 Conclusion

MoS_2 clusters have been fabricated by simple sputtering of a bulk target, paving the way for cheap abundant fabrication from raw molybdenite ore. Compounds of a few atoms up to several nm have been produced by tuning gas-phase nucleation conditions.

Scanning probe analysis shows the clusters deposited from the cluster beam are monodisperse and that they have weak pinning on graphite surfaces. Diffusion on the graphite terraces leads to a greater density of clusters at the step edges, but these stronger binding sites can still be swept by tip interaction. The cluster height of 2-6 layers for scanning probe measurements is larger than the value of 2-3 layers for STEM calculations (Section 5.6.4). This could be due to the abundance of defect sites on amorphous carbon making the flatter morphology more favourable.

The compound nature has been confirmed for cluster ensembles by analysis of the Mo oxidation state by XPS. The preferential sputtering of sulfur from the MoS_2 target leads to reduced sulfur content in the clusters, 37.6±1.2% Mo and 62.4±1.2% S, which subsequently causes oxidation at improperly sulfidised sites, again shown by the higher oxidation states of Mo. The effect of exposure to atmosphere is important to characterise for catalysts as most real-world applications will not take place in vacuum or in inert atmospheres. The abundance of reactive sites on these clusters leads to a reduction in the sulfur content of the clusters, as it is converted to H_2SO_4 by water vapour. This reduces the average composition to 73.4±3.3% Mo and 24.3±4.3% S, caused by diffusion of the SO_x species across the graphite rather than desorption. The evolution of the MoS_2 clusters with decomposition can be tracked by observing the Mo 3d peak shifts (Fig 4.35). The initial exposure to atmosphere causes an instant reaction with active surface sites to produce oxide and oxysulfide, while the core remains as stoichiometric MoS_2. Smaller cluster sizes gain a greater oxide percentage due to the increased proportion of active surface area. Increasing impact energy to 1500 eV does not produce a corresponding increase in low coordination sites. However, it should be noted that 2.3 eV per MoS_2 unit is still a modest impact energy, below the pinning threshold for similarly sized Au

Age (days)	$(MoS_2)_x$	% Mo^{4+}	% Mo^{5+}	% Mo^{6+}
1	350	47	40.4	12.5
1	650	49.3	41.7	9.0
61	300	1.1	10.1	88.8
61	500	8.8	23.7	67.5

Figure 4.35: Summary of Mo 3d peak percentages as a function of size and age.

clusters [185]. The ability to impact at higher energies is limited by the large size of these clusters and the power supplies. The effect of continued exposure, even mitigated by storage in inert atmosphere, is most significant. The majority of the cluster material has been converted to MoO_3 and SO_x. The clusters oxidise inwards from the outer layers, a process that is longer for larger clusters, which retain a higher composition of MoS_2.

This cluster fabrication study forms the basis of all clusters produced for structural analysis and catalytic study, although it is recognised that there is more scope for fine tuning these conditions. For example, a detailed study of all the nucleation parameters on stoichiometry and structure could produce significant differences. It was deemed more profitable to simply find reproducible nucleation conditions for platelet-type clusters and hold these constant. The nucleation study involving variation of the helium gas concentration showed little change to the platelet structure (Section 5.4.5), indicating that these structures are the dominant form for a large area of the parameter space.

There are also further technical additions to the system that could assist with these clusters in future. The nucleation process could benefit from additional reactants, such as H_2S, to produce binary clusters with decoupled sources. The sample deposition stage could also be upgraded with dosing equipment to add material after size-selection and the addition of annealing equipment would allow structures to be equilibrated before exposure to atmosphere.

Finally, improvements in vacuum transfer procedures would allow analysis to take place without atmospheric decomposition. A vacuum suitcase, with ion pumping is available to link directly to the load-lock chamber to provide portable sample transfer. Unfortunately the main analytical tools, XPS, STEM and electrochemical cell, were not compatible. A

simpler solution would be to apply the inert atmosphere procedures at an earlier stage. Venting the load-lock chamber with Argon rather than atmosphere prevents the initial exposure stage, and transfer by Argon filled bags to a glove box reduces the exposure in transit.

CHAPTER 5

ELECTRON MICROSCOPY STUDIES OF SIZE-SELECTED MOLYBDENUM DISULFIDE CLUSTERS

5.1 Introduction

Following on from the work of Chapter 4, in which compound clusters were created, a greater understanding of the atomic scale structure was desired. The scanning probe techniques used to analyse these clusters on HOPG substrates were not able to reveal structural information of individual clusters due to the weak binding between carbon and MoS_2. Therefore high-resolution microscopy, specifically Scanning Transmission Electron Microscopy (Section 3.4), was used as the main analytical technique. Microscopy is used to confirm the previous results of scanning probe studies and the accuracy of the size selection process for this new type of cluster. Finally the structures observed in the microscopy are characterised and size-dependent features are noted. The systematic measurement of low-coordination sites based on cluster size provides a basis for correlating with electrochemical activity in Chapter 6.

5.2 Deposition

A hot-pressed powder target of MoS_2 (PiKem, 99.9% purity) is sputtered and condensed to produce a range of clusters between $(MoS_2)_{50}$ to $(MoS_2)_{1936}$ (Section 3.2). The size-selected beam is then rastered over a holey-carbon TEM grid (Agar Scientific, Holey carbon 400 mesh Cu) with deposition energies ranging from 50 eV to 4000 eV, and a typical dose of 3000 pAs to give a total coverage of 955 clusters/μm^2. The samples are transferred via atmosphere to an Argon filled dessicator for storage. Microscopy is performed with a Jeol JEM2100F spherically aberration-corrected STEM in HAADF mode with spatial resolution of 0.1 nm and EELS energy resolution of 1 eV.

In the case of co-deposition with mass standards Au_{309} is typically used, and is deposited on grids before the MoS_2 clusters. The magic number Au_{309} clusters are generated by DC magnetron sputtering of an Au target (PiKem 99.99% purity), which are subsequently size-selected. The typical coverage is 3000 pAs, corresponding to 955 Au clusters/μm^2. Soft landing of 1 eV per Au atom is used to reduce fragmentation on deposition, while natural defects on the amorphous carbon prevent diffusive aggregation. The Au decorated grids are produced in bulk and stored in Argon until MoS_2 deposition is performed.

5.3 Image Processing Methods

Micrographs of 512 × 512 or 1024 × 1024 resolution, pixel sample time of 25 ms and 32-bit depth were supplied in collaboration with the microscopists Kenton Arkill and Zhiwei Wang. The dark field imaging uses a HAADF camera length of 100 mm. The magnification is a mixture of low-resolution wide-field micrographs and atomic-resolution micrographs. The latter micrographs are subjected to image processing in Fiji [186] to extract statistical data on the cluster structure. Each cluster is manually identified, then automatically measured for area, perimeter, aspect ratio and solidity (Fig 5.1). Intensity data is also extracted in this selected area to perform a calculation of the equivalent mass. Finally an annulus is automatically selected around the initial area to be used as a

background intensity representing scattering from the carbon background. The normalised cluster intensity is then provided by subtracting intensity due to carbon (Eqn 5.1).

$$I_{Norm} = I_{Cluster} - \frac{I_{BG}}{A_{BG}} \times A_{Cluster} \tag{5.1}$$

The normalised intensity can be used to compare mass between clusters of the same dataset, and by calibration to co-deposited mass standards, can be used to determine an absolute mass. The normalised intensity should also be a reliable measure between datasets when the same parameters are used on the microscope. Conversion factors for different pixel exposure times, image size and resolutions can be calculated to compare across experiments. The parameter that must remain the same is the camera length due to the more complex relationship between scattered intensity and the microscope geometry.

5.4 Initial Cluster Production

5.4.1 Wide-Field Imaging

The deposition of clusters must produce a coverage that is high enough to give good statistics for measurements, but not so high that agglomeration is a problem. The low resolution wide-field micrographs of cluster distribution show uniform coverage across the grid (Fig 5.2). Despite an average interparticle spacing around 20 nm there are several nanoparticles in close proximity, this indicates there is some short range diffusion on the amorphous carbon substrate. The dispersion and stability is nevertheless significantly better than was observed by scanning probes on HOPG in Chapter 4. The interparticle spacing can vary across the grid due to the shape of the cluster beam, resulting in a high density central area and lower density at the edges. This is convenient for imaging as an appropriate density can be chosen by moving areas, however for depositing samples for electrochemistry the cluster beam was rastered during deposition to make an even coverage.

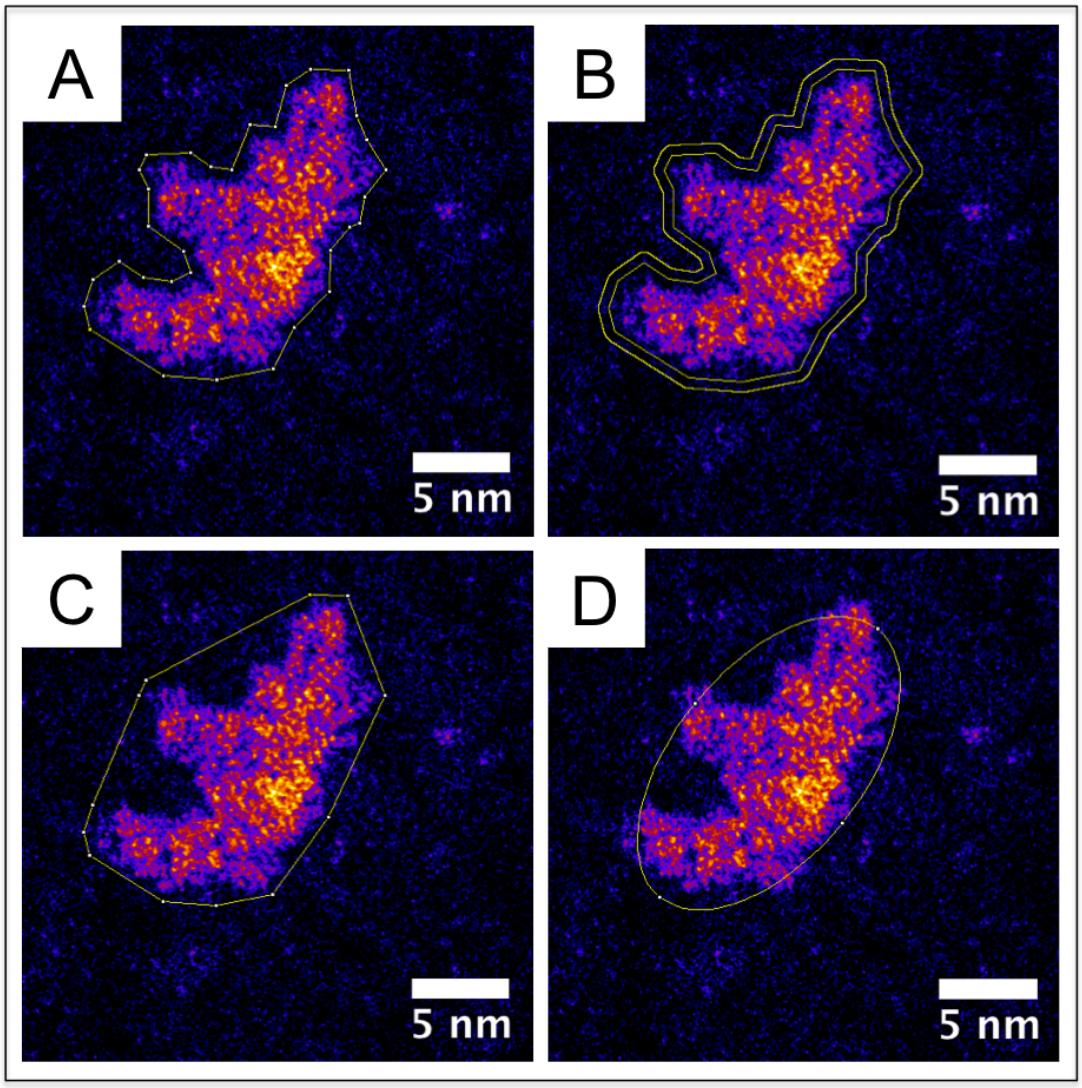

Figure 5.1: (A) An $(MoS_2)_{1000}$ cluster deposited at 100 eV, with an area of 114.6 nm^2 and perimeter of 57.9 nm. (B) The normalised intensity is measured by taking a 0.5 nm band around the original bounded area in B as a background. (C) Solidity is calculated by dividing the original bounded area by its convex hull (shown). The solidity of this cluster is 0.78. (D) Aspect Ratio is measured by fitting an ellipse to the original bounded area. The Aspect Ratio of this cluster is 1.85.

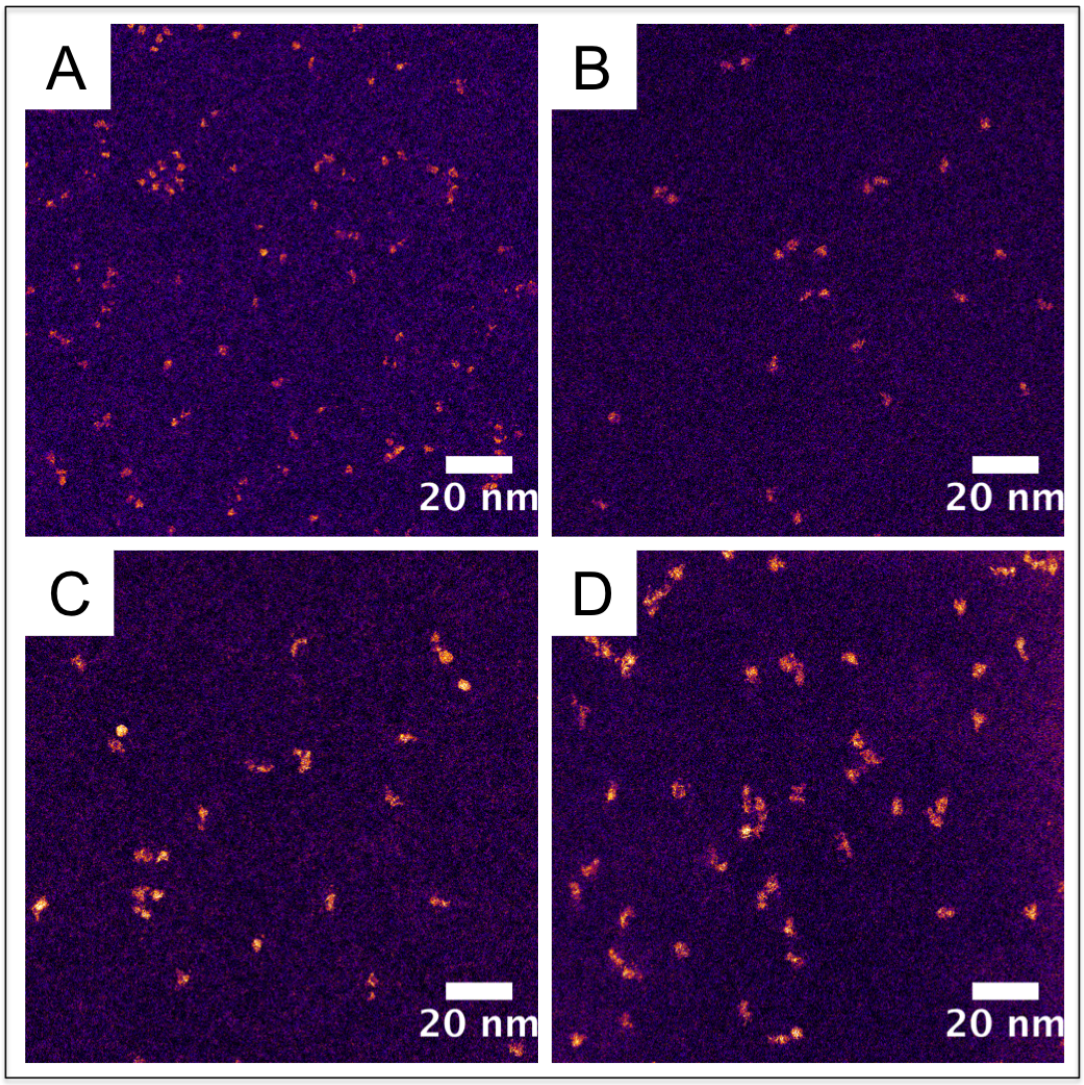

Figure 5.2: Wide-field (153 nm × 153 nm) HAADF-STEM micrographs of (A) $(MoS_2)_{200}$ (B) $(MoS_2)_{350}$ (C) $(MoS_2)_{500}$ (D) $(MoS_2)_{650}$

Nucleation Pressure (mbar)	0.23
Ar Flow (sccm)	65
He Flow (sccm)	45
Nozzle Diameter (mm)	5.6
Condensation Length (mm)	205
DC Magnetron Power (W)	55

Figure 5.3: Typical parameters for MoS_2 clusters produced at low pressure

5.4.2 Amorphous Clusters at Low Pressure

The initial tuning of MoS_2 cluster nucleation parameters relied mainly on analysis of mass spectra to produce the highest flux at the deposition stage, with periodic samples of the beam deposited on TEM grids for direct measurement. Direct analysis of nanostructure is necessary as the cluster source parameters can be set to produce a variety of quasi-stable structures, some of which have morphology more suited for particular applications. The initial tuning procedure (Section 4.2.1) began with few atom clusters of MoS_x at low pressure and increased the pressure until larger clusters formed (Fig 5.3).

Clusters of $(MoS_2)_{500}$ and $(MoS_2)_{1500}$ were produced at this low pressure and deposited on TEM grids for analysis. Contamination on the TEM grid prevented high resolution imaging for $(MoS_2)_{500}$ (Fig 5.4), though the spherical morphology can be seen in place of the expected triangular platelets. The $(MoS_2)_{1500}$ clusters equally have no preference for platelet type structures and display spherical morphology (Fig 5.5). The average Mo-Mo spacing in the clusters is consistent with that of MoS_2 (0.3 nm), however the FFT shows this varies between 0.2-0.3 nm and has no defined crystal structure (Fig 5.6), crystalline MoS_2 for example displays 6 dots at 0.26 nm for the (100) plane. The composition of the clusters can be inferred as uniform from the HAADF intensity as it is uniform across the clusters. This is also shown by Electron Energy Loss Spectra (EELS), which measures the intensity of electrons losing energy to core-loss excitations in Mo and S atoms (Fig 5.7). The relative composition shows the sulfur content is sub-stoichiometric, which may be the reason for the lack of MoS_2 crystallinity. The spherical nanostructures were not expected to give the best performance for catalysis, so these cluster growth parameters were rejected

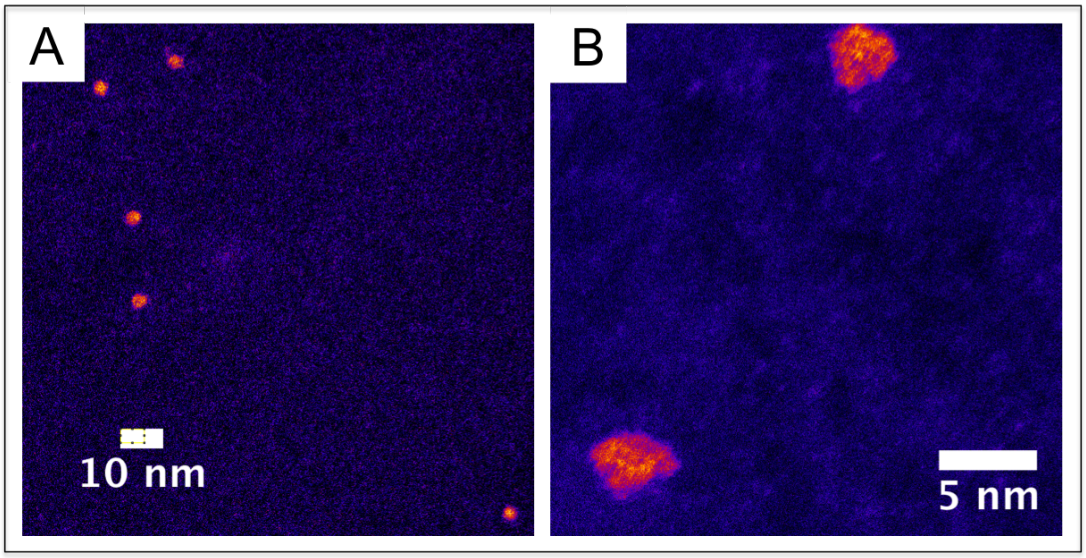

Figure 5.4: (A) Wide field STEM micrograph of $(MoS_2)_{500}$ clusters produced at low nucleation pressure. (B) High resolution STEM micrograph affected by contamination on this sample, however the clusters have a spherical morphology with an average area of 11.5 nm^2, giving an average circular diameter of 3.8 nm

from further studies.

5.4.3 Platelet Clusters at High Pressure

The exploration of the cluster source parameter space was continued in order to produce a platelet morphology rather than amorphous agglomerates. The nucleation pressure was increased to the region of 0.6 mbar, using high Argon and Helium flow with a small nozzle size. At this pressure a continuum of clusters is formed from $(MoS_2)_{100}$ to $(MoS_2)_{1000}$ (Section 4.2.1). The peak position can be shifted to provide higher flux of the desired cluster size as described in Section 3.2.4. The nucleation pressure affects the shape of the distribution most strongly, with the nozzle diameter as the parameter used to achieve this (Fig 5.8). Condensation length is usually set to the maximum for most cluster sizes, to allow for their most equilibrium state, however for very small clusters around $(MoS_2)_{200}$ this is reduced to allow less time for growth. The maximum size is limited by the maximum gas flow of 200 sccm and the minimum nozzle diameter, this produces a pressure of 1-2 mbar. At these pressures the plasma is unstable and can extinguish, requiring the magnetron to

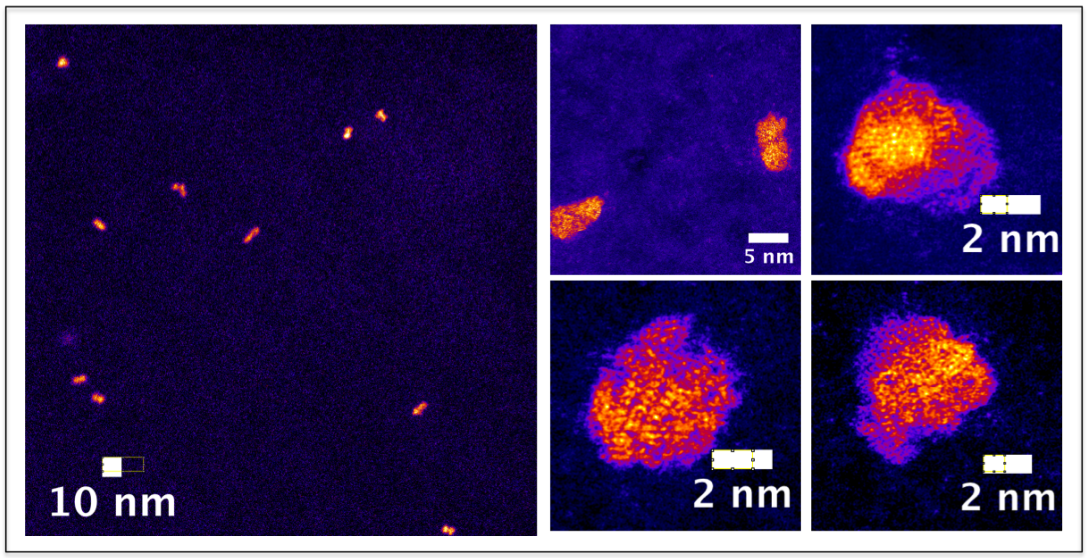

Figure 5.5: STEM micrographs of $(MoS_2)_{1500}$ clusters produced at low nucleation pressure with an average area of 21.6 nm^2, giving an average circular diameter of 5.24 nm

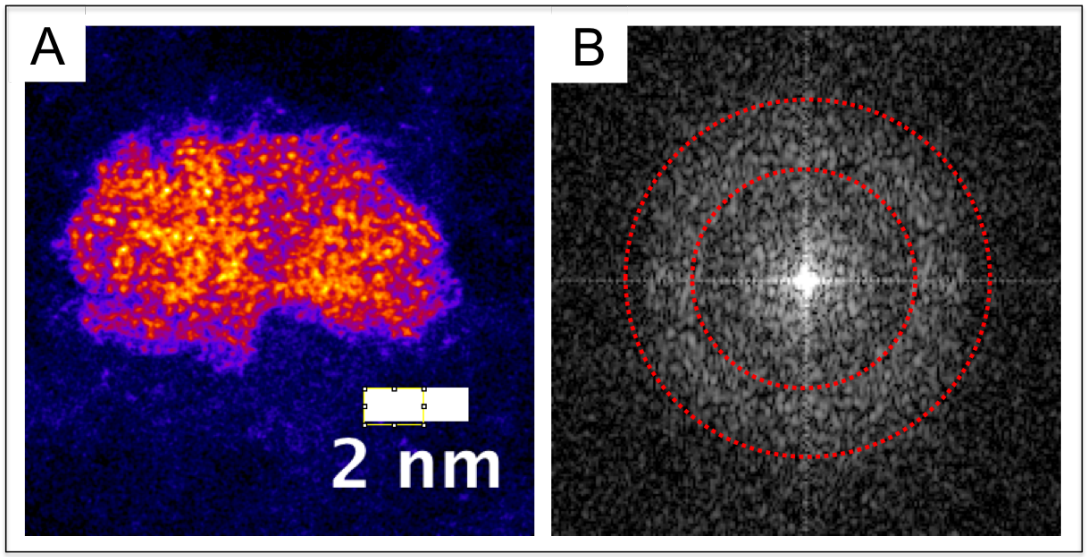

Figure 5.6: (A) STEM micrograph of$(MoS_2)_{1500}$ cluster and (B) corresponding FFT with a diffuse ring (inside ring 0.2 nm^{-1}, outside ring 0.3 nm^{-1}) but no defined crystal peaks.

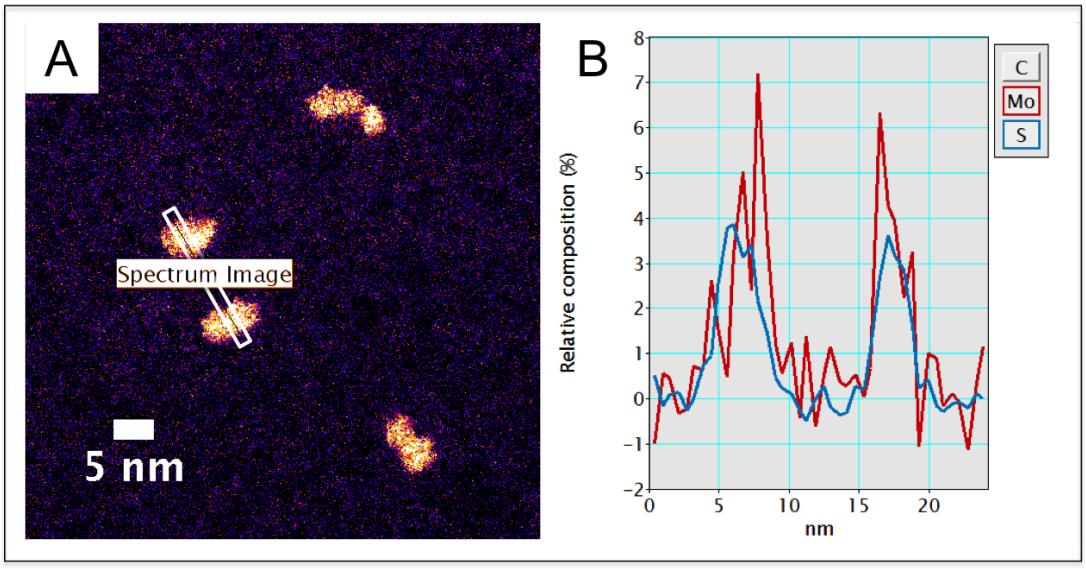

Figure 5.7: (A) STEM micrograph of $(MoS_2)_{1500}$ clusters produced at low nucleation pressure of 0.2 mbar are shown (B) by a STEM-EELS line profile to contain Mo and S.

	$(MoS_2)_{312}$	$(MoS_2)_{1250}$
Mass (amu)	50000	200000
Nucleation Pressure (mbar)	0.47	0.64
Ar Flow (sccm)	185	185
He Flow (sccm)	200	200
Nozzle Diameter (mm)	3.22	2.37
Condensation Length (mm)	250	250
DC Magnetron Power (W)	30	30

Figure 5.8: Table of typical cluster beam nucleation parameters for platelet clusters

be restarted.

It is worth noting that these parameters (Nozzle diameter and gas flow) are often used in combination to effect a pressure change and subsequent size change, but recent work has highlighted the dangers of this method. Each parameter can have a subtle influence on the structure of the clusters, often in the form of reduction of structural free energy. Work on the structure of gold clusters shows they are often in non-equilibrium states, which can be converted to the ground state by the energy of an electron beam [187]. The follow-up work is forming a picture of a highly dynamic system, in which each parameter of the nucleation process can lead to different proportions of clusters in each state (Icosahedral, Decahedral, FCC). So it is a strong possibility that within the size range of MoS_2 created

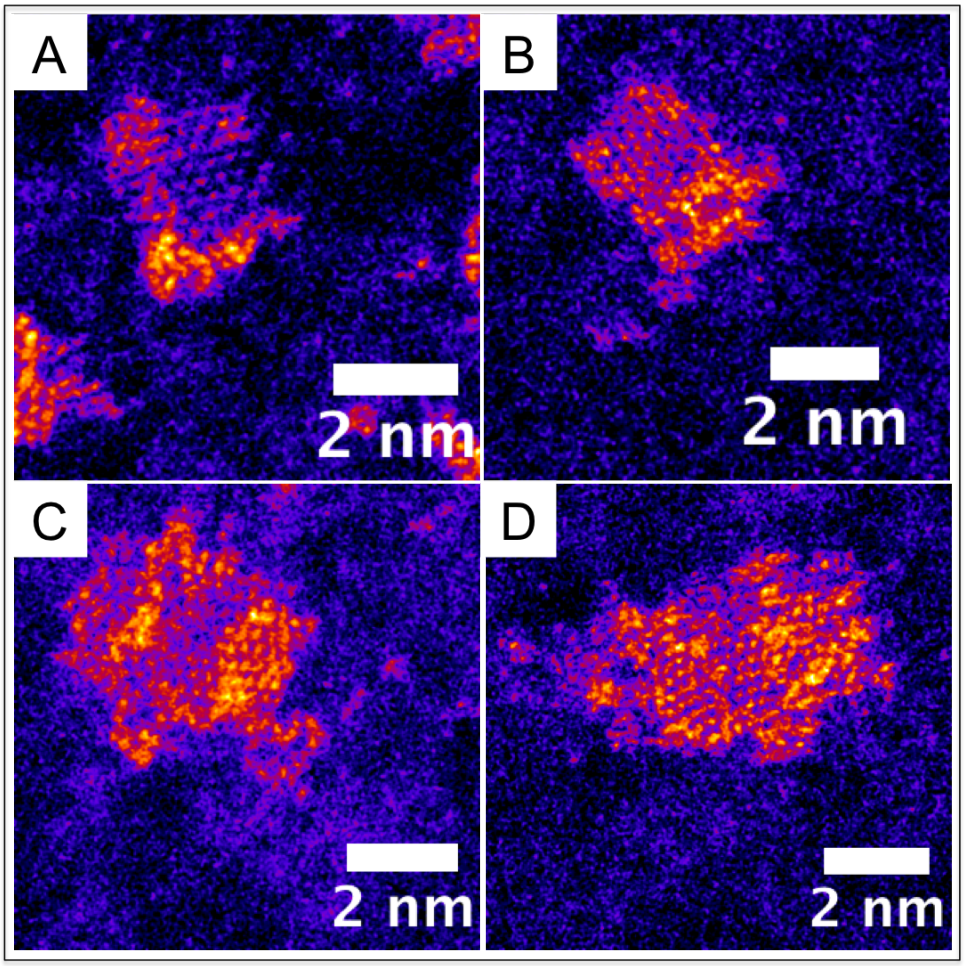

Figure 5.9: MoS_2 clusters, (A) $(MoS_2)_{200}$ (B) $(MoS_2)_{350}$ (C) $(MoS_2)_{500}$ (D) $(MoS_2)_{650}$, made at high nucleation pressure (Fig 5.8) show lamellar platelet morphology and hexagonal atomic structure

there is a subset of undefined variability in terms of free energy.

A range of sizes, $(MoS_2)_x$ (x = 200, 350, 500, 650), were deposited from this high pressure continuum and imaged by STEM. These clusters show structures consistent with MoS_2 platelets (Fig 5.9), with more edge area and low-coordination sites than platelets sulfidised on supports [69] due to the non-equilibrium conditions of gas-phase nucleation and the lack of growth template. The nucleation parameters used to produce these clusters have been used as the basis for all future work due to the prevalence of edge sites needed for catalysis.

5.4.4 STEM EELS of Single Clusters

The hexagonal crystal structure (Section 5.6.1) and uniform HAADF intensity across the cluster indicates that this high pressure nucleation has created compound clusters. In order to confirm this hypothesis, EELS was performed on individual clusters using the 200 keV electron beam in STEM. The configuration of the microscope was such that EELS spectra can be acquired from the bright-field while simultaneously imaging in the dark-field. The molybdenum and sulfur core-loss EELS signals of $(MoS_2)_{650}$ clusters were measured for single points and spectral maps. The clusters were deposited and imaged after 6 days, then imaged again after 57 and 90 days to check for effects of degradation.

The freshly prepared clusters show clear core-loss signals from S 2p (L_{23}) at 164 eV, Mo 3d (M_{45}) at 228 eV and C 1s (K_1) at 285 eV. There is strong variation in elemental ratio between the clusters suspended over the edge of a hole (Fig 5.10) and on a thicker carbon background (Fig 5.11). The carbon may directly affect the measurement by introducing plural scattering to broaden energy loss peaks [188], or the lower signal may simply introduce more error in determining the background subtraction. The spectral imaging on both clusters shows the Mo and S atoms are distributed evenly as a compound rather than a core-shell.

The average ratio of $MoS_{0.37}$ is far below the XPS value of $MoS_{1.58}$, this decreases to an average of $MoS_{0.32}$ after 57 days stored in Argon (Fig 5.12). A crystalline cluster with a clear hexagonal structure on a thin carbon region (Fig 5.13), has a composition, $MoS_{0.47}$, richer in sulfur than the average, but still lower than the XPS measurements.

The clusters aged for 90 days were measured over a larger energy loss range to include the oxygen O 1s peak at 530 eV (Fig 5.14). This peak has a weak scattering cross-section, so after normalisation any signal is greatly magnified. Therefore the exact quantification of oxygen is prone to error given the low signal to background. The Mo:S ratio has not changed between 57 and 90 days, in agreement with XPS results that show the cluster exterior is heavily oxidised by this point. The interior survives for longer as shown by the higher percentage of MoS_2 remaining in larger clusters (Section 4.4.1).

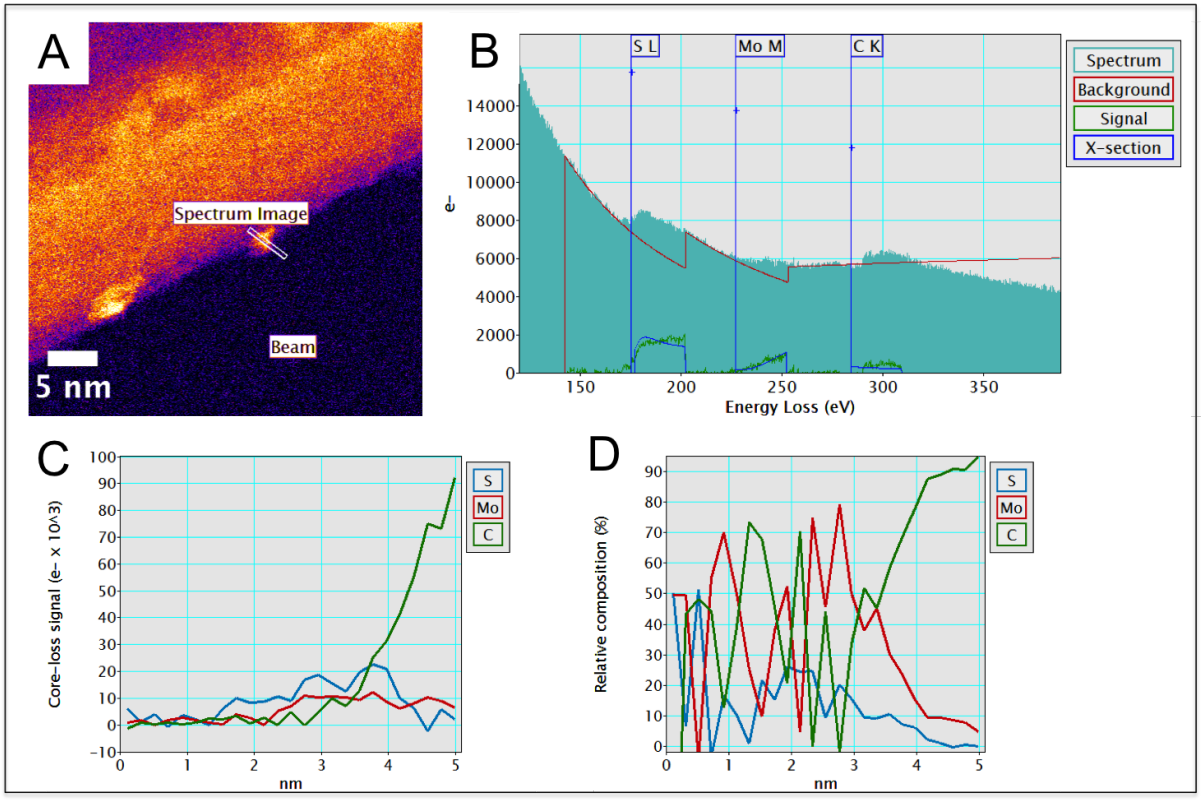

Figure 5.10: $(MoS_2)_{650}$ stored in Ar for 6 days. (A) STEM micrograph with EELS path marked, (B) Integrated EELS signal from 2 nm area over the cluster gives normalised elemental ratio of 22.75% S, 43.13% Mo, and composition of $MoS_{0.52}$ (C) Spectral EELS map (D) Normalised spectral EELS map

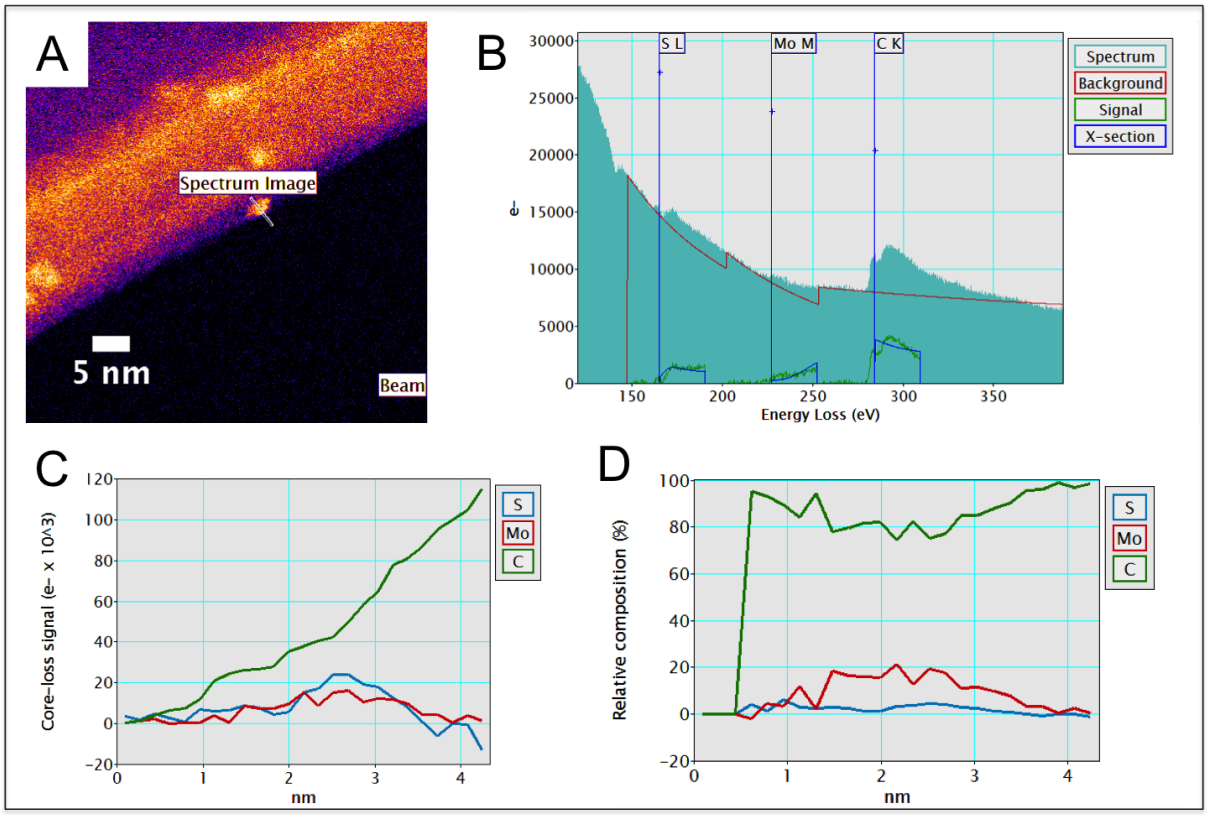

Figure 5.11: $(MoS_2)_{650}$ stored in Ar for 6 days. (A) STEM micrograph with EELS path marked, (B) Integrated EELS signal from 2 nm area over the cluster gives normalised elemental ratio of 3.46% S, 15.54% Mo, and composition of $MoS_{0.22}$ (C) Spectral EELS map (D) Normalised spectral EELS map

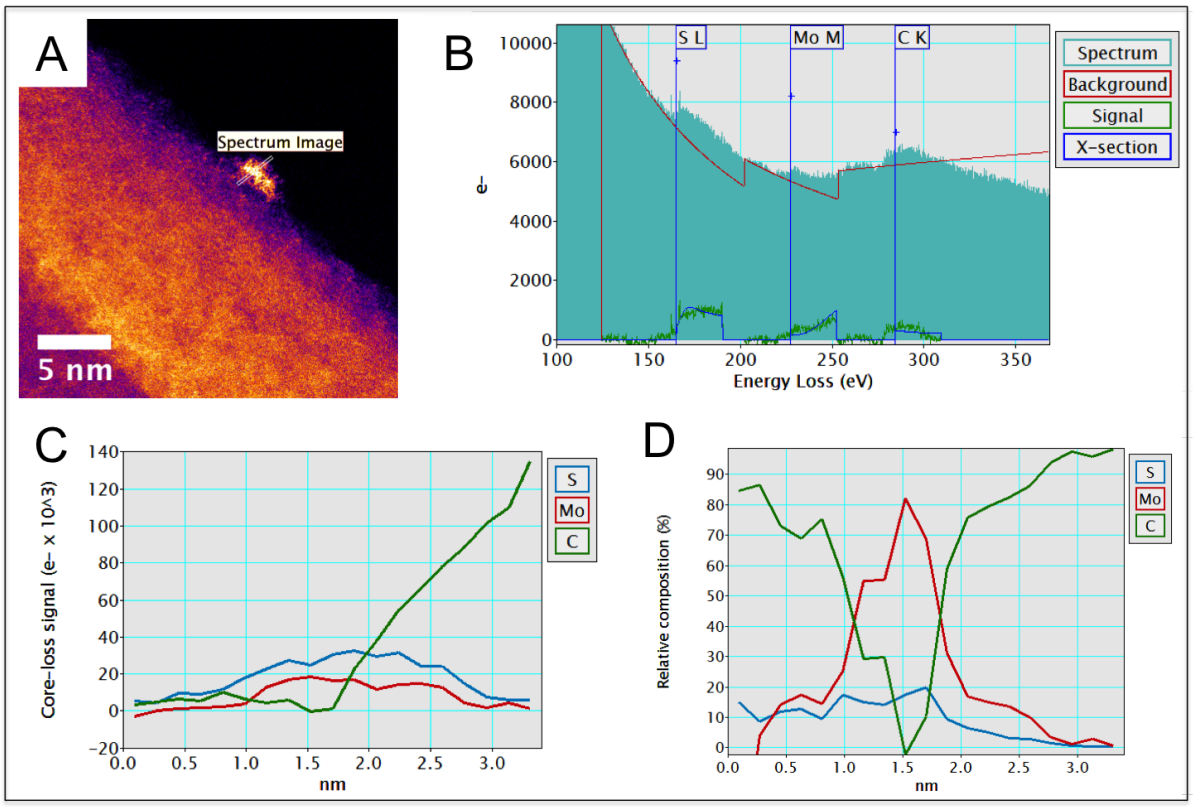

Figure 5.12: $(MoS_2)_{650}$ stored in Ar for 57 days. (A) STEM micrograph with EELS path marked, (B) Integrated EELS signal from 1 nm area over the cluster gives normalised elemental ratio of 14.74% S, 46.6% Mo, and composition of $MoS_{0.32}$ (C) Spectral EELS map (D) Normalised spectral EELS map

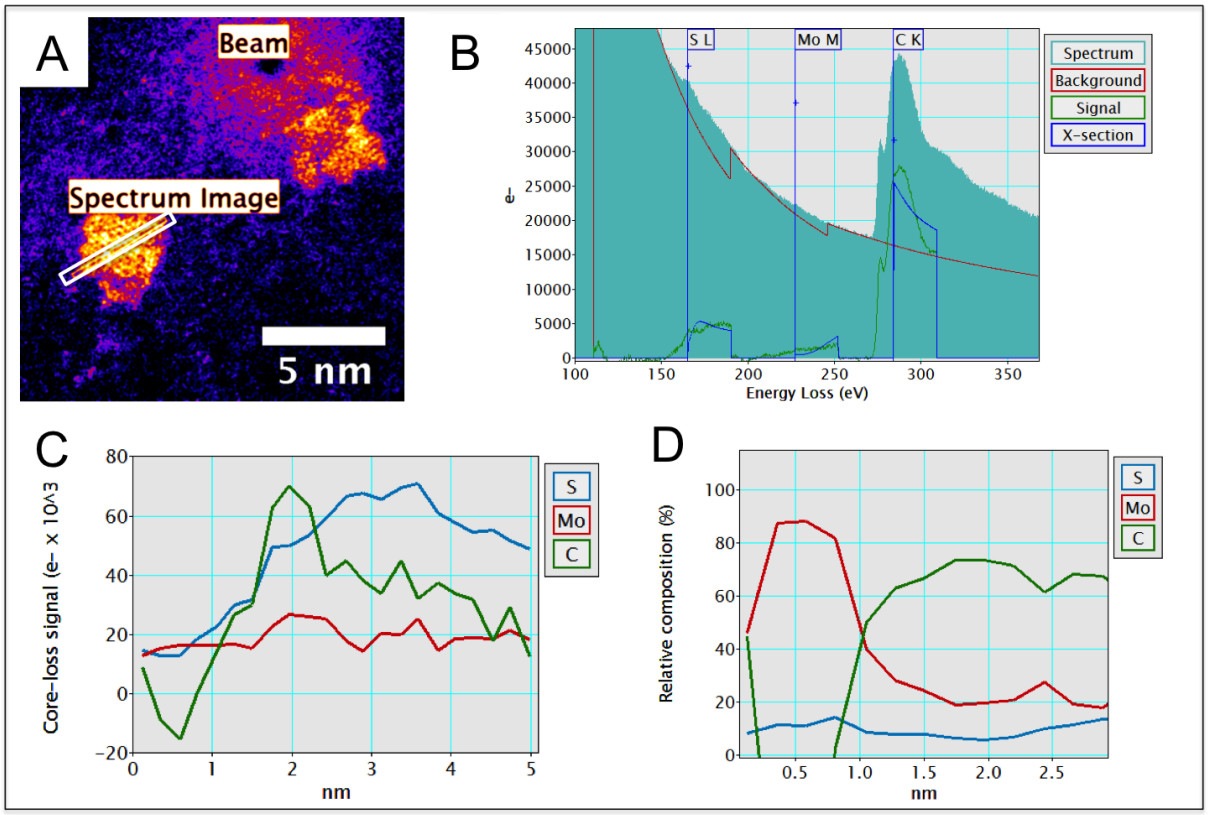

Figure 5.13: $(MoS_2)_{650}$ stored in Ar for 57 days. (A) STEM micrograph with EELS path marked, (B) Integrated EELS signal from 1 nm area over the cluster gives normalised elemental ratio of 11.04% S 23.61% Mo, and composition of $MoS_{0.47}$ (C) Spectral EELS map (D) Normalised spectral EELS map

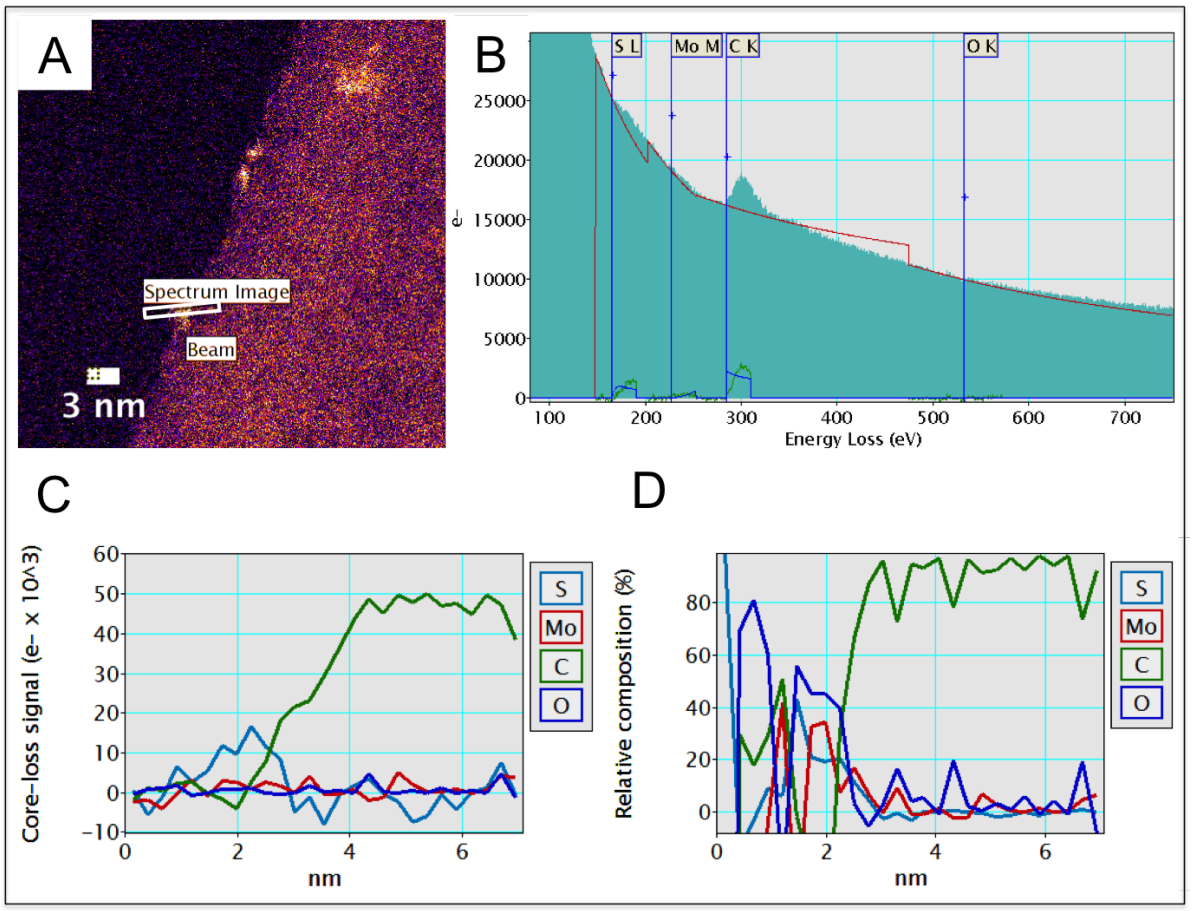

Figure 5.14: $(MoS_2)_{600}$ stored in Ar for 90 days. (A) STEM micrograph with EELS path marked, (B) Integrated EELS signal from 2 nm area over the cluster gives normalised elemental ratio of 4.2% S 8.8% Mo 13.1% O, and composition of $MoS_{0.48}O_{1.49}$ (C) Spectral EELS map (D) Normalised spectral EELS map

The most likely explanation for the variance in composition and reduction in sulfur content, compared to XPS is the high energy of the 200 keV electron probe. The energy of the X-rays used in XPS measurements is around 1.5 keV spread across a micron scale area, the electron energy in WDS is higher, at 20 keV over a similar area. The measured composition across these three techniques follows a trend of increasing sulfur content with decreasing beam energy, STEM-EELS with $MoS_{0.37}$, WDS with $MoS_{0.46}$ and XPS with $MoS_{1.58}$. The energy of the probe can be seen to decrease the size of the clusters, indicating some material is being dissociated (Fig 5.15). The high energy electron beam will preferentially remove sulfur atoms rather than heavy molybdenum atoms [189], leading to a decrease in sulfur content after scanning. The threshold for this beam (knock-on) damage can be calculated using the sublimation energy (E_{sub}) of the constituent elements and their masses. E_{sub} for sulfur is 2.88 eV [190], which can be converted to a beam threshold of 66 keV [189]. This beam damage occurs during normal imaging, however for EELS imaging the effect is exacerbated by the longer dwell time per pixel and smaller scan area. This can be seen in successive EELS spectra of the same cluster (Fig 5.16), as the ratio of sulfur to molybdenum decreases. This is also likely to be the reason why the oxide content indicated by XPS, is not found on most of the samples. Oxygen has a lower E_{sub} of 2.58 eV, giving a beam threshold of only 30 keV. Furthermore, the oxygen is confined to the outside of the cluster, making these atoms more susceptible to dissociation.

5.4.5 Nucleation Study by Helium Flow

In order to assess the impact of nucleation parameters on the MoS_2 cluster structure the amount of He carrier gas was varied to the extremes available to the system. The same size of cluster was produced, $(MoS_2)_{600}$, with the same flow of Argon gas (160 sccm), but Helium flow was set to 0, 90 and 200 sccm for 3 different samples. These samples were then imaged by STEM and their structure was analysed.

The area and perimeter of the structures (Fig 5.17a) is increased slightly with increasing He flow. The aspect ratio and solidity changes indicate the clusters become more elongated

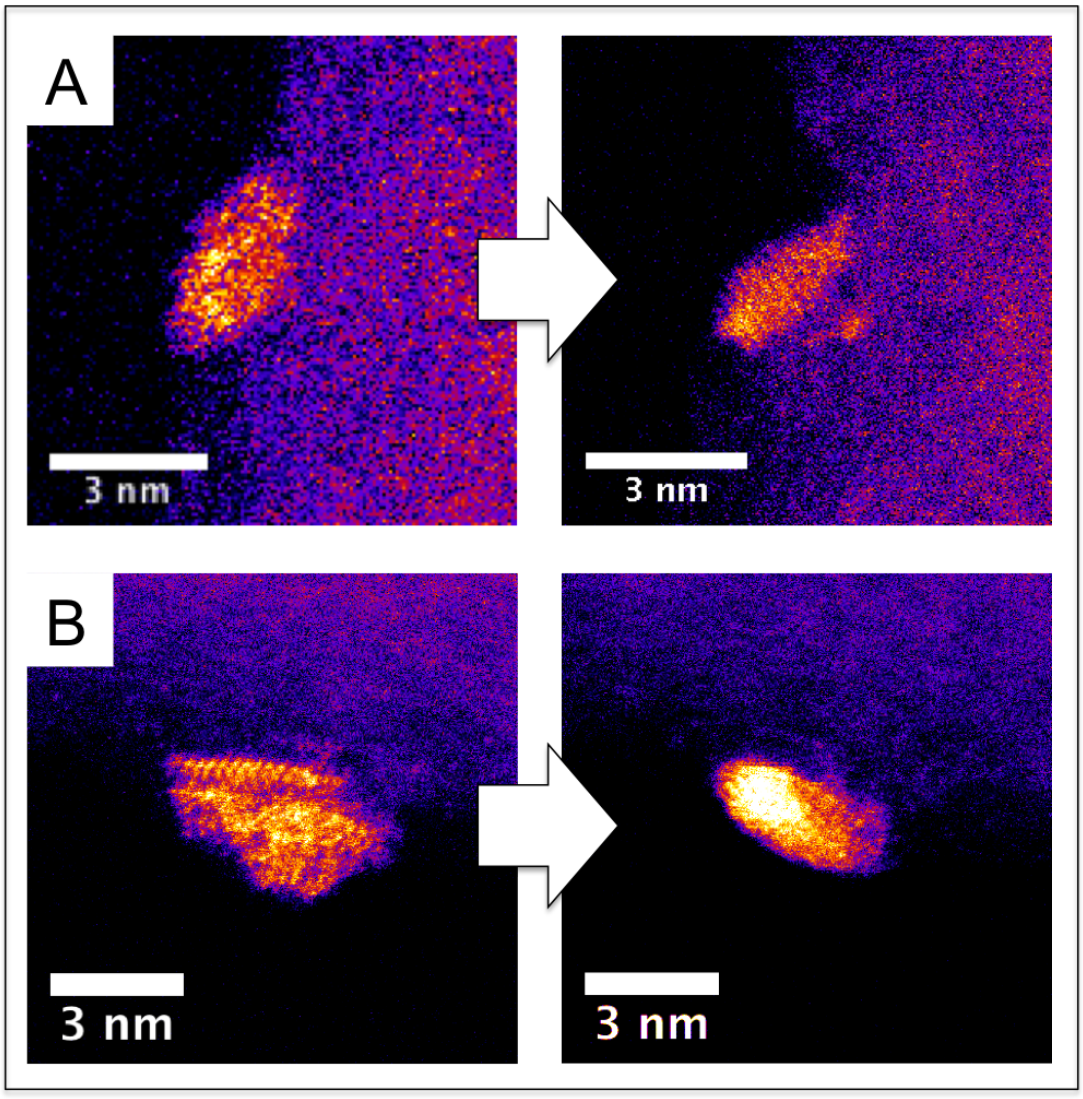

Figure 5.15: $(MoS_2)_{650}$ stored in Ar for 57 days. (A) STEM micrograph before and after EELS measurement, the area and total intensity decreases by 21% and 27% respectively. The normalised elemental ratio was 2.77% S 5.11% Mo with composition of $MoS_{0.54}$. (B) STEM micrograph before and after EELS measurement, the area and total intensity decreases by 33% and 27% respectively. The normalised elemental ratio was 8.52% S 28.43% Mo with composition of $MoS_{0.54}$.

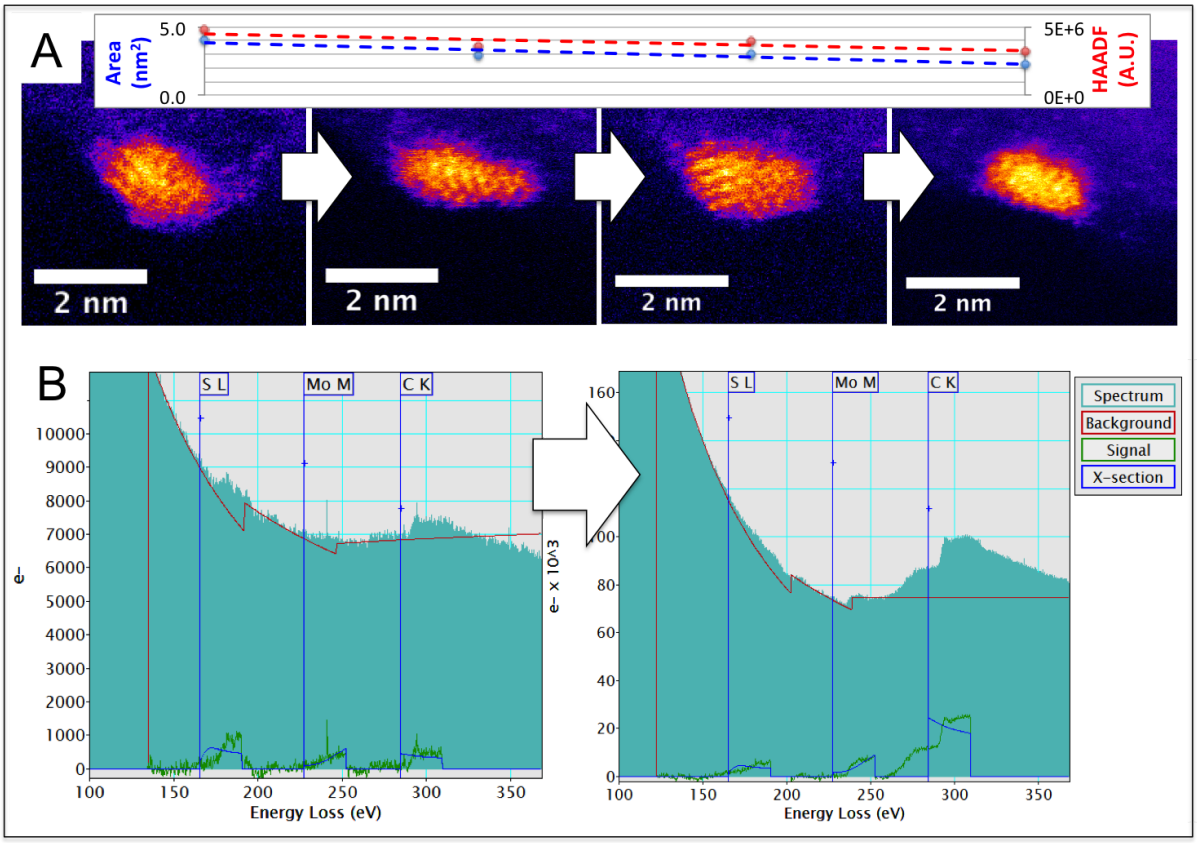

Figure 5.16: $(MoS_2)_{650}$ stored in Ar for 57 days. (A) STEM micrographs: before any measurement, after a first EELS spectra, before the second EELS spectra and after the second EELS spectra. The area and total intensity decreases by 44% and 31% respectively from the first to last micrograph. (B) The first spectra shows 9.60% S 31.73% Mo with composition of $MoS_{0.30}$. The second spectra shows 2.04% S 12.96% Mo with composition of $MoS_{0.16}$.

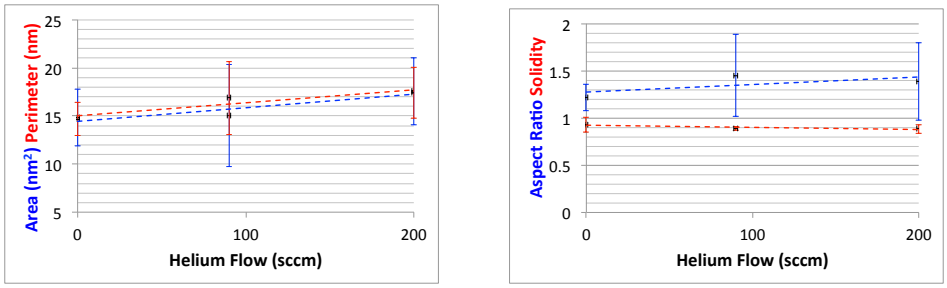

(a) Area and Perimeter vs He flow rate (b) Aspect Ratio and Solidity (Area / Convex Hull Area)

Figure 5.17: Cluster shape as a function of nucleation conditions, specifically the Ar:He gas flow ratio.

and rough (Fig 5.17b). The increased Helium concentration will provide faster cluster nucleation, causing clusters to grow by aggregating with other clusters rather than single atoms. This gas-phase cluster coalescence will produce less spherical clusters with more edge area. This may be an advantage when designing clusters for catalytic applications as a method of increasing active low-coordination sites.

The differences in structure derived from Helium flow are small, and given that the use of high helium flow has been the most effective method of producing large cluster currents, this is used as the basis for MoS_2 cluster production. Furthermore, the analysis of the cluster properties in Chapters 5 and 6 show no large deviations from the observed size-dependant trends. Aside from possible gas-phase cluster coalescence these clusters show no structural differences equivalent to the transitions between decahedral, icosahedral and FCC observed in Au clusters [187]. These observations suggest that the lamellar platelet structure is at a deep minimum in the potential energy surface, and the perturbations in the nucleation chamber do not affect the clusters sufficiently to cause transformations to other allotropes. Simulations of lowest energy cluster structures [191] include nanotubes and closed shells, but these become favourable at much larger sizes than are produced in this study.

5.4.6 Equilibration Study by Thermal Annealing

The absence of defined edge structure and incomplete top layers indicates the clusters have not fully equilibrated. This is not unusual in the cluster beam system due to short residence time in the nucleation chamber and rapid quenching of growth after the supersonic expansion. However, this will make identification of active sites difficult when correlating with chemical activity, as well as obscuring the crystal lattice for structure analysis. A simple post-processing method was devised to anneal clusters on a TEM grid at low temperature to allow them to reach their lowest energy structure, presumed to be a hexagonal platelet. $(MoS_2)_{600}$ was deposited on a holey carbon/Cu grid and imaged as usual, the structures were consistent with those observed in the remainder of this chapter (Fig 5.18A). The grid was then moved to a sample stage in an Edwards evaporator, and annealed in a vacuum of 10E-7 mbar at 523°K for 2 hours and re-imaged (Fig 5.18B). The analysis shows a reduction in cluster diameter after annealing suggesting cluster material has diffused to produce smaller clusters resulting in a higher density of clusters (Fig 5.19). The most interesting result is that rather than becoming more crystalline the clusters have become amorphous and spherical. This unexpected effect, which would reduce catalytic activity, as well as the possibility of copper contamination from the grid (Fig 5.20), led to the abandonment of this processing method. Improvements could be made by using a grid with higher melting point and performing the annealing in-situ in the cluster beam system.

5.5 Weighing by Au_{309} mass standards

The HAADF-STEM weighing technique (Section 3.4.1) was used to confirm the monodispersity and structure of the MoS_2 clusters. Gold mass standards of Au_{309} were co-deposited to provide a reference for the mass balance process. The gold clusters also act as bright markers to show local variations in substrate, thus improving the speed of focusing and reducing beam-induced damage to the MoS_2 clusters. The use of Au mass standards to

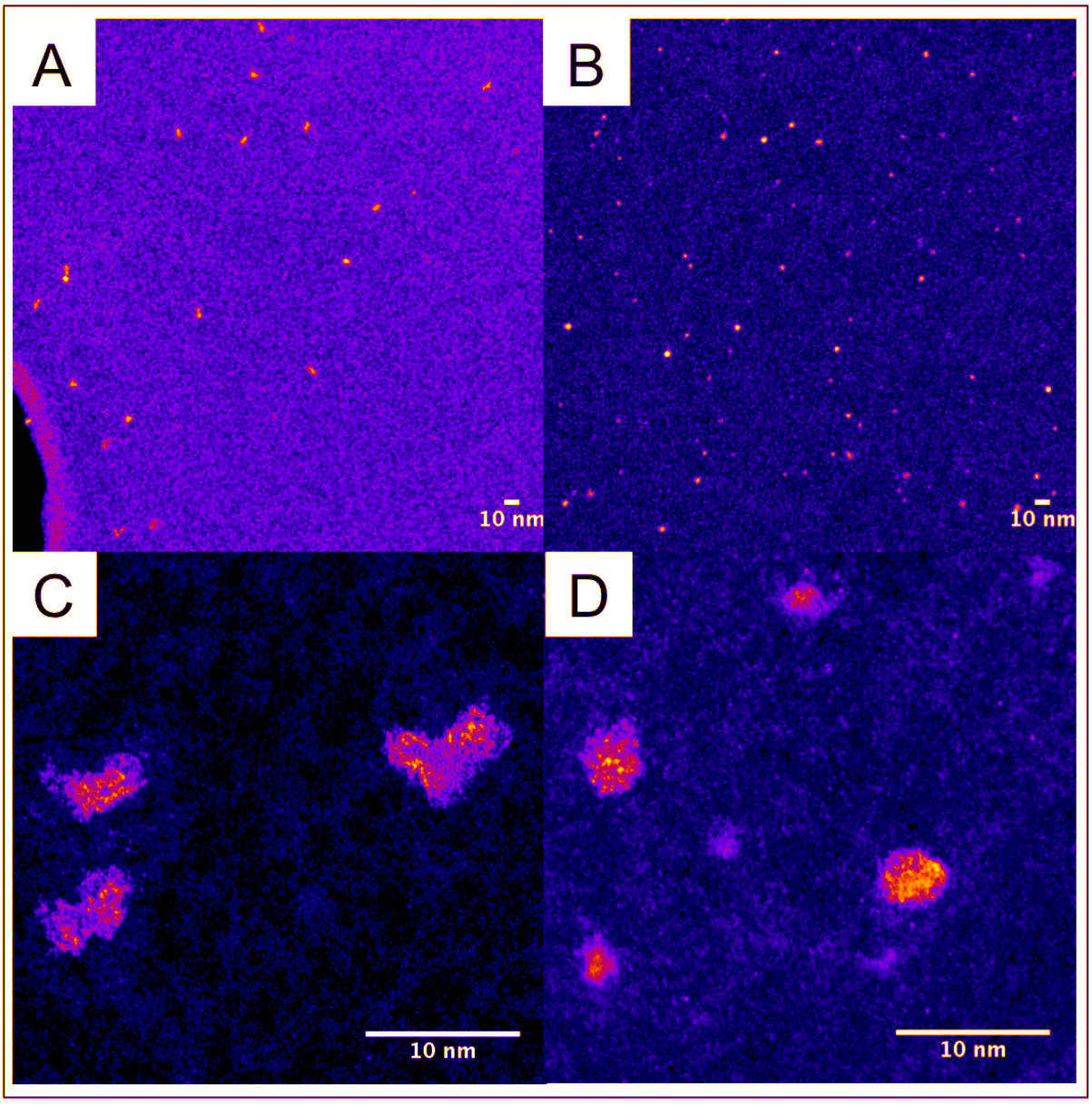

Figure 5.18: STEM micrographs of (A) $(MoS_2)_{600}$ as deposited showing (C) platelet structure. (B) The same samples imaged after 2 h annealing at 523°K with spherical crystal structure (D).

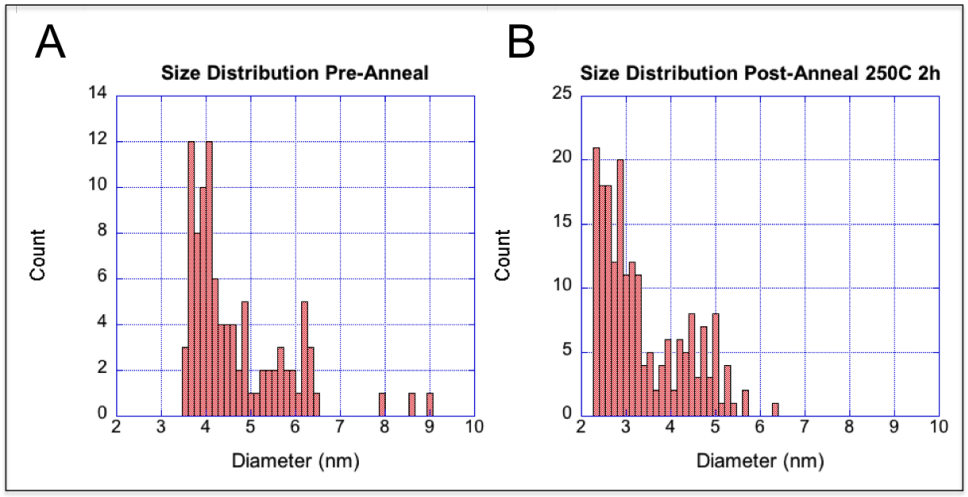

Figure 5.19: (A) Histograms of $(MoS_2)_{600}$ cluster diameter as deposited and (B) after 2 h annealing at 523°K.

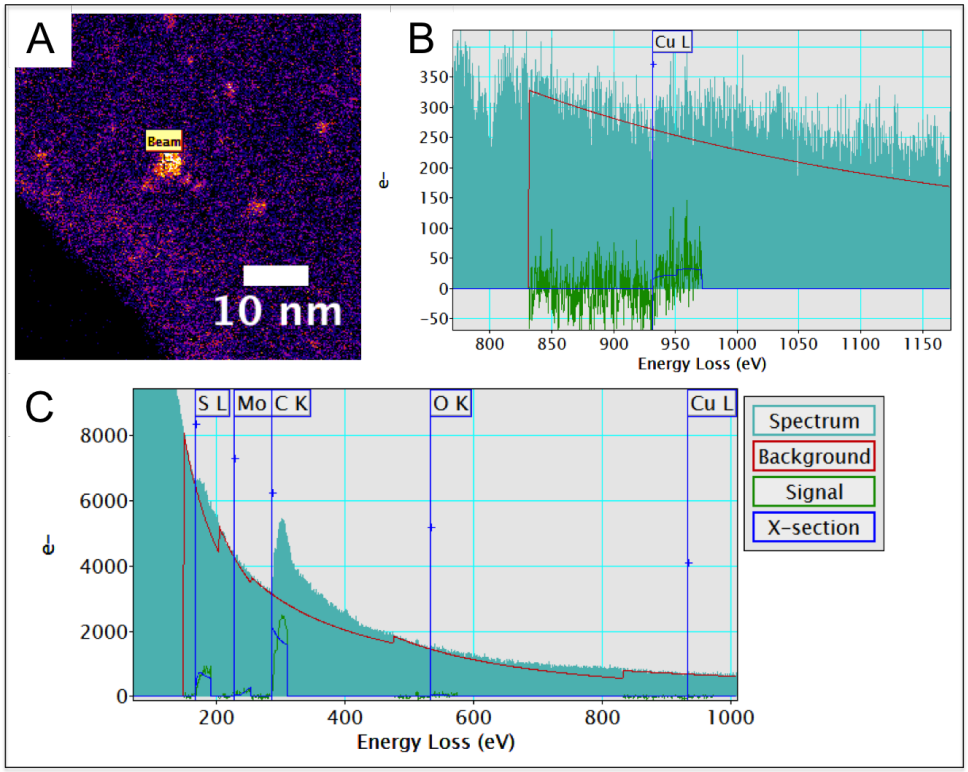

Figure 5.20: (A) Bright cluster after annealing (B) Cu 2p core-loss EELS peak. (C) Full EELS survey with MoS_2 peaks and normalised elemental ratios of 3.42% S, 4.77% Mo, 1.12% Cu, 79.15% C

confirm the mass of clusters is also very important when first using new materials. It is always assumed that the majority of clusters have one unit of charge when leaving the nucleation chamber, however with compound materials that are poor conductors this may not be the case.

The normalised intensity of Au_{309} mass standards and MoS_2 clusters are measured and binned to produce histograms. The normalised intensity is fitted to a Gaussian distribution to eliminate contributions from multiply charged dimers and trimers that pass through the mass filter. The FWHM of the Au histogram peak represents the mass resolution of the size selection process combined with subsequent perturbations such as impact damage and electron beam damage.

The FWHM of the MoS_2 histogram peaks are additionally affected by the stoichiometry of each cluster. The mass filter can be satisfied by any correct combination of molybdenum and sulfur, with sulfur-rich clusters having a lower HAADF intensity than molybdenum-rich clusters for the same total mass. An estimate of this composition variation would be obtained by subtracting the FWHM of the Au peak from the MoS_2, however the Au_{309} clusters are magic numbers so will have a natural tendency to form this structure resulting in a narrower FWHM than the instrument function.

The fitted intensities of both MoS_2 and Au_{309} mass standards are then used in the mass balance equation (Section 3.4.1) with composition constraints provided by XPS (Section 4.4.1) to give the total mass. An oxidised composition is used to best represent the suspected state of the clusters, however the presence of both sulfur and oxygen have only a small effect on calculated mass as the intensity is dominated by the strong molybdenum scattering. The mass plots are additionally shown with two corrections, in order to determine the cluster state after deposition but before exposure to atmosphere. Firstly, the oxidation was corrected by subtracting intensity due to oxygen, this assumes that the clusters are formed sulfur deficient and are subsequently oxidised. Secondly, the oxidation is corrected as above and sulfur intensity is added to bring the composition to stoichiometric MoS_2, this assumes the atmospheric decomposition removes sulfur from

the cluster. The results of these mass balance calculations are shown for sizes $(MoS_2)_{50}$ (Fig 5.21) to $(MoS_2)_{650}$ (Fig 5.22). In all cases the average cluster size closely matches the intended size, proving that the clusters carry one unit of charge similarly to elemental clusters. The measured masses are all below the intended mass, beyond the error bars associated with the mass filter resolution. This indicates that there is damage caused to the clusters by impact and the electron beam, which reduces the size and increases the peak FWHM. The FWHM of the MoS_2 peaks are indeed larger than the Au_{309} FWHM, suggesting composition variation increases FWHM by 2.8-3.4×.

The gold mass standard analysis confirms the initial size-selected mass of the MoS_2 clusters and their charge state during deposition. The measured mass is below the selected mass, indicating mass loss after deposition, caused by a combination of impact damage (Section 5.6.5) and beam damage (Section 5.6.6). The corrections to mass to elucidate in-situ composition were inconclusive due to this damage, as neither correction was able to match the originally selected size. A combination of both assumptions is probable, as sputtering is known to create sub-stoichiometric MoS_2 (Section 2.3.4) and decomposition, by exposure to water, removes sulfur in the form of H_2SO_4 [64]. Certainly, the abundance of reactive low-coordination sites on the clusters, due to non-equilibrium growth in the gas-phase, will assist any atmospheric surface reactions.

5.6 Atomic Structure of MoS_2 Clusters

Atomic resolution STEM was used to characterise the cluster structure in detail, using the methods described in Section 5.3 as well as bandpass filtering to remove high frequency noise. Size and shape of each cluster is measured and averaged, to provide an understanding of growth processes as well as parameters to correlate with composition (Chapter 4) and catalytic activity (Chapter 6).

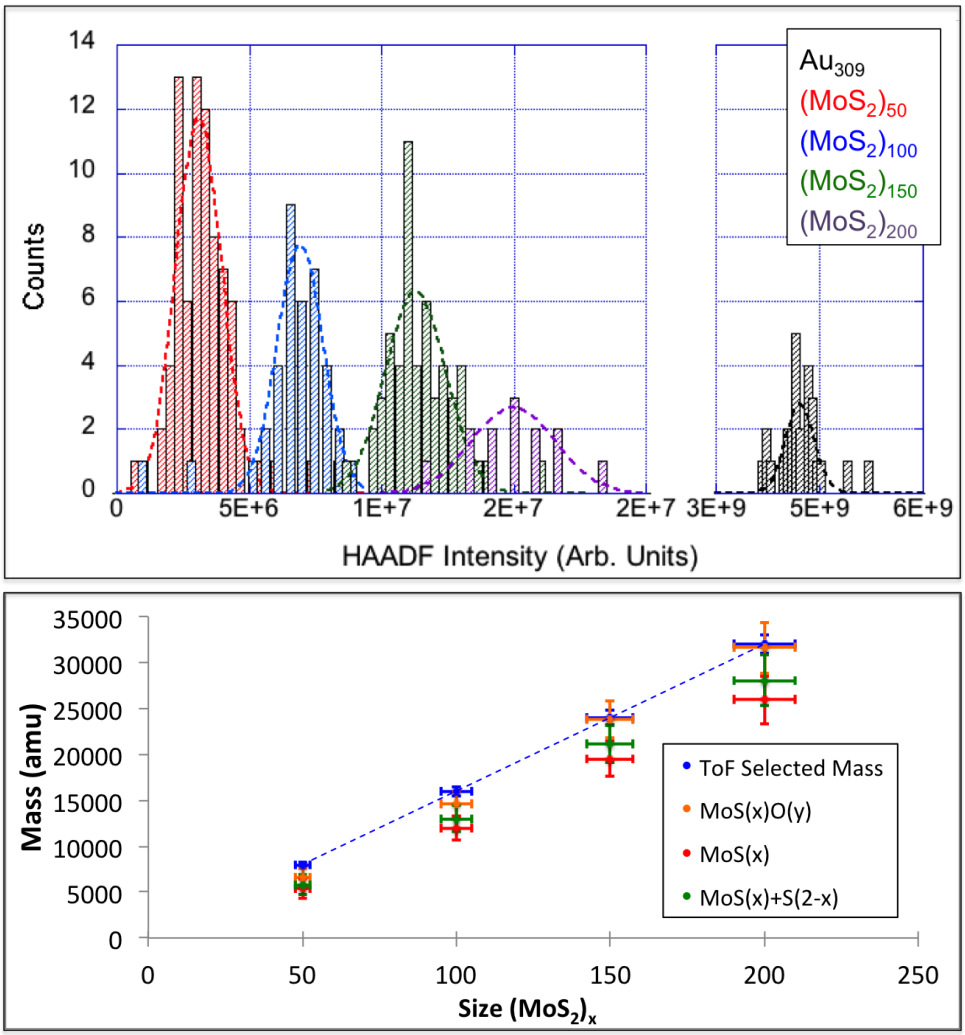

Figure 5.21: (Top)MoS_2 cluster and Au mass standard distributions, with Gaussian fits to negate the effect of outliers. FWHM of peaks: δm/m Au 5.0%, $(MoS_2)_{50}$ 27.9%, $(MoS_2)_{100}$ 12.5%, $(MoS_2)_{150}$ 10.1%, $(MoS_2)_{200}$ 10.5%. (Bottom) The size-selected mass (Blue) is compared to the measured mass of MoS_xO_y with x and y from the average XPS value (Orange), the calculated mass of MoS_x having removed the oxygen contribution (Red) and calculated mass of MoS_2 having added a stoichiometric sulfur mass (Green).

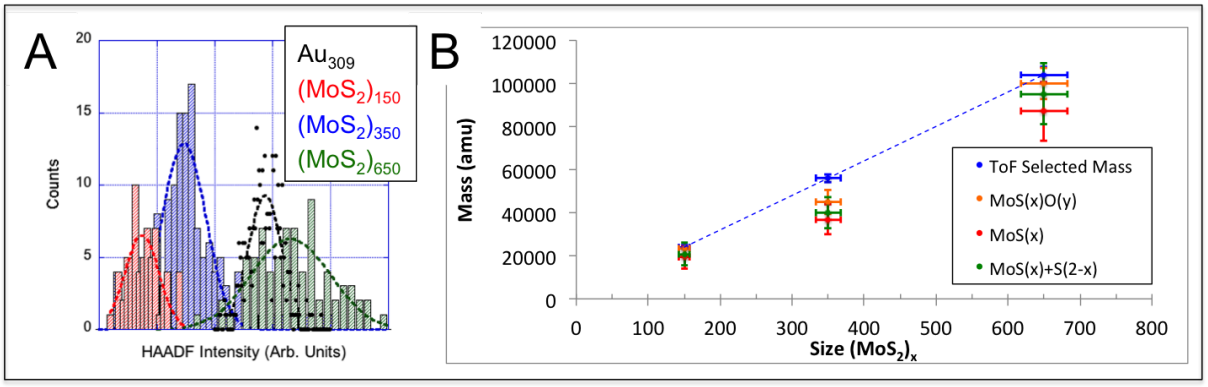

Figure 5.22: (A) Gaussian peaks are fitted to the cluster and mass standard distribution to negate the effect of outliers. FWHM of peaks: δm/m Au 10.2%, $(MoS_2)_{150}$ 39.6%, $(MoS_2)_{350}$ 25.4%, $(MoS_2)_{650}$ 20.4% (B) The size-selected mass (Blue) is compared to the measured mass of MoS_xO_y with x and y from the average XPS value (Orange), the calculated mass of MoS_x having removed the oxygen contribution (Red) and calculated mass of MoS_2 having added a stoichiometric sulfur mass (Green).

5.6.1 Crystal Structure

The clusters display clear bulk characteristics, although the sulfur component of the clusters has insignificant contrast in HAADF micrographs and their presence can only be inferred by reference to the MoS_2 structural motifs. Molybdenum atoms are clearly visible in hexagonal order in the basal plane (Fig 5.23A). FFT analysis confirms that the (100) and (110) spacings are in good agreement with bulk crystal structure [192, 193] (Fig 5.23B).

A small percentage of clusters impact perpendicularly to the surface exposing the (002) plane (Fig 5.23C). The layer spacing matches well with the van der Waals gap in the bulk structure. As cluster size increases they display lower coordination, which indicates that the growth mode beyond a certain size is gas-phase cluster coalescence. Evidence for this is shown by multiple connected facets (Fig 5.23D), too extreme to be caused by the low energy impact.

The clusters often display imperfect lattice structure alongside crystalline regions (Fig 5.24). Such regions are found in all the clusters observed for all sizes, deposition energies and nucleation parameters. These low-coordination areas are likely to be incomplete top layers due to the higher intensity of the disordered areas. Their existence is attributed

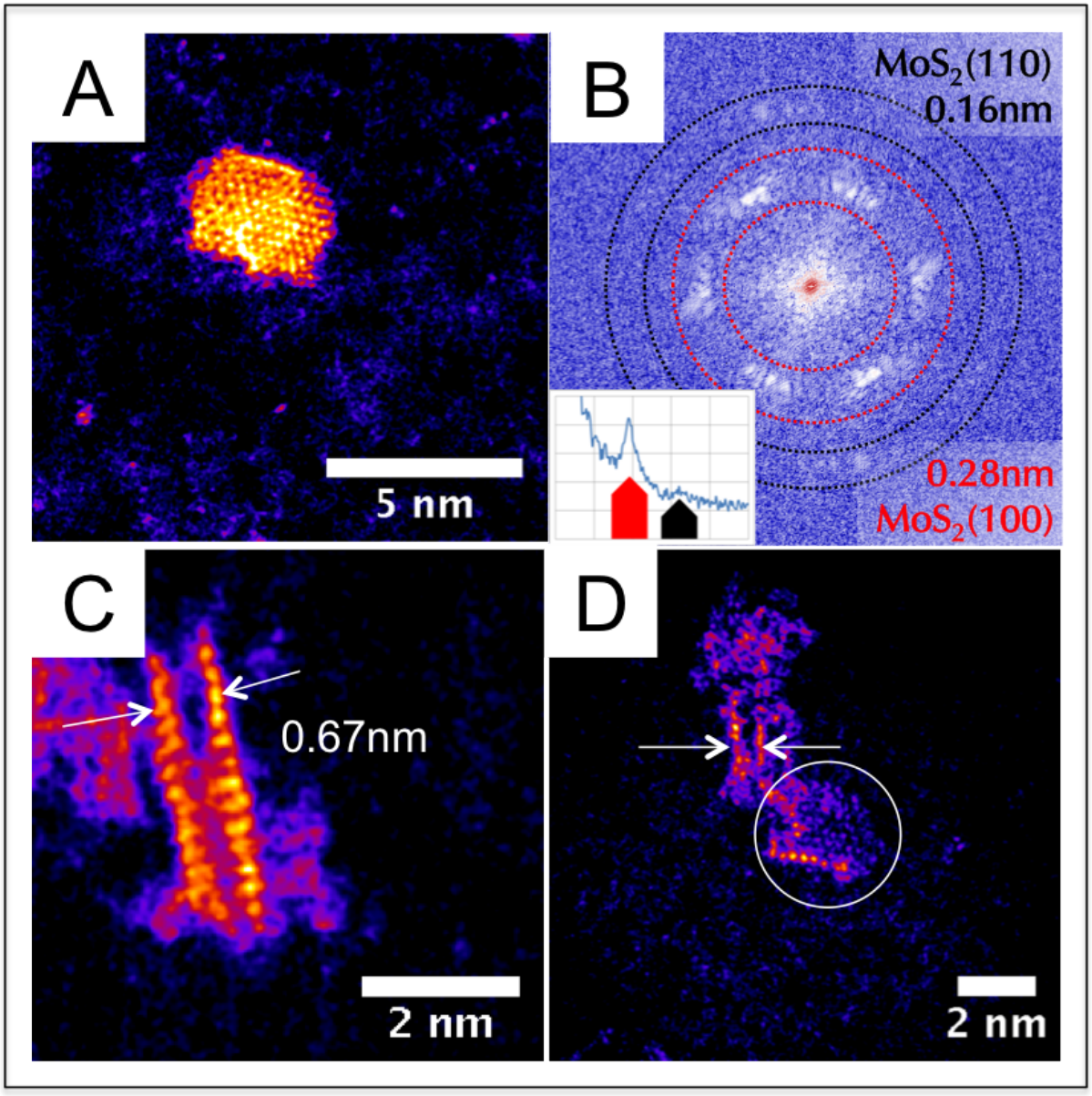

Figure 5.23: (A) $(MoS_2)_{500}$ trilayer and corresponding FFT (B) shows hexagonal crystal structure characteristic of bulk MoS_2 basal plane, with radial intensity profile highlighting the spots (B-Inset). (C) $(MoS_2)_{650}$ showing basal plane edges (002) and (D) another $(MoS_2)_{650}$ with features from both (100) and (002) faces.

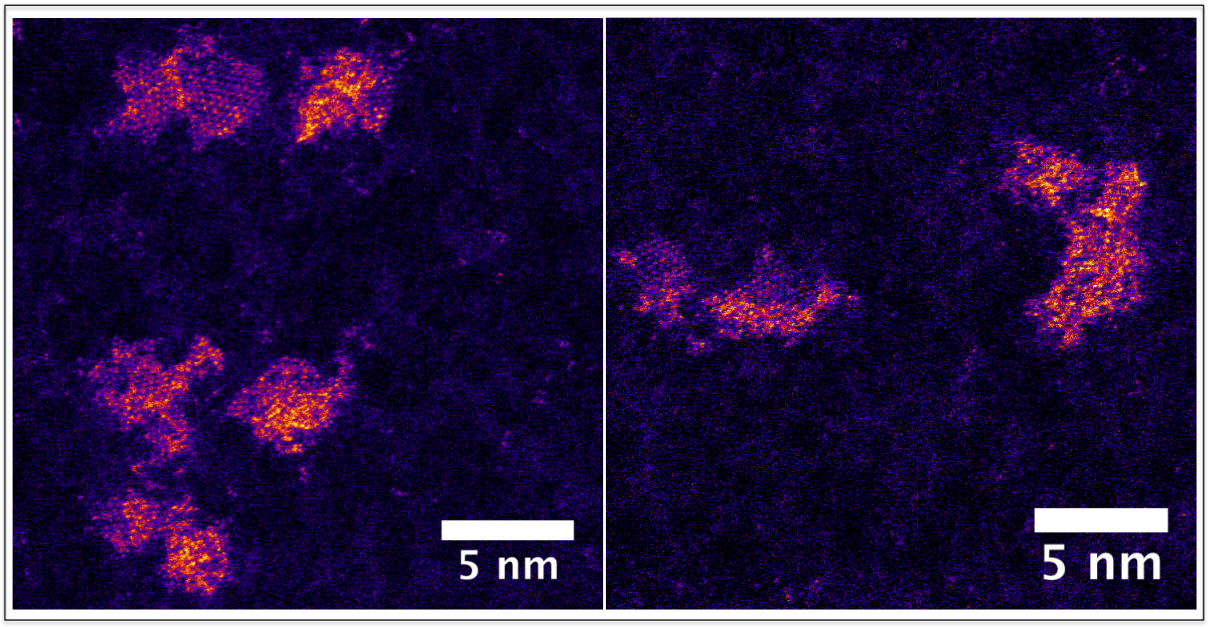

Figure 5.24: STEM micrograph of $(MoS_2)_{500}$ clusters displaying adjacent crystalline and amorphous regions.

to the nucleation sites of a new MoS_2 layer, in which layer growth first proceeds from point defects on the basal plane, to which binding is possible, then van der waals bonding proceeds with the defect points as anchors for the new layer. The crystalline sections show well ordered Mo atoms, but the absolute intensity varies between each Mo atom. The variation is likely to be caused by the point defect sulfur vacancies in the lattice. These vacancies, as well as the reactive edge sites, will be the first sites to oxidise, giving rise to the strong oxygen content shown by XPS (Section 4.4.1).

5.6.2 Layer Structure

The flat platelet sections of the clusters are similar to those of Besenbacher et al [69] with the addition of vertical layer stacking. Supported growth methods, such as sulfidising Mo islands on Au(111), are more likely to produce 2D structures due to favourable substrate interaction [194]. However, multilayer stacking is also seen for some supported MoS_2 islands at temperatures above 1000°K on HOPG [75, 116]. The growth of layers was explored for increasing sizes of MoS_2 cluster in order to understand the underlying nucleation processes.

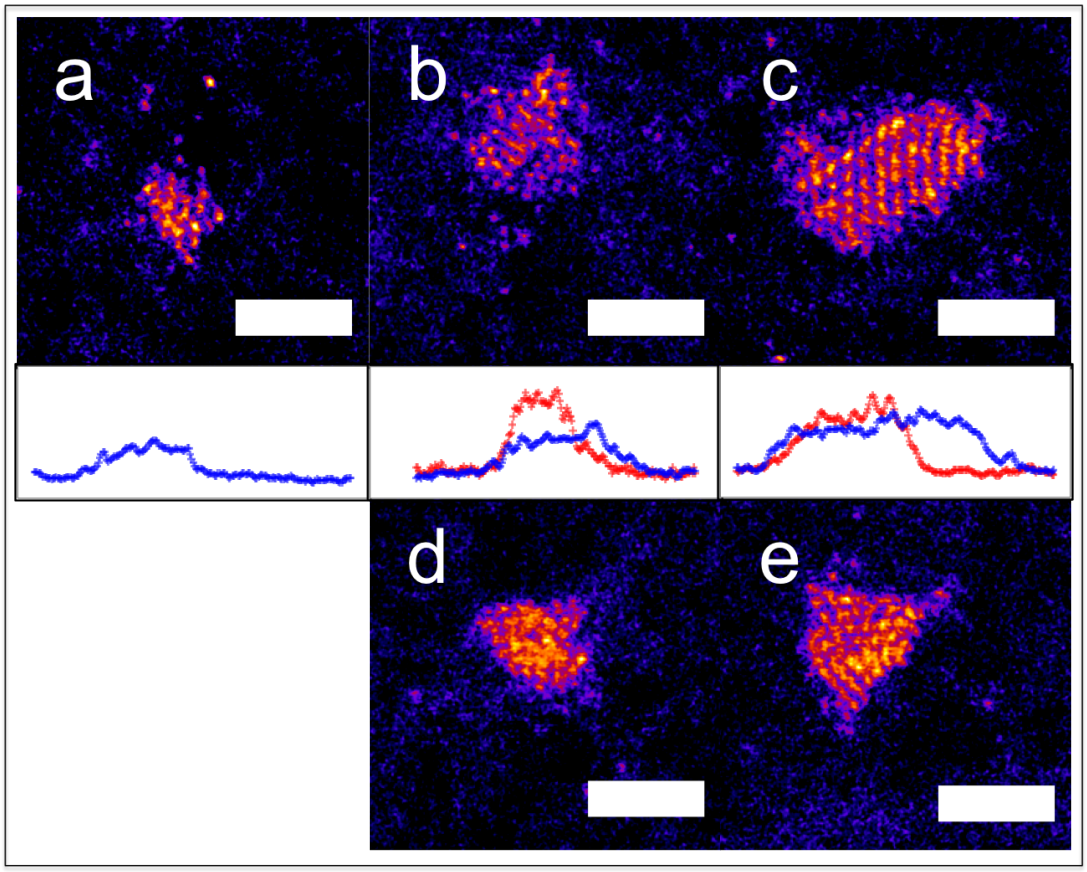

Figure 5.25: (2nm scale bars, Line profile: blue = A-C, red = D-E) STEM micrographs and corresponding line profiles of (A) $(MoS_2)_{50}$ monolayer, (B) $(MoS_2)_{100}$ monolayer, (C) $(MoS_2)_{150}$ monolayer, (D) $(MoS_2)_{100}$ bilayer and (E) $(MoS_2)_{150}$ partial bilayer.

The smallest size-selected clusters in this study, $(MoS_2)_{50}$, displays anisotropic growth to produce a monolayer raft of MoS_2 in gas phase (Fig 5.25A). At the smallest sizes the clusters show portions of the bulk hexagonal structural motif, but the sub-stoichiometric sulfur content is not enough to support a complete platelet structure at small sizes [78]. Higher concentration of beam damage and greater impact energy per atom will also add to the reduced coordination for small clusters.

The onset of multilayer structures is seen with increasing size, shown by decreased lateral area but increased scattered intensity (equivalent to height) (Fig 5.25D,E). The onset of bilayers with increasing size is in agreement with growth of other layered dichalcogenides [78], however the uneven intensity profiles show that these layers are not perfect crystals, but contain sulfur vacancies or oxygen adatoms. These low-coordination sites on the basal

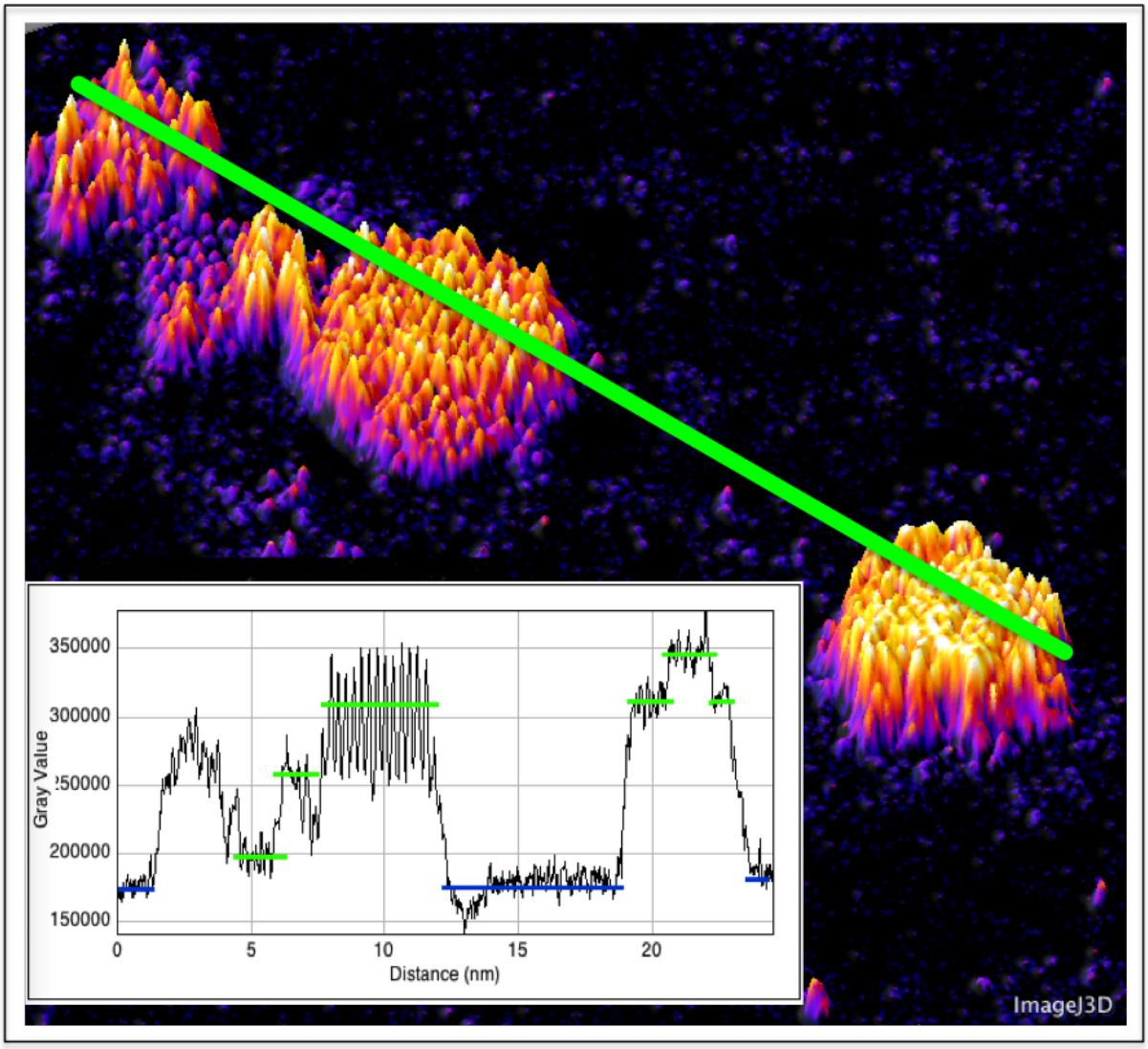

Figure 5.26: 3D projection from a STEM micrograph of an $(MoS_2)_{500}$ clusters. (Inset) Line profile along the clusters showing layers

plane might function as anchoring points for multilayer growth, as the weak van der Waals interaction alone may not be sufficient. The metallic edge states have also been discussed as a cause of preferential stacking due to a stronger interlayer interaction [75]. At larger sizes the clusters display larger sections of crystallinity (Fig 5.26) that can be quantified by the step increase in intensity between layers.

The layers of MoS_2 generally form in registry with the one below, this being the lowest energy configuration [195], however the difference in energy for rotated layers is small. This leads to Moiré patterns in the micrographs, which can be deconvoluted to find the

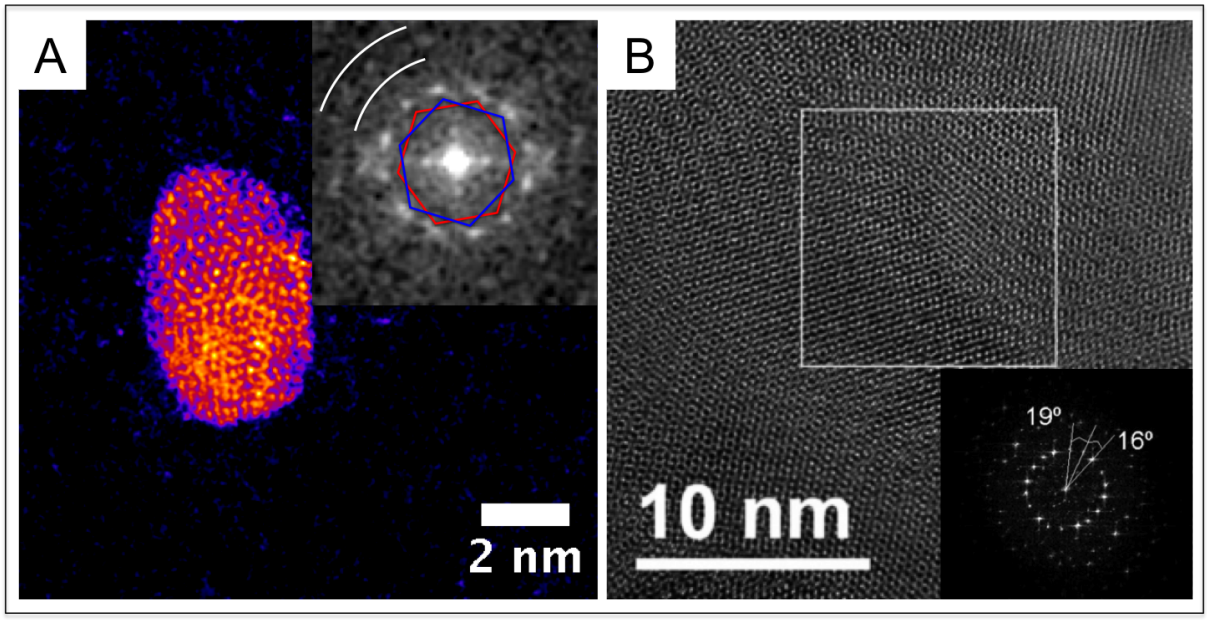

Figure 5.27: (A) STEM micrograph of $(MoS_2)_{500}$ cluster. (A-Inset) Two layers are offset by 27° to produce an offset in the (100) FFT signal (Spacing 0.26nm), the (110) plane is faintly visible between the white curves (Spacing 0.15nm) (B) HRTEM micrograph of 3 layers of offset MoS_2 displays a similar Moiré pattern (B-Inset) Electron diffraction shows rotation of 16° and 19° for these 3 layers. From [195]

relative rotation by FFT (Fig 5.27). Studies of MoS_2 thin films have noted similar patterns for rotated multilayers [196, 197, 153, 198, 199].

The layering of MoS_2 clusters is unlikely to take place by restructuring after landing as the interaction between MoS_2 and carbon is weak, even on defect-rich HOPG [75]. Evidence for the growth of multilayers in the gas phase, as opposed to restructuring on the surface, is also shown by the presence of perpendicularly oriented clusters. Growth of MoS_2 edges normal to the substrate is uncommon, only found when substrates present strongly binding nucleation sites [200] or in highly saturated growth conditions [43], so vertically oriented clusters are most likely to have impacted in this position.

5.6.3 IF-MoS_2

The existence of fullerene structure has been simulated for similar dichalcogenides in this size range [191] with sizes of $(MoS_2)_x$ (x = 576, 784, 1936). These sizes of MoS_2 cluster were deposited to determine if the fullerene form became favoured over platelets.

No cluster size was found to deviate from the predominance of platelet structures, and no peaks appeared in mass spectra to indicate an energetically stable state. Over all sizes of clusters imaged by STEM, a small amount, were fullerene-type structures co-deposited with the platelet structures (Fig 5.28). The small percentage of fullerenes is due to the energetic favourability of fullerenes decreasing with deviation from stoichiometric composition [95]. The fullerenes that exist are multi-walled, in agreement with the simulations that show single-walled shells are less stable [191]. The difference between these clusters and the almost-pure fullerene samples fabricated at high temperature [44] highlight the conformational differences induced by synthesis conditions (Section 2.3.5).

5.6.4 Growth

The morphology of MoS_2 clusters with increasing size was studied by analysis of high resolution micrographs. An understanding of the cluster surface is useful for correlating catalytic activity to particular sites or facets. The morphology also provides information on the nucleation processes that occurred to produce the cluster.

The evolution of the $(MoS_2)_x$ clusters from $(MoS_2)_{50}$ to $(MoS_2)_{1936}$ is characterized by an $x^{0.86}$ increase in area and an $x^{0.46}$ increase of perimeter (Fig 5.29). This is in close agreement with linear area growth (x^1) and root perimeter growth ($x^{0.5}$) associated with a 2D structure. This indicates anisotropic growth consistent with the lamellar structure, and that nucleation occurs via atoms attaching to the more active edge sites. The fraction of low-coordination edge sites on each size of cluster is distinct (Fig 5.30) due to these different scaling relationships and has been used to model the areas of oxidation (Section 4.4.1) and active sites for catalysis (Section 6.4).

The perimeter measurement is especially affected by the uniformity of the clusters. The perimeter is larger than the theoretical perimeter associated with a uniform circular distribution of MoS_2, due to the dendritic nature of the clusters. This non-uniformity was characterised by measuring the aspect ratio and solidity as a function of size (Fig 5.31). The aspect ratio increases with size and solidity decreases, this should not be due to

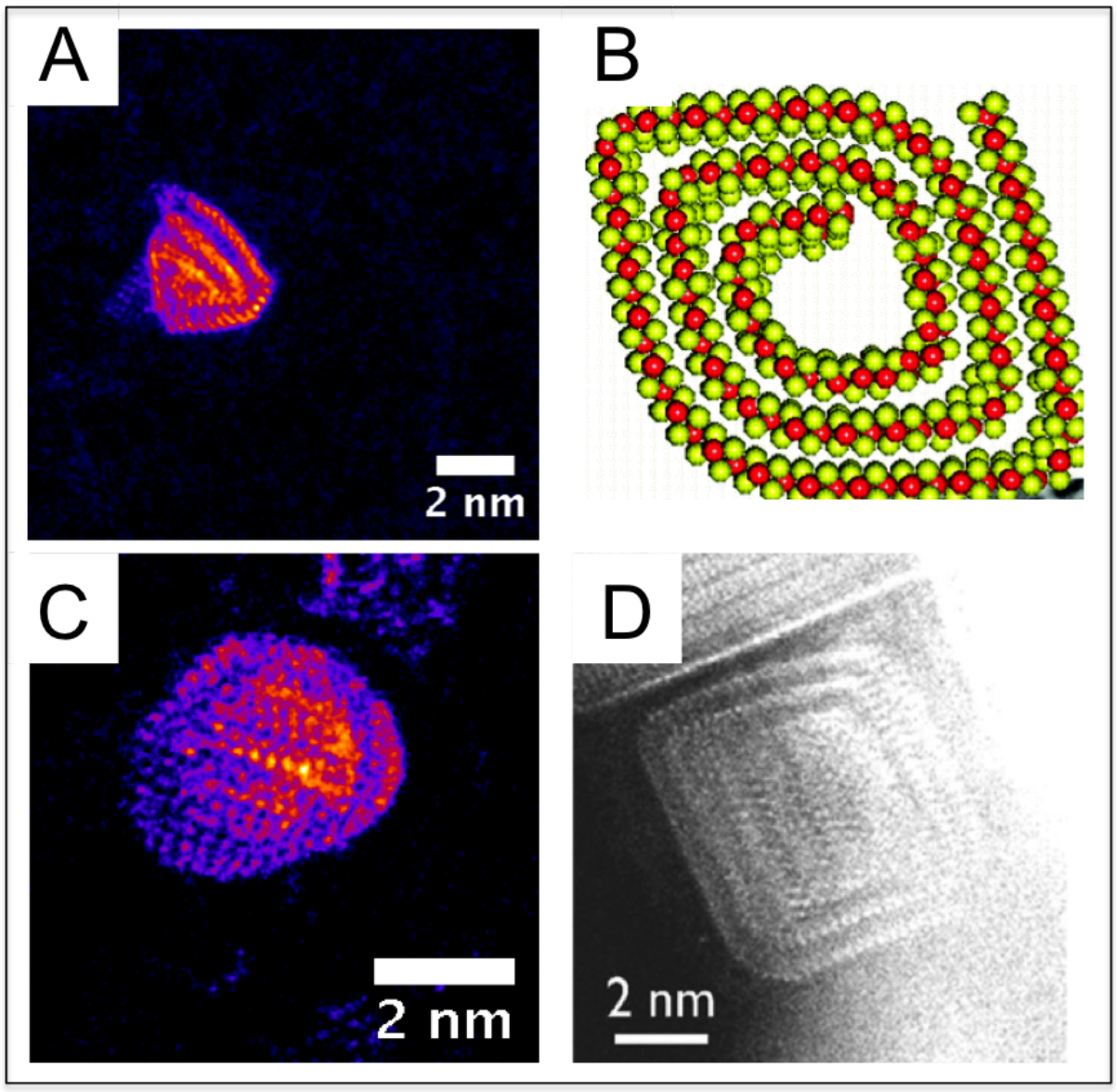

Figure 5.28: (A) STEM micrograph of seashell type $(MoS_2)_{1000}$, compared to (B) a simulated seashell structure [98]. (C) STEM micrograph of $(MoS_2)_{650}$ fullerene type cluster and (D) other MoS_2 fullerene clusters in literature [102].

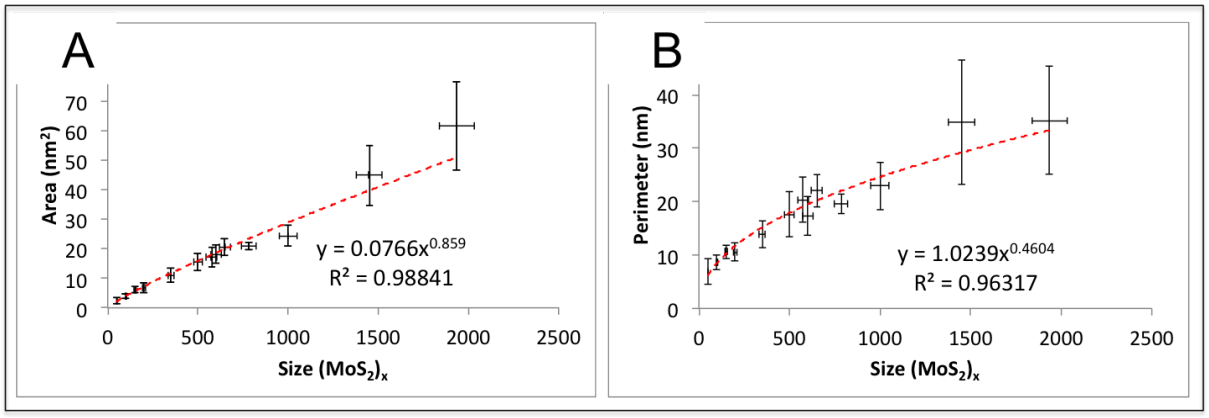

Figure 5.29: (A) Average area and (B) average perimeter for clusters by size, measured from histogram fits of individual clusters in high-resolution STEM micrographs.

$(MoS_2)_x$	Area (nm^2)	Perimeter (nm)	Edge Fraction
150	6.09±0.96	10.62±1.27	0.54±0.11
350	10.96±2.29	13.81±2.50	0.39±0.11
500	15.58±3.03	17.59±4.23	0.35±0.11
650	20.66±2.91	22.01±2.99	0.33±0.07
1000	24.46±3.65	22.99±4.48	0.29±0.07

Figure 5.30: Edge fraction of MoS_2 clusters calculated from measured area and perimeter, assuming an edge annulus equal to the MoS_2 unit cell diameter.

increased impact damage for larger clusters as the impact energy per MoS_2 unit was held constant. The cause must therefore be in the nucleation process. The smallest clusters remain relatively smooth, but as nucleation pressure is increased to produce larger clusters it is likely to cause many small platelets to form, which become the building blocks of larger clusters rather than single atoms.

The coalescence of pre-formed clusters results in the appearance of an aggregate, however as it was formed before mass selection it is of the correct total size. Typical cluster images, with associated parameters from (Figs 5.29 and 5.31), are displayed in Fig 5.32 for $(MoS_2)_{50}$ to $(MoS_2)_{500}$ and Fig 5.33 for $(MoS_2)_{650}$ to $(MoS_2)_{1936}$. The increased perimeter of these clusters should be beneficial for catalysis as the proportion of edge sites increases. This was confirmed by XPS showing atmospheric reactions proportional to the amount of edges (Section 4.4.1).

The cluster platelets generally orient on landing to be parallel to the substrate, so the

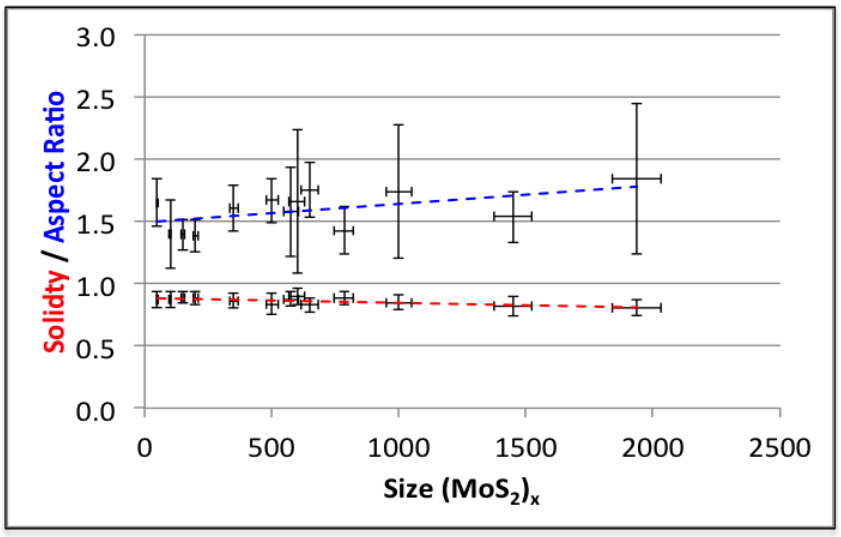

Figure 5.31: Solidity and Aspect Ratio of the clusters as a function of size, measured from histogram fits of individual clusters in high-resolution STEM micrographs.

layers are rarely visible by microscopy. The amount of layers can be calculated however using the known cluster mass and the measured lateral area. This is shown to increase linearly from monolayers at the smallest sizes up to a limiting value of 3 layers (Fig 5.34A), due to the onset of gas-phase cluster coalescence for larger size clusters. The deviation in the area and perimeter scaling relationships by size (Fig 5.29) from linear/root behaviour is due to these multi-layered structures being quasi-2D rather than 2D. The layer height by size is variable from tall narrow structures (Fig 5.34C) to short wide structures (Fig 5.34D). Layered MoS_2 catalysts are usually undesirable for practical catalysis due to the poor conductivity between planes [103], however in these clusters this may be offset by the increase in low coordination sites on disordered large clusters and better conductivity between layers if they are bridged by defects.

5.6.5 Effect of Impact Energy

In all images some atomic fragments are seen around the clusters, indicative of a combination of impact and beam damage. Impact energy-dependent experiments have shown the clusters to lose mass as impact energy increases (Fig 5.35A). Thus, for structural analysis, clusters were deposited at the lowest impact energy possible to reduce damage to the

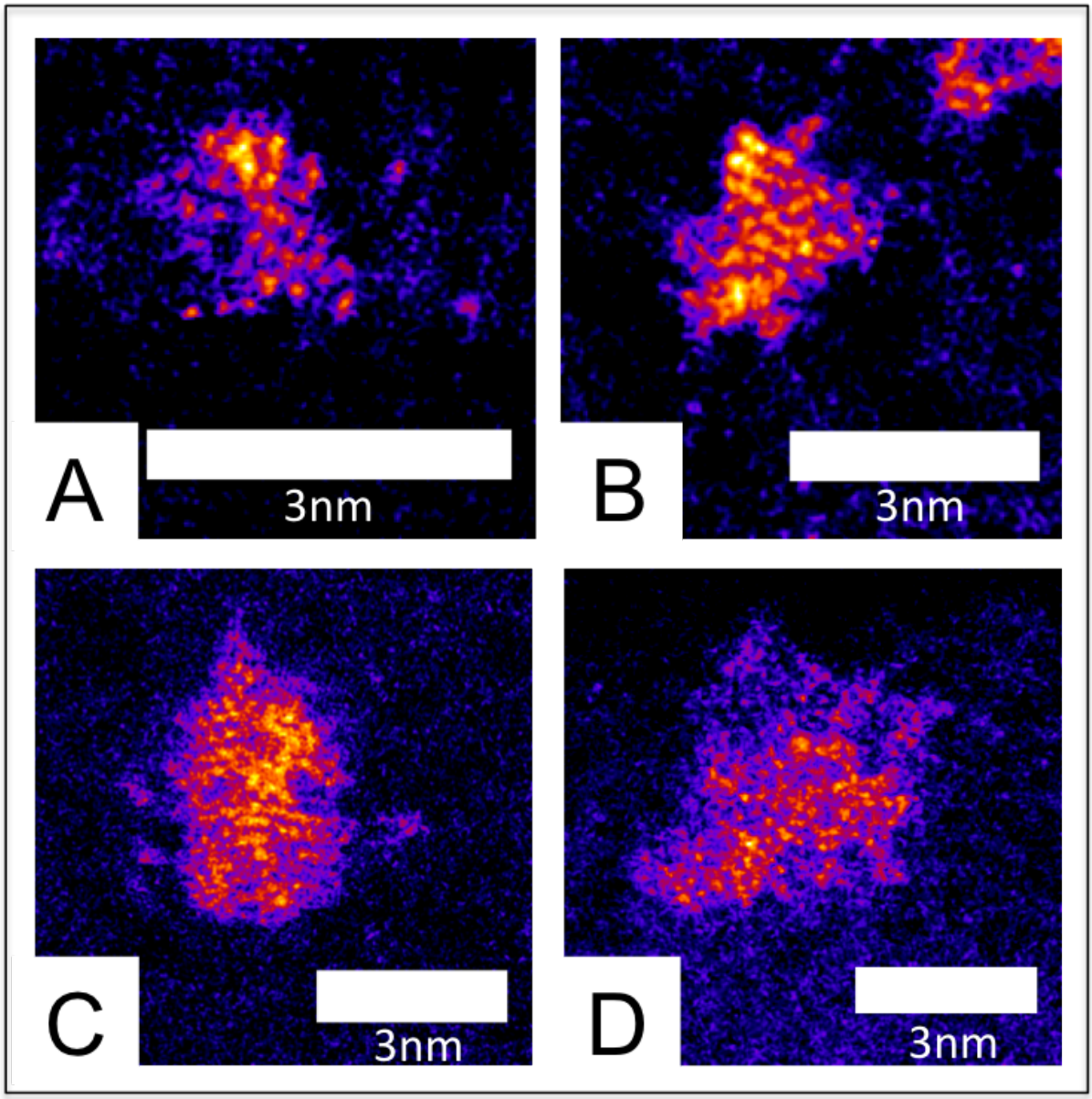

Figure 5.32: Clusters deposited at <2.5eV per MoS_2 unit: (A) $(MoS_2)_{50}$ Area: 2.6 nm^2, Perimeter: 6.7 nm, AR: 1.22, Solidity: 0.89 (B) $(MoS_2)_{200}$ Area: 5.0 nm^2, Perimeter: 10.2 nm, AR: 1.26, Solidity: 0.84 (C) $(MoS_2)_{350}$ Area: 12.7 nm^2, Perimeter: 19.1 nm, AR: 1.23, Solidity: 0.80 (D) $(MoS_2)_{500}$ Area: 19.9 nm^2, Perimeter: 19.4 nm, AR: 1.18, Solidity: 0.87

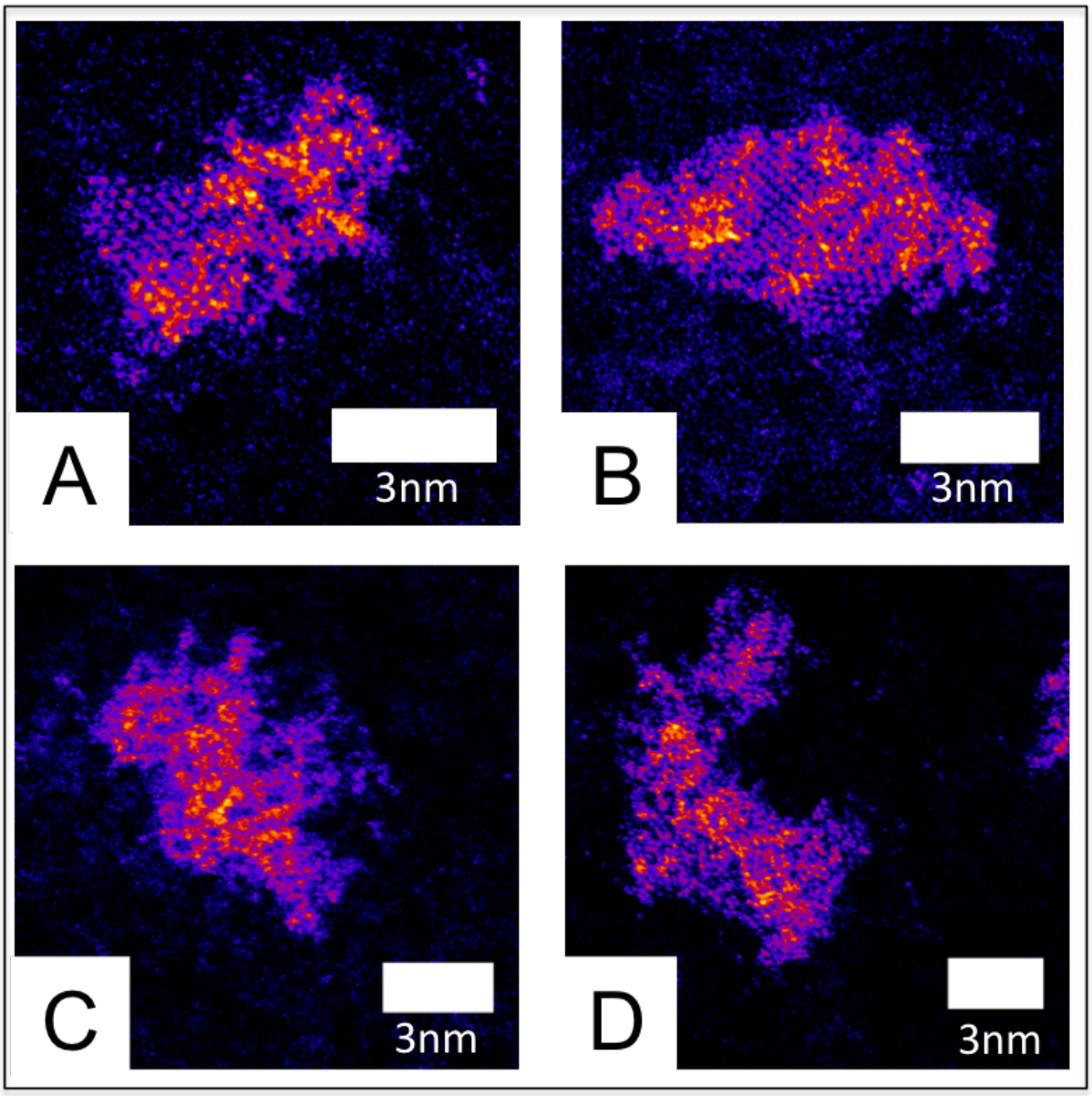

Figure 5.33: Clusters deposited at <2.5eV per MoS_2 unit: (A) $(MoS_2)_{650}$ Area: 20.8 nm^2, Perimeter: 23.3 nm, AR: 1.70, Solidity: 0.80 (B) $(MoS_2)_{1000}$ Area: 32.5 nm^2, Perimeter: 24.5 nm, AR: 1.87, Solidity: 0.92 (C) $(MoS_2)_{1450}$ Area: 44.1 nm^2, Perimeter: 34.5 nm, AR: 1.35, Solidity: 0.87 (D) $(MoS_2)_{1936}$ Area: 61.4 nm^2, Perimeter: 41.1 nm, AR: 1.69, Solidity: 0.79

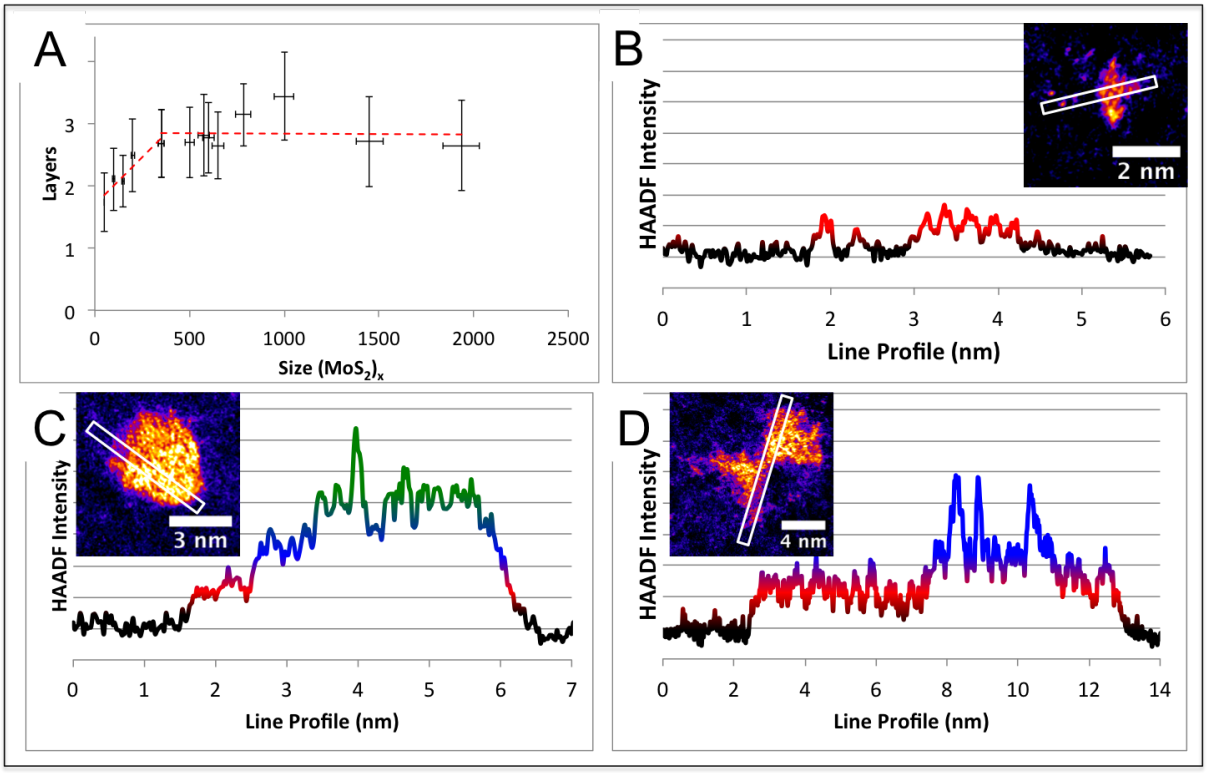

Figure 5.34: (A) Calculated layer height as a function of cluster size (calculated by dividing cluster area by MoS_2 unit area, the known selected size is then divided by this value to approximate the layers). The calculated values are in agreement with observed line profiles from STEM micrographs (Layer Height: Red = 1, Blue = 2, Green = 3): (B) $(MoS_2)_{50}$ (C) $(MoS_2)_{1000}$ (D) $(MoS_2)_{1936}$

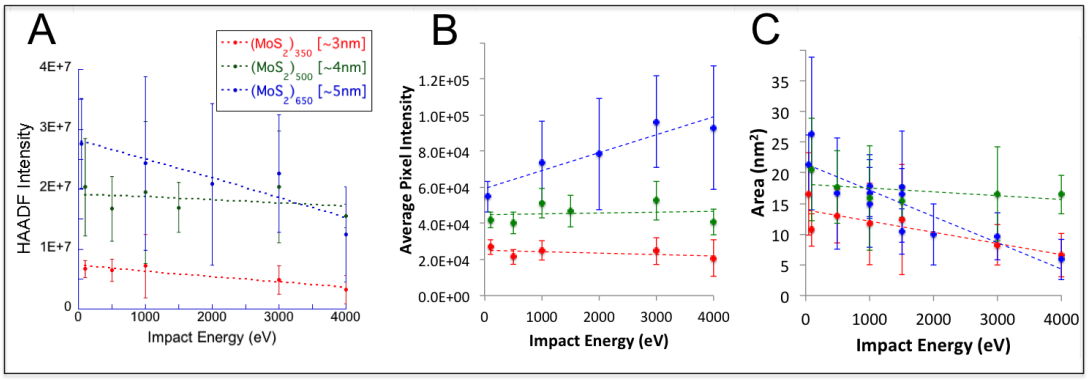

Figure 5.35: (A) Integrated HAADF intensity of MoS_2 clusters for increasing impact energy. (B) Average HAADF intensity, proportional to cluster thickness, of MoS_2 clusters for increasing impact energy. (C) Measured area for increasing impact energy.

fragile structure.

The layer height measured by average HAADF pixel intensity remains relatively independent of the impact energy (Fig 5.35B), meaning the measured mass loss must come from edge atoms, and this is indeed seen by a decrease in area with energy (Fig 5.35C). This result suggests covalent in-plane bonds are easier to break than Van der Waals inter-plane bonds. This counter-intuitive result indicates the structure is not perfectly crystalline and is further evidence of a more substantial bond between layers not existent in the bulk system.

The effect of impact energy on perfect crystals would instead be expected to cause shearing on landing. This is not evident for the majority of clusters as it would result in a significant population with lower mass in the distributions (Section 5.5). The weak van der Waals interaction between the MoS_2 trilayers has been easily broken in other studies [201, 202, 203, 14] suggesting cleavage should be possible by physical means. The total Van der Waals binding energy for a 3 nm platelet has been calculated to be less than 30 eV [201, 202], which is below the lowest deposition energy of 50 eV in this study. Landing orientation parallel to the substrate will reduce the shearing force for most clusters, allowing the majority to remain intact at low impact energy, but at higher impact energies a higher proportion should cross the shearing threshold. The data for high impact energy, greater than 1 keV, also lacks any significant population of small clusters that could be

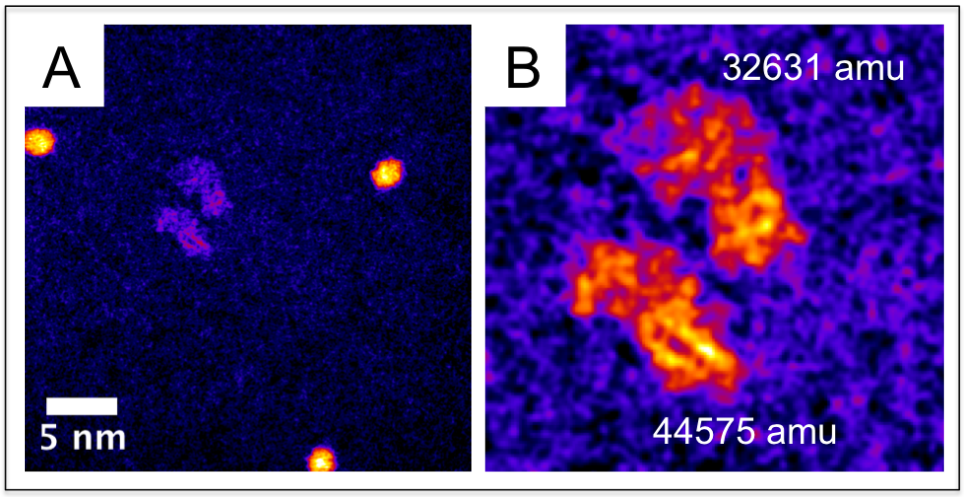

Figure 5.36: (A) Two MoS_2 platelets of similar shape adjacent to Au_{309} mass standards. The integrated intensity of local Au standards (in this micrograph) differ from the global (over all micrographs in this dataset) by 2.5%. (B) The platelets are confirmed by the mass balance technique, using average XPS stoichiometry and local Au_{309}, to be approximately half the expected mass of $(MoS_2)_{650}$. The cluster was deposited at a deposition energy of 50 eV and the total mass is 71% of the size-selected value, consistent with other measurements by mass standards (Section 5.5).

the result of shearing, however possible cleaving of the van der Waals bonds for a small percentage of clusters has been observed (Fig 5.36). The effect of shearing is identified by matching adjacent clusters to total the gas-phase selected mass and observing secondary effects such as shape correlation or exposed basal planes. There are also instances of offset platelet regions, which could be incomplete shearing. The lack of shearing confirms a stronger than expected force between the platelets, consistent with them having formed in the first place, either due to interlayer bridging or bonds involving the metallic edges.

5.6.6 Effect of Beam Energy

The stability of the clusters was investigated by continuous e-beam irradiation using the 200 keV STEM probe. The energy of the incident beam can cause structural changes that infer ground state configurations and also provide information about the strength of the chemical bonds [187]. The effects should be similar to thermal annealing, albeit directed only on a 172 nm^2 area. The experiments with thermal annealing as a post-processing

method in Section 5.4.6 produced more spherical particles, but destroyed the crystalline structure. This may have been due to the 523°K temperature being enough to dissociate sulfur, leaving a molybdenum rich cluster unable to sustain the bulk platelet structure.

The electron beam was rastered over the cluster for 1000 s while taking images, with occasional gaps to refocus as the beam drifted, during this time the particle was observed to reconfigure. Analysis of the micrographs, using a macro based on the work of Guo-Ruei Hu, shows the cluster loses mass according to the normalised HAADF intensity, and also decreases in area (Fig 5.37D). The cluster structure loses the hexagonal MoS_2 crystallinity (Fig 5.37A) over time and transitions to cubic symmetry (Fig 5.37C) consistent with BCC structure of Mo metal or MoO_3 [204]. The HAADF intensity at the centre of the cluster also increases, suggesting a transformation from 2D to 3D spherical structure, consistent with the results of annealing.

The mean pixel intensity in the cluster does not decrease (Fig 5.38A), so the cluster is therefore losing atoms from the edge. The perimeter also decreases in a stepwise fashion as it becomes more circular due to the greater density of dissociation from protruding segments (Fig 5.38B). The reconstruction to a more circular profile is in agreement with the annealing results, and the transition to a cubic structure of Mo metal is consistent with the low threshold for knock-on damage of the sulfur atoms.

The effect of beam annealing is a useful tool for exploring the stability of cluster structures and specific sites in that structure. This method has scope for use in a detailed study, with lower beam energy below the threshold for knock-on damage (Section 5.4.4), in order to determine the energy required to reconfigure the cluster to a uniform platelet and to determine the preferred edge configuration.

5.7 Conclusion

The microscopy has shown that quasi-2D platelets are the dominant structure as was expected from initial characterisation work with cluster beam parameters (Section 4.2.1).

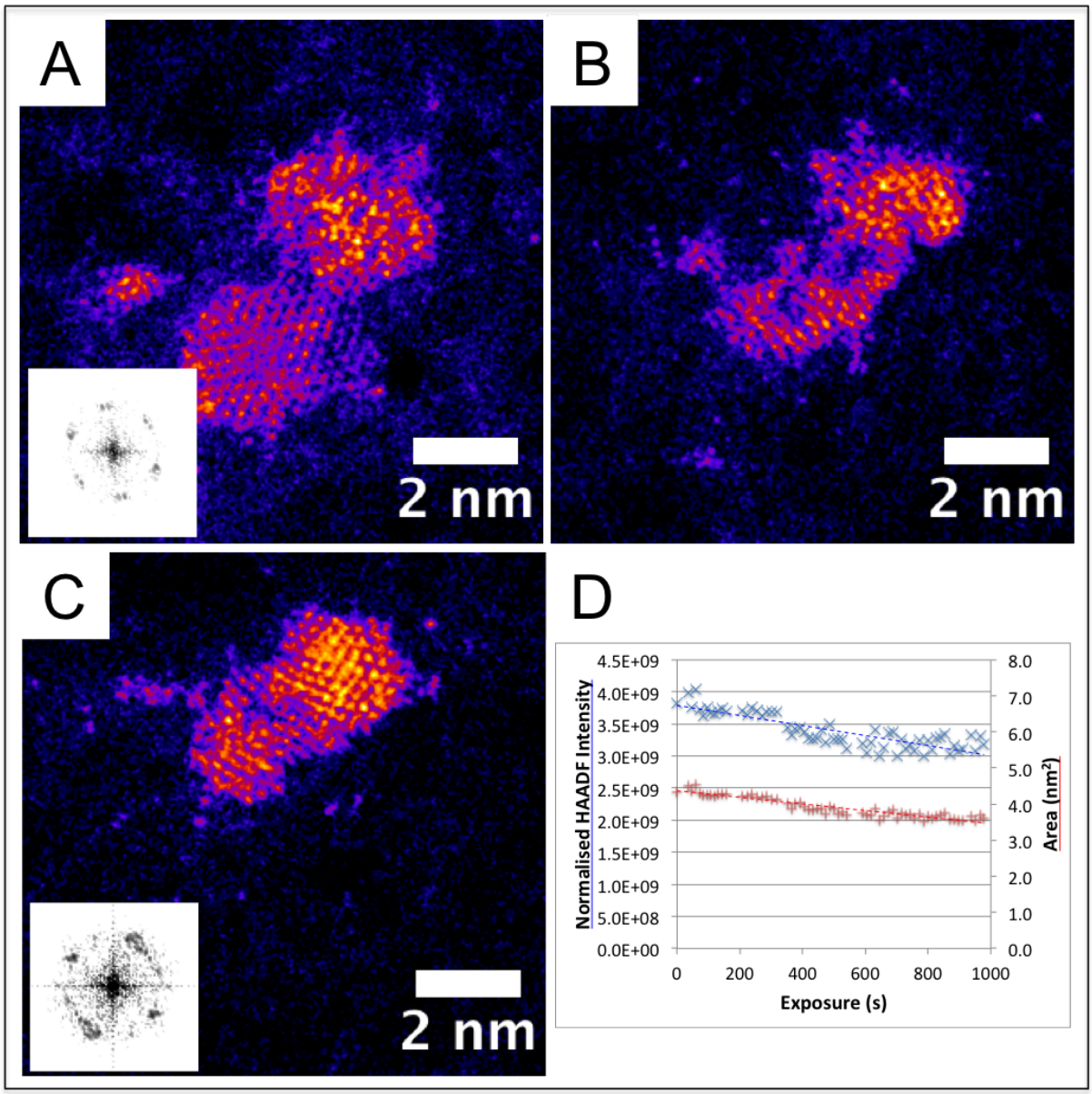

Figure 5.37: Micrographs of $(MoS_2)_{600}$ cluster exposed to continuous 200 keV electron beam and imaged repeatedly by atomic-resolution STEM. (A) Micrograph of cluster after first exposure with (A-Inset) FFT of cluster showing hexagonal symmetry, (B) after 500 s and (C) after 1000 s, (C-Inset) FFT of cluster showing cubic symmetry. (D) Plot of integrated intensity and area for increasing beam exposure time.

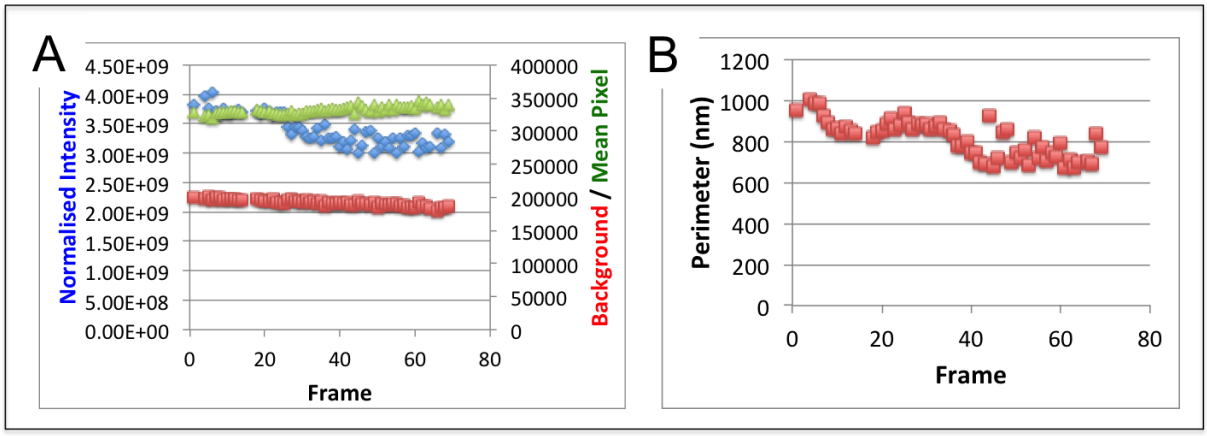

Figure 5.38: The same $(MoS_2)_{600}$ cluster from Fig5.37 was measured for (A) mean pixel intensity (as a measure of average layer height) compared with average background pixel intensity and integrated intensity. (B) Measured perimeter decrease with time.

There is also evidence for more exotic allotropes such as fullerene type structures, however the small sizes and low energy of the fabrication do not produce as many as laser ablation and furnace methods. The addition of extra energy by increasing impact velocity or by e-beam irradiation simply causes steady mass loss, indicating these processes do not cross the threshold for fullerene restructuring.

The effect of annealing was investigated as a method of controlling the structure after production, however this resulted in spherical particles and so was abandoned due to the absence of desired edge sites. STEM-EELS was used throughout the initial parameter tuning phase to confirm the clusters were homogeneous compounds, although the measured composition had a greater reduction in sulfur content than indicated by XPS due to the high beam energy. The use of Au mass standards, as well as improving focus and reducing e-beam dose, validates the mass-selection process and shows that the majority of clusters have one unit of charge.

Atomic resolution analysis shows the platelet structures retain the characteristic lattice constants of the bulk material. The layered structure of the bulk is also retained, based on observation of the (002) plane and step-wise intensity profiles. The calculated layer height increases from 1.7±0.9 layers at $(MoS_2)_{50}$ to a limiting value of 2.8±0.7 layers at sizes greater than $(MoS_2)_{350}$. The catalytically active sites on these clusters are likely to be the

usual layer edge sites, which are more abundant on these clusters than the perfect crystal structure. The scaling relationships of area ($x^{0.86}$) and perimeter ($x^{0.46}$) can be used to confirm these active sites based on atmospheric reactions and future electrochemical study of the same clusters.

The gas-phase layering and subsequent substrate impact goes some way to explain the disordered appearance of the clusters. The effect of edge fragmentation will be greater for a 2D platelet than a 3D nanoparticle, shown by the consistent reduction in measured mass compared to the selected mass (Section 5.5). The anisotropic gas-phase growth likely results in a majority of quasi-2D clusters with a wide non-uniform surface prone to simple edge fragmentation, especially at higher impact energy. Poorly crystalline edges may reduce the effectiveness for catalysis as the activity is strongly dependent on the termination [116], but the increase in total perimeter may counter this effect. Furthermore, it has been shown that defects in the basal plane [205] and in thin films [206, 59, 60] function as active sites, so the defective top layers in these clusters can increase activity. This agrees with calculations of oxidation from XPS (Section 4.4.1), that show the edges do not account for all the oxide and oxysulfide signal. The reactive sites, now in the form of oxide and oxysulfide, are potentially passivated to further chemical reactions, however MoO_3 is soluble in aqueous electrolytes [207, 76], so the active edges may be re-exposed. Thus further electrochemical studies were performed (Chapter 6) to determine the overall effect.

CHAPTER 6

MOLYBDENUM DISULFIDE CLUSTERS AS HYDROGEN EVOLUTION CATALYSTS

6.1 Introduction

Gas-phase production of clusters offers a unique opportunity to correlate catalytic properties with nanostructures. The substrates for cluster beam deposition methods are usually planar surfaces, although novel methods such as dicing have been used to create powders [208]. Planar surfaces have the advantage of simpler kinetics and a greater understanding of catalyst loading and structure. The disadvantage is that the low surface area necessitates a small catalyst loading, thus sensitive chemical measurements are required. Potentiostats, with a current range down to nanoamperes, have sufficient sensitivity to detect the small currents produced by planar supported catalysts. Such a setup provides a diverse range of characterisation based on the reaction current produced at a given potential and the rate at which reaction current responds to changing potential.

The work presented in this chapter begins with chemical synthesis of MoS_2 nanoparticles and their characterisation. This collaborative work provides a background to this common fabrication technique [151, 199, 61, 209, 210, 211, 212, 213, 214, 215, 216, 217, 218, 219, 220] and standard electrochemical characterisation processes for hydrogen evolution catalysts. Furthermore, an understanding of the challenges associated with conventional fabrication techniques and their analysis allows us to take full advantage of the benefits of gas-phase

fabrication. There follows exploratory work measuring the catalytic properties of size-selected clusters immobilised on HOPG substrates and post reaction studies to investigate the effect of reaction conditions on the clusters. Ultimately this system was replaced by deposition of clusters onto conventional electrodes, which facilitates more advanced measurements as well as improving reproducibility.

6.2 Hydrogen Evolution by Chemically-Prepared MoS_2

Work on fabrication and characterisation of chemically prepared MoS_2 was undertaken prior to electrochemical experiments on gas-phase produced clusters. This work, performed at the Technical University of Denmark (DTU), provided valuable experience of standard electrochemical procedures and served as a comparison for the advantages and disadvantages of chemical versus physical fabrication. The structure of the work consists of reproducing a simple chemical synthesis from the literature, with the addition of dopants to enhance performance. This enhancement was measured by comparison of cyclic voltammograms of the different samples. Further treatments, such as chemical exfoliation and high temperature sulfidation, were performed and examined by cyclic voltammetry. A selection of samples were also transferred to TEM grids for STEM imaging, at University of Birmingham by Zhiwei Wang, in order to correlate the electrochemical activity with the morphology.

6.2.1 Determination of Polymer Content

The method of Zong [58] was reproduced to create monodisperse nanoparticles in solution, however the publication omitted the optimum ratio of polymer to MoS_2. Thus the method was recreated as described in Section 3.6.1 with a batch of 9 samples, 3 each of molar ratio (PVP/MoS_2) 5, 10, and 20 (Fig 6.1). One batch of 3 was left as made, the second was washed in ethanol to remove the polymer, and the third was washed and then sulfidised in H_2S for 1 hour at 723°K. A portion of the as-made solutions for the three concentrations

Molar Ratio (PVP/MoS_2)	mols PVP in 25 mL (μmol)	Mass PVP in 25 mL (g)
A - 5	50	0.0014
B - 10	25	0.0028
C - 20	12.5	0.0056

Figure 6.1: PVP:MoS_2 ratio parameters for hydrothermal synthesis of MoS_2 nanoparticles.

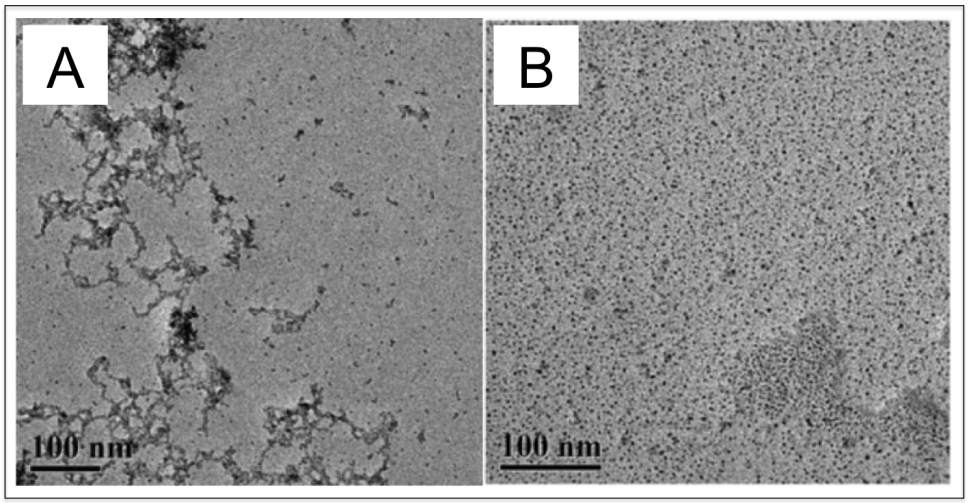

Figure 6.2: TEM micrographs from [58] of chemically prepared nanoparticles from the literature, produced by the same solvothermal synthesis at 373°K from (A) 0.5 mM MoS_2 (B) 0.1 mM MoS_2

were drop cast onto carbon TEM grids and dried before imaging by bright-field TEM for comparison with the literature method (Fig 6.2).

The TEM micrographs taken soon after preparation show distributions similar to the desired results. The remaining PVP is shown by long agglomerates in the micrographs (Fig 6.3), however due to the bulky nature of the polymer, active sites on the MoS_2 should still be accessible. This is in agreement with catalytic activity noted from cyclic voltammetry even for unwashed samples (Fig 6.4). The results from the literature show similar dispersion of nanoparticles when using a higher concentration of 0.5 mM (Fig 6.2A), suggesting the 0.1 mM solution is not uniformly covering the grids. Direct comparison of the most similar synthesis parameters, heating 0.1 mM at 373°K, shows the nanoparticles from the literature are more monodisperse (Fig 6.2B) than the prepared nanoparticles from this work (Fig 6.3). The differences may result from the use of 3x longer polymer chains in the literature method, and the specific ratio of PVP:MoS_2 which is only given as a range.

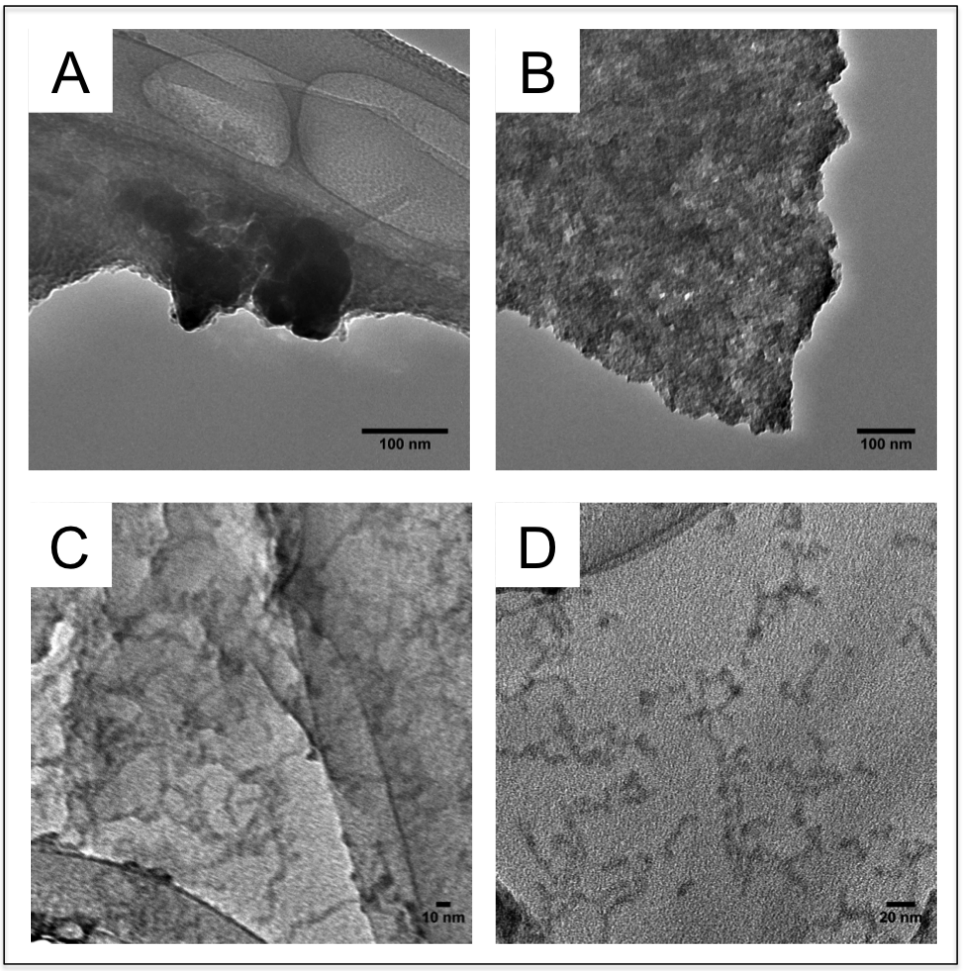

Figure 6.3: (A) TEM micrograph of sample with Molar ratio MoS_2/PVP = 5 shows agglomerates of MoS_2 and (B) densely packed layers. (C) TEM micrograph of Molar ratio MoS_2/PVP = 10. (D) TEM micrograph of Molar ratio MoS_2/PVP = 20.

Furthermore, there are more significant structural differences, such as X-Ray Diffraction (XRD) analysis showing crystal peaks in the as-made sample (XRD data not shown, performed by Anders Laursen at DTU). Therefore the as-made samples contain crystalline MoS_2, despite the literature synthesis producing amorphous MoS_2. Scherrer analysis of the XRD spectrum gives a crystallite size of 2 nm, confirming that after synthesis the nanoparticles remain distinct within the polymer matrix.

The activity of the catalysts for HER was simultaneously tested. First the as-made solutions were tested (Fig 6.4), with all MoS_2 samples having improved activity against the carbon paper background. The onset potential also shifts positively to -0.2 V consistent with MoS_2 catalysts. The 10× ratio of polymer to MoS_2 shows the greatest reaction current,

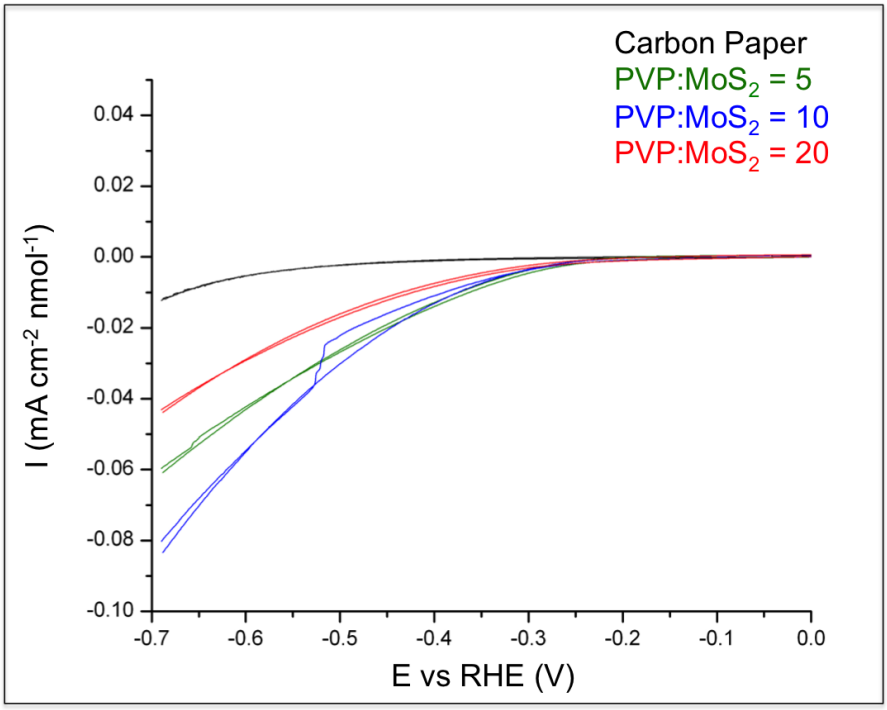

Figure 6.4: Voltammogram of HER activity for solvothermally synthesised nanoparticles with increasing polymer to MoS_2 ratios.

followed by 5×, then 20×. Secondly, the washed samples were tested (Fig 6.5), which all showed improved reaction current. This was expected as the removal of polymer exposes more active sites on the nanoparticles. In this case the 5× ratio of polymer to MoS_2 has the greatest reaction current, followed by 10×, then 20×. Finally, the sulfidised samples were tested (Fig 6.6). These samples were intended to have a transition from amorphous to crystalline structure, however XRD analysis showed the as-made nanoparticles were already crystalline. The reaction current of these samples was greatly reduced, compared to both the as-made and washed samples. This indicates the sulfidation process is damaging the nanoparticles, possibly due to sintering causing a reduction in the amount of active sites.

The optimum polymer loading was chosen by taking the highest activity sample from the washed sample, as the washed samples are the starting point for further nanoparticle modification. This corresponded to the minimum polymer loading of 5x Molar ratio of PVP:MoS_2. Thus all future samples, exploring doping and exfoliation, are prepared by

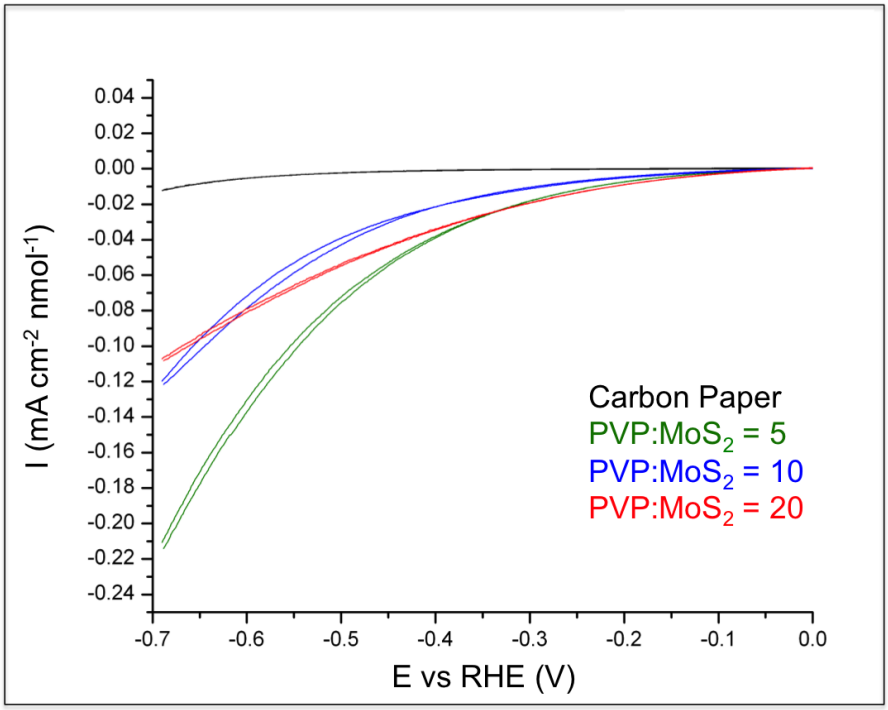

Figure 6.5: Voltammogram of HER activity for solvothermally synthesised nanoparticles with increasing polymer to MoS_2 ratios after washing in ethanol.

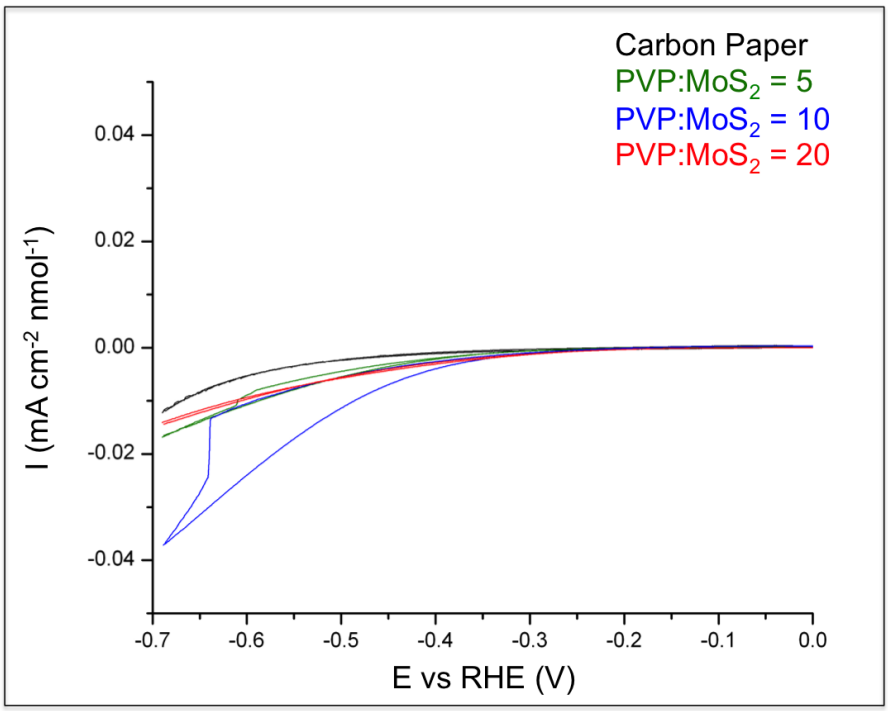

Figure 6.6: Voltammogram of HER activity for solvothermally synthesised nanoparticles with increasing polymer to MoS_2 ratios after washing in ethanol and 1 hour sulfidation in 5% H_2S/Ar at 723°K.

adding 1.4 mg of PVP in the synthesis process. Overall, the different ratios of PVP:MoS_2 and synthesis conditions do not show a consistent trend in HER onset, so more experiments may be needed to precisely reproduce the work of Zong [58].

6.2.2 Cyclic Voltammetry of Doped MoS_2

The washed MoS_2 nanoparticles were prepared as described in Section 3.6.1 with 5× Molar ratio of PVP:MoS_2 and addition of either Cu, Ni or Co dopants. Each dopant is tested at two concentrations and with the addition of low and high temperature sulfidation. The voltammograms of doped samples show both the first and last scan to demonstrate the stability of the nanoparticles. An undoped washed sample is included in all voltammograms for comparison, and has a lower onset potential (-0.15 V) than the doped samples.

The first dopant tested was copper (Fig 6.7), since shown to be active in promoting MoS_2 [221]. The absolute activity of the Cu-doped nanoparticles is comparable to the undoped samples, and after sulfidation both dopant concentrations show higher reaction current. The highest doping concentration produces the most enhancement of reaction current, with a 35% increase over the undoped sample at 50% doping and only 20% at 8% doping. The performance of Cu as a dopant in this system is around 8× worse than literature [221], which has a reaction current of 2 mA/cm^2 at -0.2 V vs SHE vs this sample with 0.25mA/cm^2 at the same potential.

Nickel and cobalt are more traditional MoS_2 dopants [118], frequently used to promote the catalyst for Hydrodesulfurisation reactions. Again nickel (Fig 6.8) and cobalt (Fig 6.9) as-made samples perform poorly against the undoped sample, but after sulfidation both show large improvements in reaction current. The trend of increasing doping producing the best performance also persists. The high temperature sulfidised nickel doped MoS_2 has an average 35% increase in reaction current at 8% doping over an undoped sample, but at 50% doping the current increases by 30% and 125% for low and high temperature sulfidation respectively. Cobalt doping, which is the most common promoter of MoS_2 [119] due to its enhancement of the sulfur-terminated edge sites [117], performs better than

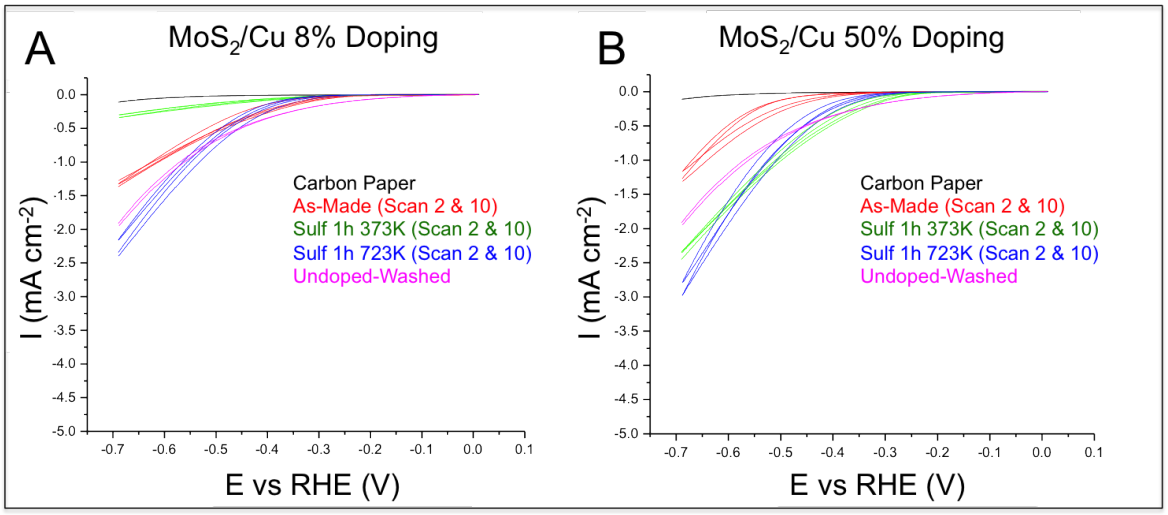

Figure 6.7: Voltammagram of HER activity for 8% and 50% doped MoS_2/Cu nanoparticles, as prepared (Red), after sulfidation at 373°K for 1h (Green), after sulfidation at 723°K for 1h (Blue), and a carbon paper blank (Black) and undoped reference (Pink).

Ni and Cu. The 8% Co-doped MoS_2 produced an enhancement, over undoped samples, of 25% and 70% for low and high temperature sulfidation respectively, while the 50% Co-doped MoS_2 enhanced reaction current by 70% and 135% for low and high temperature sulfidation.

In summary the doped nanoparticles showed enhanced activity in the order Cu < Ni < Co (Fig 6.10), with the 50% doping concentration superior to 8%. The enhancement due to cobalt is in agreement with literature [117] that calculates the hydrogen binding energy of the sulfur $(\bar{1}010)$ edge is reduced by the addition of cobalt leaving it with binding similar to the molybdenum $(10\bar{1}0)$ edge. In all cases the activity for any single doping level increased from the lowest being the doped unsulfidised sample, to the undoped samples, to low temperature sulfidation, then high temperature sulfidation. Occasionally the sulfidised samples had the lowest activity, as in the case of Ni and Cu 8% doping, but this is more likely to indicate problems with the sulfidation process, such as sintering or damage to the carbon electrodes. The poor activity of the as-made samples is because the dopants are merely adsorbates, and as such have no synergistic chemical properties, so the adsorbates only function to block active sites on the MoS_2. The enhancement after the low temperature sulfidation likely occurs as the energy of the sulfidation process allows

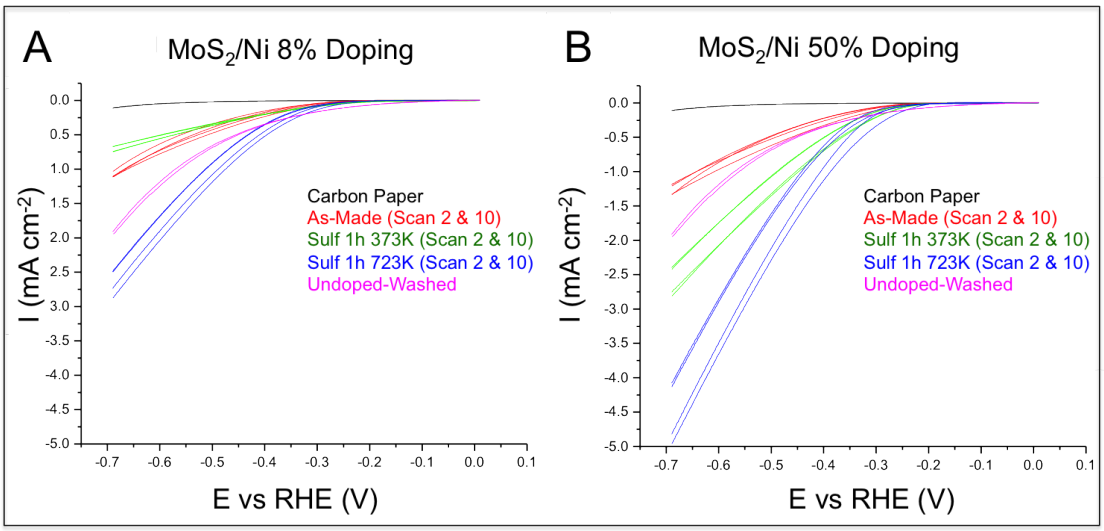

Figure 6.8: Voltammagram of HER activity for 8% and 50% doped MoS_2/Ni nanoparticles, as prepared (Red), after sulfidation at 373°K for 1h (Green), after sulfidation at 723°K for 1h (Blue), and a carbon paper blank (Black) and undoped reference (Pink).

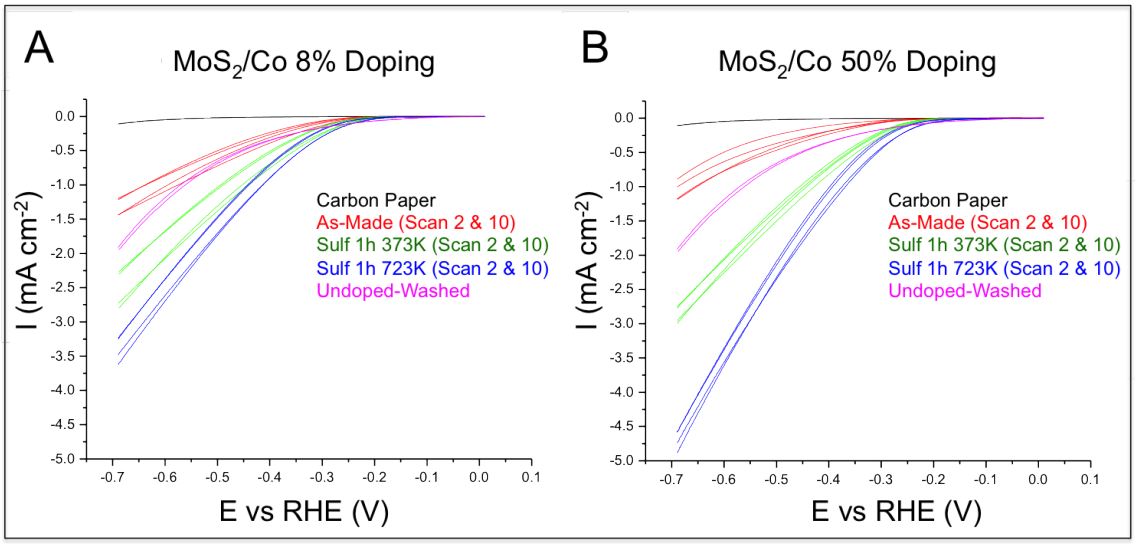

Figure 6.9: Voltammagram of HER activity for 8% and 50% doped MoS_2/Co nanoparticles, as prepared (Red), after sulfidation at 373°K for 1h (Green), after sulfidation at 723°K for 1h (Blue), and a carbon paper blank (Black) and undoped reference (Pink).

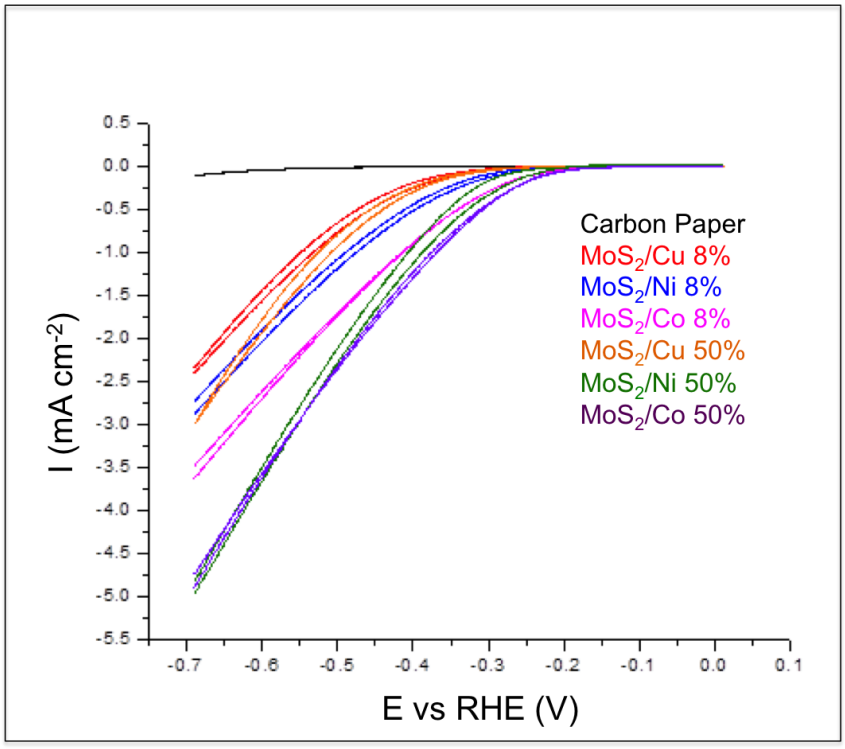

Figure 6.10: Summary Voltammagram of HER activity for doped MoS_2 sulfidised at 723°K for 1 hour

the copper ions to enter the MoS_2 lattice, with the high temperature sulfidation producing crystalline edge sites to further improve activity.

6.2.3 Cyclic Voltammetry of Exfoliated MoS_2

Lithium intercalation was used to separate the 3D nanoparticles into their constituent layers in order to get better conductivity to the active sites and higher utilisation of catalyst material. At worst, the same activity as the nanoparticles would be expected given that the number of edge sites should be the same. In fact, the results showed poor activity for this nanoplatelet synthesis compared to the original nanoparticles. This behaviour can not be explained based on the original model, thus something in the intercalation process must damage the nanoparticles. Due to the complexity of the lithiation process and the likelihood of contamination, this step was abandoned at a preliminary stage.

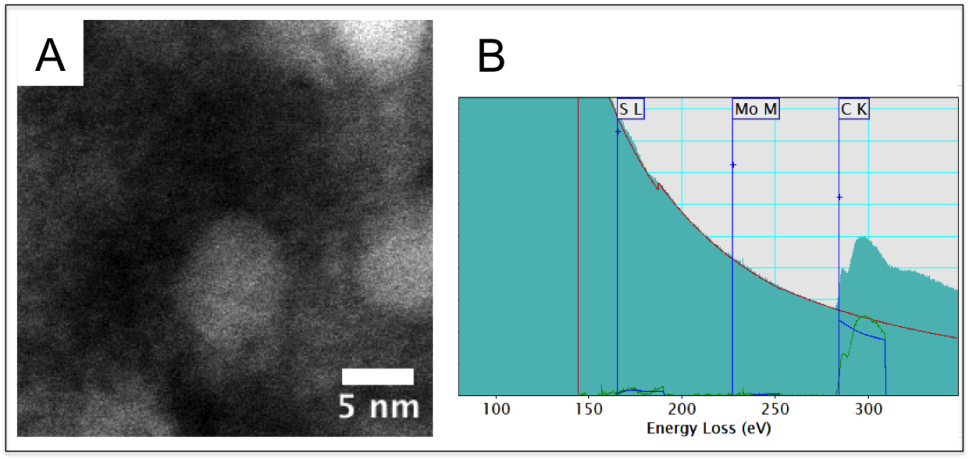

Figure 6.11: (A) As-synthesised MoS_2 in a carbon matrix. (B) STEM-EELS shows weak Mo and S peaks due to thick carbon background

6.2.4 Nanostructure of Chemically Prepared MoS_2

Three samples were prepared for aberration-corrected STEM analysis at NPRL. The first sample as-synthesised, the second after lithium exfoliation and the third following H_2S sulfidation at 723°K for 1 hour. The micrographs generally show bright features in dark field, indicating a metal component such as Mo, and sulfur is evident from EELS analysis (Fig 6.11). The bright field shows fringes indicative of crystalline material with lattice parameters consistent with MoS_2. The sulfidised sample was difficult to image due to heavy contamination, and surprisingly showed no sulfur peak in the EELS spectra, so it will not be discussed further. The first two samples produced some useful information. In general, the size distribution is larger than the 2 nm initial size, determined by XRD, suggesting that the samples have suffered from ripening processes over time (Fig 6.12A). Counter-intuitively, The exfoliated sample also contains some areas of nanoparticles that retain the original size (Fig 6.12B), this may be an unintentional passivation caused by the lithium intercalation process. This encapsulation would explain the anomalously low activity of the exfoliated MoS_2 nanoparticles for HER.

Large agglomerates on the exfoliated samples show usual MoS_2 structural characteristics (Fig 6.13). Though these structural characteristics confirm the success of the initial synthesis to produce lamellar MoS_2, the existence of layers and large structures indicates

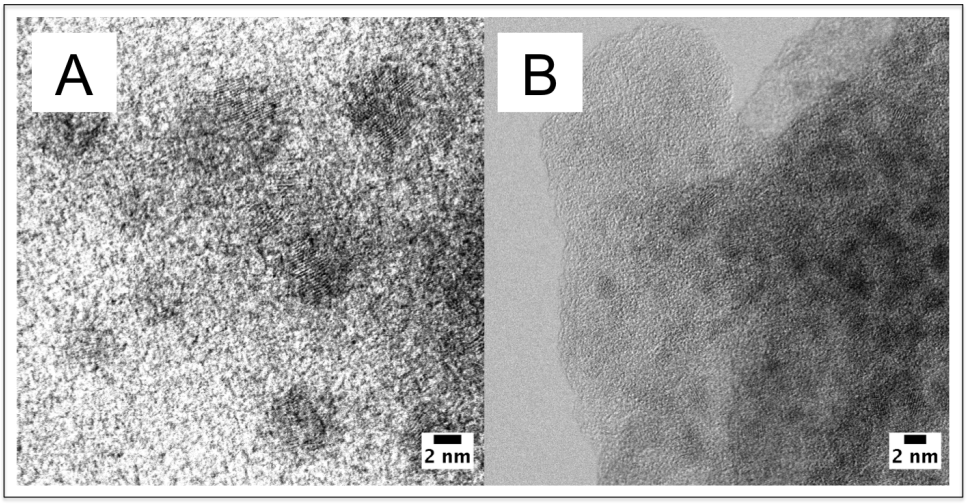

Figure 6.12: (A) As-synthesised MoS_2 show large size distribution of 2-8 nm. (B) Region of exfoliated sample with smaller size distribution, mean value of 2 nm

the exfoliation process has not worked for all nanoparticles.

These micrographs demonstrate the problems associated with chemical synthesis. Although the catalysts showed respectable activity, correlating that with any entity is difficult, due to the wide variation in structure and contamination from synthesis elements. The hydrocarbon contamination is also a problem for achieving high resolution STEM. The remaining polymer may also act as a barrier to active sites, thus confusing the analysis as to how much MoS_2 is exposed for reactions, while the aggregation precludes any analysis of size-dependent effects. In general the size-distribution was shown to increase from XRD and initial TEM to later STEM imaging. This instability over time after exposure to atmosphere mirrors the effects seen in clusters prepared by cluster beam. The more severe agglomeration seen in the chemical samples, compared to STEM in Chapter 5, is likely due to the higher initial concentration of nanoparticles.

6.3 Hydrogen Evolution by MoS_2/HOPG

The clusters produced by the cluster beam method were then tested for comparison with the chemically synthesised nanoparticles. Sputtered HOPG substrates decorated with MoS_2 clusters (Section 4.3), were inserted into a custom-made electrochemical cell

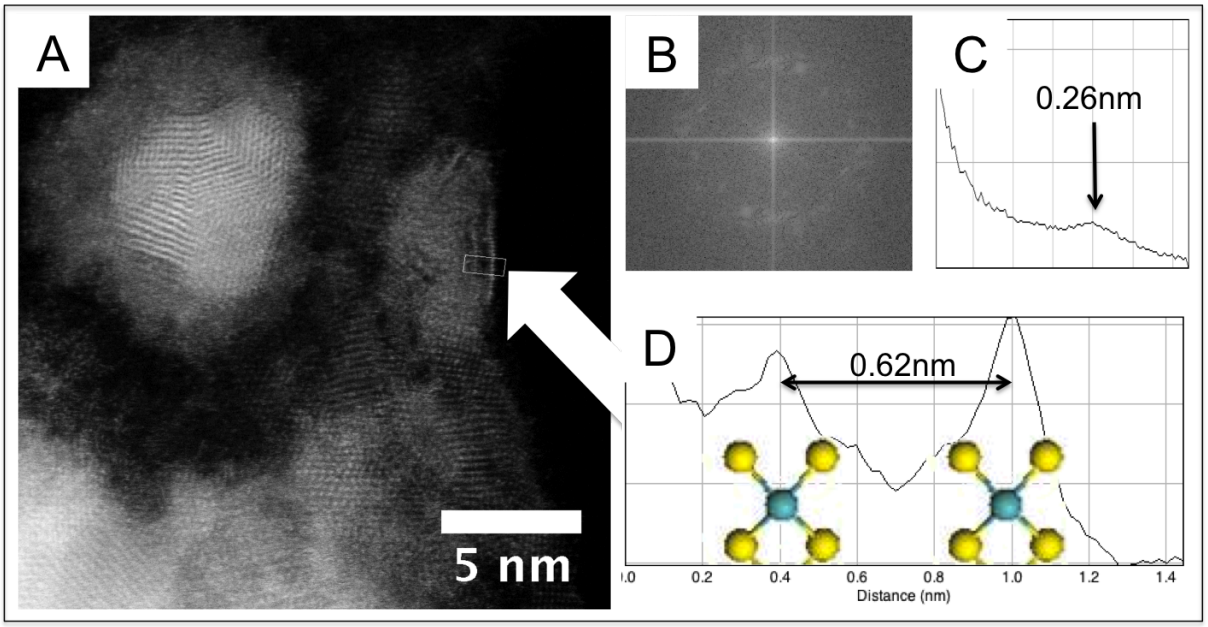

Figure 6.13: (A) STEM micrograph of exfoliated samples show usual MoS_2 structural characteristics, such as hexagonal basal plane with 0.26 nm Mo-Mo spacing, measured by (C) radial profile of a (B) whole micrograph FFT. (D) Line profile showing 002 van der Waals gap.

(Section 3.5.5) to measure their catalytic properties. Although this was a more familiar substrate for surface science, it was difficult to make it compatible with wet chemistry. The HOPG was placed between two tubes with inert o-rings and clamped in place. Electrolyte was then held in place over the section masked by the upper o-ring. The small size of the substrate and its fragile lamellar nature meant the force of clamping to produce a water-tight seal often deformed the HOPG. Electrical connection to HOPG also involved a high series resistance through the van der Waals planes. Due to these experimental difficulties, the system was eventually replaced with a more common electrode design. The HOPG system, however, has the benefit of compatibility with scanning probe microscopy in order to perform simple tests of pre- and post-reaction dispersion.

6.3.1 Cyclic Voltammetry of MoS_2/HOPG

The HOPG supported clusters were measured by 3-electrode setup in a custom Teflon clamp cell described in Section 3.5.5. The cell was degassed for 30 minutes prior to

Sample	Coverage (% ML)	Deposited	Measured
Pt	100	Same day cleaned	7/10/11
$(MoS_2)_{350}$	2.8	30/06/11	17/10/11
$(MoS_2)_{500}$	3.0	22/06/11	17/10/11
$(MoS_2)_{600}$	5.7	30/06/11	17/10/11
$(MoS_2)_{200}$	55.9	20/06/11	18/10/11
$(MoS_2)_{650}$	80.0	7/7/11	18/10/11
HOPG	100	Same day cleaved	7/10/11

Figure 6.14: MoS_2 Samples used in HOPG experiments

experimentation, and bubbled with H_2 throughout. Potential is measured with reference to an AgCl reference electrode at pH 1.19, therefore potential measurements are -0.267 V vs RHE. The same samples used for scanning probe measurements (Section 4.3) were tested for HER activity, in order to obtain pre- and post-reaction surface analysis. The MoS_2 samples consist of three sub monolayer coverages with distinct clusters, and two approximately monolayer coverages (Fig 6.14). Platinum foil, cleaned by flame annealing, and freshly cleaved HOPG were used as reference samples. These experiments were conducted before XPS measurements were taken, so the extent of oxidation over time was unknown. The age of these samples suggests that the outer layers will be heavily oxidised, which is a good test of the assumption that the outer MoO_3 layers will dissolve to expose MoS_2 edges.

The HER onset for low loading ($\sim$10% coverage) and high loading ($\sim$100% coverage) of clusters was similar, with all samples showing onsets closer to the background HOPG than the reference Pt sample (Fig 6.15). No size dependent activity is seen for the samples with low loading (Fig 6.16), the corrected onset potentials (AgCl to RHE) are similar to literature values of -0.2 V vs RHE [18, 93], with a corresponding decrease due to the oxidation of active sites on these clusters. The magnitude of the reaction current increases with increasing cluster size and coverage. These effects are expected due to the increased mass of catalyst for higher coverages and larger sizes. The activity for low-loading samples is approximately the same after normalising the MoS_2 voltammograms for catalyst loading (Fig 6.17). A reduction peak is also visible on the $(MoS_2)_{350}$ curve. This peak is similar

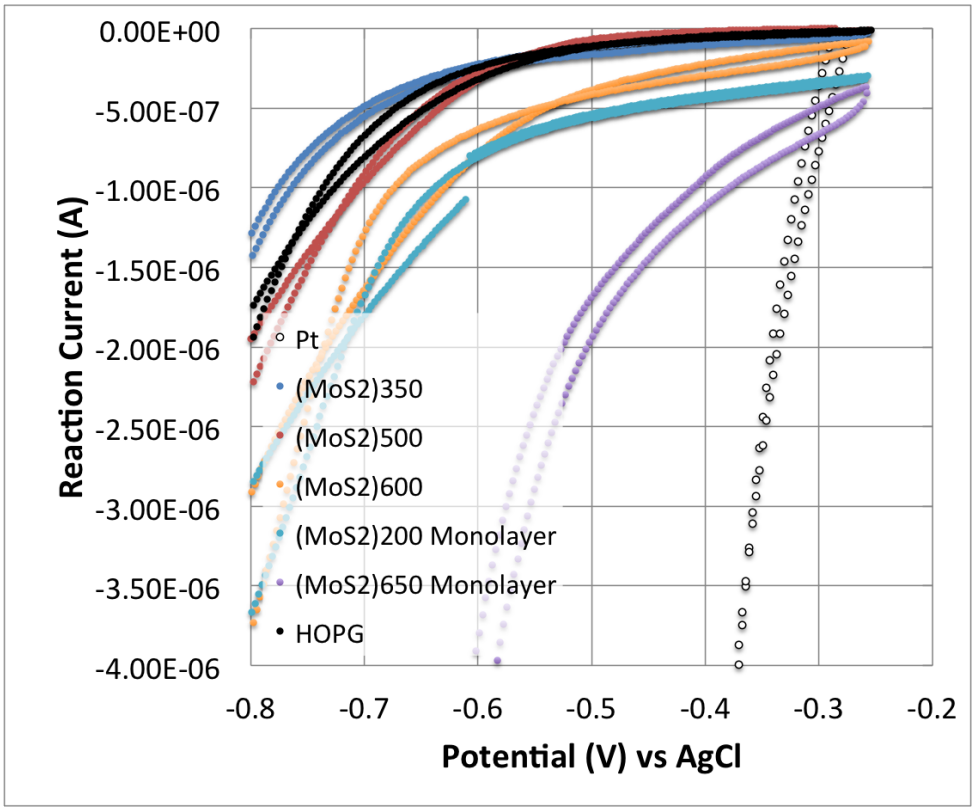

Figure 6.15: Voltammogram of HER activity for the first scan of submonolayer and monolayer coverages of MoS_2 on sputtered HOPG.

to the peaks generated on the first scan of subsequent MoS_2 samples on glassy carbon electrodes. Unfortunately the same peak can not be found on the $(MoS_2)_{500}$ and $(MoS_2)_{600}$ samples, so it is difficult to attribute to the clusters. A more likely explanation is that this is either a contaminant being reduced, which is likely on the first scan of an electrode exposed to atmosphere, or the dissolution of the soluble MoO_3 component [207, 76]. Dissolution could be confirmed by performing chromatography on the electrolyte after testing to find Mo or sulfate decomposition products. It is interesting to note that after normalisation the monolayer samples are far less active than the sub-monolayer samples. This indicates that these samples are sufficiently densely packed that catalyst material is blocked from the electrolyte.

The use of a planar support necessitates lower catalyst loading than most chemical syntheses reported in the literature. For example, recent experiments with MoS_3 nanoparticles on a 3 mm GC electrode had a loading of 565 ng [206], compared to 1-10 ng for

	Onset (V vs AgCl)	Onset (V vs RHE)
$(MoS_2)_{600}$	-0.55	-0.283
$(MoS_2)_{500}$	-0.52	-0.253
$(MoS_2)_{350}$	-0.60	-0.333

Figure 6.16: Onset potential for HER (from Fig 6.15) for samples of MoS_2/HOPG with sub-monolayer loading

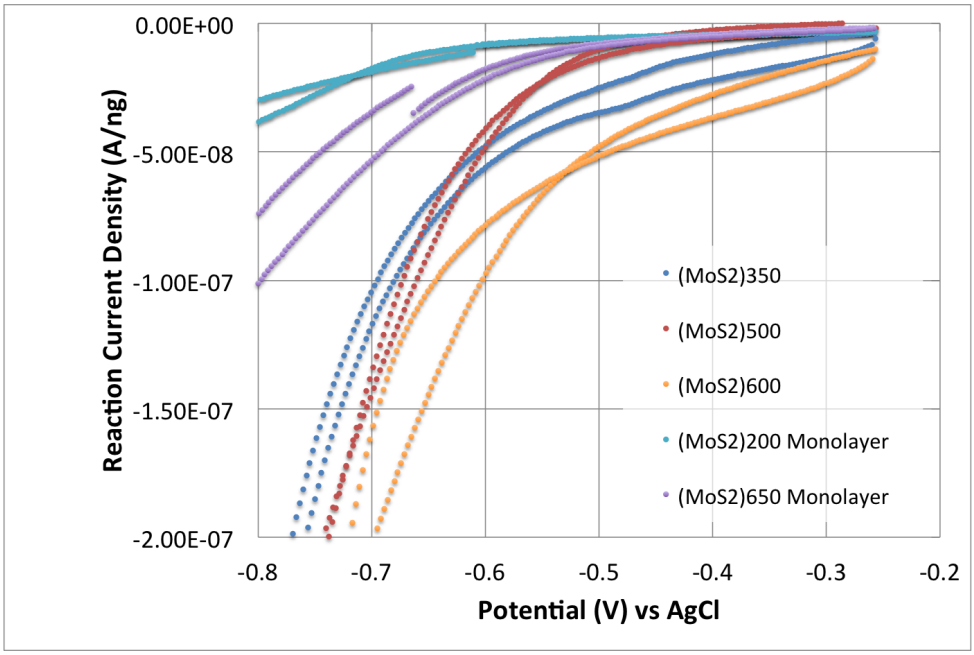

Figure 6.17: Voltammogram of HER activity for submonolayer and monolayer coverages of MoS_2 on sputtered HOPG, normalised to mass of MoS_2 deposited. Potential is measured with reference to AgCl electrode at pH 1.19, therefore +0.267 V vs RHE.

sub-monolayer coverages in this study. High coverages, such as 565 ng, would correspond to multilayer coating in a planar system. So simply increasing loading would make it difficult to attribute reactivity to particular nanoscale features, and also result in different diffusion regimes. Furthermore, the results from the normalised activity for sub-monolayers compared to monolayers on HOPG (Fig 6.17), showed the monolayers were less active due to unused material, further confusing analysis.

Direct comparison can be made if sufficient experimental details have been provided to normalise for the differences in loading. Recent work with a model catalyst system of MoS_2 platelets dispersed on graphene have shown the lowest Tafel slope recorded, 41 mV/dec [24]. This work will function as a comparison for the HER activity of clusters in this chapter (Fig 6.18). The geometric area and experimental setup are similar, with both using carbon as the background and a strong acid as electrolyte. The literature sample uses a glassy carbon electrode, similar to experiments in Section 6.4, but the catalysts themselves are dispersed on graphene sheets, allowing a much higher coverage than by planar deposition. This results in a catalyst loading for chemical synthesis that is around 3 orders of magnitude greater than the MoS_2/HOPG samples. Clearly normalising by geometric area alone does not provide a fair comparison between these catalysts, so catalyst mass is used as an additional balance. After normalisation by mass, the performance is slightly lower than the literature value (Sections 6.3.2 and 6.3.3). The age-related oxidation will have decreased the mass of active catalyst, so this is to be expected. The most promising result is that despite the shell of oxide, these catalysts have performed similarly to pristine MoS_2, indicating that the MoO_3 layer is not permanently passivating.

The electrochemistry on HOPG forms a preliminary investigation into the HER activity of small quantities of supported clusters. The difficulties discussed in the experimental procedure make this an unfavourable method for further testing, however total mass-dependent activity has been clearly demonstrated, which paves the way for further testing in a more robust system.

	MoS_2/Graphene [24]	$(MoS_2)_{600}$/HOPG	$(MoS_2)_{650}$/HOPG
Electrolyte	0.5M H_2SO_4	0.1M $HClO_4$	0.1M $HClO_4$
Geometric Area (cm^2)	0.07	0.13	0.13
Catalyst Mass (μg)	20	0.0081	0.1195
Loading (mg/cm^2)	285.7E-3	62.3E-6	919.2E-6
$J_{-0.2VvsRHE}$ (mA/cm^2)	-30	-1.92E-3	-9.62E-3
$J_{-0.2VvsRHE}$ ($mA/cm^2/\mu g$)	-1.5	-0.3	-0.1

Figure 6.18: The most active MoS_2 HER catalyst in literature [24] is compared to MoS_2/HOPG samples.

6.3.2 Post-Reaction Atomic Force Microscopy

The use of HOPG for these preliminary experiments allows comparison of pre- and post-reaction topography by scanning probe techniques. After performing the HER reaction, the $(MoS_2)_{600}$ sample was transferred to a bench top Atomic Force Microscope (AFM), as used in Section 4.3.2. Cluster features remain after reaction (Fig 6.19), and are of a slightly greater height to images taken before reaction (Section 4.3.2), 4-6 nm compared to 3-4 nm.

These height measurements would correspond to 6-10 layers of MoS_2, which does not match the results of STEM imaging. The coverage of Ar defects on these samples is double that of the clusters, to provide ample pinning sites, however this might not be sufficient if for example the Ar beam was concentrated on a different area of the substrate to the cluster beam. So the increased height of these samples could be due to aggregation of clusters. The most obvious difference after reaction is that the coverage of clusters has drastically reduced, which is further evidence for ripening during reaction conditions. The morphology of the post-reaction clusters, is a bright peak surrounded by a wide flat periphery. These flat halos appear to wet the surface like a liquid, so it is tempting to label it as electrolyte residue. However, the same halos were seen before reaction (Section 4.3.2), which were reasoned to be the decomposition product, H_2SO_4. The greater extent of the

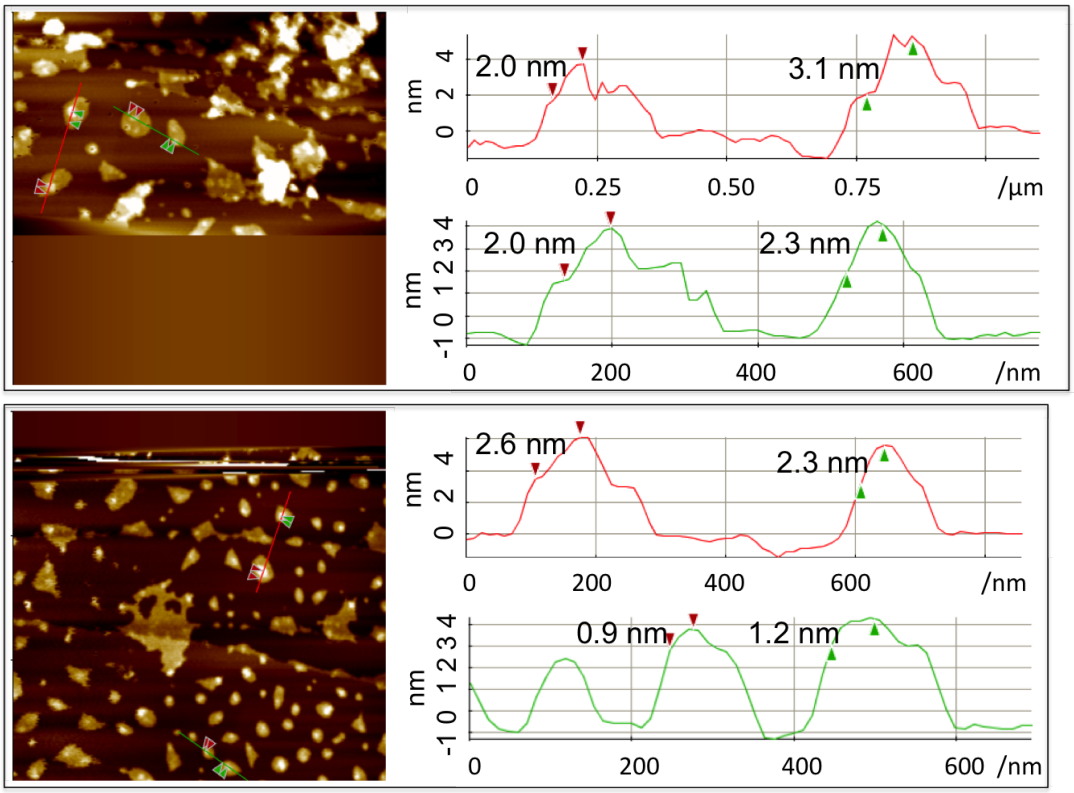

Figure 6.19: 3μm × 3μm non-contact AFM images of $(MoS_2)_{600}$ clusters on Argon sputtered HOPG after reaction conditions show low coverage of large islands 4-6 nm in height. The heights of the bright central spots above the wider halo of material are shown in the line profiles.

halo after reaction could be due to the MoO_3 dissolution in aqueous electrolyte, this would be a positive effect for exposing more catalytically active sites.

These uncertainties could be investigated by high resolution scanning probe analysis, but as discussed in Section 4.3, the increased tip interactions at high resolution drags the clusters. This could be improved by repeating the experiments on a substrate that has stronger binding with the MoS_2, such as the original platelet STM work that used Au(111) [69, 18].

6.3.3 Post-Reaction Scanning Transmission Electron Microscopy

The scanning probe post-reaction studies were limited to low resolution imaging, capable of discerning large scale changes but raising further questions about the structure and composition of individual clusters. In order to achieve higher resolution, $(MoS_2)_{600}$ clusters

were deposited on a standard Cu/holey carbon grid at the same coverage as the HOPG substrates. The grid was imaged before reaction conditions, then subsequently placed on a HOPG wafer and exposed to reaction conditions for 40 minutes. The subsequent imaging shows a broader size distribution after reaction (Fig 6.20), which is attributed to dissolution and ripening in the electrolyte. The density of nanoparticles is much higher than the original coverage, which indicates that new nanoparticles have been created. This is likely to come from the Cu grid itself, similar to experiments with annealing on these grids (Section 5.4.6), although the mechanism should not be Cu dissolution as this has been shown to occur outside the potential window of the HER experiments (+0.2 V vs RHE)[222].

The copper grids were removed as a possible source of contamination by repeating the experiment on a more inert Mo grid with exfoliated HOPG as a support. The pre-reaction STEM micrographs (Fig 6.21) show the $(MoS_2)_{1000}$ clusters are evenly dispersed across the HOPG. High-resolution imaging of another area (Fig 6.22) shows the clusters have the usual MoS_2 crystallinity. The coverage is higher than expected, compared to usual STEM micrographs on amorphous carbon substrates, due to the weaker binding to the HOPG substrate. This results in some diffusion, but the clusters remain distinct to their neighbours. The composition of the clusters before reaction is measured by taking point EELS spectra and spectral imaging of a whole cluster (Fig 6.23). The point spectrum matches those usually seen on MoS_2 clusters (Section 5.4.4), and the spectral images show the distribution of Mo and S throughout the cluster is uniform, which can also be inferred from the existence of the MoS_2 crystallinity and homogeneous HAADF intensity.

After reaction the same area on the grid from Fig 6.21 was located for comparison (Fig 6.24). All of the previously imaged clusters in the region are absent, though the area is heavily contaminated, so they may be obscured rather than removed. The low resolution micrographs show some large nanoparticles around 10 nm in size, which appear bright in the HAADF micrograph indicating they are Mo-rich structures. Such a set of nanoparticles was analysed by EELS (Fig 6.25), and shows that the bright nanoparticle visible in

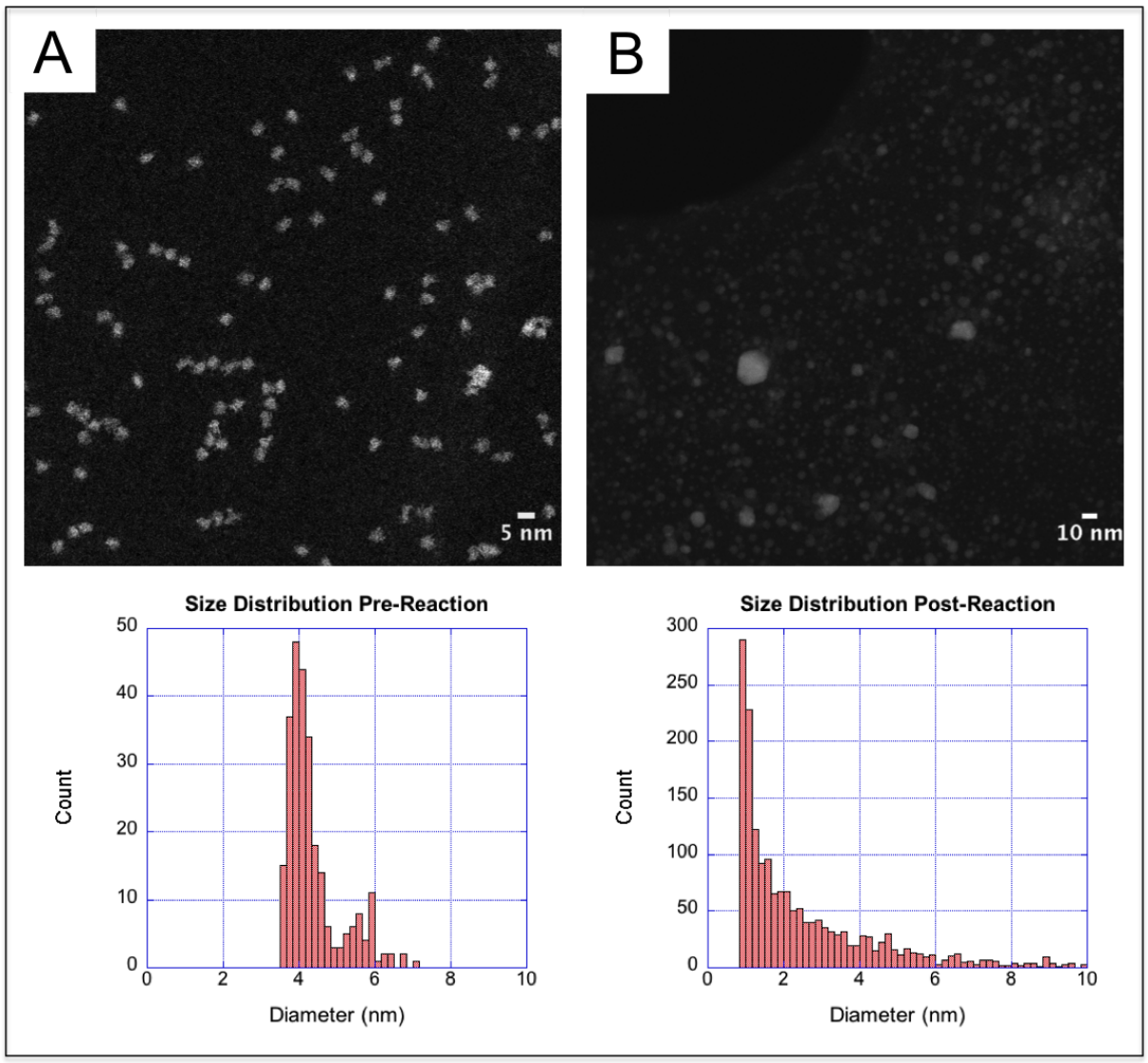

Figure 6.20: (A) $(MoS_2)_{600}$ on Cu TEM grid before reaction. (B) The same sample after exposure to reaction conditions. Histograms generated by threshold routine.

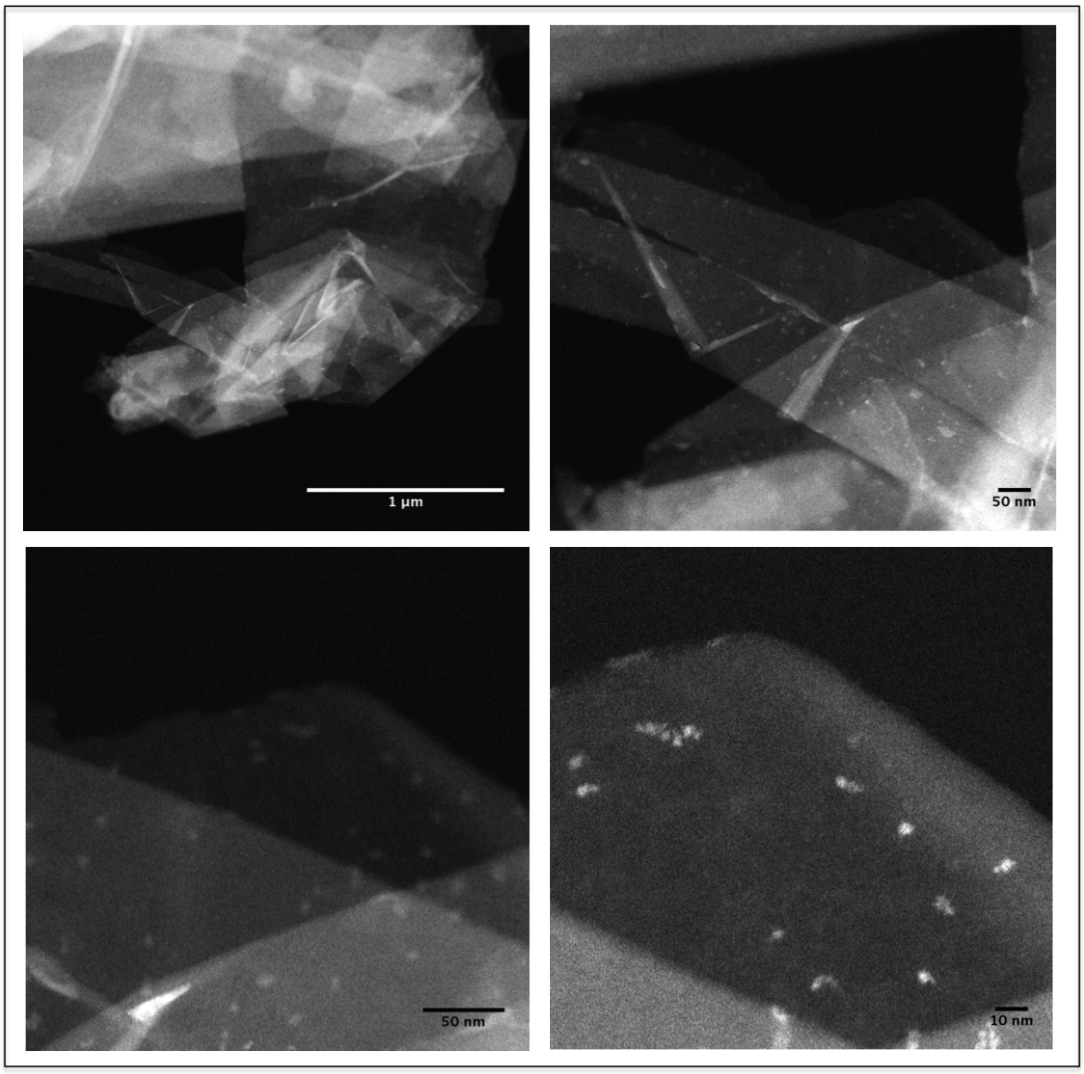

Figure 6.21: Increasing magnification STEM micrograph set shows clusters of $(MoS_2)_{1000}$ deposited on few-layer graphene. Clusters are evenly dispersed over the HOPG surface, with some minor aggregation.

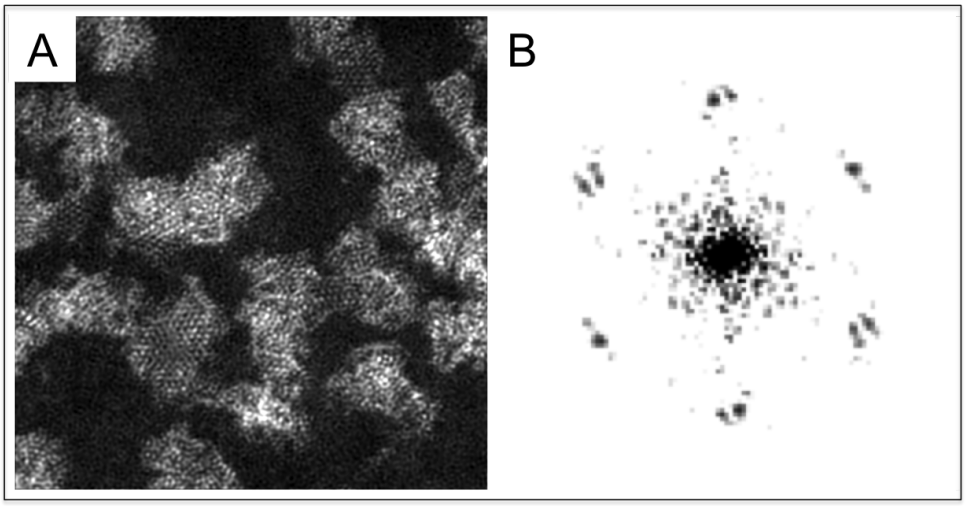

Figure 6.22: (A) Atomic resolution STEM micrograph (19.24 nm × 19.24 nm) of $(MoS_2)_{1000}$ with dense coverage. (B) FFT of these clusters shows the hexagonal MoS_2 structure.

low resolution micrographs is an agglomerate of Mo and S. The adjacent nanoparticle is composed mainly of sulfur, confirming the onset of ripening processes during reactions. The structure of these nanoparticles has changed completely from platelets to hemispheres due to minimisation of surface contact with electrolyte, which correlates with the electrolyte-cluster interaction dominating the cluster-surface interaction. The pinning of clusters on glassy carbon (GC) is expected to be stronger due to the abundance of defects, so such extreme changes to the nanoparticles may be avoided by using this type of electrode over simple HOPG substrates.

6.4 Hydrogen Evolution by MoS_2/GC

6.4.1 MoS_2/GC Deposition

The experiments on HOPG demonstrated some catalysis for the Hydrogen Evolution Reaction (HER) with mass dependence. Unfortunately the experimental procedures for using small wafers of HOPG for wet chemistry caused difficulties (Section 3.5.5). So the deposition stage was altered to accommodate a substrate more suited to electrochemistry. Common substrates take the form of an inert conducting disk, these can be made from

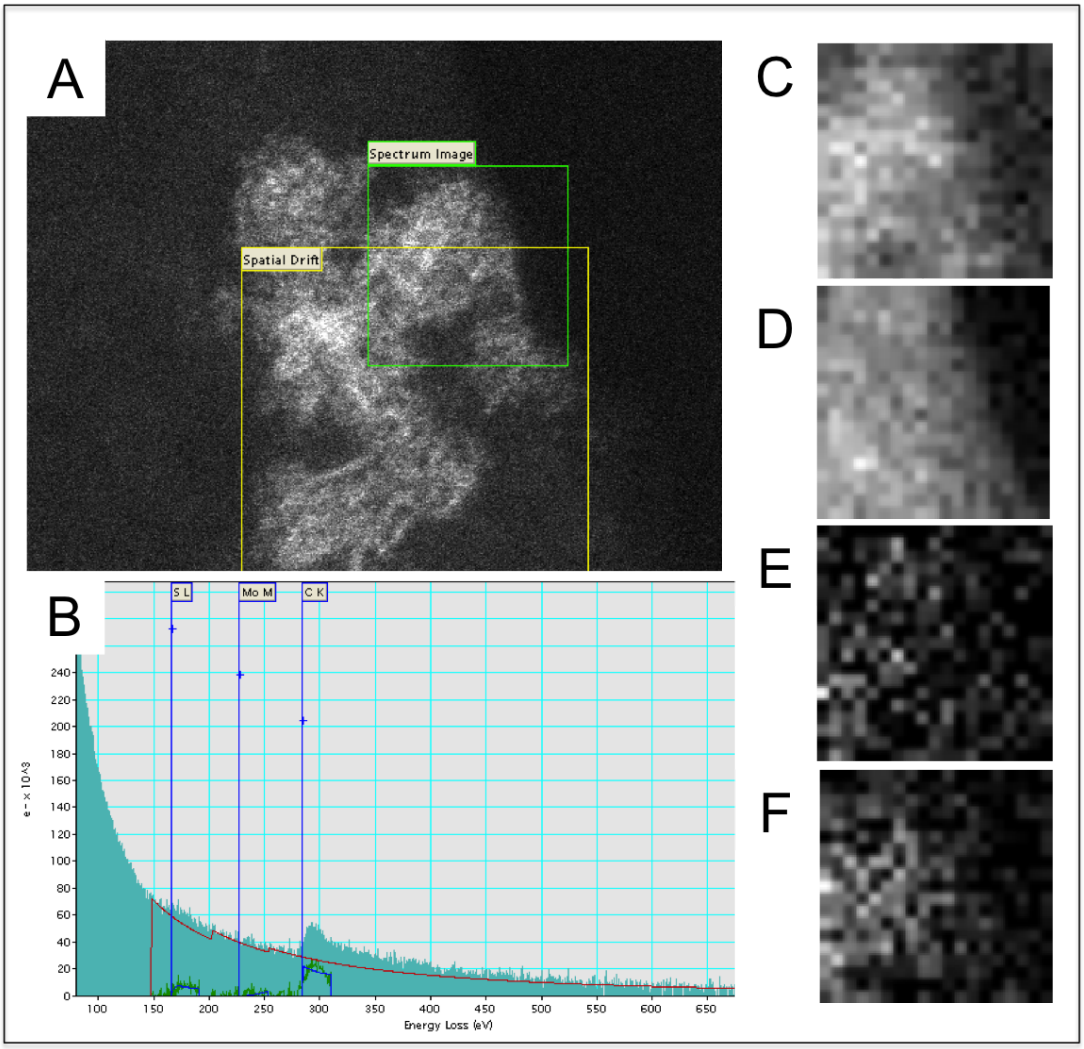

Figure 6.23: (A) $(MoS_2)_{1000}$ cluster on few layer graphene. (B) Point EELS spectrum from green region of (A) shows usual Mo and S signal. (C) Spatial EELS map of green region of (A) mapping total EELS signal. (D) Intensity of carbon core-loss peak at 284 eV. (E) Intensity of Mo core-loss peak at 226 eV. (F) Intensity of S core-loss peak at 168 eV.

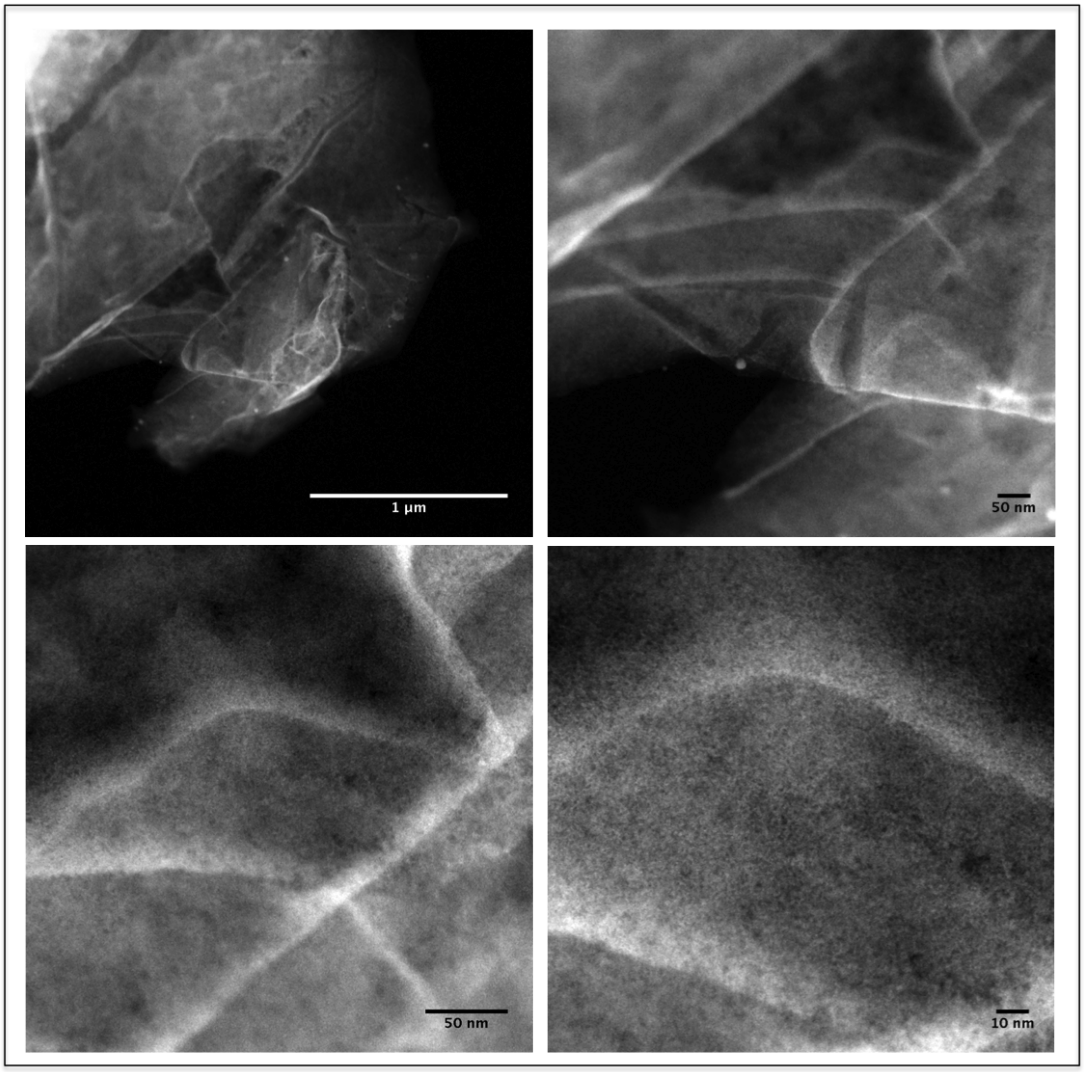

Figure 6.24: Increasing magnification STEM micrograph set shows the same region as Fig 6.21 after cyclic voltammetry in 0.1M $HClO_4$. No clusters are evident.

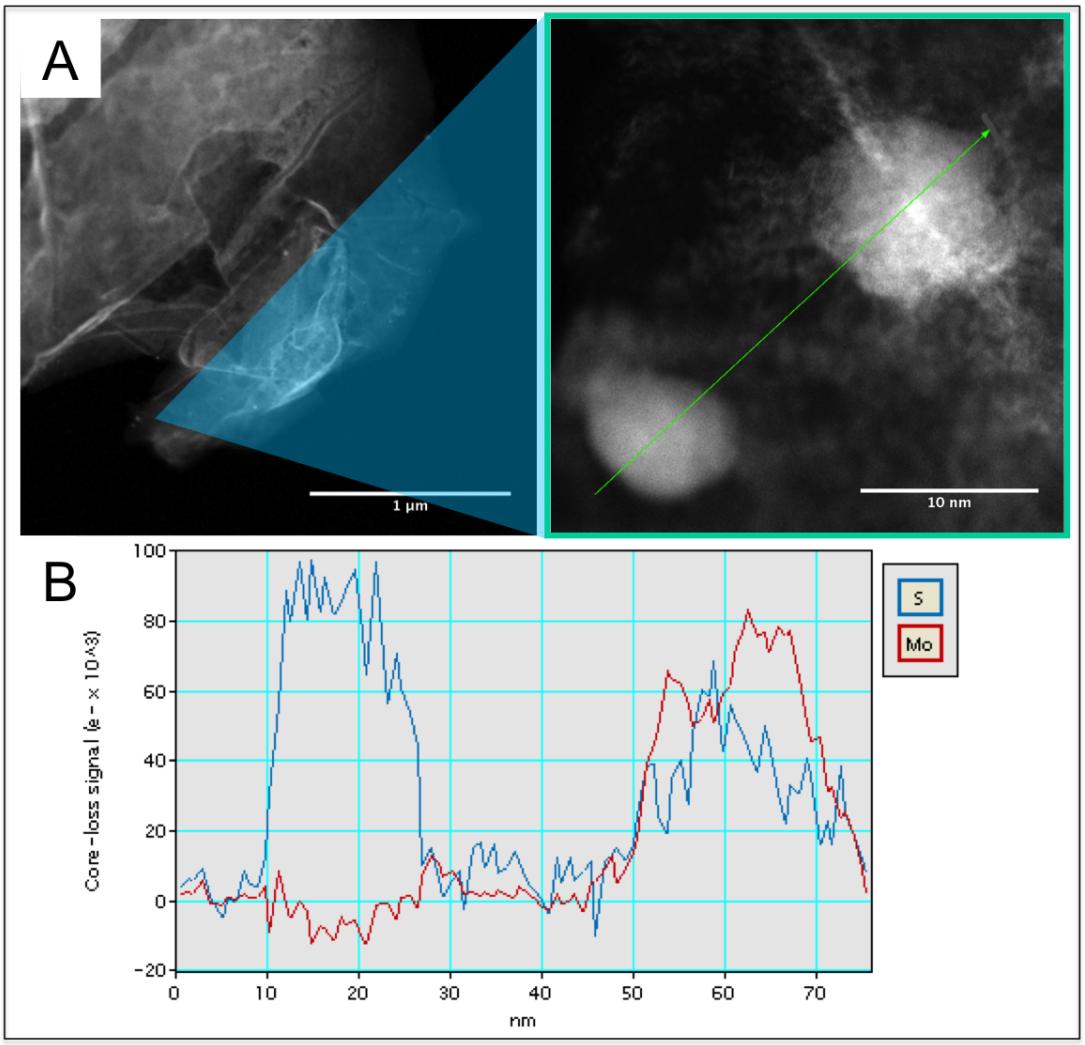

Figure 6.25: (A) Cluster material found on the substrate, structures do not display MoS_2 crystallinity. (B) Line spectrum of Mo and S core loss EELS signals

many materials, the simplest being a ceramic form of carbon known as glassy carbon (GC). The exact structure of this material is uncertain, but some studies suggest it is a mixture of complete and incomplete fullerenes, with the low reactivity due to fully closed particles and tight-packing of the fragments [165].

The disk is usually mounted permanently in a Teflon sleeve so only the face of the disk is exposed to reactions, this face is polished to keep surface area uniform. The polishing process is graded, beginning with a 1 micron alumina-suspension, to 0.3 micron and finally to 0.05 micron. Each polishing step lasts 60 seconds and is followed by rinsing in UHQ water. This ensures uniformity of background for all samples. At the nanoscale the surface is expected to be rich in defects and so nanoparticles are immobilised without need for Ar sputtering as with HOPG. These polished disks are prepared in the clean electrochemical area of the Fuel Cell lab, and transported across to the cluster beam apparatus for deposition. The full Teflon-disk assembly would not fit in the deposition sample stage, so instead custom GC disks (5 mm diameter $\times$ 3 mm height, HTW-Germany) were purchased, which would then be inserted into Teflon sleeves after deposition. The sample holder fixes the disk in place and exposes a 4 mm diameter circular area for deposition (Fig 6.26).

The cluster beam is rastered over the surface to ensure an even cluster coverage, usually to a level of 6000 pAs, corresponding to 1911 clusters per μm^2. After deposition the clusters are stored in vacuum until testing to reduce the level of oxidation, the clusters are subjected to the order of hours of atmospheric exposure due to transport and subsequent waits between testing. Before each test the cluster decorated GC disk is inserted into the Teflon sleeve by applying pressure to the rim of the GC disk. This final step can introduce contaminants on to the tested surface of the disk, so clean implements are used. In some cases the pressure can fracture the weaker edges of the disks, these burred edges will increase the GC surface area, giving a higher background activity, so must be discounted from experiments and repolished to restore a circular surface area. This is avoided by using plastic to push the electrodes into the Teflon, however future electrode setups should

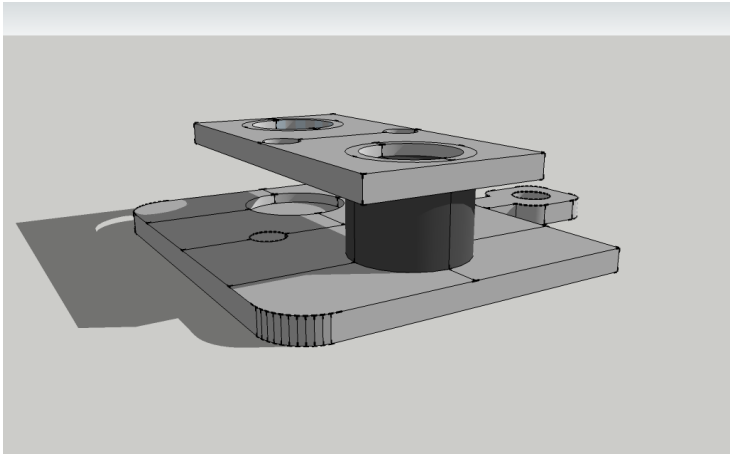

Figure 6.26: Glassy carbon (GC) Sample Holder, designed by Martin Cuddy and machined by the School of Physics and Astronomy workshop. Two 5 mm diameter × 3 mm height GC cylinders are held in place by a stainless steel retainer, with a 4 mm diameter exposed face for deposition.

use a retaining system similar to the GC sample holder for better reproducibility.

A set of 5 MoS_2 cluster sizes was deposited at 6000 pAs onto glassy carbon disks, with a repeat deposition of each. The deposition and testing took place over two weeks but the exposure of each sample to atmosphere was minimised by performing the deposition the day before the testing. The sizes tested were $(MoS_2)_x$ (x = 150,350,500,650,1000) to cover the range of sizes characterised by microscopy. At the smallest size there are less layers, as the clusters grow they reach a limiting layer height and continue to grow laterally, and at the largest sizes the growth mode tends to cluster coalescence (Section 5.6.4). The electrochemical activity can thus be correlated to these structural features.

The tests involve a series of electrochemical measurements to discern various characteristics. Firstly a cyclic voltammogram of 10 cycles from 0 V to -0.7 V shows HER behaviour, such as the overpotential required, the absolute amount of hydrogen produced and degradation of the catalyst material. The second scan is an Electrochemical Impedance Spectrograph (EIS), which can be used to model the charge transfer through the catalyst, but its only use in this study is to provide a measure of the system resistance for current correction due to Ohmic losses. The final scan is a scan from 0 V to -0.7 V then up to +1.2 V and repeated, this scan to oxidising potentials should produce a peak where first

Sample	Size	Deposited	Measured
11-12 GC	Glassy carbon	N/A	12/11/12
1-23 150-1	$(MoS_2)_{150}$	23/01/13	23/01/13
1-23 150-2	$(MoS_2)_{150}$	23/01/13	23/01/13
2-13 350-1	$(MoS_2)_{350}$	06/02/13	13/02/13
12-3 350-1	$(MoS_2)_{350}$	26/11/12	03/12/12
12-3 350-2	$(MoS_2)_{350}$	26/11/12	03/12/12
2-13 500-1	$(MoS_2)_{500}$	06/02/13	13/02/13
2-13 500-2	$(MoS_2)_{500}$	06/02/13	13/02/13
2-13 650-1	$(MoS_2)_{650}$	06/02/13	13/02/13
12-3 650-3	$(MoS_2)_{650}$	26/11/12	03/12/12
12-3 650-4	$(MoS_2)_{650}$	26/11/12	03/12/12
1-23 1000-1	$(MoS_2)_{1000}$	23/01/13	23/01/13
1-23 1000-2	$(MoS_2)_{1000}$	23/01/13	23/01/13

Figure 6.27: MoS_2 Samples used in 0.1M $HClO_4$ experiments

the reactive MoS_2 edges are oxidised, followed by a larger oxidation peak as the basal plane is oxidised at higher potential. The return scan to reducing potentials should have a corresponding reduction in activity due to the irreversible damage to the MoS_2 active sites.

6.4.2 Hydrogen Evolution in 0.1M Perchloric Acid

The use of a strong acid to provide a proton-rich electrolyte is common in the literature for HER [103, 223, 18]. The cluster-decorated GC disks were attached to a rotating disk drive, and inserted into the cell. The rotator can be used to investigate diffusion of reactive species, but in this case is simply used to remove hydrogen bubbles periodically from the electrode surface. The cyclic voltammetry for the HER in 0.1M $HClO_4$ shows significant differences between repeats and highlights the value of repeat samples for this process (Fig 6.27). The curves are colour coded for each size of cluster, and the 10th scan of each cycle is taken to allow time for the system to stabilise.

The onset potential of all MoS_2 samples are between -0.2 V and -0.4 V, which is similar to the preliminary results on HOPG (Fig 6.28A). It is clear that the repeat measurements of the same cluster sizes do not match, this could be due to errors such as the exact amount

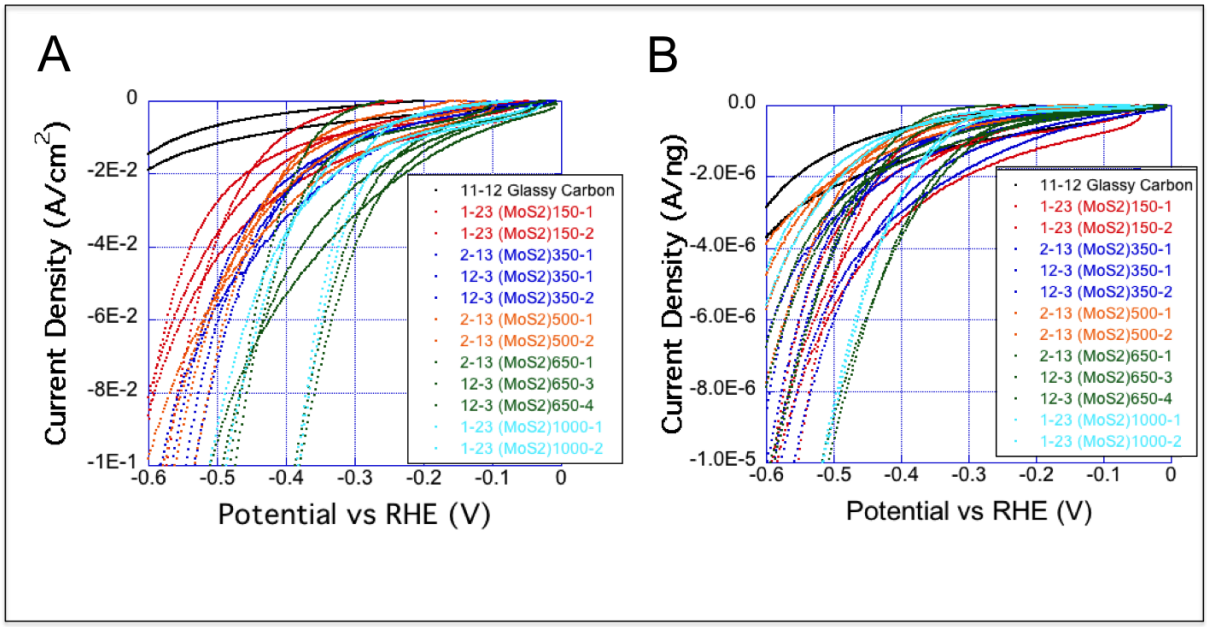

Figure 6.28: (A) 10th scan of HER activity shown for different sizes (with colour coded repeats) of MoS_2 clusters. (B) The same plot normalised to total catalyst mass

of clusters deposited, the procedure for inserting the disk into the measurement apparatus, differences in cell parameters between days or bubble formation at the electrode surface. Averaging the repeats reduces variance and a trend of increasing absolute current is seen from small clusters to large clusters (Fig 6.29). This does not necessarily signify that the large clusters are better catalysts since they have more total material and more edge sites.

After normalising the current to the total mass of MoS_2 the current at -0.5 V vs RHE remains flat with an average value of -4.2 μA/ng (Fig 6.30A). The average onset potential for each voltammogram was measured by taking the potential at which each curve crossed a current threshold of 10 μA (Fig 6.30B), this shows a steady decrease in onset potential with increasing size. This effect gives the impression of a decrease in overpotential for larger clusters but is again simply due to higher loading. The current threshold was increased corresponding to the catalyst mass and shows a constant overpotential averaging -0.6 V vs RHE for these catalysts.

The analysis so far has taken the tenth scan of each voltammogram in order to rule out measurement of atmospheric adsorbates on the surface of the electrode and to allow a stable state to be reached. However, due to the uncertain strength of the cluster pinning

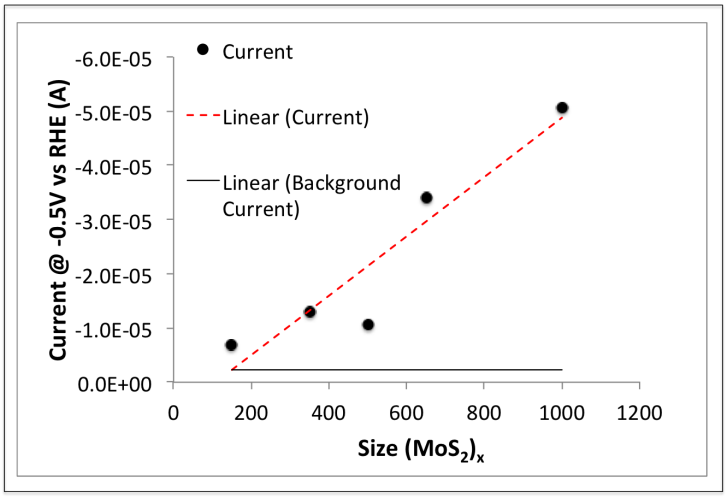

Figure 6.29: The average reaction current, measured at -0.5 V vs RHE, is plotted against the size of MoS_2 cluster

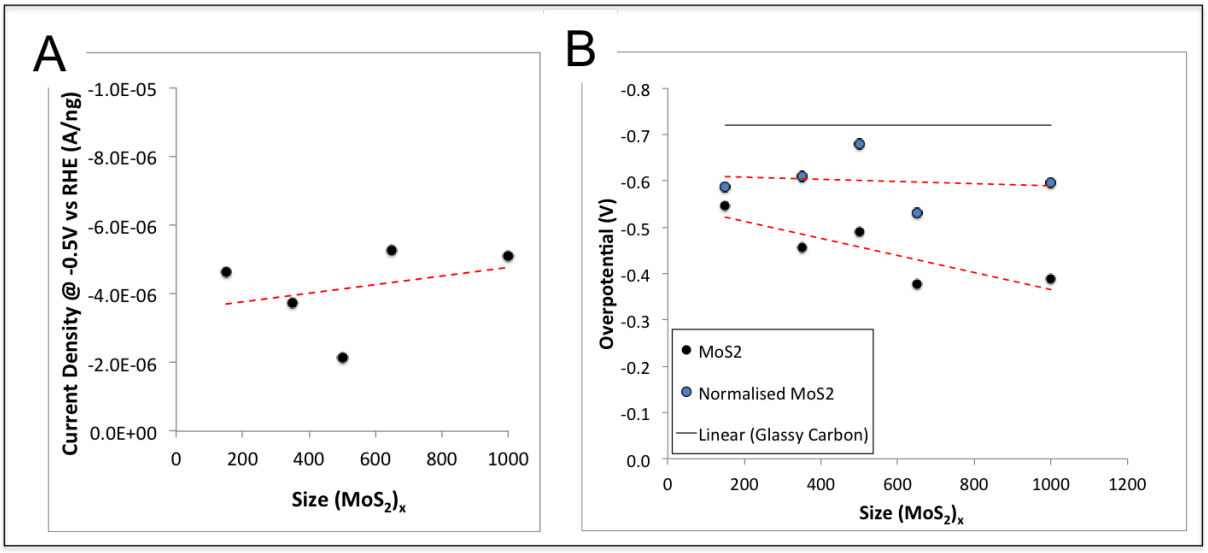

Figure 6.30: (A) The plot in Fig 6.29 is shown normalised for total mass of catalyst material, with a linear trendline as a guide. (B) The onset potential, measured as the potential at which the current reaches 10 μA, is plotted against size of MoS_2 cluster, the normalised onset potential is shown for a current threshold scaled by total cluster mass.

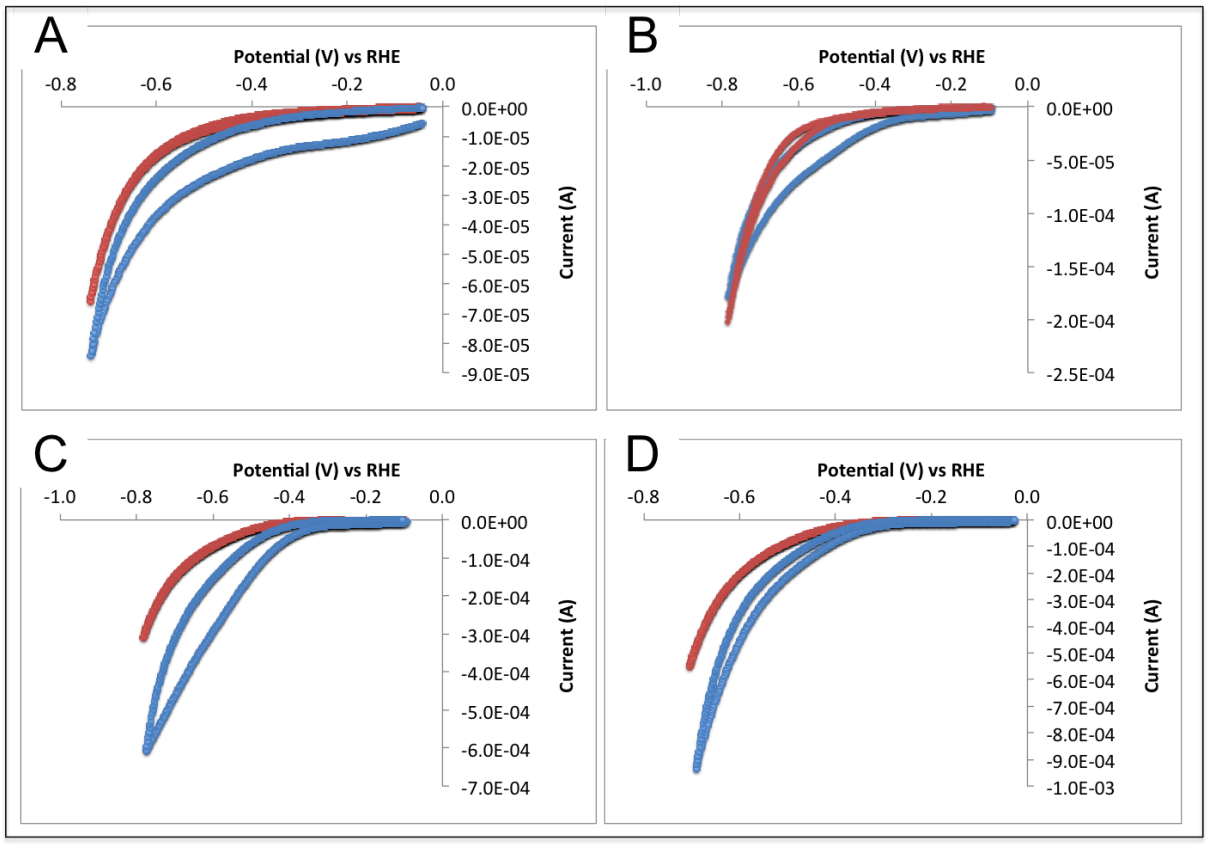

Figure 6.31: Scan 1 (Blue) and Scan 10 (Red) for (A) $(MoS_2)_{150}$, (B) $(MoS_2)_{350}$, (C) $(MoS_2)_{650}$, (D) $(MoS_2)_{1000}$ (Size 500 is omitted as the first scans were corrupted)

on HOPG (Section 6.3.2) the first cycle has also been analysed, in case the MoS_2 is also removed or deactivated over time on GC.

There is a consistent decrease in current from the first scan to a steady state, usually reached by the tenth scan at 20 mV/s scan rate (Fig 6.31). The cluster samples display a low overpotential reduction feature on the first scan in the form of a shoulder on the solvent breakdown peak. This smaller overpotential, around -0.4 V, is closer to the onset potentials of -0.2 V seen for the most active MoS_2 nanoparticles in the literature [18, 24]. Tafel plots of the first scans were analysed for the HER onset region (Fig 6.32) assuming the current peak is due to HER on subsequently deactivated MoS_2. The average Tafel slopes and exchange current densities are shown in Fig 6.33.

The Tafel slope decreases as more catalyst is added, but the value doesn't approach the theoretical limit of the Volmer-Heyrovsky (Eqn 3.7, 40 mV/dec) or Volmer-Tafel

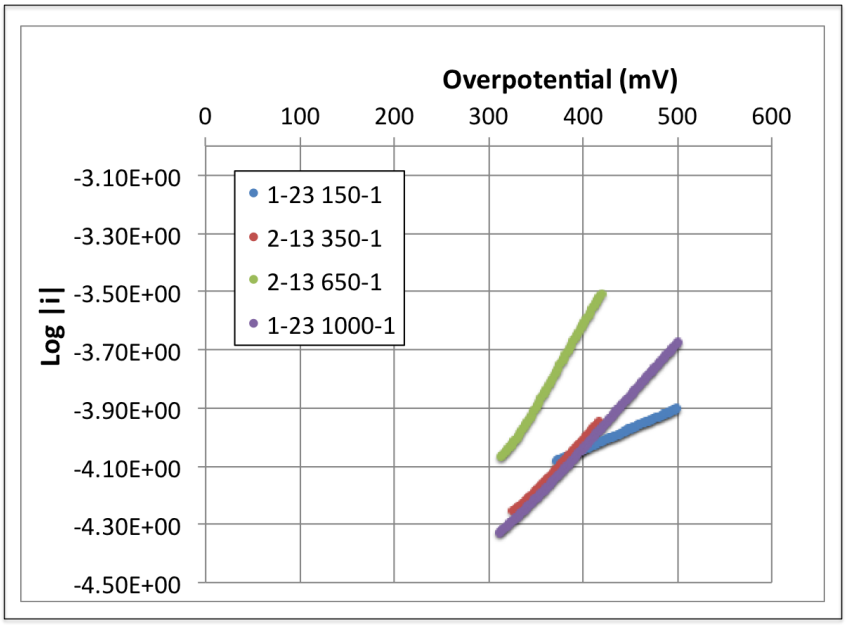

Figure 6.32: Tafel slopes for HER onset region in (MoS_2) samples. (Blue) $(MoS_2)_{150}$ b = 714 mV/dec, i_0= -2.5E-5 A/cm^2, (Red) $(MoS_2)_{350}$ b = 294 mV/dec, i_0= -4.1E-6 A/cm^2, (Green) $(MoS_2)_{650}$ b = 182 mV/dec, i_0= -1.6E-6 A/cm^2, (Purple) $(MoS_2)_{1000}$ b = 286 mV/dec, i_0= -3.6E-6 A/cm^2

Sample	Tafel Slope (mV/dec)	i_0 A/cm$^2_{geometric}$	i_0 A/cm$^2_{measured}$
GC	1250	-2.30E-5	-2.30E-5
$(MoS_2)_{150}$	774	-1.73E-5	-1.15E-3
$(MoS_2)_{350}$	371	-1.01E-5	-4.75E-4
$(MoS_2)_{650}$	166	-3.03E-6	-1.11E-4
$(MoS_2)_{1000}$	235	-3.26E-6	-9.75E-5

Figure 6.33: Tafel Slope and Exchange Current Densities for MoS_2 Samples used in 0.1M $HClO_4$ experiments

mechanisms (Eqn 3.6, 30 mV/dec), although similar values have been achieved in literature [18, 24]. This is likely to be caused by the oxidation of the active sites. The exchange current density (i_0) is a measure of the electron transfer rate of the active sites, so a high value combined with a low Tafel slope are used as indicators of good catalytic performance [20]. The exchange current density is used as the determining parameter in volcano binding energy plots [18, 224]. The exchange current densities for the MoS_2 clusters shown in the table are lower than the carbon background (Fig 6.33), however this is due to the geometric area normalisation, which only holds for the carbon background. Geometric area is frequently used as it is difficult to estimate the true catalyst area, however in this case the true active area can be estimated by using the measured perimeter, layer height and cluster coverage from Chapter 4 and 5. After normalisation the current per active site increases with decreasing cluster size (Fig 6.33). This could be a combined effect of increased stability to oxidation for smaller clusters and favourable conduction band shifts caused by 3D quantum confinement. Furthermore, the reaction current normalised to catalyst mass compares favourably with similar studies in the literature (Fig 6.42), giving further evidence for the enhanced activity due to increased low-coordination sites. The comparable activity to stoichiometric MoS_2 suggests that the suspected dissolution of oxide from the edges is occurring, thus exposing the stoichiometric MoS_2 interior seen in XPS (Section 4.4.1).

6.4.3 Catalyst Loading

The first samples produced on GC electrodes were deposited at different loadings to test the effect on reaction current (Fig 6.34). A reaction current from the catalyst clusters that is significantly greater than the background is desirable, but coverage should also be low enough to allow the diffusion to be correctly simulated. A diffusion boundary surrounds an active catalytic site, and defines an electrolyte volume that becomes depleted of reactants (Depletion Layer). This region must be refilled by reactants in the bulk electrolyte. This defines the shape of mass-transport limited reactions in cyclic voltammetry, with an initial

$(MoS_2)_x$	Beam Dose (pA/s)	Catalyst Mass (ng)	% Monolayer
350	2000	1.2	0.7
350	6000	3.5	2.0
650	2000	2.2	1.7
650	6000	6.5	5.0

Figure 6.34: Loading for two sizes of MoS_2 cluster with two repeats

peak as plentiful reactants in the immediate vicinity are reduced, followed by a lower current as reactants are provided by slower mass transport (Sections 6.4.4 and 6.5).

The diffusion boundaries for macroscopic electrodes and nanoparticles are very different. The diffusion volume around an individual supported nanoparticle is hemispherical, this has a large surface area, which is quickly replenished by reactants from the electrolyte [225]. This means the limited current regime does not decrease significantly from the initial peak, creating a plateau rather than a clear peak. The peak current in this loading regime is proportional to the number of nanoparticles. The diffusion volume for a macroscopic or highly loaded electrode is composed of overlapping volumes of every active site, this approximates to a single planar diffusion boundary over the whole electrode. This larger depletion layer is slower to replenish resulting in a lower mass-transport limited current, which produces a clear peak in the voltammogram. In an intermediate coverage regime the two diffusion models mix, which is difficult to interpret. The platelet shaped clusters are quasi-2D so have a diffusion volume that is hemispherical.

The voltammograms for two MoS_2 cluster sizes at approximately 1% and 4% of a monolayer show activity above background (Fig 6.35A). The 1% loading had problems with reproducibility, possibly due to greater error in the short deposition time and the reduced time to raster an even coating. The potential must be increased greater than -0.5 V to see a large deviation from the background signal (Fig 6.35B), at most only 7× greater than background. The 4% coverage has greater than 15× the reaction current compared to the GC background and shows better reproducibility. These measurements were taken in proton-rich 0.1M $HClO_4$ electrolyte, so a depletion layer is not formed with which to investigate the limited current, however the average spacing of 23 nm (Section 5.4.1) was

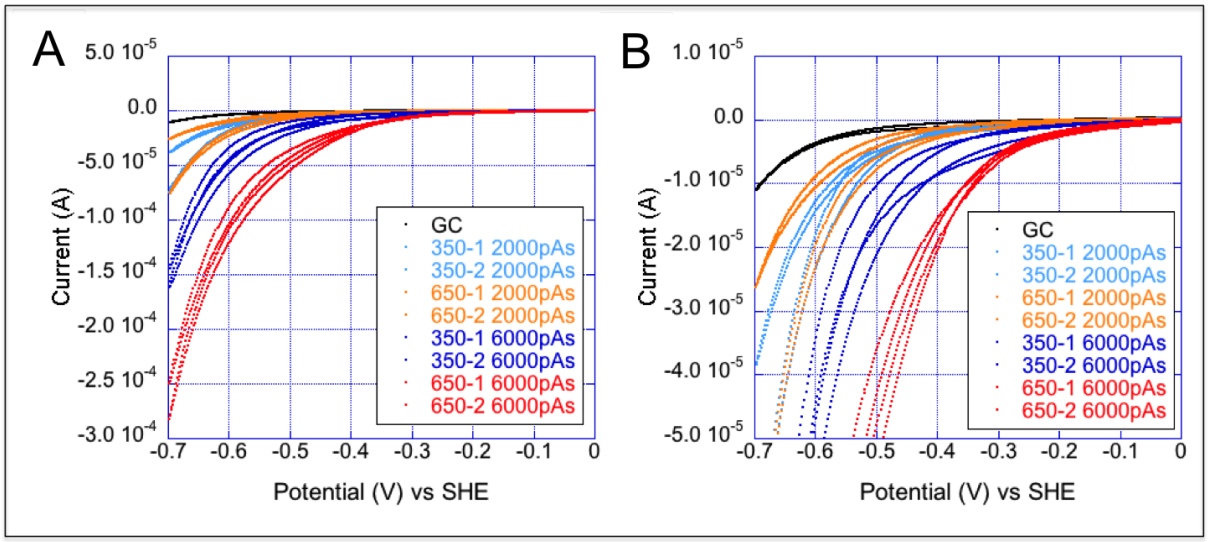

Figure 6.35: (A)HER activity for MoS_2/GC in 0.1M $HClO_4$. $(MoS_2)_3$50 Low loading (Light Blue) and Normal loading (Orange), and $(MoS_2)_6$50 Low loading (Blue) and Normal loading (Red) (B) Zoomed section

assumed to be sufficient to have hemispherical diffusion. This was subsequently confirmed by the limiting currents in proton-poor electrolyte (Section 6.4.4) and simulations of this data (Section 6.5).

6.4.4 Hydrogen Evolution in 1mM Perchloric Acid

The high concentration of protons in the standard electrolytes used for HER (0.1M $HClO_4$, 0.5M H_2SO_4) results in a featureless voltammogram that increases in current exponentially to the point of solvent breakdown. The onset potential and Tafel slope can be used to determine catalytic properties on such voltammograms, but these techniques can be subjective based on where a slope is determined to be linear. In this experiment the concentration of protons was reduced by diluting $HClO_4$ to 1mM and adding $NaClO_4$ to provide supporting perchlorate ions. The perchlorate ions have a low reactivity, due to their weak nucleophilicity, and so do not interfere with the electrochemistry. Four sizes of MoS_2 clusters, with two repeats each, were deposited at the same coverage as the samples measured in 0.1M $HClO_4$ (Fig 6.36). The coverage corresponds to 1911 clusters/μm^2, which gives an inter-cluster spacing of 23 nm. The low proton concentration also has

Sample	Size	Deposited	Measured
S1	$(MoS_2)_{350}$	12/3/13	14/3/13
S2	$(MoS_2)_{350}$	12/3/13	14/3/13
S3	$(MoS_2)_{500}$	12/3/13	14/3/13
S4	$(MoS_2)_{500}$	12/3/13	14/3/13
S5	$(MoS_2)_{650}$	13/3/13	14/3/13
S6	Data Corrupted	13/3/13	14/3/13
S7	$(MoS_2)_{1000}$	13/3/13	14/3/13
S8	Noise Problems	13/3/13	14/3/13
GC1	Glassy carbon blank	N/A	14/3/13
GC2	Glassy carbon blank	N/A	14/3/13

Figure 6.36: Samples 1-8 were deposited at a coverage of 6000 pAs, stored in vacuum and analysed 2 days later in the same session. GC1 and GC2 are blank Glassy carbon disks polished at the same time as the other samples and stored in the same conditions. Two repeats have been removed due to data corruption and high noise due to bubble attachment.

the added advantage that less hydrogen is produced, which reduces the problem of gas build-up on the electrode, improving reproducibility.

The samples were cycled at reducing potentials from 0 V to -1.3 V (Fig 6.37). The first scan shows a consistent reduction feature for all cluster samples at -0.5 V onset (Fig 6.38), with a similar peak at a higher energy in the blank samples. This feature is assumed to be the HER onset for catalytically active sites on MoS_2, thus the improvement in onset potential over the GC blank. Tafel analysis was performed on these onset regions as with the 0.1M experiments (Fig 6.39).

The average results of Tafel slope and exchange current density (geometric and measured) were calculated (Fig 6.40). These show a similar trend to the 0.1M experiment, with the Tafel slope reducing with higher loading, but not reaching the highest theoretical values of 40 mV/decade. The exchange current density again shows that the smallest size clusters have the most active sites. This is attributed to quantum confinement effects as the clusters are below the Bohr radius of 2 nm for MoS_2 [66, 67]).

The low energy reduction feature gradually shifts to higher energy during cycling until after ten cycles the peak is at the same position as that of the blanks (Fig 6.38). The initial peak is attributed to HER on the MoS_2 clusters, the reduced proton concentration

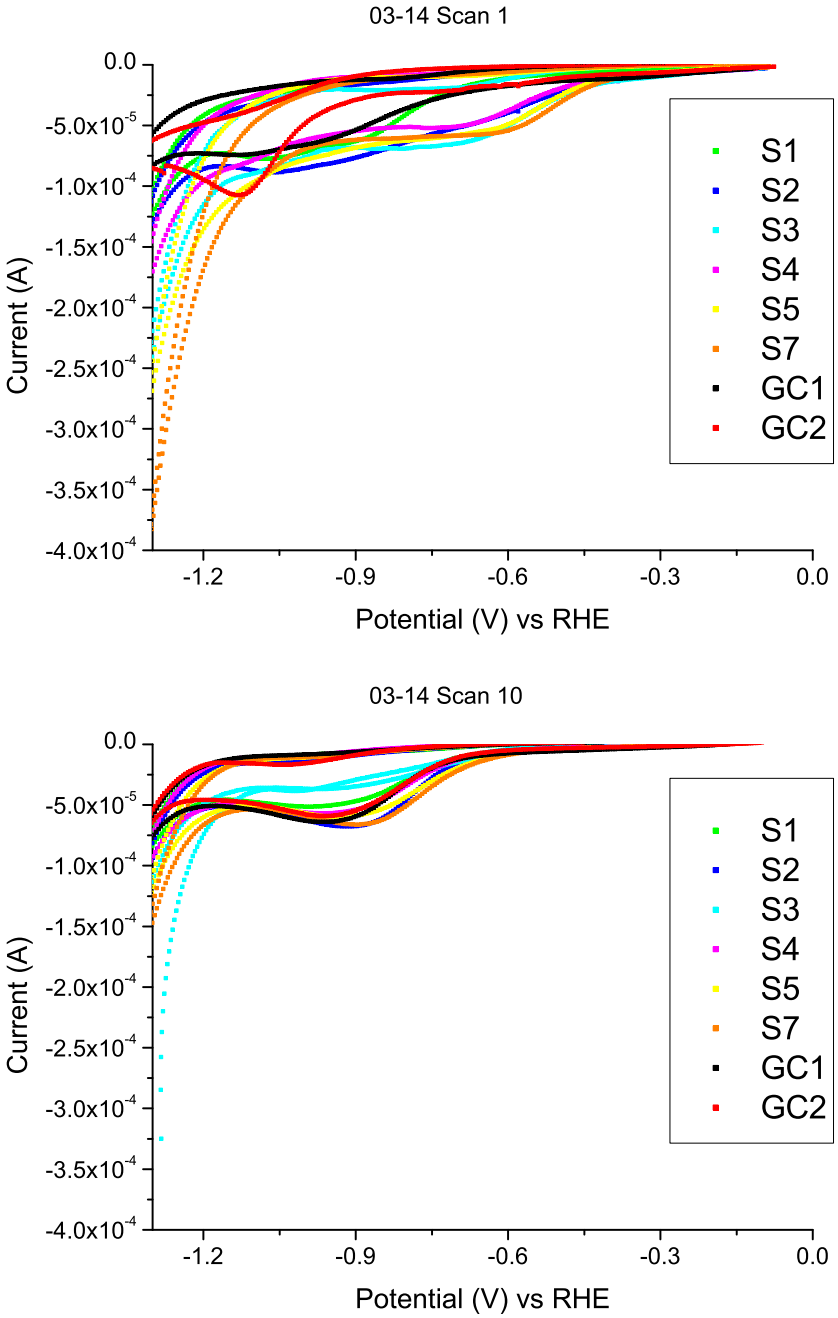

Figure 6.37: (Top) First scan from 0V to -1.3V at 20mV/s in 1mM $HClO_4$ + 0.1M $NaClO_4$. (Bottom) The tenth scan under the same conditions. All data has been converted to RHE scale.

Sample	Scan 1 Onset (V)	Scan 10 Onset (V)
GC	-0.94	-0.80
$(MoS_2)_{350}$	-0.53	-0.77
$(MoS_2)_{500}$	-0.55	-0.75
$(MoS_2)_{650}$	-0.51	-0.74
$(MoS_2)_{1000}$	-0.57	-0.75

Figure 6.38: Average onset potential measured at the half-point of the leading edge of the reduction peak, for blank GC and MoS_2 samples

produces a mass transport limitation whereby the MoS_2 catalyst exhausts the local supply of protons. This produces a decline in HER current after a certain potential. Mass transport limitation is usually characterised by a peak in the voltammogram for large catalyst particles, however for nanoscale catalysts the area of electrolyte that is exhausted of protons is small. This depleted volume is quickly replenished by diffusion, thus producing a shoulder or plateau. The limiting current of the initial peak and plateau for all cluster samples is around 75 μA, this indicates the coverage is approximately the same for all samples as limiting current is proportional to the number of nanoparticles for the low coverage regime. At potentials beyond this plateau the GC background then becomes active for HER, and so the current increases as with the 0.1M $HClO_4$.

The disappearance of the peak after multiple scans is harder to explain (Fig 6.37). There is no oxidation peak on the return scan for this feature so it is an irreversible reduction, this could still correspond to HER as the H_2 diffuses away too fast to be re-oxidised, followed by shifting of this peak due to the evolved hydrogen removing the clusters from the surface. Alternatively, the reduction peak could be associated with a reaction on the cluster surface that passivates them, causing the subsequent decrease in activity. This would be unusual for MoS_2 catalysts, as a reduction step is often used to activate amorphous MoS_2 [226]. The same study also suggests that delamination causes loss of activity over time, so HER followed by delamination or ripening, as evidenced by post-reaction studies (Section 6.3.2), is the most likely cause.

The results for the low concentration electrolyte appear to be more reproducible between repeats and also have a smoother relationship as a function of size. This may be

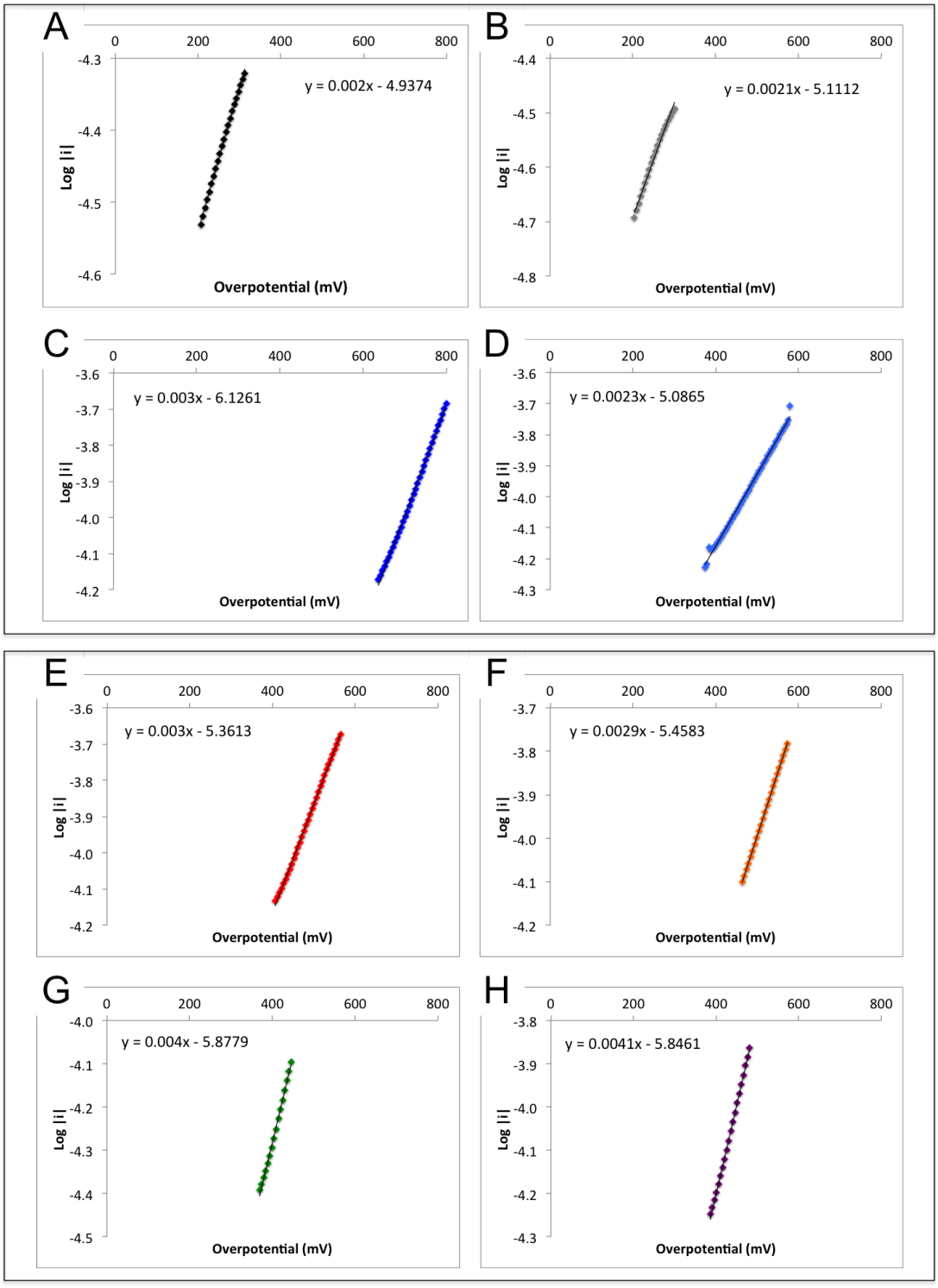

Figure 6.39: Tafel slopes with individual fits of $y = 1/b + log(i_0)$ shown for clarity. (A) GC1 (B) GC2 (C) S1 - $(MoS_2)_{200}$ (D) S2 - $(MoS_2)_{200}$ (E) S3 - $(MoS_2)_{350}$ (F) S4 - $(MoS_2)_{350}$ (G) S5 - $(MoS_2)_{500}$ (H) S7 - $(MoS_2)_{650}$. Tafel slope exchange current densities given in Fig 6.33.

Sample	Tafel Slope (mV/dec)	i_0 A/cm$^2_{geometric}$	i_0 A/cm$^2_{measured}$
GC	488	-9.65E-6	-2.30E-5
$(MoS_2)_{200}$	384	-4.47E-6	-2.96E-4
$(MoS_2)_{350}$	339	-3.92E-6	-1.84E-4
$(MoS_2)_{500}$	250	-1.32E-6	-4.86E-5
$(MoS_2)_{650}$	244	-1.43E-6	-4.26E-5

Figure 6.40: Tafel Slope and Exchange Current Densities for MoS_2 Samples used in 1mM $HClO_4$ experiments

due to the experiments being carried out on the same day, thus preventing any electrolyte or electrode differences, and the decrease in hydrogen production, which in 0.1M electrolyte tends to cause bubbles on the electrode. The smooth increase in activity with size can be seen by measuring the maximum current against cluster size (Fig 6.41). The size dependence of $x^{0.85}$ closely matches the scaling relationship of cluster area with size ($x^{0.86}$) (Section 5.6.4) and not the scaling relationship of the perimeter ($x^{0.46}$). This indicates the whole cluster is active rather than just the periphery, in opposition to the usual model of MoS_2 catalysts. This new model matches with the microscopy from Chapter 5 that shows defects and incomplete layers on the cluster surface, and the XPS analysis that suggests there are more total reactive sites than edge sites. In general, this work joins the increasing progress on activity of amorphous MoS_x catalysts in the literature [60, 223, 58].

Another comparison of activity with literature [24] was made based on experiments with a glassy carbon electrode (Fig 6.42). Similarly to the samples on HOPG, the planar deposition prohibits high coverage that would otherwise cause aggregation. Catalyst loading for cluster deposition is three orders of magnitude below that of chemical synthesis, so for a fair comparison of activity this should be added to the normalisation. The final normalised current is of the same order, even exceeding, the literature value. This is a strong indicator that the high density of low-coordination sites on these clusters, combined with the quantum size effects, produce a good HER catalyst.

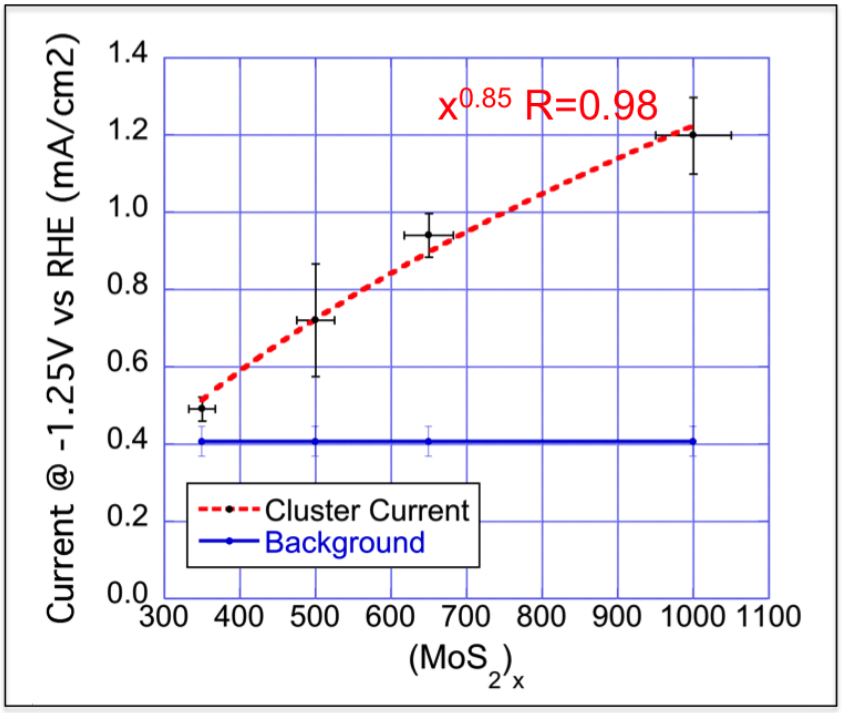

Figure 6.41: Current measured at -1.25V vs RHE increases with cluster size proportional to $x^{0.85}$

	MoS_2/Graphene [24]	$(MoS_2)_{1000}$/GC	$(MoS_2)_{1000}$/GC
Electrolyte	0.5M H_2SO_4	0.1M $HClO_4$	1mM $HClO_4$
Geometric Area (cm^2)	0.07	0.20	0.20
Catalyst Mass (μg)	20	0.01	0.01
Loading (mg/cm^2)	285.7E-3	50.0E-6	50.0E-6
$J_{-0.2VvsRHE}$ (mA/cm^2)	-30	-4.4E-2	-2.5E-2
$J_{-0.2VvsRHE}$ ($mA/cm^2/\mu g$)	-1.5	-4.4	-2.5

Figure 6.42: The most active MoS_2 HER catalyst in literature [24] is compared to MoS_2/GC samples in both electrolyte experiments.

6.5 Electrochemical Simulation of HER in 1mM $HClO_4$

The peaks generated by mass-transport limitations in low proton concentration electrolyte can be modelled by simulation software. The HER charge-transfer reaction, protons reduced to molecular hydrogen, was simulated using the DigiElch software and compared to experimental results in 1mM $HClO_4$. Simulation was carried out by Josh Tibbetts as a summer undergraduate project.

The simulations model a high current peak, as protons are reduced around the electrode, followed by a reduction in current to a diffusion limited state as the nearby protons are exhausted. Reversible reactions are usually characterised by an equal oxidation peak on the return scan, which in this case would change molecular hydrogen to protons. This oxidation peak does not occur in the data as the reaction is irreversible due to the overpotential required compared to the thermodynamic redox potential. Furthermore, an oxidation peak would be reduced in current due to the diffusion of hydrogen away from the electrode before it can be oxidised. This effect would be reduced at higher scan rates as the hydrogen will have had less time to diffuse from the electrode. The simulation and experiment diverge at higher potentials beyond the initial current peak due to HER on glassy carbon and solvent breakdown not being modelled. As such the region beyond the initial peak is neglected.

The simulation requires the user to define an electrode geometry, however this was treated as a variable and defined in three ways in order to assess the best fit to the data. This would then provide information about the structure at the nanoscale that can be compared to microscopy (Chapter 5) and spectrometry (Chapter 4). The first geometry was planar, which can apply to nanoparticles that are sufficiently close together that their depletion layers overlap to create a diffusion layer with area identical to the geometrical electrode area. The second was a model that treated each nanoparticle as an individual electrode with hemispherical geometry, with each nanoparticle having a distinct depletion layer. The third model considered an array of rings, which corresponds best to the model of active edge sites for MoS_2 catalysts.

Charge Transfer (CT) Reaction	$A + e^- \rightarrow B$
Standard Redox Potential	-0.145 V
Alpha (α)	0.5
Proton Conc. (mol/dm^3)	0.001
Scan Rate (V/s)	0.02
A Diffusivity (Proton, H_3O) (cm^2/s)	1.0E-4 [227, 228, 229]
B Diffusivity (H_2) (cm^2/s)	4.5E-5 [230, 231, 229]

Figure 6.43: Table of constant starting parameters for all electrochemical simulations. Diffusivity values include references to appropriate literature.

The simulation parameters regarding the chemical reactions are defined at the beginning by the experimental parameters of the 1mM $HClO_4$ experiments (Section 6.4.4). The values listed in Fig 6.43 are constant throughout all simulations. The standard thermodynamic redox potential of the HER reaction is at 0 V vs SHE, however as the experiment was carried out in electrolyte of pH 2.46, this value was shifted to -0.145 V according to the Nernst equation. The α value signifies the imbalance between forward and backward reactions, and at low overpotentials this is approximately 0.5. The initial proton concentration is defined by the molarity of the 1mM electrolyte. The experiment was performed at different scan rates (20, 100, 250, 500, 750, 1000 mV/s) in order to investigate mass-transport limits. However, as the reduction peak being simulated only appears on the first scan, at 20 mV/s, all other scan rates were ignored.

The shape of the simulated peak is controlled by several parameters. The main variable in the simulation is the heterogeneous rate constant (k_s), this determines the overpotential required for the reaction to occur and as such shifts the peak along the potential axis. The physical meaning of the rate constant is given by the Butler-Volmer equation (Eqn 6.1) and the relationship to exchange current density (Eqn 6.2).

$$I = i_0 \left(exp\left[\frac{\alpha_a n F \nu}{RT}\right] - exp\left[\frac{\alpha_c n F \nu}{RT}\right] \right) \tag{6.1}$$

The exchange current density (i_0) should be high for a good catalyst, due to its relationship with k_s (Eqn 6.2) [232, 233, 234]. The remainder of the Butler-Volmer equation depends on charge transfer coefficients (α) and the number of electrons involved

in the cathodic and anodic reactions (n). Faraday's constant (F), electrode area (A), universal gas constant (R) and temperature (T) are all constant. Concentration of surface reactants (C) may change depending on diffusion and the speed of the reaction.

$$i_0 = nAFk_sC \tag{6.2}$$

The rate constant, k_s, is determined by activation energy, temperature, and the amount of active sites. The dependence on number of active sites means the rate constant will naturally increase with the size of catalyst, but by normalisation the rate constant should be reduced to dependence on the activation energy and thus catalytic performance.

The other parameters that control the peak shape are the scan rate and diffusivity. The height of the current peak is governed by the amount of reactant that can reach the electrode, this increases with scan rate and diffusivity, as raising these parameters reduces the size of the depletion layer. As mentioned earlier, the scan rate dependence was not used as the feature of interest occurred only on the first scan at 20 mV/s.

The modelling uses a non-linear fitting procedure to fit a simulated voltammogram to the experimental data. At potentials much greater than the first reduction feature the current increases to the point of solvent breakdown, which is not modelled in the simulation, so the data beyond the initial peak is excluded.

6.5.1 Planar Model

The first case considered was the planar model, which is expected to be applicable for macroscopic electrodes or closely packed nanoparticles. The initial parameters for the planar simulation are listed in Fig 6.44, with diffusivity values taken from literature and the area calculated from the geometry of the glassy carbon surface. The simulation was applied to the samples measured in the previous section, and the heterogeneous rate constant (k_s) was varied to give the best fit.

The simulation based on a planar electrode has a large difference between diffusion

Geometry	Planar
A Diffusivity (Proton, H_3O) (cm^2/s)	1.0E-4 [227, 228, 229]
B Diffusivity (H_2) (cm^2/s)	4.5E-5 [230, 231, 229]
Area (cm^2)	0.192

Figure 6.44: Table of starting parameters for planar electrochemical simulation

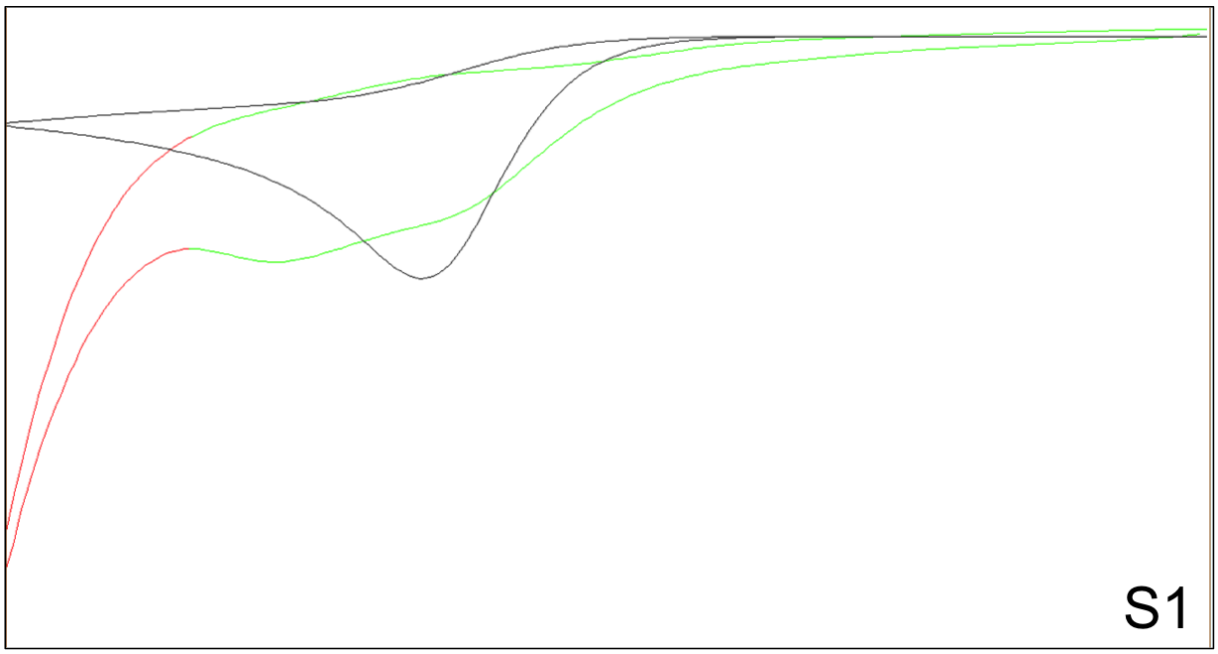

Figure 6.45: Simulated HER based on planar geometry for Sample S1 with simulation fitted to variable rate constant. Experimental data (Green), omitted experimental data (Red) and best fit simulation (Black)

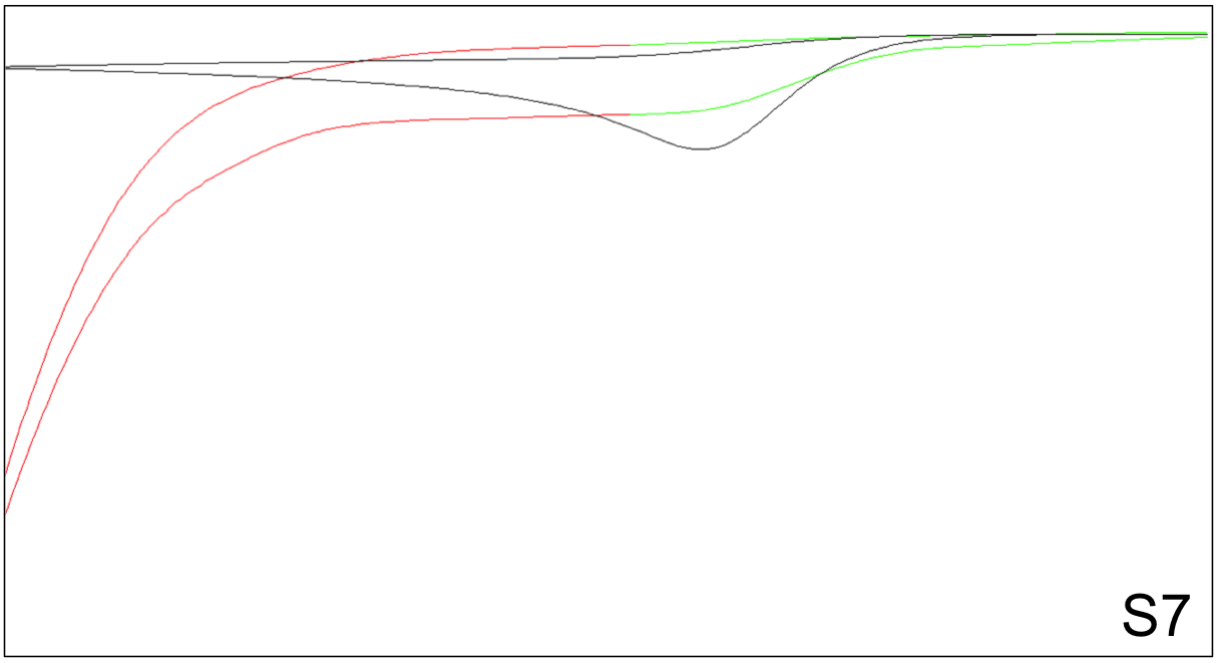

Figure 6.46: Simulated HER based on planar geometry for Sample S7 with simulation fitted to variable rate constant. Experimental data (Green), omitted experimental data (Red) and best fit simulation (Black)

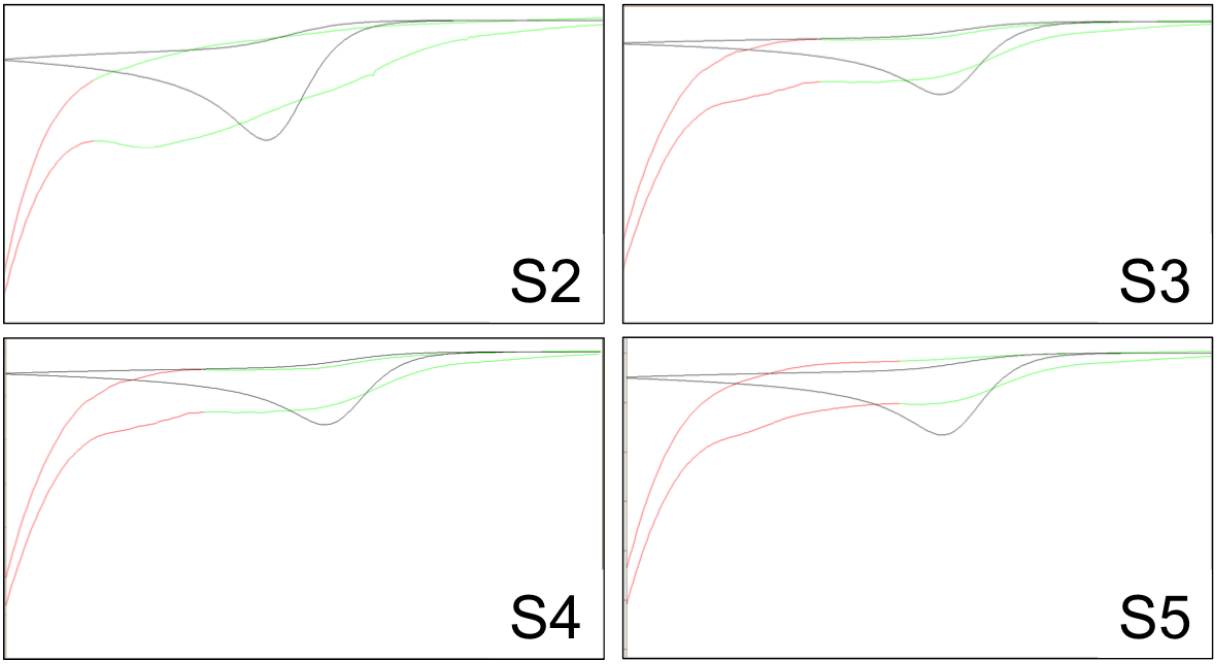

Figure 6.47: Simulated HER based on planar geometry for Samples S2,3,4,5 with simulation fitted to variable rate constant. Experimental data (Green), omitted experimental data (Red) and best fit simulation (Black)

Sample	Size	k_s (cm/s)	R^2 of fit
S1	350	9.39E-9	0.864
S2	350	8.23E-8	0.665
S3	500	1.11E-6	0.862
S4	500	7.42E-7	0.922
S5	650	1.33E-6	0.865
S7	1000	2.33E-6	0.914

Figure 6.48: Fitted value of rate constant for all MoS_2 samples modelled with planar geometry

Sample	Size	Average Radius (nm)
S1	350	1.87
S2	350	1.87
S3	500	2.23
S4	500	2.23
S5	650	2.57
S7	1000	2.79

Figure 6.49: Fitted value of rate constant for all MoS_2 samples modelled with hemispherical geometry

limited current and peak current. This is due to the relatively small surface area presented by a macroscopic electrode. This area presents a correspondingly small volume above which is quickly diminished of reactants, thus causing the low limiting current and producing a peak. Clearly the data does not fit well to this model as it is in the form of a plateau rather than a peak (Figs 6.45, 6.46 and 6.47). The rate constants were extracted from the fits (Fig 6.48), but due to the poor fit of the model it is concluded that the clusters are sufficiently spread to be treated as individual electrodes.

6.5.2 Hemispherical Model

The second model treats each cluster individually, with a diffusion layer as a hemisphere of radius equal to that of each cluster (Fig 6.49). The radius of each cluster size is taken from average values measured by STEM in Chapter 5. The same starting parameters were used as the planar model.

A good fit was not possible with rate constant as the only variable (Figs 6.50 and

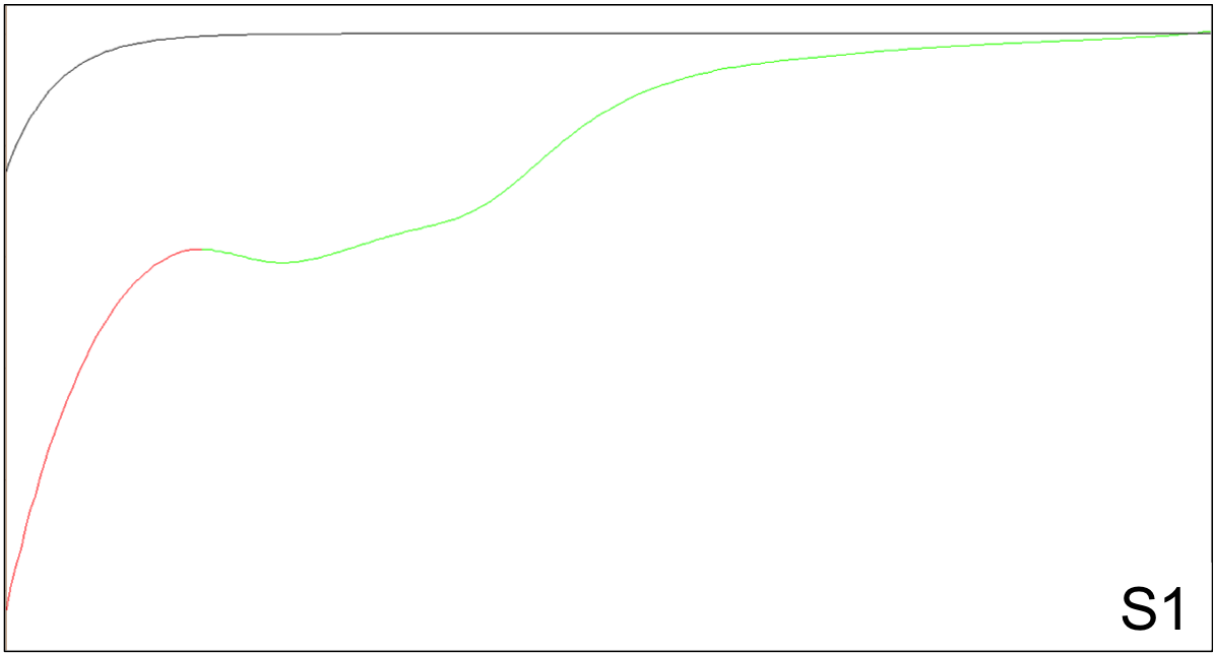

Figure 6.50: Simulated HER based on planar geometry for Sample S1 with simulation fitted to variable rate constant. Experimental data (Green), omitted experimental data (Red) and best fit simulation (Black)

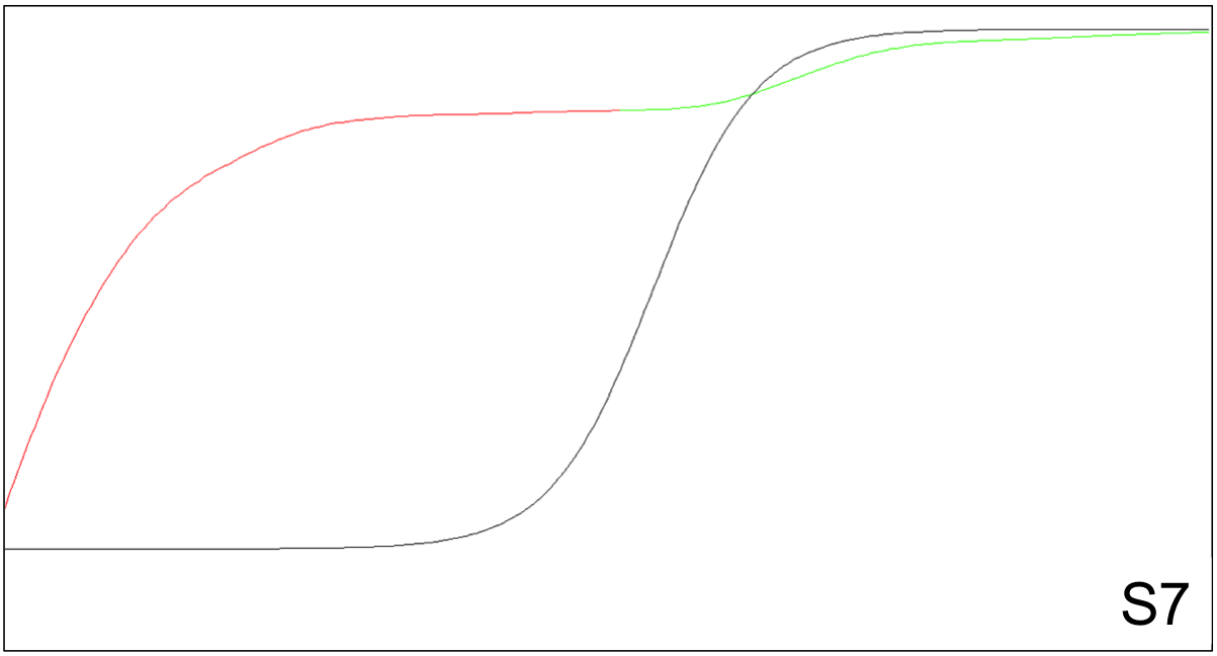

Figure 6.51: Simulated HER based on hemispherical geometry for Sample S7 with simulation fitted to variable rate constant. Experimental data (Green), omitted experimental data (Red) and best fit simulation (Black)

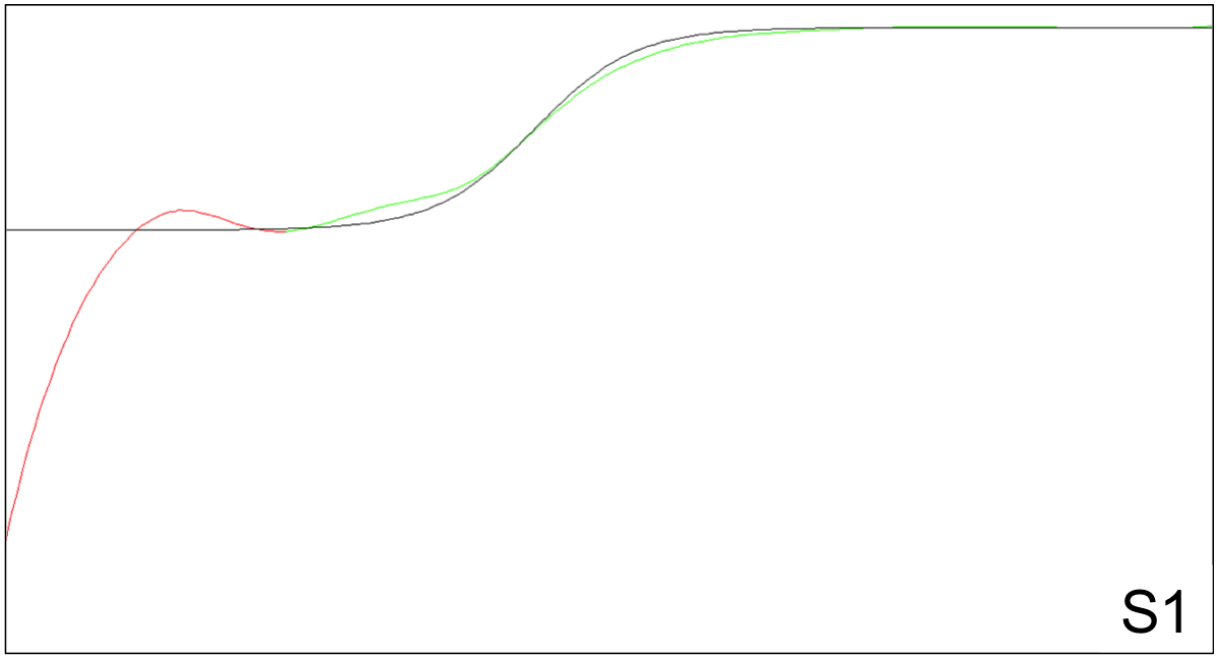

Figure 6.52: Simulated HER based on hemispherical geometry for Sample S1 with simulation fitted to variable rate constant, proton diffusivity and α coefficient. Experimental data (Green), omitted experimental data (Red) and best fit simulation (Black)

6.51). However the shape of the fit, with an increase followed by a plateau, matches the data better than the planar model. The new model based on an array of nanoelectrodes, which have a much larger surface area, results in more reactants diffusing to the electrode surface. This causes a much higher diffusion limited current, almost equal to the peak current, resulting in a plateau feature developing as shown in data and simulations.

The diffusivity of protons and α coefficient were made variable to produce a better fit. This is shown in (Figs 6.52, 6.53 and 6.54) Unfortunately the fitted values (Fig 6.55) are orders of magnitude away from the starting parameters. Diffusivity especially is far too low, over 2 orders of magnitude lower than literature values, despite the goodness of fit. This highlights the danger of fitting data with too many free variables, as almost any shape can be recreated. This can be mitigated by ensuring physical parameters remain within a reasonable range consistent with literature, and by testing with many samples to ensure the fit is not coincidental.

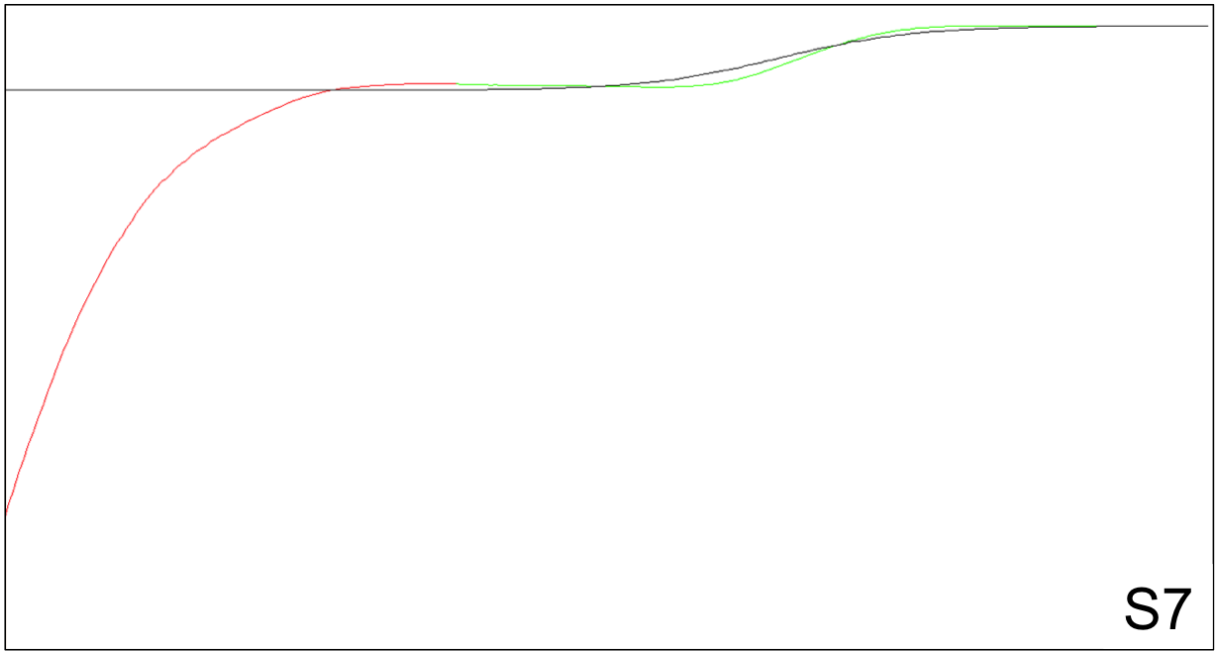

Figure 6.53: Simulated HER based on hemispherical geometry for Sample S1 with simulation fitted to variable rate constant, proton diffusivity and α coefficient. Experimental data (Green), omitted experimental data (Red) and best fit simulation (Black)

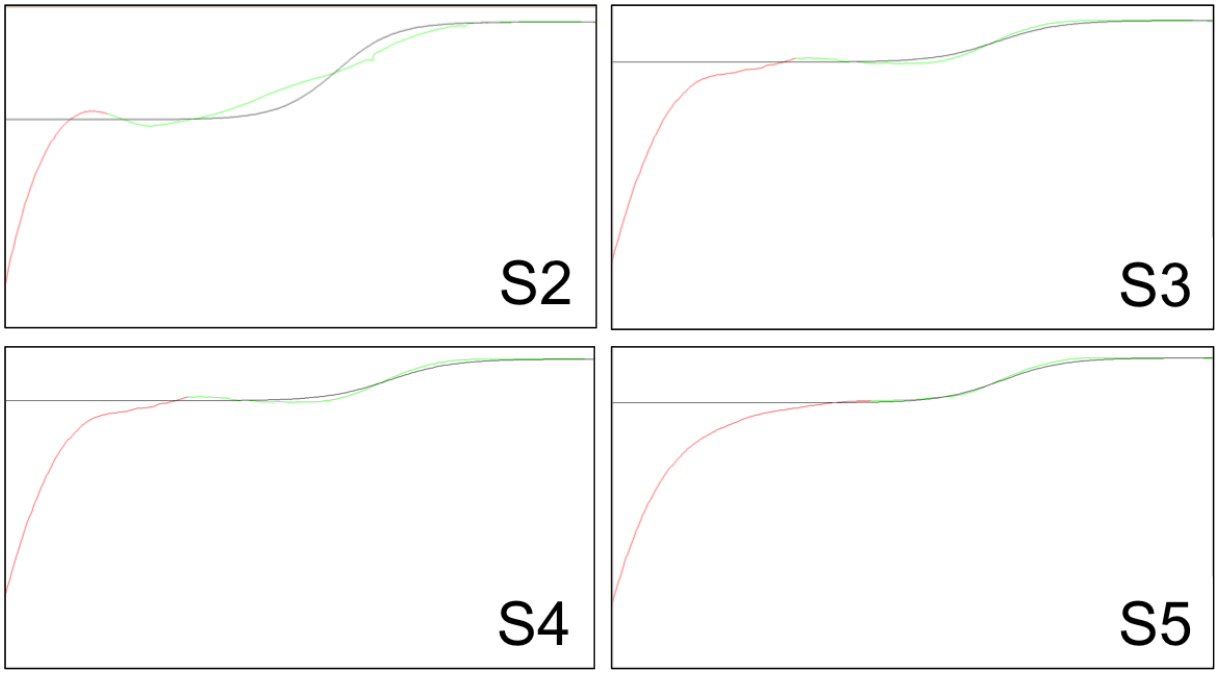

Figure 6.54: Simulated HER based on hemispherical geometry for Samples S2,3,4,5 with simulation fitted to variable rate constant, proton diffusivity and α coefficient. Experimental data (Green), omitted experimental data (Red) and best fit simulation (Black)

Sample	Size	k_s (cm/s)	H^+ Diffusivity (cm^2/s)	α	R^2 of fit
S1	350	3.67E-7	1.41E-8	0.501	0.998
S2	350	2.58E-5	1.28E-8	0.424	0.972
S3	500	1.10	7.80E-7	0.400	0.992
S4	500	0.12	6.22E-7	0.479	0.991
S5	650	1.03	7.80E-7	0.410	0.994
S7	1000	1.27	6.71E-7	0.380	0.982

Figure 6.55: Fitted value of rate constant, proton diffusivity and α coefficient for all MoS_2 samples modelled with hemispherical geometry

6.5.3 Micro-Ring Model

The ring model, based on the work of Bond [235], should be the most applicable to the standard picture of MoS_2 catalysts with active edge sites and inert basal planes. The ring outer radius was based on average measured radii of clusters in micrographs and the thickness of the ring was assumed to be one unit cell of MoS_2, approximately 0.3 nm. The E_0 value was changed slightly to -0.177 V to fit this model, however the greatest change was in the number of nanoparticles, which produced very good fits to the experiment (Fig 6.56). The coverage as deposited gave a total number of clusters of 37.5E+9, however this model fits perfectly using a value of the order E+6 for all cluster sizes (Fig 6.57).

The initial coverage by the cluster beam source should be correct from the charge transfer measured on impact. This suggests the coverage is much lower than expected, which could be due to multiple factors. So it is likely to be a destructive effect of oxidation or the reaction process. The oxidation creates a soluble MoO_3 shell, which after dissolution would leave a smaller cluster, with fewer active sites. This is supported by the lower post-reaction coverage seen by AFM on HOPG (Section 6.3.2). The 1000× decrease in cluster number cannot be explained by this process alone. The weak binding of the clusters to the carbon support may result in the majority detaching. These hypotheses could be tested by analysing the residual electrolyte to measure for MoO_3 content or whole clusters.

The rate constant can be used as a measure of catalytic performance, however it is dependent on the amount of catalyst, therefore to compare between cluster sizes, the rate constant is normalised by the size of MoS_2 deposited (the total number being held constant

in the deposition). The normalised rate constants are almost identical for cluster sizes above 350, showing the active edge sites perform similarly as expected. The only size effect noted is for $(MoS_2)_{350}$ itself, which has a rate constant 2 orders of magnitude below the others. In terms of the expected size effects, a quantum confinement band shift was hoped for, which may unexpectedly be one possible reason for the poor performance, as the conduction band is shifted past the redox potential for HER. The more likely explanation is that at this smaller size, the oxidation or dissolution processes have damaged the majority of the cluster due to its high surface to volume ratio. The independence of rate constant with size disagrees with the exchange current density, measured by Tafel analysis, from the experimental data (Section 6.4.4). This previously showed a higher exchange current density was achieved for decreasing size. The reason for this is unclear, however it may be because there is not a completely direct relationship between rate constant and exchange current density, for example surface concentration (C) may be greater on small clusters or the charge transfer more efficient as there are fewer inter-layer resistances.

The determination of consistent rate constants for the MoS_2 clusters and fitting to realistic experimental parameters shows that the micro-ring picture models the system well. This is in good agreement with the understanding of MoS_2 catalysts in the literature and of the findings of this study, particularly scaling of reactivity and oxidation reactions with edge area.

6.6 Conclusion

The HER activity of MoS_2 in various forms was investigated and quantified by Tafel slopes and exchange current density. The fabrication and measurement techniques employed have covered the full range of surface science fabrication on HOPG, to chemical synthesis with ATM precursor. The benefits of both of these methods were combined to form a hybrid of gas-phase surface science style deposition with standard electrochemical measurement on GC electrodes.

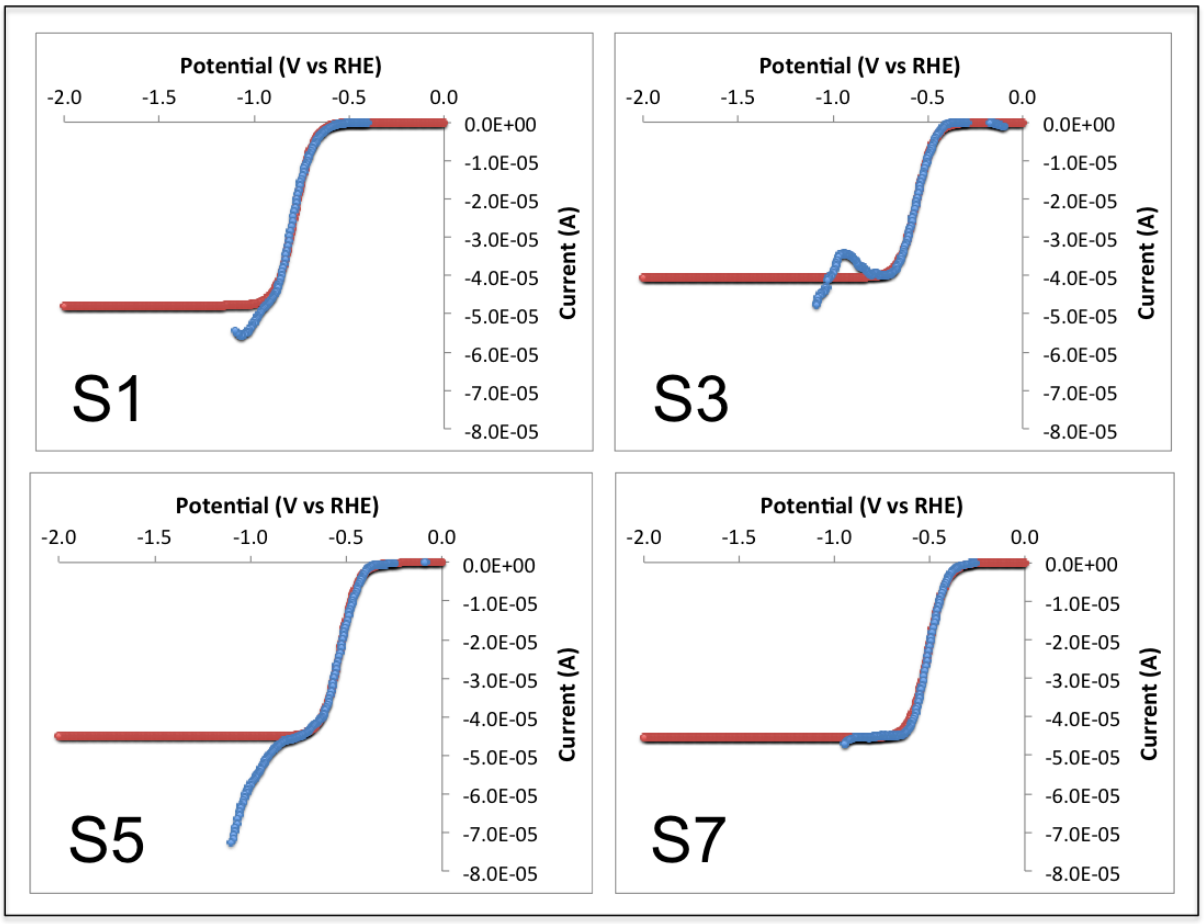

Figure 6.56: Simulated HER based on ring geometry for Samples S1, S3, S5 and S7. Simulation is fitted to a ring geometry with variable rate constant, α coefficient and number of rings. Experimental data (Blue) and best fit simulation (Red)

Sample	Size	k_s (cm/s)	$k_{s\ norm}$(cm/(s.MoS_2))	α	Number of Rings
S1	350	1.0E-4	2.9E-7	0.55	7.5E+6
S3	500	8.0E-3	1.6E-5	0.56	5.4E+6
S5	650	1.4E-2	2.2E-5	0.56	6.0E+6
S7	1000	2.3E-2	2.3E-5	0.56	4.9E+6

Figure 6.57: Fitted value of rate constant and α coefficient for all MoS_2 samples modelled with the micro-ring geometry. The rate constant is shown normalised to the smallest cluster size for comparison without the effect of greater loading.

The collaborative work at DTU served as an excellent introduction to chemical synthesis. Active nanoparticles were synthesised and doped by simple techniques. The cobalt dopant was found to be the most effective, in agreement with its widespread use as a promoter of MoS_2 for the HDS reaction. The disadvantage of chemical synthesis was in the nanoscale characterisation, as aggregation and the presence of remaining polymer stabiliser, made modelling the system difficult.

HER activity for MoS_2 clusters supported on sputtered HOPG was confirmed by cyclic voltammetry and the effects of reaction conditions on the clusters were explored with scanning probe measurements. The stability of clusters on graphite surfaces was shown to be poor, both by AFM and STEM, with a reduction in coverage and composition change signifying dissolution and ripening. The disadvantages of this fabrication technique contrasted with chemical synthesis, by allowing simple characterisation with many surface science tools, but being unsuited to electrochemical measurement. The relatively smooth surface of sputtered HOPG, compared to amorphous carbon, did not provide strong anchoring sites for clusters. Nevertheless, this electrochemical system has the potential for further investigation using substrates with stronger binding. This would open the possibility of more detailed scanning probe work, such as in-situ measurements during electrochemistry [236, 65] to bridge the gap between pre- and post-reaction analysis.

The Tafel slopes in this work have been measured greater than 120 mV/decade, which is larger than the greatest true Tafel slope, limited to 120 mV by one electron transfer in the rate determining step (Section 3.5.8). Values greater than 120 mV/decade are indicative of resistance caused by an oxide barrier [237], which suggests the oxide layer is not dissolved during the timescale of the reaction. Pt has a Tafel slope of 30 mV/decade, consistent with the Volmer-Tafel HER mechanism (2 electrons transferred before rate determining step, Tafel desorption). MoS_2 in the literature has not been measured lower than 40 mV/decade (Section 2.4), consistent with the Volmer-Heyrovsky HER mechanism (1 electron transferred before the rate determining step followed by one more electron transfer in the rate determining step, Heyrovsky desorption). The discrepancy between

Tafel analysis in this study and the literature is attributed to the difficulties in quantifying the electron transfer through the oxide layer. Further experiments to discern the extent and structure of the oxide would be useful in rectifying this issue.

The oxidation noted in Chapter 4 can be correlated to the percentage of perimeter sites in Chapter 5, confirming the obvious assumption that the reactive edge sites should be the first to be oxidised. Correspondingly, in Chapter 6, the smallest clusters are shown to have the greatest normalised exchange current density due to the greater percentage of edge sites (Section 6.4.4). In general, normalisation by mass provides favourable comparison of reaction current for all the cluster samples with literature, putting them in the same region, and above, as some of the best chemically-prepared catalysts [24].

The current for clusters in 1mM $HClO_4$, the most reproducible system in this work, has been shown to scale ($x^{0.85}$) with the area rather than perimeter by comparison to growth relationships from Chapter 5. This indicates that the basal plane of the clusters is not inert, as the standard models suggest [111, 112]. The conclusion in this case is not that the model of active edge sites is flawed, but rather that these clusters effectively have extra edge sites in the form of incomplete top layers or defects in the basal plane, consistent with the percentage of oxidation seen in Chapter 4. These catalysts then form a bridge between the active sites seen in amorphous thin films and the usual edge sites in single crystal MoS_2.

CHAPTER 7

CONCLUSIONS AND OUTLOOK

7.1 Summary

Gas phase production of compound molybdenum disulphide (MoS_2) clusters has been demonstrated, based on the versatile magnetron sputtering gas condensation technique, followed by time-of-flight mass selection prior to deposition. Direct sputtering of an MoS_2 target without an additional sulphur source was used. The nucleation parameters were optimised to produce a platelet morphology presenting potentially active edge sites for catalysis. The stability of this structure was tested by parameter manipulation (Ar/He ratio) and post-deposition annealing. The novel size selection technique was applied to produce a controlled distribution of clusters, in the quantum confinement size regime, between 50 and 1936 units of MoS_2, capable of deposition on substrates for microscopy, surface science or electrochemistry. Scanning probe measurements have shown weak interaction of the MoS_2 clusters with both bare HOPG and heavily sputtered HOPG. This prevents atomic resolution measurements by scanning probe methods, necessitating the use of electron microscopy for structural characterisation.

Atomic-resolution STEM shows the hexagonal structure of bulk MoS_2 persists at the nanoscale, however the non-equilibrium nucleation process produces crystals rich in vacancies, interfaces and adatoms. These defects are active on exposure to atmosphere resulting in the addition of oxide species, to make an average composition of $MoS_{1.58}O_{1.36}$

for $(MoS_2)_{650}$, although the majority (49.3%) of each cluster remains in the stable Mo^{4+} state after 5 hours of exposure. This is demonstrated by XPS of $(MoS_2)_{350}$ and $(MoS_2)_{650}$ clusters and the absence of evidence for the cubic structure of MoO_3 in the STEM. The compound nature of individual clusters is shown by STEM EELS, although low signal to background prevents definitive quantitative analysis. The stoichiometry from one cluster to another is similar, shown by the HAADF intensity distribution.

The clusters suffer oxidation upon prolonged atmospheric exposure until they are almost entirely in the Mo^{5+} (23.7%) and Mo^{6+} (67.5%) state after 61 days. Thus for microscopy and catalytic experiments fresh clusters are produced and analysed within 2 days. The positive result of the XPS analysis, was that oxidation reactions took place not just on edge sites but on the supposedly inert basal plane. This indicates that the defects and incomplete layers produced by the non-equilibrium gas-phase growth has the potential to make very active catalysts.

The cluster growth mode has been identified by STEM as anisotropic, as expected due to the appearance of the bulk lamellar structure at the nanoscale. Clusters larger than $(MoS_2)_{350}$ display growth by coalescence of pre-formed clusters. Intensity calibration based on magic number gold mass standards was successfully used to test the accuracy of cluster mass selection, rule out fragmentation or aggregation on the surface as a cause of the observed cluster structures and confirm the charge state during mass selection. Gas-phase layer growth is observed by STEM for all sizes, reaching a maximum of 2.8 ± 0.7 layers at sizes larger than $(MoS_2)_{350}$, despite the relatively weak attractive force between layers. The growth of layers on top of a monolayer sheet in the gas-phase forms an ongoing collaboration with computational theorists, and could be due to growth from defect points in the monolayers.

The performance of the MoS_2 clusters for HER shows definite catalytic enhancement despite the oxidation and the very low catalyst loading on a planar support. The oxide layer is however a barrier to charge transfer, causing the lower than expected catalytic activity of these clusters. There is some evidence in the literature that MoO_3 is soluble in

aqueous media [207, 238], thus the oxide barrier may be removed to expose active edge sites during reaction, though this may be in competition with the decomposition reaction, which produces MoO_3 and H_2SO_4. Further pre and post reaction measurements are needed to determine the structural changes in the clusters due to these reactions. Additional XPS ensemble studies of the glassy carbon supported clusters would be effective in identifying the decomposition products, while chromatography of the electrolyte would improve understanding of the cluster solubility during reactions. Ideally these measurements should also be taken before atmospheric oxidation, by use of vacuum transfer techniques, to explore the active sites on the pristine clusters.

Nevertheless, the reaction kinetics of the active catalytic sites were investigated in more detail by using a low concentration of reactants to expose mass transport limitations. These were then compared to simulations of the system, which suggested the number of active sites was less than expected. This is in agreement with activity loss due to oxide charge transfer resistance and dissolution of the oxidised components.

The electrocatalytic properties of the clusters were confirmed by cyclic voltammetry, with an activity scaling relationship that most closely matches the perimeter scaling relationship measured by STEM. This confirms these platelet clusters obey the edge model [112] as expected. These low-coordination sites cause a much enhanced hydrogen evolution current compared with the bare glassy carbon surface. After normalisation to catalyst loading the MoS_2 clusters are comparable to the best MoS_2 catalysts prepared by chemical synthesis [24], but with the added benefit of simple characterisation and reduced contamination.

The goal of critical metal replacement, namely platinum by MoS_2, has clear potential from a basic cost-activity argument. The cost of Pt is \$44000/kg [239], while Mo is \$30/kg [240]. Thus an MoS_2 based catalyst can be 1000× poorer in performance and still have a greater performance/cost ratio than Pt. The exchange current density of the most active platinum facet, Pt(111), is 4.5E-4 A/cm^2, compared to 7.9E-6 A/cm^2 for MoS_2 monolayer platelets [18]. A similar level of activity is also seen for the clusters in this study (Fig 6.40).

Therefore, on a cost-activity basis nanoscale MoS_2 is approximately 25× better than Pt.

In conclusion, this work demonstrates a powerful fabrication method for size-selected nanoscale molybdenum disulphide (MoS_2) platelets. The clusters display layered atomic-scale structure and anisotropic growth in the gas-phase condensation process. Finally, and most significantly, the non-equilibrium growth provides a cluster morphology that makes best use of the available material to enhance HER activity. This is exactly what is needed for the main objective of critical metal replacement.

7.2 Future Investigations

The challenges associated with this work derive from lack of control over cluster composition in the nucleation phase, and the effects of atmospheric oxidation. The composition during nucleation can be controlled by decoupling the sources of Mo and S with the addition of H_2S gas in the Argon feed. The addition of such precursor gases could also be extended to producing other binary and ternary compounds to explore synergistic effects at the nanoscale.

One method of preventing the oxidation is to carry out in-situ UHV studies. The scope of these experiments could include spectrometry of clusters in flight with ion traps and UHV deposition for surface science analysis. In-situ analysis by laser spectrometry could be complimentary to sample deposition by providing a greater understanding of the type of clusters being produced rather than just the flux. Control over cluster composition would then provide a rich parameter space to explore in order to determine the effect on structure and properties. The use of a vacuum suitcase for UHV transfer between instruments would broaden the available characterisation techniques. The vacuum suitcase capability is currently available, however attachment is not sufficiently standardised to be compatible with most systems.

Another method of tackling the problems of oxidation is to extend the inert gas storage to the point of deposition so the clusters are never exposed to atmosphere. This would

require venting the load-lock chamber with argon and extracting samples into an argon filled container. Long term storage could be achieved by use of a glove box and an inert atmosphere desiccator. These protocols would lead to minor exposure to atmosphere, especially during the transfer processes between deposition and measurement, but the advantage is that it is much simpler and more versatile than achieving hard vacuum transfer. The transfer process is also compatible with non-vacuum instruments, such as electrochemical cells.

In addition to these protocols to control composition and reduce oxidation, post-processing functionality could be added in order to control the structure after deposition. In-situ annealing has the potential to equilibrate the structure to reduce the amount of low-coordination sites that become oxidised. The attempts at annealing ex-situ showed a tendency to produce spherical clusters due to sulphur loss, thus combining annealing with a gas inlet to dose sulphur might allow crystallisation to uniform MoS_2 platelets. The cyclic voltammetry of the poorly coordinated clusters in this study suggests that such sites are beneficial, so the fully crystalline platelets could then be processed electrochemically to induce defects. The crystalline form would merely serve as a less reactive state for use in transport. Dosing in-situ could also be extended to dopants, to decorate the edges, for use in improving the binding energy of reactants at the active sites or introducing co-catalysts.

This work has covered many aspects of characterisation, from spectrometry to microscopy and voltammetry. There remain many avenues of exploration for the future with MoS_2 clusters produced by the cluster beam technique that do not require modifications. Firstly, the transition between few-atom clusters and platelets in the gas-phase has not been studied in detail in this work. The study of this small size regime would give a greater understanding of how platelets nucleate in order to control the morphology and availability of reactive sites. Secondly, the promising results of electrochemical HER catalysis should be extended to the photo-electrochemical system. The electronic band structure of MoS_2 should be size-dependent and thus well suited to the cluster beam system. Enhanced HER activity by photo-excitation would push MoS_2 further towards the goal of Pt replacement.

In general, future studies should centre on control and functionalisation of the catalyst nanostructure, with cluster beam processing as an attractive option. Nanoparticles and clusters offer the opportunity to maximise useful reactions while minimising wasted material. The future of critical metal replacement relies on the use of novel morphologies to transform the properties of abundant materials, such as MoS_2.

APPENDIX A

RELATED COLLABORATIONS

A.1 Sulphidation of MoS_2/GC at Stanford University

Samples of MoS_2 clusters (50000 and 200000 amu) supported on GC disks were sent to Stanford for parallel analysis, performed by Jesse Benck, under supervision of Thomas Jaramillo. The samples, tested by similar methods, were of a low coverage, 2000 pAs, so activities were expected to be correspondingly reduced. XPS measurements before and after were taken to check for changes during reaction. The results match well with the results of this study (Fig A.1). The primary goal of the collaboration was the sulphidation of the clusters to remove oxide and restore crystallinity. Unfortunately the results of the sulphidation were inconclusive, showing little change, possibly due to excessive atmospheric exposure or the low cluster coverage.

A.2 MoS_2 Nanopillars at NPRL

A further collaboration, with DTU and a fellow NPRL member, Ahmed Abdela, was conducted on top-down fabrication of high aspect ratio MoS_2 nanostructures. This work required fabrication of MoS_2 thin films, prepared with assistance from Ander Laursen at DTU, for etching at NPRL. Finally the etched substrates were returned to DTU for

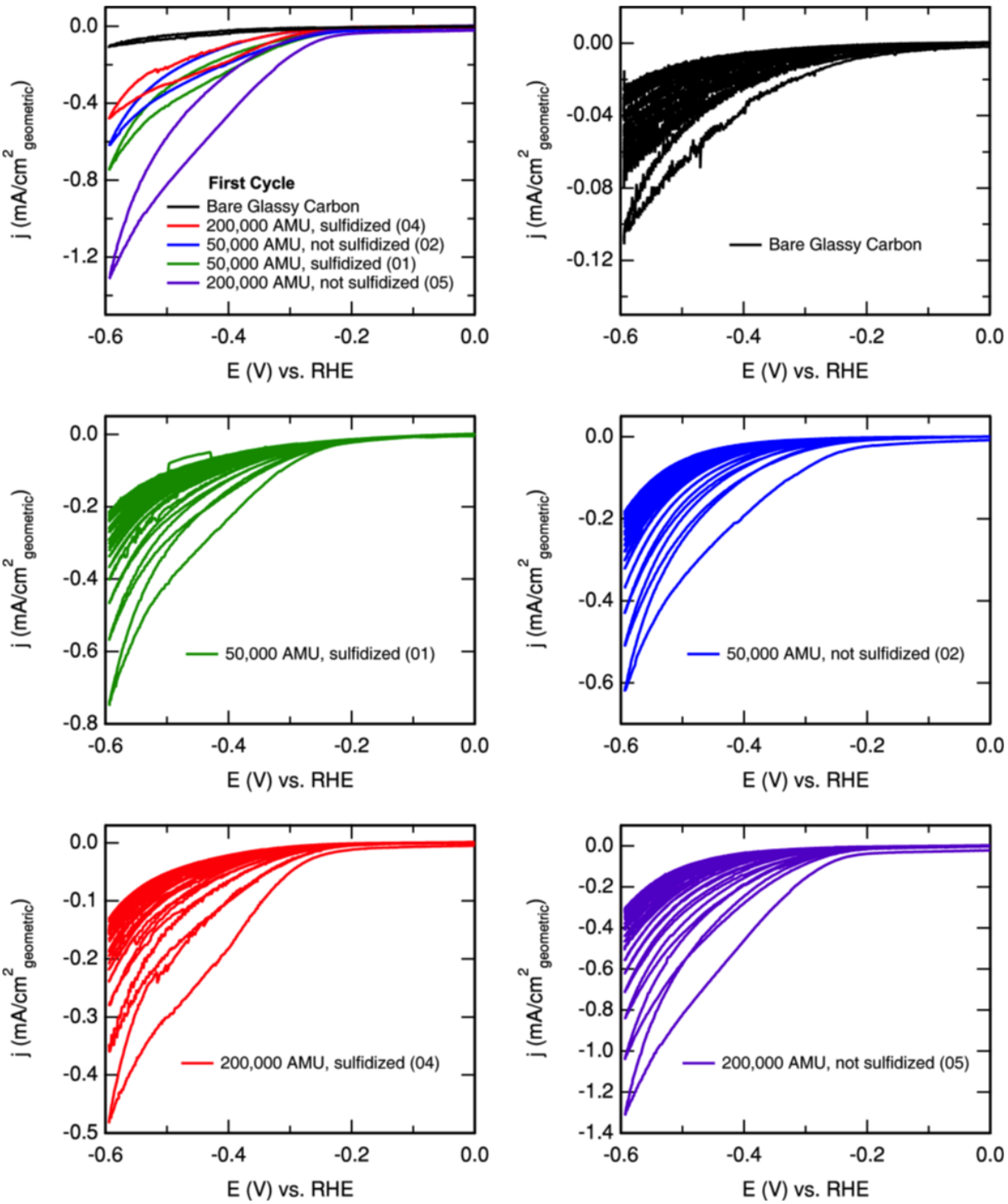

Figure A.1: HER activity for (MoS_2) clusters of 50000 and 200000 amu, as-made and sulphidised, were measured by cyclic voltammetry by Jesse Benck of Stanford University.

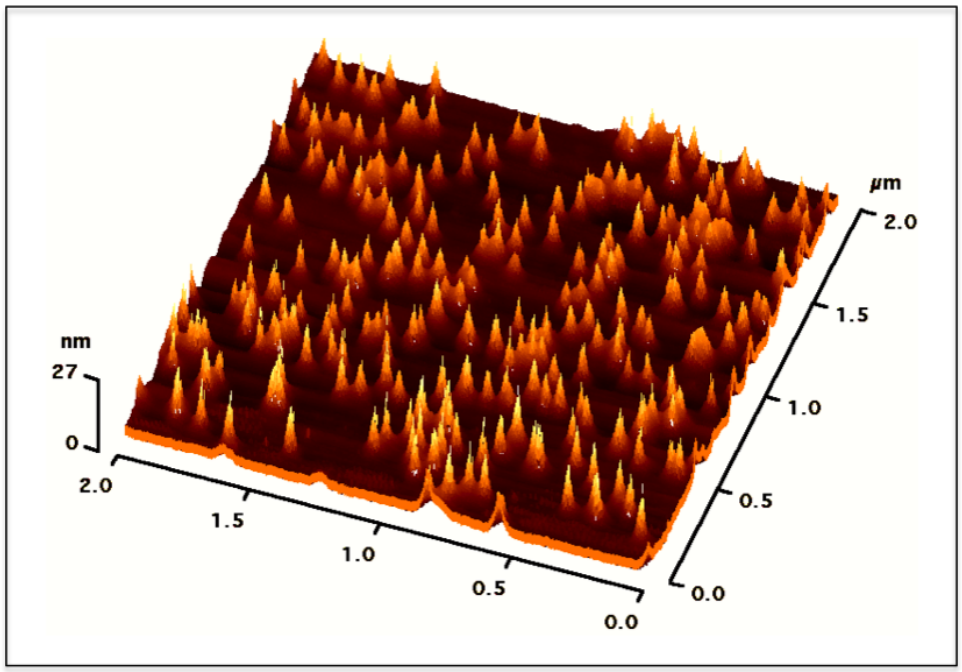

Figure A.2: MoS_2 nanopillars etched using size-selected Pd as an etch mask, courtesy of Ahmed Abdela

electrochemical testing, which required the design of a novel electrode.

The first nanopillar etch experiments were performed on bulk crystals (Fig A.2). The fragile crystals were too small to directly insert into the electrochemical apparatus, so I designed a simple technique to create more suitable electrodes (Fig A.3). First the etched crystal was placed on a copper sheet, and silver paste was applied to the edges up to the top layer, to provide good electrical contact from copper to the active layer. Finally a 1 mm $\times$ 1 mm hole was cut in Teflon tape and placed over the centre of the crystal. The exposed region containing nanopillars is tested electrochemically while the unetched crystal, copper substrate and silver paste is masked off.

The simple design could be refined further after problems encountered. The small mask hole made bubble formation a problem, once hydrogen bubbles formed they were difficult to remove, being strongly pinned in the hole. The adhesive on the Teflon tape is also exposed at the contact points around the perimeter of the masked area, although no obvious contamination peaks were noted on the cyclic voltammogram, the presence of an unknown chemical species is a concern.

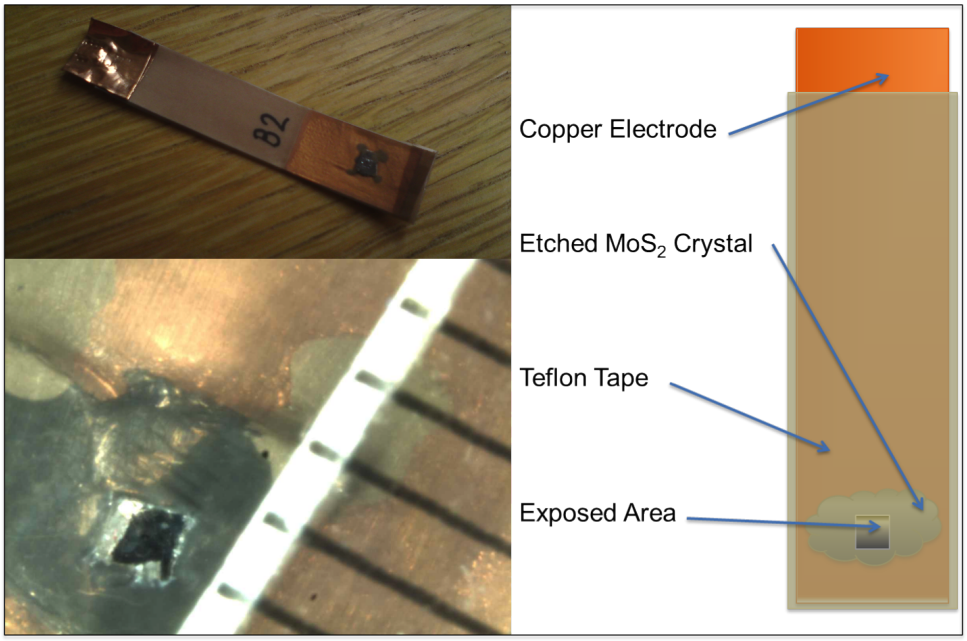

Figure A.3: Schematic of etched MoS_2 electrode construction. Mask measurement technique designed by Martin Cuddy.

These nanopillar electrodes were tested by Ahmed Abdela, using similar procedures to HER experiments in Chapter 6. The results showed decreasing activity with pillar height due to the increased resistance through the van der Waals planes. The most effective catalyst was a plasma roughened surface, consistent with the findings in this work that a high density of low-coordination sites improves activity.

LIST OF REFERENCES

[1] S. Shafiee and E. Topal, "When will fossil fuel reserves be diminished?," *Energy Policy*, vol. 37, pp. 181–189, Jan. 2009.

[2] S. Pacala and R. Socolow, "Stabilization wedges: solving the climate problem for the next 50 years with current technologies.," *Science (New York, N.Y.)*, vol. 305, pp. 968–72, Aug. 2004.

[3] I. Jain, "Hydrogen the fuel for 21st century," *International Journal of Hydrogen Energy*, vol. 34, no. 17, pp. 7368–7378, 2009.

[4] G. W. Crabtree, M. S. Dresselhaus, and M. V. Buchanan, "The Hydrogen Economy," *Physics Today*, vol. 57, no. 12, p. 39, 2004.

[5] M. Zach, C. Hagglund, D. Chakarov, and B. Kasemo, "Nanoscience and nanotechnology for advanced energy systems," *Current Opinion in Solid State and Materials Science*, vol. 10, no. 3-4, pp. 132–143, 2006.

[6] S. S. Mao, S. Shen, and L. Guo, "Nanomaterials for renewable hydrogen production, storage and utilization," *Progress in Natural Science: Materials International*, vol. 22, pp. 522–534, Dec. 2012.

[7] U. Sahaym and M. G. Norton, "Advances in the application of nanotechnology in enabling a hydrogen economy," *Journal of Materials Science*, vol. 43, no. 16, pp. 5395–5429, 2008.

[8] G. Marbán and T. Valdés-Solís, "Towards the hydrogen economy?," *International Journal of Hydrogen Energy*, vol. 32, no. 12, pp. 1625–1637, 2007.

[9] E. Serrano, G. Rus, and J. García-Martínez, "Nanotechnology for sustainable energy," *Renewable and Sustainable Energy Reviews*, vol. 13, no. 9, pp. 2373–2384, 2009.

[10] L. J. Minggu, W. R. Wan Daud, and M. B. Kassim, "An overview of photocells and photoreactors for photoelectrochemical water splitting," *International Journal of Hydrogen Energy*, vol. 35, pp. 5233–5244, June 2010.

[11] B. C. Steele and A. Heinzel, "Materials for fuel-cell technologies.," *Nature*, vol. 414, pp. 345–52, Nov. 2001.

[12] M. Conte, A. Iacobazzi, M. Ronchetti, and R. Vellone, "Hydrogen economy for a sustainable development: state-of-the-art and technological perspectives," *Journal of Power Sources*, vol. 100, pp. 171–187, 2001.

[13] C.-J. Yang, "An impending platinum crisis and its implications for the future of the automobile," *Energy Policy*, vol. 37, pp. 1805–1808, May 2009.

[14] V. W.-H. Lau, A. F. Masters, A. M. Bond, and T. Maschmeyer, "Ionic-Liquid-Mediated Active-Site Control of MoS(2) for the Electrocatalytic Hydrogen Evolution Reaction.," *Chemistry (Weinheim an der Bergstrasse, Germany)*, vol. 18, pp. 8230–9, June 2012.

[15] B. Hinnemann, P. G. Moses, J. Bonde, K. P. Jø rgensen, J. H. Nielsen, S. Horch, I. Chorkendorff, and J. K. Nø rskov, "Biomimetic hydrogen evolution: MoS2 nanoparticles as catalyst for hydrogen evolution.," *Journal of the American Chemical Society*, vol. 127, pp. 5308–9, Apr. 2005.

[16] T. R. Thurston and J. P. Wilcoxon, "Photooxidation of Organic Chemicals Catalyzed by Nanoscale MoS 2," *The Journal of Physical Chemistry B*, vol. 103, pp. 11–17, Jan. 1999.

[17] J. V. Lauritsen, M. Nyberg, R. T. Vang, M. V. Bollinger, B. S. Clausen, H. Topsoe, K. W. Jacobsen, E. L Gsgaard, J. K. N Rskov, and F. Besenbacher, "Chemistry of one-dimensional metallic edge states in MoS 2 nanoclusters," *Nanotechnology*, vol. 14, pp. 385–389, Mar. 2003.

[18] T. F. Jaramillo, K. P. Jø rgensen, J. Bonde, J. H. Nielsen, S. Horch, and I. Chorkendorff, "Identification of active edge sites for electrochemical H2 evolution from MoS2 nanocatalysts.," *Science (New York, N.Y.)*, vol. 317, pp. 100–2, July 2007.

[19] M. J. Patterson, J. M. Lightstone, and M. G. White, "Structure of molybdenum and tungsten sulfide M(x)S(y)+ clusters: experiment and DFT calculations.," *The journal of physical chemistry. A*, vol. 112, pp. 12011–21, Nov. 2008.

[20] A. B. Laursen, S. Kegnæ s, S. Dahl, and I. Chorkendorff, "Molybdenum sulfideseffi-cient and viable materials for electro - and photoelectrocatalytic hydrogen evolution," *Energy & Environmental Science*, vol. 5, no. 2, p. 5577, 2012.

[21] Z. Chen, D. Cummins, B. N. Reinecke, E. Clark, M. K. Sunkara, and T. F. Jaramillo, "Core-shell MoO3-MoS2 nanowires for hydrogen evolution: a functional design for electrocatalytic materials.," *Nano letters*, vol. 11, pp. 4168–75, Oct. 2011.

[22] R. Bichsel, P. Buffat, and F. Lévy, "Correlation between process conditions, chemical composition and morphology of MoS2 films," *Journal of Physics D: Applied Physics*, vol. 19, pp. 1575–1585, 1986.

[23] F. Lévy, "High-resolution cross-sectional studies and properties of molybdenite coatings," *Surface and Coatings Technology*, vol. 68-69, pp. 433–438, Dec. 1994.

[24] Y. Li, H. Wang, L. Xie, Y. Liang, G. Hong, and H. Dai, "MoS2 Nanoparticles Grown on Graphene: An Advanced Catalyst for the Hydrogen Evolution Reaction," *Journal of the American Chemical Society*, vol. 12, pp. 11398–406, Oct. 2011.

[25] B. Seger, A. B. Laursen, P. C. K. Vesborg, T. Pedersen, O. Hansen, S. Dahl, and I. Chorkendorff, "Hydrogen Production Using a Molybdenum Sulfide Catalyst on a Titanium-Protected n+p-Silicon Photocathode," *Angewandte Chemie International Edition*, pp. n/a–n/a, Aug. 2012.

[26] Q. Xiang, J. Yu, and M. Jaroniec, "Synergetic Effect of MoS(2) and Graphene as Cocatalysts for Enhanced Photocatalytic H(2) Production Activity of TiO(2) Nanoparticles.," *Journal of the American Chemical Society*, vol. 134, pp. 6575–8, Apr. 2012.

[27] F. Yin, Z. W. Wang, and R. E. Palmer, "Controlled formation of mass-selected Cu-Au core-shell cluster beams.," *Journal of the American Chemical Society*, vol. 133, pp. 10325–7, July 2011.

[28] J. M. Lightstone, H. a. Mann, M. Wu, P. M. Johnson, and M. G. White, "Gas-Phase Production of Molybdenum Carbide, Nitride, and Sulfide Clusters and Nanocrystallites," *The Journal of Physical Chemistry B*, vol. 107, pp. 10359–10366, Sept. 2003.

[29] H. Yasumatsu, "Generation of intense and cold beam of Pt-Ag bi-element cluster ions having single-composition," *The European Physical Journal D*, vol. 63, pp. 195–200, Mar. 2011.

[30] S.-W. Min, H. S. Lee, H. J. Choi, M. K. Park, T. Nam, H. Kim, S. Ryu, and S. Im, "Nanosheet thickness-modulated MoS2 dielectric property evidenced by field-effect transistor performance.," *Nanoscale*, vol. 5, pp. 548–51, Jan. 2013.

[31] M. Buscema, M. Barkelid, V. Zwiller, H. S. J. van der Zant, G. a. Steele, and A. Castellanos-Gomez, "Large and tunable photothermoelectric effect in single-layer MoS2.," *Nano letters*, vol. 13, pp. 358–63, Feb. 2013.

[32] X. Bian, J. Zhu, L. Liao, M. D. Scanlon, P. Ge, C. Ji, H. H. Girault, and B. Liu, "Nanocomposite of MoS2 on ordered mesoporous carbon nanospheres: A highly active catalyst for electrochemical hydrogen evolution," *Electrochemistry Communications*, vol. 22, pp. 128–132, Aug. 2012.

[33] H. I. Karunadasa, E. Montalvo, Y. Sun, M. Majda, J. R. Long, and C. J. Chang, "A Molecular MoS2 Edge Site Mimic for Catalytic Hydrogen Generation," *Science*, vol. 335, pp. 698–702, Feb. 2012.

[34] C. Zhang, H. B. Wu, Z. Guo, and X. W. D. Lou, "Facile synthesis of carbon-coated MoS2 nanorods with enhanced lithium storage properties," *Electrochemistry Communications*, vol. 20, pp. 7–10, July 2012.

[35] S. K. Das, R. Mallavajula, N. Jayaprakash, and L. Archer, "Self-assembled MoS2 carbon nanostructures: influence of nanostructuring and carbon on lithium battery performance," *Journal of Materials Chemistry*, vol. 22, no. 26, p. 12988, 2012.

[36] F. Wypych and R. Schöllhorn, "1T-MoS2, a new metallic modification of molybdenum disulfide," *Journal of the Chemical Society, Chemical . . .*, no. 1386, pp. 1386–1388, 1992.

[37] D. Yang, S. Sandoval, W. Divigalpitiya, J. Irwin, and R. Frindt, "Structure of single-molecular-layer MoS2," *Physical Review B*, vol. 43, no. 14, p. 12053, 1991.

[38] P. Joensen, R. Frindt, and S. Morrison, "Single-layer MoS2," *Materials Research Bulletin*, vol. 21, no. c, pp. 457–461, 1986.

[39] R. Hultgren, "Equivalent chemical bonds formed by s, p, and d eigenfunctions," *Physical Review*, vol. 40, 1932.

[40] B. C. Windom, W. G. Sawyer, and D. W. Hahn, "A Raman Spectroscopic Study of MoS2 and MoO3: Applications to Tribological Systems," *Tribology Letters*, vol. 42, pp. 301–310, Mar. 2011.

[41] T. Weber, J. C. Muijsers, J. H. M. C. V. Wolput, C. P. J. Verhagen, and J. W. Niemantsverdriet, "Basic Reaction Steps in the Sulfidation of Crystalline MoO3 to MoS2, As Studied by X-ray Photoelectron and Infrared Emission Spectroscopy," *J. Phys. Chem*, vol. 33, no. 100, pp. 14144–14150, 1996.

[42] F. L. Deepak, A. Mayoral, and M. J. Yacaman, "Faceted MoS2 nanotubes and nanoflowers," *Materials Chemistry and Physics*, vol. 118, no. 2-3, pp. 392–397, 2009.

[43] D. Kong, H. Wang, J. Cha, M. Pasta, and K. Koski, "Synthesis of MoS2 and MoSe2 films with vertically aligned layers," *Nano letters*, 2013.

[44] Y. Feldman, E. Wasserman, D. J. Srolovitz, and R. Tenne, "High-Rate, Gas-Phase Growth of MoS2 Nested Inorganic Fullerenes and Nanotubes.," *Science (New York, N.Y.)*, vol. 267, pp. 222–5, Jan. 1995.

[45] A. Zak and Y. Feldman, "Growth mechanism of MoS2 fullerene-like nanoparticles by gas-phase synthesis," *Journal of the American Chemical Society*, no. 13, pp. 11108–11116, 2000.

[46] R. Rosentsveig, A. Margolin, A. Gorodnev, R. Popovitz-Biro, Y. Feldman, L. Rapoport, Y. Novema, G. Naveh, and R. Tenne, "Synthesis of fullerene-like MoS2 nanoparticles and their tribological behavior," *Journal of Materials Chemistry*, vol. 19, no. 25, p. 4368, 2009.

[47] E. Barborini, P. Piseri, and P. Milani, "A pulsed microplasma source of high intensity supersonic carbon cluster beams," *Journal of Physics D: Applied Physics*, vol. 105, 1999.

[48] M. Jose-Yacaman, H. Lopez, P. Santiago, D. H. Galvan, I. L. Garzon, and a. Reyes, "Studies of MoS2 structures produced by electron irradiation," *Applied Physics Letters*, vol. 69, no. 8, p. 1065, 1996.

[49] K. S. Novoselov, A. Geim, S. V. Morozov, D. Jiang, Y. Zhang, S. V. Dubonos, I. V. Grigorieva, and a. a. Firsov, "Electric field effect in atomically thin carbon films.," *Science (New York, N.Y.)*, vol. 306, pp. 666–9, Oct. 2004.

[50] S. Balendhran, J. Z. Ou, M. Bhaskaran, S. Sriram, S. Ippolito, Z. Vasic, E. Kats, S. Bhargava, S. Zhuiykov, and K. Kalantar-Zadeh, "Atomically thin layers of MoS2 via a two step thermal evaporation-exfoliation method.," *Nanoscale*, vol. 4, pp. 461–6, Jan. 2012.

[51] A. Splendiani, L. Sun, Y. Zhang, T. Li, J. Kim, C.-Y. Chim, G. Galli, and F. Wang, "Emerging photoluminescence in monolayer MoS2.," *Nano letters*, vol. 10, pp. 1271–5, Apr. 2010.

[52] O. Lopez-Sanchez, D. Lembke, M. Kayci, A. Radenovic, and A. Kis, "Ultrasensitive photodetectors based on monolayer MoS2.," *Nature nanotechnology*, vol. 8, pp. 497–501, July 2013.

[53] K. Seeger and R. Palmer, "Fabrication of ordered arrays of silicon nanopillars," *Journal of Physics D: Applied Physics*, vol. 32, p. L129, Sept. 1999.

[54] Y. Huang, J. Wu, X. Xu, Y. Ho, G. Ni, Q. Zou, G. K. W. Koon, W. Zhao, a. H. Castro Neto, G. Eda, C. Shen, and B. Özyilmaz, "An innovative way of etching MoS2: Characterization and mechanistic investigation," *Nano Research*, vol. 6, pp. 200–207, Feb. 2013.

[55] Y. Liu, H. Nan, X. Wu, W. Pan, W. Wang, J. Bai, W. Zhao, L. Sun, X. Wang, and Z. Ni, "Layer-by-Layer Thinning of MoS2 by Plasma.," *ACS nano*, vol. 7, pp. 4202–9, May 2013.

[56] A. Sobczynski, "Molybdenum disulfide as a hydrogen evolution catalyst for water photodecomposition on semiconductors," *Journal of Catalysis*, vol. 131, pp. 156–166, Sept. 1991.

[57] P. K. Panigrahi and A. Pathak, "A novel route for the synthesis of nanotubes and fullerene-like nanostructures of molybdenum disulfide," *Materials Research Bulletin*, vol. 46, pp. 2240–2246, Dec. 2011.

[58] X. Zong, Y. Na, F. Wen, G. Ma, J. Yang, D. Wang, Y. Ma, M. Wang, L. Sun, and C. Li, "Visible light driven H(2) production in molecular systems employing colloidal MoS(2) nanoparticles as catalyst.," *Chemical communications (Cambridge, England)*, pp. 4536–8, Aug. 2009.

[59] D. Merki and X. Hu, "Recent developments of molybdenum and tungsten sulfides as hydrogen evolution catalysts," *Energy & Environmental Science*, pp. 3878–3888, 2011.

[60] D. Merki, H. Vrubel, L. Rovelli, S. Fierro, and X. Hu, "Fe, Co, and Ni ions promote the catalytic activity of amorphous molybdenum sulfide films for hydrogen evolution," *Chemical Science*, vol. 3, no. 8, p. 2515, 2012.

[61] S.-Y. Tai, C.-J. Liu, S.-W. Chou, F. S.-S. Chien, J.-Y. Lin, and T.-W. Lin, "Few-layer MoS2 nanosheets coated onto multi-walled carbon nanotubes as a low-cost and highly electrocatalytic counter electrode for dye-sensitized solar cells," *Journal of Materials Chemistry*, vol. 22, no. 47, p. 24753, 2012.

[62] J. Wilcoxon, D. Bliss, J. Martin, P. Newcomer, and GA, "Photocatalytic Semiconductor Clusters for Fuel Production," *DTIC*, no. October, 1995.

[63] J. Wilcoxon, "Method for the preparation of metal colloids in inverse micelles and product preferred by the method," *US Patent 5,147,841*, 1992.

[64] S. Ross and A. Sussman, "Surface oxidation of molybdenum disulfide," *The Journal of Physical Chemistry*, pp. 1953–1956, 1955.

[65] A. Gewirth and B. K. Niece, "Electrochemical Applications of in Situ Scanning Probe Microscopy.," *Chemical reviews*, vol. 97, pp. 1129–1162, June 1997.

[66] B. Abrams and J. Wilcoxon, "Nanosize Semiconductors for Photooxidation," *Critical Reviews in Solid State and Material Sciences*, vol. 30, no. 3, pp. 153–182, 2005.

[67] J. P. Wilcoxon, P. P. Newcomer, and G. A. Samara, "Synthesis and optical properties of MoS[sub 2] and isomorphous nanoclusters in the quantum confinement regime," *Journal of Applied Physics*, vol. 81, no. 12, p. 7934, 1997.

[68] S. Gemming, G. Seifert, N. Bertram, T. Fischer, M. Götz, and G. Ganteför, "One-dimensional (Mo3S3)n clusters: Building blocks of clusters materials and ideal nanowires for molecular electronics," *Chemical Physics Letters*, vol. 474, no. 1-3, pp. 127–131, 2009.

[69] S. Helveg, J. Lauritsen, E. Laegsgaard, I. Stensgaard, J. Norskov, B. Clausen, H. Topsoe, and F. Besenbacher, "Atomic-scale structure of single-layer MoS2 nanoclusters," *Physical review letters*, vol. 84, pp. 951–4, Jan. 2000.

[70] B. Hammer and J. Norskov, "Why gold is the noblest of all the metals," *Nature*, 1995.

[71] B. Hammer, Y. Morikawa, and J. Norskov, "CO chemisorption at metal surfaces and overlayers.," *Physical review letters*, vol. 76, pp. 2141–2144, Mar. 1996.

[72] M. Bollinger, K. Jacobsen, and J. Nø rskov, "Atomic and electronic structure of MoS2 nanoparticles," *Physical Review B*, vol. 67, p. 085410, Feb. 2003.

[73] J. V. Lauritsen, J. Kibsgaard, S. Helveg, H. Topsoe, B. S. Clausen, E. Laegsgaard, and F. Besenbacher, "Size-dependent structure of MoS2 nanocrystals," *Nature Nanotechnology*, vol. 2, pp. 53–58, Jan. 2007.

[74] H. Grönbeck, A. Curioni, and W. Andreoni, "Thiols and disulfides on the Au (111) surface: The headgroup-gold interaction," *Journal of the American Chemical Society*, no. 111, pp. 3839–3842, 2000.

[75] J. Kibsgaard, J. V. Lauritsen, E. Laegsgaard, B. S. Clausen, H. Topsø e, and F. Besenbacher, "Cluster-support interactions and morphology of MoS2 nanoclusters in a graphite-supported hydrotreating model catalyst.," *Journal of the American Chemical Society*, vol. 128, pp. 13950–8, Oct. 2006.

[76] Y. Yu, S. Huang, Y. Li, and S. Steinmann, "Layer-dependent Electrocatalysis of MoS2 for Hydrogen Evolution," *arXiv*, 2013.

[77] H. Schweiger, "Shape and Edge Sites Modifications of MoS2 Catalytic Nanoparticles Induced by Working Conditions: A Theoretical Study," *Journal of Catalysis*, vol. 207, pp. 76–87, Apr. 2002.

[78] N. Bertram, J. Cordes, Y. Kim, G. Gantefor, S. Gemming, and G. Seifert, "Nanoplatelets made from MoS2 and WS2," *Chemical Physics Letters*, vol. 418, no. 1-3, pp. 36–39, 2006.

[79] K. H. Hu, X. G. Hu, Y. F. Xu, and X. Z. Pan, "The effect of morphology and size on the photocatalytic properties of MoS2," *Reaction Kinetics, Mechanisms and Catalysis*, pp. 153–163, Mar. 2010.

[80] A. Carlsson, M. Brorson, and H. Topsoe, "Supported metal sulphide nanoclusters studied by HAADF-STEM.," *Journal of microscopy*, vol. 223, pp. 179–81, Sept. 2006.

[81] M. Bollinger, J. Lauritsen, K. Jacobsen, J. Norskov, S. Helveg, and F. Besenbacher, "One-Dimensional Metallic Edge States in MoS2," *Physical Review Letters*, vol. 87, no. 19, pp. 3–6, 2001.

[82] Q. H. Wang, K. Kalantar-Zadeh, A. Kis, J. N. Coleman, and M. S. Strano, "Electronics and optoelectronics of two-dimensional transition metal dichalcogenides.," *Nature nanotechnology*, vol. 7, pp. 699–712, Nov. 2012.

[83] L. King, W. Zhao, M. Chhowalla, D. J. Riley, and G. Eda, "Photoelectrochemical properties of chemically exfoliated MoS2," *Journal of Materials Chemistry A*, vol. 1, no. 31, p. 8935, 2013.

[84] A. K. Geim and I. V. Grigorieva, "Van der Waals heterostructures.," *Nature*, vol. 499, pp. 419–25, July 2013.

[85] Z. Huang, X. Peng, H. Yang, C. He, L. Xue, G. Hao, C. Zhang, W. Liu, X. Qi, and J. Zhong, "The structural, electronic and magnetic properties of bi-layered MoS2 with transition-metals doped in the interlayer," *RSC Advances*, vol. 3, no. 31, p. 12939, 2013.

[86] T. Olsen and K. Jacobsen, "Large Excitonic Effects in the Optical Properties of Monolayer MoS2," *arXiv*, pp. 0–3, 2011.

[87] H. Li, Q. Zhang, C. C. R. Yap, B. K. Tay, T. H. T. Edwin, A. Olivier, and D. Baillargeat, "From Bulk to Monolayer MoS2: Evolution of Raman Scattering," *Advanced Functional Materials*, pp. n/a–n/a, Jan. 2012.

[88] X. Zhang, W. Lauwerens, L. Stals, J. He, and J.-P. Celis, "Fretting wear rate of sulphur deficient MoS x coatings based on dissipated energy," *Journal of Materials Research*, vol. 16, pp. 3567–3574, Jan. 2011.

[89] H. Dimigen, H. Hubsch, P. Willich, and K. Reichelt, "Stoichiometry and friction properties of sputtered MoSx layers," *Thin Solid Films*, vol. 129, no. 1-2, pp. 79–91, 1985.

[90] D. Carre, P. Fleischauer, and J. Lince, "Effects of Argon-Ion Bombardment on the Basal Plan Surface of MoS2," *DTIC*, no. 3, pp. 805–808, 1987.

[91] H. Feng and J. Chen, "Effects of low-energy argon-ion bombardment on MoS2," *Journal of Physics C: Solid State Physics*, vol. 75, pp. 1–5, 1974.

[92] V. Weiss, "Reactive magnetron sputtering of molybdenum sulfide thin films: In situ synchrotron x-ray diffraction and transmission electron microscopy study," *Journal of Applied Physics*, vol. 95, no. 12, p. 7665, 2004.

[93] D. Merki, S. Fierro, H. Vrubel, and X. Hu, "Amorphous molybdenum sulfide films as catalysts for electrochemical hydrogen production in water," *Chemical Science*, vol. 2, no. 7, p. 1262, 2011.

[94] V. Bellido-González and A. Jones, "Tribological behaviour of high performance MoS 2 coatings produced by magnetron sputtering," *Surface and Coatings Technology*, vol. 97, pp. 687–693, 1997.

[95] M. Bar-Sadan, A. N. Enyashin, S. Gemming, R. Popovitz-Biro, S. Y. Hong, Y. Prior, R. Tenne, and G. Seifert, "Structure and stability of molybdenum sulfide fullerenes.," *The journal of physical chemistry. B*, vol. 110, pp. 25399–410, Dec. 2006.

[96] P. Parilla, A. Dillon, K. Jones, G. Riker, D. Schulz, D. Ginley, and M. Heben, "The first true inorganic fullerenes?," *Nature*, vol. 397, no. 6715, p. 114, 1999.

[97] I. Alexandrou, N. Sano, A. Burrows, R. R. Meyer, and H. Wang, "Structural investigation of MoS2 coreshell nanoparticles formed by an arc discharge in water," *Nanotechnology*, vol. 14, pp. 913–917, 2003.

[98] A. N. Enyashin, M. Bar-Sadan, J. Sloan, L. Houben, and G. Seifert, "Nanoseashells and Nanooctahedra of MoS 2 : Routes to Inorganic Fullerenes," *Chemistry of Materials*, vol. 21, no. 23, pp. 5627–5636, 2009.

[99] A. N. Enyashin, S. Gemming, M. Bar-Sadan, R. Popovitz-Biro, S. Y. Hong, Y. Prior, R. Tenne, and G. Seifert, "Structure and stability of molybdenum sulfide fullerenes.," *Angewandte Chemie (International ed. in English)*, vol. 46, no. 4, pp. 623–7, 2007.

[100] M. Remskar, A. Mrzel, Z. Skraba, A. Jesih, M. Ceh, J. Demsar, P. Stadelmann, F. Levy, and D. Mihailovic, "Self-assembly of subnanometer-diameter single-wall MoS2 nanotubes.," *Science (New York, N.Y.)*, vol. 292, no. 5516, pp. 479–81, 2001.

[101] L. Houben and A. Enyashin, "Diffraction from Disordered Stacking Sequences in MoS2 and WS2 Fullerenes and Nanotubes," *The Journal of Physical Chemistry C*, 2012.

[102] M. Bar Sadan, L. Houben, A. N. Enyashin, G. Seifert, and R. Tenne, "Atom by atom: HRTEM insights into inorganic nanotubes and fullerene-like structures.," *Proceedings of the National Academy of Sciences of the United States of America*, vol. 105, pp. 15643–8, Oct. 2008.

[103] J. Kibsgaard, Z. Chen, B. Reinecke, and T. Jaramillo, "Engineering the surface structure of MoS2 to preferentially expose active edge sites for electrocatalysis," *Nature Materials*, vol. 11, no. October, pp. 963–969, 2012.

[104] E. L. Miller, "IEA-HIA Task 26 Research and Development Progress in Renewable Hydrogen Production Through Photoelectrochemical Water Splitting," *Energy Procedia*, vol. 29, pp. 438–444, Jan. 2012.

[105] A. Fujishima, X. Zhang, and D. Tryk, "Heterogeneous photocatalysis: From water photolysis to applications in environmental cleanup," *International Journal of Hydrogen Energy*, vol. 32, no. 14, pp. 2664–2672, 2007.

[106] A. Kudo, "Development of photocatalyst materials for water splitting," *International Journal of Hydrogen Energy*, vol. 31, no. 2, pp. 197–202, 2006.

[107] A. Kudo and Y. Miseki, "Heterogeneous photocatalyst materials for water splitting.," *Chemical Society reviews*, vol. 38, no. 1, pp. 253–78, 2009.

[108] F. E. Osterloh, "Inorganic Materials as Catalysts for Photochemical Splitting of Water," *Chemistry of Materials*, vol. 20, pp. 35–54, Jan. 2008.

[109] S. Srinivasan and F. Salzano, "Prospects for hydrogen production by water electrolysis to be competitive with conventional methods," *International Journal of Hydrogen Energy*, vol. 2, no. 1, pp. 53–59, 1977.

[110] O. Ulleberg, "Modeling of advanced alkaline electrolyzers: a system simulation approach," *International Journal of Hydrogen Energy*, vol. 28, pp. 21–33, Jan. 2003.

[111] R. Chianelli, "The reactivity of MoS2 single crystal edge planes," *Journal of Catalysis*, vol. 92, pp. 56–63, Mar. 1985.

[112] M. Daage and R. Chianelli, "Structure-Function Relations in Molybdenum Sulfide Catalysts," *Journal of Catalysis*, vol. 149, no. 2, pp. 414–427, 1994.

[113] H. Tributsch and J. Bennett, "Electrochemistry and photochemistry of MoS2 layer crystals. I," *Journal of Electroanalytical Chemistry*, vol. 81, pp. 97–111, Aug. 1977.

[114] Z. Wu, B. Fang, Z. Wang, C. Wang, Z. Liu, F. Liu, W. Wang, A. Alfantazi, D. Wang, and D. P. Wilkinson, "MoS2 nanosheets: A designed structure with high active site density for the HER," *ACS Catalysis*, July 2013.

[115] J. Xie, H. Zhang, S. Li, R. Wang, and X. Sun, "DefectRich MoS2 Ultrathin Nanosheets with Additional Active Edge Sites for Enhanced Electrocatalytic Hydrogen Evolution," *Advanced Materials*, pp. 1–7, 2013.

[116] L. P. Hansen, Q. M. Ramasse, C. Kisielowski, M. Brorson, E. Johnson, H. Topsø e, and S. Helveg, "Atomic-Scale Edge Structures on Industrial-Style MoS2 Nanocatalysts," *Angewandte Chemie International Edition*, vol. 50, p. 10153, Aug. 2011.

[117] J. Bonde, P. G. Moses, T. F. Jaramillo, J. K. Nø rskov, and I. Chorkendorff, "Hydrogen evolution on nano-particulate transition metal sulfides," *Faraday Discussions*, vol. 140, p. 219, 2009.

[118] C. Zuriaga-Monroy, J.-M. Martínez-Magadán, E. Ramos, and R. Gómez-Balderas, "A DFT study of the electronic structure of cobalt and nickel mono-substituted MoS2 triangular nanosized clusters," *Journal of Molecular Catalysis A: Chemical*, vol. 313, no. 1-2, pp. 49–54, 2009.

[119] M. Ramos, D. Ferrer, E. Martinez-Soto, H. Lopez-Lippmann, B. Torres, G. Berhault, and R. R. Chianelli, "In-situ HRTEM study of the reactive carbide phase of Co/MoS2 catalyst.," *Ultramicroscopy*, vol. 127, pp. 64–9, Apr. 2013.

[120] L. Byskov, B. Hammer, J. Norskov, B. Clausen, and H. Topsoe, "Sulfur bonding in MoS 2 and Co-Mo-S structures," *Catalysis letters*, vol. 47, no. 3, pp. 177–182, 1997.

[121] J. Spirko, "Electronic structure and reactivity of defect MoS2 I. Relative stabilities of clusters and edges, and electronic surface states," *Surface Science*, vol. 542, no. 3, pp. 192–204, 2003.

[122] T. Jaramillo, J. Bonde, and J. Zhang, "Hydrogen evolution on supported incomplete cubane-type 4+ electrocatalysts," *The Journal of Physical Chemistry C*, no. 111, pp. 17492–17498, 2008.

[123] Y. Sakashita, Y. Araki, K. Honna, and H. Shimada, "Orientation and morphology of molybdenum sulfide catalysts supported on titania particles, observed by using high-resolution electron microscopy," *Applied Catalysis A: General*, vol. 197, pp. 247–253, May 2000.

[124] J. C. Tokash and B. E. Logan, "Electrochemical evaluation of molybdenum disulfide as a catalyst for hydrogen evolution in microbial electrolysis cells," *International Journal of Hydrogen Energy*, vol. 36, pp. 9439–9445, June 2011.

[125] H. Shimada, "Morphology and orientation of MoS2 clusters on Al2O3 and TiO2 supports and their effect on catalytic performance," *Catalysis Today*, vol. 86, pp. 17–29, Nov. 2003.

[126] X. Zong, G. Wu, H. Yan, G. Ma, J. Shi, F. Wen, L. Wang, and C. Li, "Photocatalytic H 2 Evolution on MoS 2 /CdS Catalysts under Visible Light Irradiation," *The Journal of Physical Chemistry C*, vol. 114, no. 4, pp. 1963–1968, 2010.

[127] B. Pourabbas and B. Jamshidi, "Preparation of MoS2 nanoparticles by a modified hydrothermal method and the photo-catalytic activity of MoS2/TiO2 hybrids in photo-oxidation of phenol," *Chemical Engineering Journal*, vol. 138, pp. 55–62, May 2008.

[128] I. Tacchini, E. Terrado, A. Ansón, and M. Martinez, "Preparation of a TiO2-MoS2 nanoparticle-based composite by solvothermal method with enhanced photoactivity for the degradation of organic molecules in water under UV light," *Micro & Nano Letters, IET*, vol. 6, no. 11, pp. 932–936, 2011.

[129] S. Min and G. Lu, "The Sites for High Efficient Photocatalytic Hydrogen Evolution on Limited-layered MoS2 Co-catalyst Confined on Graphene Sheets," *The Journal of Physical Chemistry C*, 2012.

[130] J. P. Wilcoxon, "Catalytic Photooxidation of Pentachlorophenol Using Semiconductor Nanoclusters," *The Journal of Physical Chemistry B*, vol. 104, no. 31, pp. 7334–7343, 2000.

[131] K. H. Hu, Z. Liu, F. Huang, X. G. Hu, and C. L. Han, "Synthesis and photocatalytic properties of nano-MoS2/kaolin composite," *Chemical Engineering Journal*, vol. 162, pp. 836–843, Aug. 2010.

[132] M. Gratzel, "Photoelectrochemical cells," *Nature*, vol. 414, no. November, p. 338, 2001.

[133] H. Kato, K. Asakura, and A. Kudo, "Highly efficient water splitting into H2 and O2 over lanthanum-doped NaTaO3 photocatalysts with high crystallinity and surface nanostructure.," *Journal of the American Chemical Society*, vol. 125, pp. 3082–9, Mar. 2003.

[134] Y. Liu, Y. Yu, and W. Zhang, "MoS2/CdS Heterojunction with High Photoelectrochemical Activity for H2 Evolution Under Visible Light: The Role of MoS2," *The Journal of Physical Chemistry C*, 2013.

[135] Y.-P. Yuan, S.-W. Cao, L.-S. Yin, L. Xu, and C. Xue, "NiS2 Co-catalyst decoration on CdLa2S4 nanocrystals for efficient photocatalytic hydrogen generation under visible light irradiation," *International Journal of Hydrogen Energy*, vol. 38, pp. 7218–7223, June 2013.

[136] J. Yang, H. Yan, and X. Zong, "Roles of cocatalysts in semiconductor-based photocatalytic hydrogen production," *Philosophical Transactions of the Royal Society A*, no. July, 2013.

[137] D. Ravelli, D. Dondi, M. Fagnoni, and A. Albini, "Photocatalysis. A multi-faceted concept for green chemistry.," *Chemical Society reviews*, vol. 38, no. 7, pp. 1999–2011, 2009.

[138] F. A. Frame and F. E. Osterloh, "CdSe-MoS 2 : A Quantum Size-Confined Photocatalyst for Hydrogen Evolution from Water under Visible Light," *The Journal of Physical Chemistry C*, vol. 114, pp. 10628–10633, June 2010.

[139] Y. Hou, B. Abrams, P. Vesborg, M. Björketun, K. Herbst, L. Bech, A. Setti, C. Damsgaard, T. Pedersen, O. Hansen, and Others, "Bioinspired molecular cocatalysts bonded to a silicon photocathode for solar hydrogen evolution," *Nature Materials*, no. April, pp. 1–5, 2011.

[140] X. Guo, X. Tong, Y. Wang, C. Chen, G. Jin, and X.-Y. Guo, "High photoelectrocatalytic performance of a MoS2SiC hybrid structure for hydrogen evolution reaction," *Journal of Materials Chemistry A*, vol. 1, no. 15, p. 4657, 2013.

[141] O. Goldbart, O. Elianov, D. Shumalinsky, L. Lobik, S. Cytron, R. Rosentsveig, H. D. Wagner, and R. Tenne, "Study of urological devices coated with fullerene-like nanoparticles.," *Nanoscale*, vol. 5, pp. 8526–32, Aug. 2013.

[142] R. Tenne and M. Redlich, "Recent progress in the research of inorganic fullerene-like nanoparticles and inorganic nanotubes.," *Chemical Society reviews*, vol. 39, pp. 1423–34, May 2010.

[143] P.-Y. Prodhomme, P. Raybaud, and H. Toulhoat, "Free-energy profiles along reduction pathways of MoS2 M-edge and S-edge by dihydrogen: A first-principles study," *Journal of Catalysis*, vol. 280, pp. 178–195, June 2011.

[144] B. Kim, M. Park, M. Lee, S. Baek, and H. Jeong, "Effect of Sulphur Vacancy on Geometric and Electronic Structure of MoS2 Induced by Molecular Hydrogen Treatment at Room Temperature," *RSC Adv.*, no. 207890, 2013.

[145] M. Brorson, A. Carlsson, and H. Topsoe, "The morphology of MoS2, WS2, CoMoS, NiMoS and NiWS nanoclusters in hydrodesulfurization catalysts revealed by HAADF-STEM," *Catalysis Today*, vol. 123, pp. 31–36, May 2007.

[146] L. Benoist, D. Gonbeau, and G. Pfister-Guillouzo, "XPS analysis of oxido-reduction mechanisms during lithium intercalation in amorphous molybdenum oxysulfide thin films," *Solid state ionics*, vol. 76, pp. 81–89, 1995.

[147] J. Xiao, D. Choi, L. Cosimbescu, P. Koech, J. Liu, and J. P. Lemmon, "Exfoliated MoS 2 Nanocomposite as an Anode Material for Lithium Ion Batteries," *Chemistry of Materials*, p. 100730114233099, July 2010.

[148] C. Feng, J. Ma, H. Li, R. Zeng, Z. Guo, and H. Liu, "Synthesis of molybdenum disulfide (MoS2) for lithium ion battery applications," *Materials Research Bulletin*, vol. 44, pp. 1811–1815, Sept. 2009.

[149] S. Butler, S. Hollen, L. Cao, and Y. Cui, "Progress, Challenges, and Opportunities in Two-Dimensional Materials Beyond Graphene.," *ACS nano*, no. 4, pp. 2898–2926, 2013.

[150] B. Radisavljevic, M. B. Whitwick, and A. Kis, "Integrated Circuits and Logic Operations Based on Single-Layer MoS2," *ACS nano*, vol. 5, pp. 9934–8, Dec. 2011.

[151] K.-K. Liu, W. Zhang, Y.-H. Lee, Y.-C. Lin, M.-T. Chang, C.-Y. Su, C.-S. Chang, H. Li, Y. Shi, H. Zhang, C.-S. Lai, and L.-J. Li, "Growth of large-area and highly crystalline MoS2 thin layers on insulating substrates.," *Nano letters*, vol. 12, pp. 1538–44, Mar. 2012.

[152] Y.-H. Lee, X.-Q. Zhang, W. Zhang, M.-T. Chang, C.-T. Lin, K.-D. Chang, Y.-C. Yu, J. T.-W. Wang, C.-S. Chang, L.-J. Li, and T.-W. Lin, "Synthesis of large-area MoS2 atomic layers with chemical vapor deposition.," *Advanced materials (Deerfield Beach, Fla.)*, vol. 24, pp. 2320–5, May 2012.

[153] Y. Zhan, Z. Liu, S. Najmaei, P. M. Ajayan, and J. Lou, "Large-Area Vapor-Phase Growth and Characterization of MoS(2) Atomic Layers on a SiO(2) Substrate.," *Small (Weinheim an der Bergstrasse, Germany)*, pp. 966–971, Feb. 2012.

[154] H. Haberland, "Thin films from energetic cluster impact: A feasibility study," *Journal of Vacuum Science & Technology A: Vacuum, Surfaces, and Films*, vol. 10, p. 3266, Sept. 1992.

[155] S. Pratontep, S. J. Carroll, C. Xirouchaki, M. Streun, and R. E. Palmer, "Size-selected cluster beam source based on radio frequency magnetron plasma sputtering and gas condensation," *Review of Scientific Instruments*, vol. 76, no. 4, p. 045103, 2005.

[156] R. Neuendorf, R. Palmer, and R. Smith, "Low energy deposition of size-selected Si clusters onto graphite," *Chemical Physics Letters*, vol. 333, no. January, pp. 304–307, 2001.

[157] C. Grimaud and R. Palmer, "Implantation of Pt3-and Ag3-clusters into graphite: an STM study," *Journal of Physics: Condensed Matter*, vol. 1869, pp. 13–17, 2001.

[158] V. N. Popok, I. Barke, E. E. Campbell, and K.-H. Meiwes-Broer, "Clustersurface interaction: From soft landing to implantation," *Surface Science Reports*, vol. 66, pp. 347–377, Oct. 2011.

[159] S. Duckett, *Spectroscopic Properties of Inorganic and Organometallic Compounds*, vol. 43 of *Spectroscopic Properties of Inorganic and Organometallic Compounds*. Cambridge: Royal Society of Chemistry, 47 ed., 2012.

[160] C. Wagner, D. Briggs, and M. Seah, "Practical surface analysis," *Auger and X-Ray Photoelectron Spectroscopy*, 1990.

[161] J. Moulder, *Handbook of x-ray photoelectron spectroscopy : a reference book of standard spectra for identification and interpretation of XPS data*. 1992.

[162] Z. Wang, "Intensity calibration and atomic imaging of size-selected Au and Pd clusters in aberration-corrected HAADF-STEM," *Journal of Physics: Conference Series*, pp. 11–14, 2012.

[163] C. Wang, D. van der Vliet, K. L. More, N. J. Zaluzec, S. Peng, S. Sun, H. Daimon, G. Wang, J. Greeley, J. Pearson, A. P. Paulikas, G. Karapetrov, D. Strmcnik, N. M. Markovic, and V. R. Stamenkovic, "Multimetallic Au/FePt3 nanoparticles as highly durable electrocatalyst.," *Nano letters*, vol. 11, pp. 919–26, Mar. 2011.

[164] Z. W. Wang and R. E. Palmer, "Mass spectrometry and dynamics of gold adatoms observed on the surface of size-selected Au nanoclusters.," *Nano letters*, vol. 12, pp. 91–5, Jan. 2012.

[165] P. J. F. Harris , "Fullerene-related structure of commercial glassy carbons," *Philosophical Magazine*, vol. 84, pp. 3159–3167, Oct. 2004.

[166] S. Fletcher, "Tafel slopes from first principles," *Journal of Solid State Electrochemistry*, vol. 13, pp. 537–549, Oct. 2008.

[167] N. Markovic, B. Grgur, and P. Ross, "Temperature-dependent hydrogen electrochemistry on platinum low-index single-crystal surfaces in acid solutions," *The Journal of Physical Chemistry B*, vol. 5647, no. 97, pp. 5405–5413, 1997.

[168] B. Conway and B. Tilak, "Interfacial processes involving electrocatalytic evolution and oxidation of H 2, and the role of chemisorbed H," *Electrochimica acta*, vol. 47, 2002.

[169] S. Ahmed, "Surface and photoelectrochemical studies of semiconducting MoS2," *Electrochimica Acta*, vol. 27, no. 6, pp. 707–712, 1982.

[170] S. Berger, A. Synytska, L. Ionov, K.-J. Eichhorn, and M. Stamm, "Stimuli-Responsive Bicomponent Polymer Janus Particles by Grafting from/Grafting to Approaches," *Macromolecules*, vol. 41, pp. 9669–9676, Dec. 2008.

[171] E. Benavente, M. Santa Ana, F. Mendizabal, and G. Gonzalez, "Intercalation chemistry of molybdenum disulfide," *Coordination Chemistry Reviews*, vol. 224, no. 1-2, pp. 87–109, 2002.

[172] N. Bertram, Y. Kim, G. Ganteför, Q. Sun, P. Jena, J. Tamuliene, and G. Seifert, "Experimental and theoretical studies on inorganic magic clusters: M4X6 (M=W, Mo, X=O, S)," *Chemical Physics Letters*, vol. 396, no. 4-6, pp. 341–345, 2004.

[173] A. Hashimoto, K. Suenaga, K. Urita, T. Shimada, T. Sugai, S. Bandow, H. Shinohara, and S. Iijima, "Atomic Correlation Between Adjacent Graphene Layers in Double-Wall Carbon Nanotubes," *Physical Review Letters*, vol. 94, p. 045504, Feb. 2005.

[174] J. Rivière and S. Myhra, *Handbook of surface and interface analysis: Methods for problem-solving*. 2010.

[175] C. R. Brundle and A. F. Carley, "XPS and UPS studies of the adsorption of small molecules on polycrystalline Ni films," *Faraday Discussions of the Chemical Society*, vol. 60, p. 51, 1975.

[176] A. Brooks, C. Clayton, K. Doss, and Y. Lu, "On the Role of Cr in the Passivity of Stainless Steel," *Journal of The Electrochemical Society*, 1986.

[177] A. Galtayries, C. Cousi, S. Zanna, and P. Marcus, "SO2 adsorption at room temperature on Ni(111) surface studied by XPS," *Surface and Interface Analysis*, vol. 36, pp. 997–1000, Aug. 2004.

[178] D. Genuit, I. Bezverkhyy, and P. Afanasiev, "Solution preparation of the amorphous molybdenum oxysulfide MoOS2 and its use for catalysis," *Journal of Solid State Chemistry*, vol. 178, pp. 2759–2765, Sept. 2005.

[179] V. Yufit, D. Golodnitsky, L. Burstein, M. Nathan, and E. Peled, "X-ray Photoelectron Spectroscopy and Time-Of-Flight Secondary Ion Mass Spectroscopy studies of electrodeposited molybdenum oxysulfide cathodes for lithium and lithium-ion microbatteries," *Journal of Solid State Electrochemistry*, vol. 12, pp. 273–285, Aug. 2007.

[180] P. Spevack and N. McIntyre, "A Raman and XPS investigation of supported molybdenum oxide thin films. 2. Reactions with hydrogen sulfide," *The Journal of Physical Chemistry*, vol. 97, no. 42, pp. 11031–11036, 1993.

[181] A. Aubert, J. Nabot, J. Ernoult, and P. Renaux, "Preparation and properties of MoS x films grown by dc magnetron sputtering," *Surface and Coatings Technology*, vol. 41, pp. 127–134, 1990.

[182] N. Mikkelsen and G. Sorensen, "Solid lubricating films produced by ion bombardment of sputter deposited MoS x films," *Surface and Coatings Technology*, vol. 51, pp. 118–123, 1992.

[183] X. Zhang, P. Zhang, H. Liu, W. Zhao, and S. Xu, "The microstructure and tribology of MoSx films modified by ion beam bombardment," *Thin Solid Films*, vol. 229, pp. 58–62, June 1993.

[184] N. Renevier, V. Fox, D. Teer, and J. Hampshire, "Coating characteristics and tribological properties of sputter-deposited MoS2/metal composite coatings deposited by closed field unbalanced magnetron sputter ion plating," *Surface and Coatings Technology*, vol. 127, pp. 24–37, May 2000.

[185] M. Di Vece, S. Palomba, and R. Palmer, "Pinning of size-selected gold and nickel nanoclusters on graphite," *Physical Review B*, vol. 72, p. 073407, Aug. 2005.

[186] J. Schindelin, I. Arganda-Carreras, E. Frise, V. Kaynig, M. Longair, T. Pietzsch, S. Preibisch, C. Rueden, S. Saalfeld, B. Schmid, J.-Y. Tinevez, D. J. White, V. Hartenstein, K. Eliceiri, P. Tomancak, and A. Cardona, "Fiji: an open-source platform for biological-image analysis.," *Nature methods*, vol. 9, pp. 676–82, Jan. 2012.

[187] Z. Wang and R. Palmer, "Determination of the Ground-State Atomic Structures of Size-Selected Au Nanoclusters by Electron-Beam-Induced Transformation," *Physical Review Letters*, vol. 108, pp. 1–5, June 2012.

[188] D. Su, H. Wang, and E. Zeitler, "The influence of plural scattering on EELS elemental analysis," *Ultramicroscopy*, vol. 59, pp. 181–190, July 1995.

[189] R. Egerton, R. McLeod, F. Wang, and M. Malac, "Basic questions related to electron-induced sputtering in the TEM," *Ultramicroscopy*, vol. 110, pp. 991–997, July 2010.

[190] Y. Kudriavtsev, A. Villegas, A. Godines, and R. Asomoza, "Calculation of the surface binding energy for ion sputtered particles," *Applied Surface Science*, vol. 239, pp. 273–278, Jan. 2005.

[191] a. Enyashin, S. Gemming, and G. Seifert, "Nanosized allotropes of molybdenum disulfide," *The European Physical Journal Special Topics*, vol. 149, no. 1, pp. 103–125, 2007.

[192] R. Dickinson and L. Pauling, "The crystal structure of molybdenite," *Journal of the American Chemical Society*, vol. 45, no. 1922, pp. 1466–1471, 1923.

[193] P. Young, "Lattice parameter measurements on molybdenum disulphide," *Journal of Physics D: Applied Physics*, vol. 936, 1968.

[194] B. Stegemann, B. Kaiser, and K. Rademann, "Subsequent layer growth of supported nanoparticles by deposition of Sb4 clusters onto MoS2 (0001)," *New Journal of Physics*, vol. 89, 2002.

[195] C. F. Castro-Guerrero, F. L. Deepak, A. Ponce, J. Cruz-Reyes, M. D. Valle-Granados, S. Fuentes-Moyado, D. H. Galván, and M. José-Yacamán, "Structure and catalytic properties of hexagonal molybdenum disulfide nanoplates," *Catalysis Science & Technology*, vol. 1, no. 6, 2011.

[196] M. Disko, "Spatially resolved electron energy-loss spectroscopy of MoS2 platelets," *Ultramicroscopy*, vol. 23, no. 3-4, pp. 313–319, 1987.

[197] S. Najmaei, Z. Liu, W. Zhou, X. Zou, G. Shi, S. Lei, B. I. Yakobson, J.-C. Idrobo, P. M. Ajayan, and J. Lou, "Vapour phase growth and grain boundary structure of molybdenum disulphide atomic layers.," *Nature materials*, vol. 12, pp. 754–9, Aug. 2013.

[198] D. Kim, D. Sun, W. Lu, Z. Cheng, Y. Zhu, D. Le, T. S. Rahman, and L. Bartels, "Toward the Growth of an Aligned Single-Layer MoS(2) Film.," *Langmuir : the ACS journal of surfaces and colloids*, pp. 0–3, Aug. 2011.

[199] Y. Shi, W. Zhou, A.-Y. Lu, W. Fang, Y.-H. Lee, A. L. Hsu, S. M. Kim, K. K. Kim, H. Y. Yang, L.-J. Li, J.-C. Idrobo, and J. Kong, "van der Waals epitaxy of MoS layers using graphene as growth templates.," *Nano letters*, vol. 12, pp. 2784–91, June 2012.

[200] W. Zhou, Z. Yin, Y. Du, X. Huang, Z. Zeng, Z. Fan, H. Liu, J. Wang, and H. Zhang, "Synthesis of Few-Layer MoS(2) Nanosheet-Coated TiO(2) Nanobelt Heterostructures for Enhanced Photocatalytic Activities.," *Small*, vol. 9, pp. 140–7, Jan. 2013.

[201] H. Rydberg, M. Dion, N. Jacobson, E. Schröder, P. Hyldgaard, S. Simak, D. Langreth, and B. Lundqvist, "Van der Waals Density Functional for Layered Structures," *Physical Review Letters*, vol. 91, pp. 1–4, Sept. 2003.

[202] T. Björkman and A. Gulans, "Van der Waals bonding in layered compounds from advanced density-functional first-principles calculations," *Physical Review Letters*, vol. 108, June 2012.

[203] K. Lee, H.-Y. Kim, M. Lotya, J. N. Coleman, G.-T. Kim, and G. S. Duesberg, "Electrical Characteristics of Molybdenum Disulfide Flakes Produced by Liquid Exfoliation," *Advanced Materials*, pp. n/a–n/a, Aug. 2011.

[204] T. Liu, Y. Xie, and B. Chu, "Use of block copolymer micelles on formation of hollow MoO3 nanospheres," *Langmuir*, vol. 15, no. 10, pp. 9015–9022, 2000.

[205] C. Ataca and S. Ciraci, "Dissociation of H_{2}O at the vacancies of single-layer MoS_{2}," *Physical Review B*, vol. 85, pp. 1–6, May 2012.

[206] H. Vrubel, D. Merki, and X. Hu, "Hydrogen evolution catalyzed by MoS3 and MoS2 particles," *Energy & Environmental Science*, 2012.

[207] T. Arnoldussen, "Electrochromism and photochromism in MoO3 films," *Journal of the Electrochemical Society*, vol. 123, no. 4, pp. 527–531, 1976.

[208] V. Habibpour, M. Y. Song, Z. W. Wang, J. Cookson, C. M. Brown, P. T. Bishop, and R. E. Palmer, "Novel Powder-Supported Size-Selected Clusters for Heterogeneous Catalysis under Realistic Reaction Conditions," *The Journal of Physical Chemistry C*, vol. 116, pp. 26295–26299, Dec. 2012.

[209] J. Zaman, "Production of hydrogen and sulfur from hydrogen sulfide," *Fuel Processing Technology*, vol. 41, pp. 159–198, Jan. 1995.

[210] E. Ponomarev, "Electrochemical deposition of MoS2 thin films by reduction of tetrathiomolybdate," *Thin Solid Films*, vol. 280, pp. 86–89, July 1996.

[211] D. H. Galvan, A. P. Amarillas, and M. José-Yacamán, "Metallic States at the Edges of MoS2 Clusters," *Catalysis Letters*, vol. 132, no. 3-4, pp. 323–328, 2009.

[212] P. Afanasiev, "The influence of reducing and sulfiding conditions on the properties of unsupported MoS2-based catalysts," *Journal of Catalysis*, vol. 269, no. 2, pp. 269–280, 2010.

[213] Q. Li, J. Newberg, E. Walter, J. Hemminger, and R. Penner, "Polycrystalline Molybdenum Disulfide (2H MoS2) Nano-and Microribbons by Electrochemical/Chemical Synthesis," *Nano Letters*, vol. 4, pp. 277–281, Feb. 2004.

[214] G. Camachobragado, J. Elechiguerra, A. Olivas, S. Fuentes, D. Galvan, and M. Yacaman, "Structure and catalytic properties of nanostructured molybdenum sulfides," *Journal of Catalysis*, vol. 234, no. 1, pp. 182–190, 2005.

[215] X. Wang, Y. Yan, X. Ge, Z. Liu, J. Wang, and J. Lee, "Facile synthesis of low crystalline MoS2 nanosheet-coated CNTs for enhanced hydrogen evolution reaction," *Nanoscale*, no. 207890, 2013.

[216] E. W. Finckh, S. Lu, A. Leist, S. Stauf, and S. Lo, "Semiporous MoS2 obtained by the decomposition of thiomolybdate precursors," *J. Mater. Chem.*, vol. 8, no. 1, pp. 241–244, 1998.

[217] M. Polyakov, S. Indris, S. Schwamborn, a. Mazheika, M. Poisot, L. Kienle, W. Bensch, M. Muhler, and W. Grunert, "Mechanochemical activation of MoS2Surface properties and catalytic activities in hydrogenation and isomerization of alkenes and in H2/D2 exchange," *Journal of Catalysis*, vol. 260, pp. 236–244, Dec. 2008.

[218] C. J. Wright, C. Sampson, D. Fraser, R. B. Moyes, P. B. Wells, and C. Riekel, "Hydrogen sorption by molybdenum sulphide catalysts," *Journal of the Chemical Society, Faraday Transactions 1*, vol. 76, p. 1585, 1980.

[219] N. Elizondo-Villarreal, R. Velázquez-Castillo, D. H. Galván, a. Camacho, and M. José Yacamán, "Structure and catalytic properties of molybdenum sulfide nanoplatelets," *Applied Catalysis A: General*, vol. 328, pp. 88–97, Aug. 2007.

[220] T. Prasad, E. Diemann, and A. Müller, "Thermal decomposition of (NH4)2MoO2S2, (NH4)2MoS4, (NH4)2WO2S2 and (NH4)2WS4," *Journal of Inorganic and Nuclear Chemistry*, vol. 35, pp. 1895–1904, June 1973.

[221] P. D. Tran, M. Nguyen, S. S. Pramana, A. Bhattacharjee, S. Y. Chiam, J. Fize, M. J. Field, V. Artero, L. H. Wong, J. Loo, and J. Barber, "Copper molybdenum sulfide: a new efficient electrocatalyst for hydrogen production from water," *Energy & Environmental Science*, vol. 5, no. 10, p. 8912, 2012.

[222] D.-T. Pham, K. Gentz, C. Zorlein, N. T. M. Hai, S.-L. Tsay, B. Kirchner, S. Kossmann, K. Wandelt, and P. Broekmann, "Surface redox chemistry of adsorbed viologens on Cu(100)," *New Journal of Chemistry*, vol. 30, no. 10, p. 1439, 2006.

[223] A. B. Laursen, P. C. K. Vesborg, and I. Chorkendorff, "A high-porosity carbon molybdenum sulphide composite with enhanced electrochemical hydrogen evolution and stability.," *Chemical communications (Cambridge, England)*, vol. 49, pp. 4965–7, May 2013.

[224] J. Greeley, I. Stephens, A. Bondarenko, T. Johansson, H. Hansen, T. Jaramillo, J. Rossmeisl, I. Chorkendorff, and J. Nø rskov, "Alloys of platinum and early transition metals as oxygen reduction electrocatalysts," *Nature Chemistry*, vol. 1, no. 7, pp. 552–556, 2009.

[225] P. Gellings and H. Bouwmeester, *Handbook of solid state electrochemistry*. CRC Press, 2010.

[226] J. D. Benck, Z. Chen, L. Y. Kuritzky, A. J. Forman, and T. F. Jaramillo, "Amorphous Molybdenum Sulfide Catalysts for Electrochemical Hydrogen Production: Insights

into the Origin of their Catalytic Activity," *ACS Catalysis*, vol. 2, pp. 1916–1923, Sept. 2012.

[227] J. Buffle, Z. Zhang, and K. Startchev, "speciation at (bio) interfaces. Part I: Critical evaluation and compilation of physicochemical parameters for complexes with simple ligands and fulvic/humic substances," *Environmental Science & Technology*, 2007.

[228] M. Selvan, J. Liu, D. Keffer, S. Cui, B. Edwards, and W. Steele, "Molecular Dynamics Study of Structure and Transport of Water and Hydronium Ions at the Membrane/Vapor Interface of Nafion," *Journal of Physical Chemistry C*, vol. 112, pp. 1975–1984, Feb. 2008.

[229] P. Atkins, *Physical Chemistry*. Oxford Univ. Press, 9th ed., 2010.

[230] R. T. Ferrell and D. M. Himmelblau, "Diffusion coefficients of hydrogen and helium in water," *AIChE Journal*, vol. 13, pp. 702–708, July 1967.

[231] J. V. Macpherson and P. R. Unwin, "Determination of the diffusion coefficient of hydrogen in aqueous solution using single and double potential step chronoamperometry at a disk ultramicroelectrode.," *Analytical chemistry*, vol. 69, pp. 2063–9, June 1997.

[232] J. Zhang, *PEM fuel cell electrocatalysts and catalyst layers: fundamentals and applications*. 2008.

[233] A. Cornell, "A first course in electrode processes," *Journal of Applied Electrochemistry*, 2010.

[234] J. Clark and D. Macquarrie, *Handbook of green chemistry and technology*. Wiley, 2008.

[235] A. M. A. Bond, K. B. K. Oldham, and C. C. G. Zoski, "Steady-state voltammetry," *Analytica Chimica Acta*, vol. 216, pp. 177–230, Jan. 1989.

[236] P. Christensen, "Electrochemical Aspects of STM and Related Techniques," *Chem. Soc. Rev.*, no. October, 1992.

[237] L. Guczi and A. Erdohelyi, *Catalysis for alternative energy generation*. 2012.

[238] K. Rempel, A. Migdisov, and A. Williams-Jones, "The solubility and speciation of molybdenum in water vapour at elevated temperatures and pressures: Implications for ore genesis," *Geochimica et Cosmochimica Acta*, vol. 70, pp. 687–696, Feb. 2006.

[239] Www.hardassetalliance.com, "Pt Price (USD/kg)," 2014.

[240] Www.infomine.com, "Mo Price (USD/tonne)," 2014.